

THÈSE

En vue de l'obtention du

DOCTORAT DE L'UNIVERSITÉ DE TOULOUSE

Délivré par :

Institut National Polytechnique de Toulouse (INP Toulouse)

Discipline ou spécialité :

Science et Génie des Matériaux

Présentée et soutenue par :

Mme CAITLIN MAE HURLEY

le jeudi 3 septembre 2015

Titre :

ROLE DE L'HYDROGENE DANS LA CORROSION DES ALLIAGES BASE NICKEL EN MILIEU PRIMAIRE DES REP: ETUDE CINETIQUE DES MECANISMES D'ABSORPTION ET DE PIEGEAGE

Ecole doctorale :

Sciences de la Matière (SDM)

Unité de recherche :

Centre Interuniversitaire de Recherche et d'Ingénierie des Matériaux (C.I.R.I.M.A.T.)

Directeur(s) de Thèse :

M. ERIC ANDRIEU

MME CHRISTINE BLANC

Rapporteurs :

M. ALAN TURNBULL, NATIONAL PHYSICAL LABORATORY

M. XAVIER FEAUGAS, UNIVERSITE DE LA ROCHELLE

Membre(s) du jury :

M. DAVID DELAFOSSE, ECOLE NLE SUP DES MINES SAINT ETIENNE, Président

M. DANIEL CAILLARD, CEMES TOULOUSE, Membre

M. ERIC ANDRIEU, INP TOULOUSE, Membre

M. FRANTZ MARTIN, CEA SACLAY, Membre

M. HANNU HANINNEN, AALTO UNIVERSITY, Membre

M. LOIC MARCHETTI, CEA MARCOULE, Membre

Membres du jury invités :

Pr. Christine BLANC (ENSCIACET-CIRIMAT)
and
D.R. Jacques CHÊNE (CNRS)

Thanks - Remerciments

I would like to first thank all of the defense committee members, Pr. Xavier Feaugas, Dr. Alan Turnbull, Pr. Hannu Hänninen, Pr. David Delafosse and D.R. Daniel Caillard, who have graciously accepted to be a part of this committee and to have read, judged and provided feedback on this manuscript.

Dans un premier temps, je tiens à remercier tous les membres de jury: Pr. Xavier Feaugas, Dr. Alan Turnbull, Pr. Hannu Hänninen, Pr. David Delafosse et D.R. Daniel Caillard, d'avoir accepté gracieusement de participer à ce jury de thèse et d'avoir lu, jugé et donné leur avis sur le manuscrit.

Je vais écrire le reste en français car si j'écris
en anglais il va falloir qu'un "native English speaker" le relis...

Je remercier particulièrement Dr. Frantz Martin et Dr. Loïc Marchetti, co-encadrants de cette thèse et chercheurs respectivement au CEA de Saclay et de Marcoule, pour leur encadrement impeccable, leur conseils, leur gentillesse et bonne humeur mais surtout pour leur confiance en moi. J'aimerais aussi remercier D.R. Jacques Chêne, également co-encadrant de cette thèse, pour son aide, ces conseils et les discussions. Vous m'avez tout appris sur l'hydrogène et sur les acteurs et films américains (i.e. le great Robert Redford). Je ne sais pas où je serais sans vous trois. Vous avez formé vraiment la meilleur équipe, la "Dream Team" des encadrants.

Je remercie Pr. Christine Blanc et Pr. Eric Andrieu, co-directeurs de cette thèse et professeurs à l'INP de Toulouse (ENSIACET-CIRIMAT), pour tous leurs conseils et leur aide durant ces trois ans. Malgré la distance j'ai beaucoup apprécié travailler avec vous.

Je tiens à remercier toute la fine équipe du Laboratoire d'Etude de la Corrosion Aqueuse et les ex-membres de l'équipe du CEA de Saclay avec qui j'ai eu vraiment la chance de partager ces trois ans. Je vous suis reconnaissante pour votre accueil chaleureux le 2 octobre 2012. Merci de m'avoir inclue toute de suite dans la vie du laboratoire. Je n'oublierai jamais le labyrinthe du bâtiment 458, les heures passées dans la salle café en train de rigoler et parler de tout et n'importe quoi, les sorties du labo comme l'accrobranche et la randonnée des vingt-cinq bosses ("coureur!"), l'équipe du LECADORS/LECA D'OR pour la course de la fête de la musique et du sport du CEA et nos midis sportifs dans les bois autour du centre. C'est grâce à vous tous que ces trois dernières années étaient si bien passées...je n'ai pas les mots en français ni en anglais pour vous exprimer toute ma reconnaissance et ma joie d'avoir été avec vous. Un petit mot, en plus, pour ma collègue et proche amie, Elizabeth (Chaumun) Deneuvillers, pour son soutien et son amabilité (et les câlins quand la journée était difficile et stressante).

Également, je souhaite remercier toutes les personnes en dehors du laboratoire avec qui j'ai eu la chance de travailler au cours des trois ans : Dr. Clara Desgranges (LM2T, pour ses conseilles et l'aide avec la numérique), Mme. Marie Christine Lafont (CIRIMAT-ENSIACET, pour les observations MET), M. Bruno Coltrinari (pour les ampoules en quartz), M. Daniel Nunes (pour son aide avec les traitements thermiques), l'équipe d'OCAS NV à Gand (pour leur aide, ténacité et patience sur nos essais), toutes personnes avec qui j'ai travaillé pendant la semaine à Toulouse ansi que les personnes avec qui j'ai pu discuter durant cette période, vous êtes trop nombreux pour être tous nommés, mais sachez que votre aide a été inestimable.

Ces trois ans n'auraient pas été possible sans mes amis parisiens et surtout "les tards": Sara, Michelle, Michèle, Fernando, Paolo et Guillaume...les amis qui sont devenus ma famille au cours des dernières années. Même de loin je resterais toujours votre petite Cutelin. Je n'ai aucun souvenir partagé avec vous qui n'est pas rempli de bonheur, de sourires et de rire. Aussi, un petit mot et thank you pour mon copain, je te remercie mille fois pour ton soutien, ta sérénité, de m'avoir supporté et d'avoir partagé cette expérience (même parfois de loin) avec moi...and now à le prochain chapitre.

Finally, I would like to thank my family and friends back home for all they have done, even from a far. You have always pushed me to be my best and it is thanks to all your support over the past twenty-six years that this was all possible.

P.S. pour tous qui se demandent...Nabilla n'est pas morte.

P.P.S. vous allez tous me manquer enormement!!!

Résumé

Dans les réacteurs nucléaires à eau pressurisée (REP) encore en service dans le parc nucléaire civil français, certaines pièces en contact avec le milieu du circuit primaire, comme les éléments constitutifs des tubes de générateurs de vapeur (en alliage base nickel A600) ou les internes de cuve (en acier inoxydable 316L), sont sujettes à des phénomènes de corrosion sous contrainte (CSC). La mise en évidence expérimentale de la fissuration par CSC de l'alliage A600, réputé résistant, a conduit à de nombreuses études consacrées à la description et à la compréhension de ce phénomène de CSC en milieu primaire des REP. Dans l'optique d'un allongement de la durée de vie des réacteurs en service, il est rapidement devenu critique et stratégique de pouvoir modéliser ces phénomènes de CSC, afin d'optimiser les matériaux, conditions de fonctionnement etc. et d'appréhender les paramètres critiques pour limiter la CSC des composants.

Cette étude s'intéresse au rôle de l'hydrogène dans le phénomène de CSC et plus particulièrement aux interactions H-matériau. En effet, l'hydrogène, venant du milieu primaire (H dissous ou H de l'eau), peut être absorbé par l'alliage pendant le processus d'oxydation au cours du fonctionnement du réacteur. Une fois absorbé, H peut être transporté à travers le matériau, interagissant à la fois avec les sites interstitiels du réseau cristallin et des défauts locaux, comme les dislocations, les précipités, les lacunes, etc. La présence de ces sites peut ralentir le transport de l'hydrogène et provoquer une accumulation locale d'hydrogène dans l'alliage. Cette accumulation pouvant modifier les propriétés mécaniques locales du matériau et favoriser sa rupture prématurée, il est essentiel d'identifier la nature de ces interactions H-matériau, et plus particulièrement la vitesse de diffusion et les cinétiques de piégeage de l'hydrogène sur ces défauts.

Concernant ces interactions H-piège, la littérature propose très peu de données cinétiques complètes ; il est donc nécessaire d'étudier et caractériser ces interactions finement. Ce travail est composée de deux parties interdépendantes : (i) le développement d'un code de calcul capable de gérer les interactions H-matériau et (ii) l'extraction les données cinétiques de piégeage et de dépiégeage à partir de résultats expérimentaux afin d'alimenter le code de calcul et créer une base de données fiable.

Du fait de la complexité des matériaux industriels (A600 et 316L), des "matériaux modèles" ont été élaborés en utilisant une série de traitements thermomécaniques permettent d'étudier des systèmes simples et de décorréler les différentes contributions possibles entre hydrogène interstitiel et piégé. Ces échantillons ont été chargés en deutérium (traceur isotopique de l'hydrogène) par polarisation cathodique. Après chargement, les échantillons ont été soumis à un essai de spectroscopie de

désorption thermique (TDS) où le flux de désorption de deutérium est enregistré pendant une rampe de température et/ou un isotherme. L'extraction des données de diffusion interstitielle et des constantes cinétiques de piégeage se fait par une démarche d'ajustement des spectres expérimentaux obtenus par TDS acquis sur les "matériaux modèles" en utilisant un code de calcul basé sur la résolution numérique des équations de McNabb et Foster.

Grâce à cette étude, les coefficients de diffusion de l'hydrogène ont pu être déterminés dans deux alliages (A600 et 316L) sur une grande gamme de températures. Les constantes cinétiques relatives au piégeage et au dépiégeage sur deux types de pièges (défauts), les carbures de chrome et les dislocations, ont été déterminées. Ces constantes constituent une base de données qui sera intégrée dans un modèle numérique plus large visant à simuler les phénomènes de CSC dans les REP.

Mots clés : alliage base nickel, alliage inoxydable, corrosion sous contrainte, diffusion, hydrogène, piégeage, spectroscopie de désorption thermique

Summary

In France all of the nuclear power plant facilities in service today are pressurized water reactors (PWR). Some parts of the PWR in contact with the primary circuit medium, such as the steam generator tubes (fabricated in nickel base alloy A600) and some reactor core internal components (fabricated in stainless steel 316L), can fall victim to environmental degradation phenomena such as stress corrosion cracking (SCC). In the late 1950's, H. Coriou observed experimentally and predicted this type of cracking in alloys traditionally renowned for their SCC resistance (A600). Just some 20 to 30 years later his predictions became a reality. Since then, numerous studies have focused on the description and comprehension of the SCC phenomenon in primary water under reactor operating conditions. In view of reactor lifetime extension, it has become both critical and strategic to be capable of simulating SCC phenomenon in order to optimize construction materials, operating conditions, etc. and to understand the critical parameters in order to limit the damage done by SCC.

This study focuses on the role hydrogen plays in SCC phenomenon and in particular H-material interactions. Hydrogen, from primary medium in the form of dissolved H gas or H from the water, can be absorbed by the alloy during the oxidation process taking place under reactor operating conditions. Once absorbed, hydrogen may be transported across the material, diffusing in the interstitial sites of the crystallographic structure and interacting with local defects, such as dislocations, precipitates, vacancies, etc. The presence of these [local defect] sites can slow the hydrogen transport and may provoke local H accumulation in the alloy. This accumulation could modify the local mechanical properties of the material and favor premature rupture. It is therefore essential to identify the nature of these H-material interactions, specifically the rate of H diffusion and hydrogen trapping kinetics at these defects. Concerning these H-trap site interactions, literature presents very few complete sets of kinetic data; it is therefore necessary to study and characterize these interactions in-depth. This work is composed of two interdependent parts: (i) the development of a calculation code capable to manage these H-material interactions and (ii) to extract the kinetic constants for trapping and detrapping from experimental results in order to fuel the simulation code and create a solid database.

Due to the complexity of industrial materials (A600 and SS316L), "model materials" were elaborated using a series of thermomechanical treatments allowing for the study of simplified systems and the deconvolution of the different possible trapped and interstitial hydrogen contributions. These "model" specimens were charged with deuterium (an isotopic hydrogen tracer) by cathodic polarization. Af-

ter charging, specimens were subjected to thermal desorption mass spectroscopy (TDS) analysis where the deuterium desorption flux is monitored during a temperature ramp or at an isotherm. Interstitial diffusion and kinetic trapping and detrapping constants were extracted from experimental TDS spectra using a numerical fitting routine based upon the numerical resolution of the McNabb and Foster equations.

This study allowed for the determination of the hydrogen diffusion coefficient in two alloys, Ni base alloy 600 and stainless steel 316L, and the kinetic trapping and detrapping constants at two trap site types, chromium carbides and dislocations. These constants will be used to construct a kinetic database which will serve as input parameters for a numerical model for the prediction and simulation of SCC in PWRs.

Key words: diffusion, hydrogen, nickel base alloy, stainless steel, stress corrosion cracking, thermal desorption mass spectroscopy, trapping

Contents

1 Introduction **41**
- 1.1 Context and objectives . . . 43
- 1.2 PWR operation . . . 44
- 1.3 Hydrogen and Stress Corrosion Cracking . . . 45
- 1.4 Manuscript objectives and organization . . . 46

2 Literature Review **47**
- 2.1 Stress Corrosion Cracking in NPPs . . . 49
- 2.2 Role of hydrogen in SCC . . . 51
- 2.3 Hydrogen absorption mechanisms . . . 52
  - 2.3.1 Hydrogen absorption in gaseous environments . . . 53
  - 2.3.2 Hydrogen absorption in aqueous environments: cathodic charging . . . 53
  - 2.3.3 Hydrogen absorption mechanisms in primary water . . . 54
- 2.4 Hydrogen diffusion and trapping in metals . . . 55
  - 2.4.1 Diffusion interactions . . . 56
  - 2.4.2 Trapping interactions . . . 63
  - 2.4.3 Models describing hydrogen - trap site interactions . . . 74
- 2.5 Experimental analysis of H-material interactions . . . 81
  - 2.5.1 A brief review of common methods . . . 81
  - 2.5.2 Thermal desorption mass spectroscopy . . . 85
  - 2.5.3 TDS spectral analysis . . . 85
- 2.6 Conclusions . . . 92

3 Materials and Method **95**
- 3.1 Model material fabrication & characterization . . . 97
  - 3.1.1 Material characterization techniques . . . 99
  - 3.1.2 As-received material characterizations . . . 101
  - 3.1.3 Pure diffusion system (PDS) . . . 103
  - 3.1.4 Diffusion and trapping system - Dislocations . . . 110
  - 3.1.5 Diffusion and trapping system - Chromium carbides (Cr_xC_y) 115

3.1.6 Material overview . . . 116
3.2 Experimental method: TDS . . . 119
3.2.1 Sample preparation: mechanical polishing . . . 119
3.2.2 Sample preparation: deuterium (^{2}H) charging . . . 120
3.2.3 TDS testing . . . 123
3.2.4 TDS calibration . . . 125
3.3 Numerical simulation method . . . 128
3.3.1 Mathematical model and simulation approach . . . 130
3.3.2 Experimental parameters . . . 131
3.3.3 Trapping parameters . . . 138
3.3.4 Simulation advancements . . . 146
3.3.5 Conclusions on numerical simulation method . . . 147
3.4 Chapter summary . . . 148

4 Results **149**
4.1 Deuterium charging of Model Materials . . . 151
4.2 Experimental TDS observations . . . 153
4.2.1 TDS spectra immediately after ^{2}H charging . . . 153
4.2.2 TDS spectra after aging . . . 160
4.3 Numerical simulation . . . 178
4.3.1 Diffusion coefficient derivation . . . 179
4.3.2 Deriving kinetic trapping and detrapping constants . . . 195
4.4 Brief conclusions . . . 208

5 Discussion and Perspectives **211**
5.1 ^{2}H Diffusion in A600 and SS316L . . . 213
5.2 ^{2}H Trapping in A600 . . . 216
5.2.1 Comments on derived activation energies (E_k, E_p) and their relation to the activation energy of interstitial diffusion (E_D) 216
5.2.2 Trapping at chromium carbides . . . 219
5.2.3 Trapping at dislocations . . . 223
5.2.4 General comments on k_0'/p_0 relationship . . . 223
5.2.5 Trap site density . . . 224
5.3 Technical perspectives . . . 226
5.3.1 Effect of charging solution . . . 226
5.3.2 TDS system improvements . . . 227
5.4 Scientific perspectives . . . 228
5.4.1 Model materials . . . 228
5.4.2 Desorption mechanism . . . 234

6 Conclusions **235**
6.1 General overview of the study 237
6.2 Final conclusions 238

7 Résumé en français **243**
7.1 Contexte et objectifs 245
7.1.1 Principe de fonctionnement d'un REP 245
7.1.2 Hydrogène et corrosion sous contrainte 247
7.1.3 Plan et objectifs du manuscrit 249
7.2 Etat de l'art : résumé 249
7.3 Matériaux et Méthodes: résumé 251
7.3.1 Matériaux 251
7.3.2 Technique expérimentale et méthode numérique 252
7.4 Résultats : résumé 255
7.4.1 Observations expérimentales issues des spectres TDS 256
7.4.2 Simulation de la diffusion de ^{2}H dans l'A600 et le SS316L . . 258
7.4.3 Simulation du piégeage de ^{2}H dans l'alliage 600 262
7.5 Conclusions 266
7.5.1 Vue d'ensemble des résultats obtenus dans le cadre de cette étude 267
7.5.2 Conclusions finales 268

List of variables

Variable	units	name
α	–	near neighbor factor
α_s	–	segregation factor pre-exponential factor
α_{c}	TS.cm^{-2} interface	trap sites per interface surface area
α_{d}	TS.cm^{-1} dislocation	trap sites per dislocation length
γ	–	hydrogen atom jump probability
δ	nm	grain boundary width
ϵ	%	deformation percent
$\dot{\varepsilon}$	s^{-1}	deformation rate
θ	–	fraction of occupied traps
θ_L	–	fraction of occupied lattice sites
θ_x	–	fraction of occupied trap sites
λ	nm	lattice spacing in the matrix
μ	mol H.mol A600^{-1}	interstitial hydrogen concentration
$\bar{\mu}$	GPa	shear modulus
μ_0	mol H.mol A600^{-1}	hydrogen surface concentration
π	–	Pi
$\rho_{\mathrm{dislocations}}$	cm^{-2}	dislocation density
τ	s	relative time of H transfer from one site to another
ϕ	K.min^{-1}	temperature ramp rate
ψ	–	trap capture probability
A	–	trap site "activity"
b	nm	Burger's vector
c_0	mol.cm^{-3}	hydrogen surface concentration
c_f	mol.cm^{-3}	interstitial hydrogen concentration
c_L	mol.cm^{-3}	local interstitial hydrogen concentration
c_{t0}	TS.cm^{-3}	concentration of all trap sites
c_T	mol.cm^{-3}	total local hydrogen concentration
c_x	mol.cm^{-3}	local trapped hydrogen concentration
$\bar{C}$	kJ.mol^{-1}	hydrogen chemical potential
d	μm	average grain size
$\bar{d}$	cm	average diameter
D	cm^2.s^{-1}	diffusion coefficient
D_{app}	cm^2.s^{-1}	apparent diffusion coefficient
D_{eff}	cm^2.s^{-1}	effective diffusion coefficient

D_{GB}	$\mathrm{cm}^2.\mathrm{s}^{-1}$	grain boundary diffusion coefficient
D_H	$\mathrm{cm}^2.\mathrm{s}^{-1}$	diffusion coefficient of hydrogen
D_{isotope}	$\mathrm{cm}^2.\mathrm{s}^{-1}$	diffusion coefficient of a hydrogen isotope
D_0	$\mathrm{cm}^2.\mathrm{s}^{-1}$	diffusion pre-exponential constant
E	V	potential
E_B	$\mathrm{kJ.mol}^{-1}$	trap site binding energy
E'_B	$\mathrm{kJ.mol}^{-1}$	novel trap site binding energy
E_D	$\mathrm{kJ.mol}^{-1}$	diffusion activation energy
E_k	$\mathrm{kJ.mol}^{-1}$	trapping activation energy
E_p	$\mathrm{kJ.mol}^{-1}$	detrapping activation energy
E_s	$\mathrm{kJ.mol}^{-1}$	chemical potential difference between an octahedral site and a site in the grain boundary
f	–	volume fraction of grain boundaries
$\bar{f}$	$\mathrm{C.mol}^{-1}$	Faraday constant
$\tilde{f}$	cm^2	"permeablity"
F	$\mathrm{mol.s}^{-1}$	flux
$\bar{G}$	kJ	trap site enthalpy
i	A	ionic current
j	$\mathrm{mA.cm}^{-2}$	current density
k	s^{-1}	trapping kinetic constant
k_0	s^{-1}	trapping pre-exponential constant
k'_0	$\mathrm{cm}^3.\mathrm{s}^{-1}$	trapping pre-exponential constant
k_B	$\mathrm{m}^2.\mathrm{kg.s}^{-2}.\mathrm{K}^{-1}$	Boltzmann constant
K	–	equilibrium constant for trapped and interstitial hydrogen populations
K_d	–	factor which considers dislocations which lie parallel to thin foil normal
$\bar{l}$	–	mean linear intercept of grains
L	cm	specimen thickness
$L_{\mathrm{dislocatoin}}$	cm	dislocation length
m/z	–	mass to charge ratio (MS)
m_{H}		mass of hydrogen
m_{isotope}		mass of hydrogen isotope
$\bar{n}$	$\mathrm{mol.cm}^{-3}$	total hydrogen concentration
N	mol TS.mol material	trap site density
N'_{c}	$\mathrm{mol\ TS.cm}^{-3}$	chromium carbide trap site density
N'_{d}	$\mathrm{mol\ TS.cm}^{-3}$	dislocation trap site density
N_L	$\mathrm{sites.cm}^{-3}$	density of intersititial sites
N_x	$\mathrm{sites.cm}^{-3}$	density of trap sites

p	s^{-1}	detrapping kinetic constant
$\bar{p}$	–	volumic proportion of a site around a point in matrix
p_0	s^{-1}	trapping pre-exponential constant
Q_{total}	mol	TDS spectrum integral
R	$kJ.K^{-1}.mol^{-1}$	ideal gas constant
s	–	segregation factor
S	$mol.cm^{-3}$	solubility of hydrogen in a matrix
t	s	time
t_{charging}	s	charging time
t_{aging}	s	aging time
t_d	s	time before testing (aging time)
t_f	s	final time
t_s	s	charging time
t_{transfer}	s	transfer time
T	K	temperature
T_0	K	temperature at start of TDS testing
T_{aging}	K	aging temperature
T_{charging}	K	charging temperature
T_d	K	temperature before testing (aging temperature)
T_f	K	final temperature
$T_{\text{iso-HT}}$	K	temperature f high temperature isotherm
$T_{\text{iso-RT}}$	K	temperature of room temperature isotherm
T_m	K	temperature of maximum desorption flux (TDS)
T_s	K	charging temperature
T_{transfer}	K	transfer temperature
V_{image}	cm^3	(microscope) image volume
V_m	$cm^3.mol^{-1}$	molar volume
x	(cm)	for position coordinates
X_C	cm	location of “trapping front” in material
y	(cm)	for coordinates
y_t	$(cm.s^{-1})$	“unknown” trapping parameter
y_{t0}	$(cm.s^{-1})$	“unknown” trapping parameter prefactor
z	(cm)	for position coordinates

List of abbreviations

Abbreviation	full name
^{2}H	deuterium
^{3}H	tritium
A600	Nickel base Alloy 600
AR	As-Received
bcc	body centered cubic
BWR	Boiling Water Reactor
CE	Counter Electrode
CEA	Atomic Energy Commission (France)
CEPM	Corrosion Enhanced Plasticity Model
Cr_xC_y	Chromium carbides
DFT	Density Functional Theory
DSC	Differential Scanning Calorimetry
DTS	Diffusion and Trapping System
EDM	Electrical Discharge Machining (spark erosion)
EDS	Energy Dispersion X-ray Spectroscopy
ENS	Elastic Neutron Scattering
EP	Electrochemical Permeation
fcc	face centered cubic
FEG	Field Emission Gun
GB	Grain Boundary
GBC	Grain Boundary Carbides
GND	Geometrically Necessary Dislocations
H_{abs}	absorbed hydrogen
H_{ads}	adsorbed hydrogen
H_{co}	H in commercial SS316L
H_{HT}	H in heat treated SS316L
HE	Hydrogen Embrittlement
HEDE	Hydrogen Enhanced DEcohesion
HELP	Hydrogen Enhanced Localized Plasticity
HESV	Hydrogen Enhanced Stress Induced Vacancy (mechanism)
HSLA	High Strength Low Alloyed (steel)
IASCC	Irradiation Assisted Stress Corrosion Cracking
IIC	Inter- Intragranular Chromium carbides
HP	High Pressure
HT	High Temperature

LAC	Low-Alloy Carbon (steel)
LECA	Aqueous Corrosion Laboratory (CEA-Saclay)
LECNA	Non-Aqueous Corrosion Laboratory (CEA-Saclay)
LEM	Local Equilibrium Model
LWR	Light Water Reactor
M	Metal
MM	Model Material
n.s.	non-specified
NEM	Non-Equilibrium Model
NPP	Nuclear Power
NUS	Non-Uniform Solubility (model)
OM	Optical Microscope
PAS	Positron Annihilation Spectroscopy
PDS	Pure Diffusion System
PWR	Pressurized Water Reactor
Py	Python™
RE	Reference Electrode
RSW	Resistive Spot Welding
s.c.	single crystal
SEM	Scanning Electrom Microscope
SG	Steam Generator (tubes)
SCC	Stress Corrosion Cracking
SS316L	Stainless Steel 316L
TDS	Thermal Desorption mass Spectroscopy
TEM	Transmission Electron Microscopy
TiCN	Titanium Carbo-Nitrides
TPD	Temperature Programed Desorption
TS	Trap Site
TT	Thermal Treatment
WE	Working Electrode
WM	WolframMathematica©
XRD	X-Ray Diffraction

List of Model Materials

Notation	Complete description
A600-AR	As Received nickel base Alloy 600
A600-PDS	nickel base Alloy 600 Pure Diffusion System
A600-DTS-D-20T	nickel base Alloy 600 Diffusion and Trapping System with Dislocations created by a 20 % deformation by interrupted Tensile testing as the major trap sites
A600-DTS-D-40T	nickel base Alloy 600 Diffusion and Trapping System with Dislocations created by a 40 % deformation by interrupted Tensile testing as the major trap sites
A600-DTS-GBC	nickel base Alloy 600 Diffusion and Trapping System with chromium carbides inter- and intragranularly
A600-DTS-IIC	nickel base Alloy 600 Diffusion and Trapping System with chromium carbides inter- and intragranularly
A600-like s.c.	model nickel base Alloy 600 Single Crystal
SS316L-AR	As Received Stainless Steel 316L
SS316L-PDS	Stainless Steel 316L Pure Diffusion System
SS316L-DTS-D-20T	Stainless Steel 316L Diffusion and Trapping System with Dislocations created by a 20 % deformation by interrupted Tensile testing as the major trap sites
SS316L-DTS-D-40T	Stainless Steel 316L Diffusion and Trapping System with Dislocations created by a 40 % deformation by interrupted Tensile testing as the major trap sites

List of Figures

1.1 Map of localization of nuclear reactors in France (www.world-nuclear.org) 43
1.2 Typical Pressurized Water Reactor design (www.world-nuclear.org). 44
1.3 Diagram of potential hydrogen diffusion and trapping sites in a crystalline material: (a) interstitial site, (b) surface and (c) subsurface sites, (d) grain boundaries, (e) dislocations and stress fields and (f) vacancies [1]. 46

2.1 Stress corrosion crack in Ni base alloy 600 after exposure in high temperature water [2]. 50
2.2 Fracture surfaces of Ni-base alloy X-750 specimens tested in (a) hydrogenated gas at 611 K and (b) hydrogenated water at 633 K [8]. 51
2.3 Schematic energy diagram for interstitial diffusion in a *fcc* material. 57
2.4 Room temperature (a) permeation and (b) degassing data in (i) single crystal (ii) small (25 μm) grain, (iii) large (150 μm) grain and (iv) in (b) cold worked pure Ni specimen showing the influence of microstructure (specifically grain size) on diffusivity and hydrogen flux [54]. The simulated Fick's diffusion profiles for constant H concentration and constant H flux can also be seen in (b) [54]. . . . 58
2.5 Audioradiographs of a polycrystalline pure nickel specimen exposed 46 h at 253 K to tritium (a) after 24 h of aging and (b) after 10 days of aging [53] at 253 K. The light areas highlight the location of tritium in the specimen. 59
2.6 High temperature (373 K) permeation in (i) small (25 μm) grain, (ii) large (150 μm) grain and (iii) in (b) cold worked pure Ni specimen as compared to Fick's diffusion profile showing the influence of microstructure (specifically grain size) on diffusivity. 60
2.7 Effective diffusion coefficient (D_{eff}) of H in high purity (99.99%) polycrystalline Ni (grain size 10 nm - 168 μm) at 298 K with regards to grain size as reported by Oudriss *et al.* [57]. 61
2.8 Arrhenius plot of [corrected (Eq. (2.8) [65])]diffusion data for H and its isotopes in Ni-base alloy 600 [40, 41, 42, 43] and (b) in stainless steel 316L [44, 45, 46, 47, 48]. 63

2.9 Schematic diagram of diffusion and trapping at (a) one TS or (b) at two TS. E_k^1 and E_k^2 and E_p^1 and E_p^2 are the respective trapping and detrapping activation energies associated with the trap site types. . 64

2.10 Trap model energy schematic diagram as presented by Oriani [69]. In this diagram λ refers to the lattice spacing in the matrix. 65

2.11 (a) Electrochemical permeation curves for recrystalized, single crystal and 98 % cold worked pure Ni specimen and (b) decreased diffusivity of H in a HSLA steel in function of cold working percent [73] at 293 K. 66

2.12 (a) Early-stage tritium desorption from small grained, large grained and 98 % predeformed pure Ni specimen measured by β counting at 298 K and (b) ^{3}H desorption from a pre-charged (in tritiated molten salts) γ-Ni base alloy single crystal during tensile testing measured by liquid scintillation counting [73]. 67

2.13 Thermal desorption mass spectroscopy analysis results for hydrogen-vacancy clusters in Ni. The first desorption peak was associated with interstitial diffusion and the two higher temperature peaks were attributed to H binding with vacancies [79]. 68

2.14 Schematic diagram for diffusion and "physical" trapping in the lattice. Two types of "physical" TS are represented (Type 2 and Type 3) along with normal lattice sites (Type 1). All sites have the same potential energy barrier (dotted line), and therefore the H has the same capture probability (ψ) for all sites [112]. 78

2.15 Electrochemical permeation cell diagram. The set-up is split into two electrochemical cells exposing the specimen, the working electrode (WE) to a cathodic environment on the "entry side" and anodic environment on the "exit side" (CE = counter electrode, RE = reference electrode, H_{ads} = adsorbed H, H_{abs} = absorbed H, and $\xrightarrow{\text{diff}}$ = H_{abs} diffusion across the membrane). 83

2.16 Example desorption spectra for a (a) TPD spectrum acquired by M. Mendelsohn *et al.* on hydrogenated zirconium alloy specimen where system pressure evolution was measured in function of time during a temperature ramp [133] and (b) TDS spectrum acquired by E. Tal-Gutelmacher *et al.* on hydrogenated titanium alloy specimen [139] 86

2.17 Example of (a) spectral acquisitions[1] for "Choo-Lee plot" construction and analysis and (b) Gaussian decomposition of an experimental spectrum [141]. 88
2.18 "Choo-Lee" plot analysis for the "TDS" spectra presented in Fig. 2.17 [141]. 88

3.1 Schematic diagram of the NanoTest pendulum. [Original design-[146]] 101
3.2 OM image of A600 heat WL344 (Imphy) in its as received material state. The small black spots seen in the image are chromium carbide (Cr_xC_y) precipitates and the larger more angular black structures have been identified as TiCN by SEM-EDS analysis. 102
3.3 SEM image of the as-received commercial grade SS316L (CEA). The white arrows indicate some of the isolated retained ferrite phases present in the slab. 103
3.4 Diagram of quartz tube encasing used for the TT under vacuum. Two material plaques where encased in each tube and separated by quartz points so as not to touch during the TT. 104
3.5 Diagram detailing the series of thermal and if desired mechanical treatments used to create the studied model materials (MM). * elimination of residual cold working, chromium carbides (if A600) and recrystallization, ** elimination of [thermal] vacancies, *** and **** precipitation of new chromium carbides (A600 only). 105
3.6 (a) SEM and (b) TEM micrograph of A600-PDS MM. In Fig. 3.6b some isolated dislocations can be observed. The white arrows in Fig. 3.6a indicate the TiCN present in the material. 107
3.7 OM image of a SS316L-PDS model material. 108
3.8 Photo of tensile test specimen with extensometer before tensile testing. The grip, extensometer, and test specimen are indicated by the labeled red arrows in the figure. 110
3.9 Experimental stress-deformation curves for tensile tests interrupted at ϵ=20% and ϵ=40% and continued until rupture (only for (b)) for (a) A600 and (b) SS316L. 111
3.10 OM images of A600-DTS-D MM (a) $\epsilon = 20\%$ and (b) $\epsilon = 40\%$ after polishing and electrochemical etching. 112
3.11 TEM thin foil observation of A600-DTS-D ($\epsilon = 40\%$) MM. 113
3.12 Optical microscope observations of the SS316L-DTS-D MM (ϵ=40%). 114

[1]It should be noted that these spectra were acquired using a Jobin Yvon Horiba EMGA-621W gas analyzer system and not a traditional TDS technique. These figures were choosen just for demonstrative purposes.

3.13 OM image of (a) A600-DTS-GBC and (b) A600-DTS-IIC. Micrograph (a) shows the preferential localization of Cr_xC_y along the GBs, whereas (b) a relatively homogeneous reprecipitation along GBs and in volume. 117
3.14 TEM image of A600-DTS-IIC. The white arrows indicate some of the observed chromium carbide precipitates. 118
3.15 TEM image of A600-DTS-IIC and electron diffraction pattern allowing for their identification as Cr_7C_3 type chromium cabrides. . . 118
3.16 Hardness (GPa) in function of depth (nm) measured using nanoindentation (indentation depth $\leq$ 2000 nm) or microindentation (depth $>$ 2000 nm) methods for an A600 PDS (**circles**) and A600 DTS-D $\epsilon = 40$ % (**squares**) model materials. 120
3.17 Diagram of cathodic charging cell used for ^{2}H charging. 121
3.18 Chronopotentiometry results for charging conditions A, see Table 3.6, for (a) SS316L and (b) A600 materials. 122
3.19 Photo of thermal desorption mass spectrometry experimental system at the Laboratoire d'Etude de la Corrosion Aqueuse (LECA) at the CEA Saclay. 123
3.20 Schematic diagram for the thermal desorption mass spectrometry experimental system at the Laboratoire d'Etude de la Corrosion Aqueuse (LECA) at the CEA Saclay. In this diagram V = valve, P = vacuum pump and M.S. = mass spectrometer. 124
3.21 Calibrated LACO Inc. CALMASTER^{TM} deuterium ($^2H_2$) leak standards attached to TDS system by in V2 Fig. 3.20. 125
3.22 TDS calibration spectrum: (a) raw calibration data for all four calibrated leaks, the corresponding leak rate in $mol.s^{-1}$ for each leak is shown on the graph, (b) the mesured flux for calibrated leak 5.02 10^{-11} mol.s^{-1} during a temperature ramp (ϕ = 10 K.min^{-1}) repeated twice, and (c) the final calibration curve showing the correlation between the measured ionic current at m/z = 4 (A) and the real molecular flux (mol $^2H_2$.s^{-1}). 127
3.23 Logic diagram for the numerical approach used to derive diffusion and trapping parameters [90]. 129
3.24 Simulated normalized interstitial and trapped hydrogen concentration profiles after charging. Profiles are normalized to the maximum total H concentration (interstitial + trapped) for each type. 132
3.25 Simulated normalized TDS spectrum immediately after hydrogen charging for Type A and Type B charging. 133
3.26 Simulated normalized concentration profiles for charging Type A and Type B after 30 min of aging at 298 K 133

3.27 Simulated normalized TDS spectra for Type A and Type B charging subjected to 30 min of aging at 298 K between charging and TDS ($\phi = 2$ K.min^{-1}). All desorption flux ($x = 0$ and $x = L$) are shown. 135

3.28 Simulated theoretical desorption spectra for ϕ ranging from 2 - 15 K.min $^{-1}$ for charging (a) Type A and (b) Type B. Simulations incorporated a 30 min aging period between charging and TDS analysis. 135

3.29 Choo-Lee plots for all observed peaks in simulated TDS spectra for pure Fe charged Type A and Type B seen in Fig. 3.28 and the corresponding T_m and derived E_p values. 136

3.30 Effect of sample thickness on final desorption spectra ($\phi = 2$ K.min^{-1}) for a charging of Type B aged 30 min at room temperature between charging and TDS. The graphic insert presents the concentration profiles (after aging) before TDS with normalized L (y-axis: concentration (mol) and x-axis: normalized sample thickness (x/L)) . . 137

3.31 Simulated TDS spectrum for a linear theoretical T ramp ($\phi = 2$ K.min^{-1}) as compared to an experimental T ramp ($\phi = 2$ K.min^{-1}). The graphic insert shows the linear T ramp as compared to an experimental acquired T ramp: y-axis: T (K), x-axis: t (s). 138

3.32 Effect of pre-exponential factor: (a) k_0 and (b) p_0, on simulated TDS spectra (ϕ= 2 K.min^{-1}) for aged (30 min at 298 K) samples of charging Type B 140

3.33 Influence of k_0/p_0 with a constant ratio ($k_0/p_0 = 1.25$) on a simulated TDS spectrum ($\phi = 2$ K.min^{-1}), see Table 3.10 for the corresponding k_0 and p_0 simulation values (A−F). The samples were Type B charged (Table 3.9) and aged 30 min at 298 K. 141

3.34 Effect of activation energy: (a) E_k and (b) E_p, on simulated TDS spectra (ϕ= 2 K.min^{-1}) for aged samples of charging Type B. . . . 142

3.35 Influence of E_k and E_p when E_b is held constant at 48 kJ.mol^{-1} on simulated TDS spectra, see Table 3.11 for the corresponding E_k and E_p simulation values (A−F). The samples were supposed charged using Type B conditions (Table 3.9) and aged 30 min at 298 K. . . 144

3.36 Influence of trap site density, N, on simulated TDS spectra, see Table 3.12 for the corresponding imposed trap site densitites in simulations (A−G). The samples were supposed charged using Type B conditions (Table 3.9) and aged 30 min at 298 K. 145

4.1 Graphical representation of deuterium amount (mol) desorbed during TDS testing for A600 model materials: **P**ure **D**iffusion **S**ystem (PDS), A600-like **s**ingle **c**rystal (s.c.), **D**iffusion and **T**rapping **S**ystem-**I**nter **I**ntra-granular **C**arbides (DTS-IIC), **D**iffusion and **T**rapping **S**ystem-**G**rain **B**oundary **C**arbides (DTS-GBC), **D**iffusion and **T**rapping **S**ystem-**D**islocations-ϵ=**40 %** (DTS-D-40T) and **D**iffusion and **T**rapping **S**ystem-**D**islocations-ϵ=**20 %** (DTS-D-20T). 152

4.2 Two TDS desorption spectra (a) before normalization (i.e. quantified spectra) and (b) after normalization by total amount of desorbed deuterium. 153

4.3 Quantified (mol ^{2}H.cm^{-2}.s^{-1}) TDS desorption spectra for A600 MM immediately after deuterium charging. All specimen were charged under Charging conditions A (Table 3.6) and analyzed in TDS using the conditions in Table 4.1 154

4.4 "Normalized" (with regards to total amount of desorbed deuterium) TDS desorption spectra for A600 model materials immediately after deuterium charging. See Fig. 4.3 for quantified spectra. 155

4.5 "Normalized" desorption flux evolution for A600-PDS and A600-like s.c. MMs immediately after ^{2}H charging (Table 3.6, Table 4.1). . . . 156

4.6 "Normalized" desorption flux evolution for A600-PDS and 600-DTS-GBC model materials immediately after ^{2}H charging (Table 3.6, Table 4.1). 157

4.7 "Normalized" desorption flux evolution for A600-PDS and A600-DTS-IIC immediately after ^{2}H charging (Table 3.6, Table 4.1). . . . 158

4.8 "Normalized" desorption flux evolution for A600-PDS and A600-DTS-D-40T model materials immediately after ^{2}H charging (Table 3.6, Table 4.1) 159

4.9 "Normalized" desorption flux evolution of a pre-charged (Conditions A, Table 3.6) A600-PDS MM specimen subjected to 6 hr of room temperature aging followed by TDS analysis ($\phi = 10$ K.min^{-1}) (normalized desorption flux evolution, experimentally measured temperature). 161

4.10 Percentage (%) of total amount of ^{2}H desorbed during the TDS part of the "hybrid" spectra as compared to the total amount of ^{2}H desorbed from the material. 162

4.11 "Normalized" isothermal room temperature (294 ± 2 K) desorption flux spectra for pre-charged (Conditions A, Table 3.6) A600 MMs. The temperature during the isotherm is indicated by the red dotted line. 163

4.12 “Normalized” experimental “hybrid” desorption spectra for 6 h of room temperature aging followed by TDS analysis ($\phi = 10$ K.min^{-1}) for pre-charged (Conditions A, Table 3.6) A600-PDS and A600-like s.c. MM. The temperature is shown in red. The axes of these two plots are not the same, on the left a “double-ordinate axis” plot can be seen with normalized desorption flux on the left-hand ordinate-axis and temperature (K) on the right-hand ordinate-axis, both presented with regards to time on the abscissa-axis, whereas in the “zoomed” plot of only TDS analysis the ordinate-axis is normalized desorption flux and the abscissa-axis is temperature. 164

4.13 Compilatoin of “normalized” TDS spectra performed on A600-DTS-IIC MM **immediately after charging**, **after 1 h**, **after 3 h**, **after 6 h** and **after 12 h** of room temperature aging. A small desorption shoulder is highlighted by the black arrow. 166

4.14 “Normalized” experimental “hybrid” desorption spectra for 6 h of room temperature aging followed by TDS analysis ($\phi = 10$ K.min^{-1}) for pre-charged (Conditions A, Table 3.6) A600-PDS and A600-DTS-IIC MM. The temperature ramp is shown in red. 167

4.15 Compilation of “normalized” TDS spectra after room temperature aging of a pre-charged for A600-DTS-D40T MM for aging durations ranging from 0 h, 6 h, 12 h and 48 h. A small desorption shoulder is highlighted by the black arrows. 169

4.16 “Normalized” experimental “hybrid” desorption spectra for 6 h of room temperature aging followed by TDS analysis ($\phi = 10$ K.min^{-1}) for pre-charged (Conditions A, Table 3.6) A600-PDS and A600-DTS-D-40T MM. The temperature ramp is shown in red. 170

4.17 (a) “Normalized” experimental aging (48 h at RT) and TDS desorption spectra ($\phi = 10$ K.min^{-1}) for pre-charged (Conditions A, Table 3.6) A600-PDS and A600-DTS-D-40T MM and the temperature ramp is shown in red and (b) zoom on the TDS spectra after 48 h of room temperature aging. 171

4.18 “Normalized” high temperature “isothermal” desorption flux spectra (a) for first 2 10^4 s and (b) focused on the desorption peak during the isotherm for pre-charged (Conditions A, Table 3.6) A600 model materials. The temperature is shown in red for the aging period. In (b) the maximum desorption temperature range in t is indicated by the black vertical lines and the corresponding T_m range is written below. 173

4.19 “Normalized” experimental desorption spectra for A600-PDS and A600-like s.c. for (a) aging at 409 K (first 1 10^4 s) and (b) TDS analysis (ϕ = 10 K.min^{-1}). 174
4.20 “Normalized” TDS spectra (ϕ = 10 K.min^{-1}) for A600-PDS and A600-DTS-IIC (inter- and intragranular chromium carbides) after aging 3 h, 6 h or 9 h at 409 K. 176
4.21 “Normalized” TDS spectra (ϕ = 10 K.min^{-1}) for A600-PDS, A600-DTS-GBC and A600-DTS-IIC after aging 6 h at 409 K. 176
4.22 “Normalized” TDS spectra (ϕ = 10 K.min^{-1}) for A600-PDS, A600-DTS-D-40T and A600-DTS-D-20T (diffusion and trapping systems with dislocations) after aging 6 h or 9 h at 409 K. 177
4.23 “Normalized” experimental A600 pure diffusion system experimental desorption flux and simulated TDS spectra calculated using diffusion coefficients for H and its isotopes in A600 from literature [40, 41] in function of time (abscissa-axis) and temperature (ordinate-axis right). 180
4.24 “Normalized” experimental desorption flux acquired on an A600-PDS, simulated TDS spectra calculated using diffusion coefficients for H and its isotopes in A600 [40, 41] and the best-fit calculated using the numerical fitting routine (Table 4.3) in function of time (abscissa-axis) and temperature (ordinate-axis right) 181
4.25 Tolerated calculation error on derived diffusion coefficient. Simulation parameters associated with “A” and “B” can be seen in Table 4.4. Desorption spectra were “normalized” with regards to total desorbed deuterium. 182
4.26 “Normalized” experimental A600 pure diffusion system desorption flux and simulated TDS spectra (6 h isothermal aging at RT, followed by TDS testing with a ϕ = 10 K.min^{-1} temperature ramp rate) calculated using the diffusion coefficients for H and its isotopes found in literature [40, 41] and that derived in this study from a TDS spectrum immediately after ^{2}H charging (Table 4.3). . 183
4.27 Zooms of the pure diffusion experimental and simulated (Table 4.3,[40, 41]) spectra seen in Fig. 4.26: (a) focusing on the beginning of the isothermal (RT) desorption spectra (b) focusing on the isotherm (6 h at RT) and TDS desorption spectra (ϕ = 10 K.min^{-1}). 184
4.28 “Normalized” PDS experimental and simulated (Table 4.3,[40, 41]) desorption spectra for 6 h aging at 409 K followed by TDS analyses (ϕ = 10 K.min^{-1}): (a) shows the total analysis (aging and TDS) and (b) is a zoom of the TDS analysis part showing experimental and simulated spectra. 186

4.29 "Normalized-TP" (i.e. with regards to "TDS part") spectral integrals A600-PDS experimental and simulated TDS desorption spectra using derived ^{2}H (Table 4.3, "This study") and literature [40, 41] diffusion data. 187
4.30 (a) "Normalized-TP" PDS experimental and simulated TDS desorption spectra using the derived ^{2}H diffusion coefficient (Table 4.2, "This study") or "A" (Table 4.4) and (b) simulated spectral contributions with these diffusion coefficients. In (b) -0 and -L refers to the origin of the spectral contribution, respectively either the $x = 0$ face (charged face) or the $x = L$ face (non-charged) face. 188
4.31 "Normalized" A600-like single crystal experimental TDS spectrum immediately after deuterium charging as compared to simulated TDS spectra (a) using the derived diffusion coefficient parameters determined for A600-PDS (Table 4.3) and (b) using the maximum tolerated error parameters associated with "A" and "B" from Table 4.4. 189
4.32 "Normalized" experimental "hybrid" desorption spectrum acquired for an A600-like single crystal aged 6 h in TDS at room temperature ($\approx$ 295 K) followed by TDS analysis ($\phi = 10$ K.min^{-1}) as compared to its simulated TDS spectrum using the derived diffusion coefficient parameters (Table 4.3) determined for A600-PDS model materials. . 190
4.33 "Normalized" isothermal spectrum acquired on desorption A600-like single crystal aged 6 h in TDS at high temperature ($\approx$ 409 K) as compared to its simulated TDS spectrum using the derived diffusion coefficient parameters (Table 4.3) determined for A600-PDS model materials. Only the first 5000 s of the experimental and simulated desorption spectra are shown in this figure to provide a better view of the reproduction of the first desorption peak. 191
4.34 "Normalized" experimental, literature simulated [45, 46] and "best-fit" TDS spectra ($\phi = 10$ K.min^{-1}) for SS316L pure diffusion system model material immediately after ^{2}H charging (Table 3.6). 192
4.35 Normalized experimental and simulated [45, 46] desorption spectra for SS316L-PDS model materials for 6 h of aging at room temperature (294 K) followed by TDS analysis ($\phi = 10$ K.min^{-1}). 193
4.36 "Normalized-TP" experimental and "best-fit" TDS spectra for trapping at chromium carbides (Cr_7C_3, according to TEM diffraction patterns, see Chapter 3) in A600 after aging 6 h at 409 K. 196
4.37 Experimental and simulated "normalized-TP" TDS spectra ($\phi = 10$ K.min^{-1}) after (a) 3 h of aging at 409 K and (b) 9 h of aging at 409 K, used for validation of the derived trapping/detrapping parameters. 197

4.38 (a) "Normalized-TP" experimental and simulated TDS spectrum (aged 6 h at 409 K, ϕ = 10 K.min^{-1}) for a trap site densities (n) ranging from 0.01 10^{-5} mol TS.mol A600^{-1} to 100.0 10^{-5} mol TS.mol A600^{-1}. 198

4.39 Quantified experimental and simulated TDS spectrum (aged 6 h at 409 K, ϕ = 10 K.min^{-1}) for a trap site densities (N) ranging from 0.01 10^{-5} to 100.0 10^{-5} mol TS.mol A600^{-1}. Figure (a) shows all simulations, and (b) shows a zoom of the experimental spectrum. . 199

4.40 Quantified experimental, fitted and simulated TDS spectra for high temperature agings (409 K) of (a) 6 h, (b) 3 h and (c) 9 h using the derived diffusion and trapping/detrapping at chromium carbides parameters (Table 4.3 and Table 4.7) and a trap site density (n) of 1.0 10^{-5} mol TS.mol A600^{-1}. 201

4.41 "Normalized-TP" experimental TDS spectra for A600-DTS-GBC and a simulated (Simulated-IIC) desorption spectra for a sample aged 6 h at 409 K using the kinetic constants seen in Table 4.7. . . 202

4.42 "Normalized-TP" experimental and "best-fit" TDS spectra for diffusion and trapping in A600 with chromium carbides located along the grain boundaries after 6 h of agin at 409 K. A trap site density of 2.5 10^{-6} mol TS.mol A600^{-1} was determined from simulation. . . 203

4.43 Quantified experimental and "best-fit" TDS spectra for diffusion and trapping in A600 with chromium carbides located along the grain boundaries after aging 6 h at 409 K. A trap site density of 2.5 10^{-6} mol TS.mol A600^{-1} was imposed for this simulation. 203

4.44 "Normalized-TP" experimental and "best-fit" TDS spectra (Table 4.9) for trapping at dislocations in A600 after aging 9 h at 409 K. 204

4.45 Experimental and simulated "normalized-TP" desorption spectra for trapping at dislocations in A600 after aging 6 h at 409 K. Simulation was done using the constants seen in Table 4.9. These values are coupled with the diffusion constant presented in Table 4.3. . . . 205

5.1 Arrhenius plots of H diffusion data from literature in (a) A600 [40, 41, 43, 42] and (b) SS316L [44, 45, 46, 47, 48] as compared to the derived D ("This study") from A600 and SS316L pure diffusion system model materials. The error for D is indicated by the dotted gray lines. In (b) H_{co} and H_{HT} refer to the derived hydrogen diffusion coefficient in a commercial or heat treated 316L stainless steel respectively. 214

5.2 Energy diagram for trapping when the trapping activation energy (E_k) is greater than that of interstitial diffusion (E_D), as would be suggested by the derived activation energies for H trapping at chromium carbides (Table 5.2). 217
5.3 Energy diagram for trapping when the trapping activation energy (E_k) is less than that of interstitial diffusion (E_D), as would be suggested by the derived activation energies for H trapping at dislocations (Table 5.2). 217
5.4 Experimental TDS spectra as acquired by Young *et al.* [82] for trapping at chromium carbides. 220
5.5 Simulated (pure diffusion) normalized[2] H concentration profiles recreated using the charging conditions and diffusivity in the publications: (a) Symons *et al.* [22] and (b) Young *et al.* [82] after various aging periods.. 221
5.6 Simulated normalized[3] TDS desorption spectra, to attempt recreation of experimental TDS spectra by Young *et al.* [82] with (a) variation in (linear) temperature ramp and (b) variation in trap site density N. The text located on the figures is to remind the reader of peak identification as stated in the publication [82]. 222
5.7 Some examples of exotic isothermal and ramp desorption testing which may be interesting for trap site isolation: (a) demonstrates an instantaneous temperature jump, isotherm, freeze, TDS combination (b) consecutive instantaneous temperature jumps and isotherms and (c) a mixture of the two previous. 228
5.8 Simulated (a) non-aged and (b) aged 6 h at 409 K TDS spectra (ϕ = 10 K.min^{-1}) for a model A600 material with two trap sites: (i) dislocations (TS1) and (ii) chromium carbides (TS2). 229
5.9 Simulated non-aged TDS spectra (ϕ = 10 K.min^{-1}) for a material with two trap sites (TS1 and TS2) and simulated TDS spectra for each type of isolated trap site TS1 (dislocations) or TS2 (Cr_7C_3). . 230
5.10 Simulated high temperature aged (409 K for 6 h) TDS spectra (ϕ = 10 K.min^{-1}) for a material with two trap sites (TS1 and TS2) and simulated TDS spectra each type of isolated trap site TS1 (dislocations) or TS2 (Cr_7C_3). 231

7.1 Schéma de principe d'un réacteur à eau pressurisée (www.world-nuclear.org). 246

[2]with regards to total amout of H in the specimen immediately after charging
[3]with respect to total mol H desorbed

7.2 Schéma des différents types de sites avec lesquels l'hydrogène est susceptible d'interagir dans un matériau cristallin : site interstitiel (a), sites de surface (b) et de subsurface (c), joint de grains (d), dislocation et champ de contrainte associé (e), et lacune (f) [1]. . . . 248

7.3 Observations microscopique(par microscope électronique à balayage (a) ou microscope optique (b)) du matériau modèle PDS (a) A600 et (b) SS316L. Les flèches blanches indiquent les TiCN qui restent présents dans le matériau même après le traitement thermique. . . . 251

7.4 Observations en microscopie optiques des échantillons DTS-D en (a) A600 et (b) SS316L. 252

7.5 Observations en microscopie optique des échantillons (a) DTS-GBC et (b) DTS-IIC. 253

7.6 Diagramme détaillant la série de traitements thermomécaniques mis en oeuvre afin d'élaborer les matériaux modèles (MM) étudiés. * recristallisation et élimination de l'écrouissage résiduel et des carbures de chrome éventuellement (cas de l'A600), ** élimination des lacunes, *** et **** reprécipitation de carbures de chrome (seulement dans le cas de l'A600). 253

7.7 Diagramme logique de la méthode numérique utilisée pour dériver les paramètres de diffusion et de piégeage/dépiégeage [90]. 256

7.8 Evolution du flux de désorption "normalisé" obtenu sur échantillon de type A600-PDS directement après chargement (Table 3.6) en fonction du temps et de la température (ϕ = 10 K.min^{-1}) ; comparaison (i) aux spectres TDS simulés à l'aide des coefficients de diffusion de H et de ses isotopes dans l'A600 publiés dans la littérature [40, 41] et (ii) ajustement du spectre expérimental à l'aide du code numérique (Table 4.3) développé dans ces travaux. 259

7.9 Evolution du flux de désorption "normalisé" obtenu sur échantillon de type SS316l-PDS directement après chargement (Table 3.6) en fonction du temps et de la température (ϕ = 10 K.min^{-1}) ; comparaison (i) aux spectres TDS simulés à l'aide des coefficients de diffusion de H dans le SS316L publiés dans la littérature [45, 46] et (ii) ajustement du spectre expérimental à l'aide du code numérique (Table 4.3) développé dans ces travaux. 260

7.10 Spectres TDS normalisés, obtenus expérimentalement ou simulés à partir des données publiées [40, 41] et collectées dans le cadre de ces travaux, dans le cas d'un échantillon de type A600-PDS vieilli 6h à température ambiante puis soumis à une expérience de TDS (ϕ = 10 K.min^{-1}). 261

7.11 Spectres TDS normalisés, obtenus expérimentalement ou simulés à partir des données publiées [45, 46] et collectées dans le cadre de ces travaux, dans le cas d'un échantillon de type SS316L-PDS vieilli 6h à température ambiante puis soumis à une expérience de TDS ($\phi =$ 10 K.min^{-1}). 262
7.12 Spectres TDS expérimentaux quantifiés obtenus sur des échantillons d'alliage 600 de type DTS-IIC après des vieillissements à haute température (409 K) de 6 h, 3 h and 9 h ; comparaison avec l'ajustement (pour un vieillissement de 6 h) et les simulations (pour des vieillissements de 3 h et de 9 h) réalisés. Ces simulations s'appuient sur les données de diffusion et les constantes cinétiques de piégeage/dépiégeage déterminées précédemment (Table 4.3 and Table 4.7) ainsi que sur une densité de site de piégeage (n) de 1,0 10^{-5} mol TS.mol A600^{-1}. 264

List of Tables

1.1 Characteristic PWR primary water conditions. 45

2.1 Characteristic PWR primary water conditions. 49
2.2 Literature review of hydrogen trapping constants at various TS. . . 70
2.2 continued. 71
2.2 continued. 72
2.2 continued. 73

3.1 Chemical composition (wt.%) of studied alloys: an industrial Ni-base alloy 600 (A600 heat WL344, Imphy), an A600-like single crystal (s.c.) (Ecole Nationale Supérieur des Mines de Saint-Etienne), and a commercial grade stainless steel of type 316L (SS316L) 98
3.2 Dilute electrochemical etching solutions used to reveal the microstructure of austenitic materials. 99
3.3 Dislocation density for A600-DTS-D (ϵ=20% and ϵ=40%) estimated using the Bailey equation [154], Eq. (3.4), and an average value for a non-deformed PDS material estimated from TEM micrographs using the numerical method presented in Eq. (3.1). 114
3.4 Dislocation density calculated for SS316L-DTS-D MM (ϵ=20% and ϵ=40%) using the Bailey equation [154], Eq. (3.4). A typical dislocation density for heat treated (1.5 h at 1373 - water quench) non-tempered SS316L [159] is given for a comparative purpose. . . . 115
3.5 Table of materials to be studied experimentally (s.c. = single crystal, x = to be studied, – = non-fabricated) 119
3.6 Typical experimental cathodic [deuterium] charging conditions: solution, time (t), temperature (T), and current density (j) used in this work. 121
3.7 Boundary conditions used in simulation where L = sample thickness, t_{charging} =final charging time, and t_{transfer} =final transfer time. 130
3.8 Diffusion and trapping simulation parameters (1 trap site) in pure iron [105, 129] 131

3.9 Charging conditions for simulating Type A (homogeneous) and Type B (partial) charging; μ_0^{Fe} is taken to be the solubility of H in pure Fe [129] 132

3.10 Simulation constants used when holding the k_0/p_0 ratio constant at 1.25. The resulting spectra can be seen in Fig. 3.33 and are labeled using an alphabetic key. 140

3.11 Trapping (E_k) and detrapping (E_p) activation energies used when holding the binding energy constant (E_b) at 48.00 kJ.mol^{-1}. 143

3.12 Imposed trap site densities (N) used to simulate the TDS spectra shown in Fig. 3.36. 145

4.1 Experimental TDS conditions. $T_{\text{iso-RT}}$ refers to a room temperature isothermal aging period and $T_{\text{iso-HT}}$ refers to an elevated temperature aging period. 154

4.2 Diffusion coefficients of H (and its isotopes) in A600 reported in literature. 180

4.3 Derived diffusion coefficients for a A600 pure diffusion system (PDS) model material. 181

4.4 Error on diffusion coefficient values, demonstrating the "fastest" (A) and "slowest" (B) tolerated D values. Simulations using these parameter can be seen in Fig. 4.25. 182

4.5 Derived diffusion coefficients for a SS316L pure diffusion system (PDS) model material. 193

4.6 Derived diffusion coefficients for A600 and SS316L pure diffusion system (PDS) model materials. 194

4.7 Derived "best-fit" trapping (k) and detrapping (p) kinetic constants for trapping at chromium carbides located both inter- and intragranularly in A600. These values are coupled with the diffusion constant presented in Table 4.3. 196

4.8 Derived "best-fit" trapping (k) and detrapping (p) kinetic constants for trapping at chromium carbides (Cr_7C_3, according to TEM diffraction patterns, see Chapter 3) along grain boundaries in A600. These values are coupled with the diffusion constant derived parameters presented in Table 4.3. 204

4.9 Derived "best-fit" trapping (k) and detrapping (p) kinetic constants for trapping at dislocations in A600. These values are coupled with the diffusion constant derived parameters presented in Table 4.3. . . 205

4.10 Derived "best-fit" trapping (k) and detrapping (p) kinetic constants for trapping at chromium carbides (Cr_7C_3, according to TEM diffraction patterns, see Chapter 3) located both inter- and intragranularly (IIC) and at primarily grain boundaries (GBC) and dislocations in A600. These values are coupled with the diffusion constant presented in Table 4.3. 207

5.1 Derived diffusion coefficients for A600 and SS316L pure diffusion system (PDS) model materials. 213
5.2 Derived trapping (k) and detrapping (p) kinetic constants for trapping at chromium carbides (Cr_7C_3) and dislocations in A600. 216
5.3 Calculated binding energies for trapping at chromium carbides (Cr_7C_3) and dislocations in A600 using the derived trapping parameters (Table 5.2). E_b refers to the traditional definition of binding energy ($E_b = E_p - E_D$) and E'_b refers to the proposed definition of binding energy ($E'_b = E_p - E_k$). 218
5.4 Collection of activation energies for diffusion and trapping in A600 as presented by Young *et al.* [82] and Symons *et al.* [22]. The activation energies (E_D and E_p) were determined by "Choo-Lee plot" analysis [91] and binding energy (E_b) was calculated by Eq. (5.1). . 219
5.5 Dislocation densities ($\rho_{\text{dislocations}}$) imposed trap site density in simulations (N) and calculated TS densities (N'_{d}) and α_{d} associated with dislocations, these parameters were determined experimentally, derived from numerical simulations, or calculated using Eq. (5.4) or Eq. (5.5). 225
5.6 Average surface area of a chromium carbide in the A600 matrix (S_a), imposed trap site density in simulations (N) and calculated TS densities (N'_{c}) and α_{c} associated with chromium carbides. These parameters were determined by microscope observations and image analysis, derived from numerical simulations, or calculated using Eq. (5.4) or Eq. (5.6). 225

6.1 Derived diffusion coefficients for a A600 and SS316L pure diffusion system model materials 238
6.2 Derived "best-fit" trapping (k) and detrapping (p) kinetic constant parameters for trapping at chromium carbides (Cr_7C_3, according to TEM diffraction patterns, see Chapter 3) located both inter- and intragranular (IIC) or uniquely along grain boundaries (GBC) and dislocations in A600. 239

7.1 Conditions du milieu primaire des REP. 247

7.2 Synthèse des coefficients de diffusion de H obtenus à partir des données expérimentales collectées sur des matériaux modèles dans lesquels la diffusion est prépondérante (PDS), pour l'A600 et le SS316L. 258
7.3 Constantes cinétiques de piégeage (k) et de dépiégeage (p) du deutérium pour différents types de sites présents dans l'alliage 600 : des carbures de chrome (de type Cr_7C_3 d'après les analyses de diffraction électronique présentées au chapitre 3) inter- et intragranulaire (IIC) ou localisés principalement aux joints de grains (GBC) et des dislocations (D). Ces valeurs sont associées aux constantes de diffusion présentées dans le tableau Table 4.3. 265

Chapter 1

Introduction

1.1 Context and objectives

Of the almost 440 existing nuclear reactors in the world today, nearly 350 are **L**ight **W**ater **R**eactors (LWR). This class of nuclear reactor is often separated into two subdivisions: (i) **P**ressurized **W**ater **R**eactors (PWR) and (ii) **B**oiling **W**ater **R**eactors (BWR). In France all of the 58 nuclear reactors (Fig. 1.1) are PWRs and produce nearly 75 % of the country's electricity. Many of these reactors were designed for operation between 30 and 40 years, but with the necessary maintenance and additional investments it may be possible to extend their lifetime to up to 80 years.

As a large part of these nuclear reactors in France approach near the end of their forecasted lifetime, the question of lifetime extension has been brought to the table. One key factor in extending their operation is safety. Over the past forty years, on top of supplementary maintenance and security measures (i.e. component replacement and repairs, upgrading control systems, etc.), a great deal of research has been conducted with the goal of better understanding the degradation phenomena taking place in reactors. Reactor degradation is often due to component corrosion and cracking which has furthermore been linked to the extreme environmental conditions the components are subjected to during reactor operation (i.e. high temperature, high pressure, irradiation, internal stresses, elevated hydrogen partial pressures, etc.).



Fig. 1.1 Map of localization of nuclear reactors in France (www.world-nuclear.org)

One of these degradation mechanisms is **S**tress **C**orrosion **C**racking (SCC). This corrosion mechanism comes into play when extreme environmental conditions are coupled with internal stresses in the material. Furthermore, some researchers have linked this corrosion mechanism to the presence of hydrogen, which in PWR primary water at 598 K is at an overpressure of about 0.3 bar. The goal of this study

is to better understand the role of hydrogen in these degradation mechanisms, with specific focus on interactions between hydrogen and the material in terms of (i) diffusion and (ii) trapping at microstructural defects and impurities intrinsically present in an industrial material.

1.2 PWR operation

Pressurized water reactors can be split respectively into three circuits, Fig. 1.2, the (i) primary circuit, (ii) secondary circuit, and a (iii) cooling circuit which may be the ocean, a river, or a closed circuit (not shown in figure).

At the heart of the nuclear core is the fuel, source of both heat and energy in the reactor. The PWR reactor fuel is often fabricated in the form of ceramic pellets of pressed and sintered uranium oxide (UO_2). These pellets are then encased in metal fuel rods, often fabricated in a zirconium base alloy. After assembly, the fuel rods are placed in the reactor core where they will be in contact with the primary circuit medium.

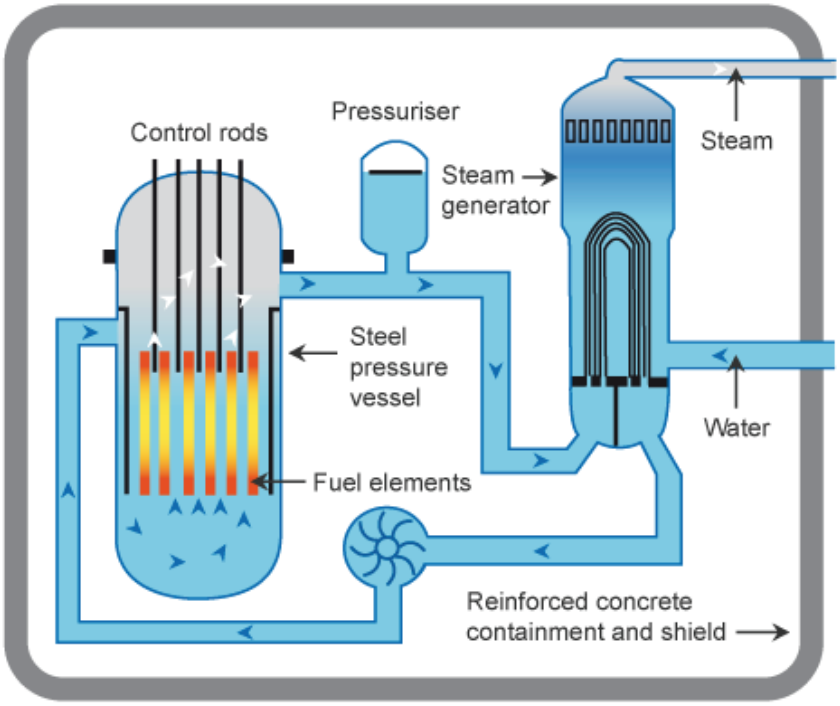

Fig. 1.2 Typical Pressurized Water Reactor design (www.world-nuclear.org).

The heat produced by the fission process in the reactor core is transfered to the water in the primary circuit, the composition and conditions of this medium can

be seen in Table 1.1. The heat of the primary circuit medium is then transfered to the secondary circuit medium via the steam generator tubes (i.e. heat exchanger) which serve as the physical barrier between the two circuits as well as a barrier to the radioactive core products from the environment.

Table 1.1 Characteristic PWR primary water conditions.

Temperature	558 - 598	K
Pressure	155	bar
Boron (H_3BO_3)	10 - 1200	ppm
Lithium (LiOH)	0.7 - 2.2	ppm
Hydrogen (H_2)	25 - 50	$cm^3.kg^{-1}$(NPT)
pH_{573K}	≈ 7	

The heat transfer from the primary to secondary circuit results in the vaporization of the secondary circuit medium. The water vapor is then transported across a turbine which produces electricity. After this passage, the steam is condensed by the cooling circuit and recondensed water is repumped towards the heat exchanger where the cycle will continue.

1.3 Hydrogen and Stress Corrosion Cracking

Stress corrosion cracking is an environmental degradation mechanism combines both internal material factors and external environmental factors and affects primarily materials reputed for their good corrosion resistant properties. These types of cracks have been observed in PWR reactor components, in particular in the steam generator tubes fabricated in nickel base alloys and in reactor internal components fabricated in an austenitic stainless steel alloy.

Some researchers, over the past 60 years, have suggested that the presence of hydrogen may play a role in SCC phenomenon. Hydrogen is present in both the reactor primary and secondary circuit media in the form of (i) water (H_2O) present in both the primary and secondary circuits and (ii) dissolved hydrogen gas (25 - 50 $cm^3.kg^{-1}$ (NPT)) present in the primary circuit medium (Table 1.1). Moreover, hydrogen can have multiple influences in corrosion processes including, (i) a kinetic effect on the formation of protective oxide scales on both the primary and secondary circuit sides (ii) a thermodynamic influence on the structure and stability of the oxide scale formed on the alloy, (iii) a kinetic influence on crack initiation, formation and propagation and (iv) an influence on the alloy's mechanical properties after it has been absorbed.

Once absorbed by the alloy, the hydrogen can be transported across the material, where it will interact with interstitial lattice sites along with the different crystallographic defects or heterogeneities present in the material (Fig. 1.3). Hydrogen atoms may interact differently with these sites, which may present a "trapping"

effect thereby slowing the diffusion and causing local accumulation of hydrogen at these **T**rap **S**ites (TS) which may in turn cause a degradation of local mechanical properties and thereby increase the susceptibility of the alloy to environmental degradation mechanisms and crack formation.

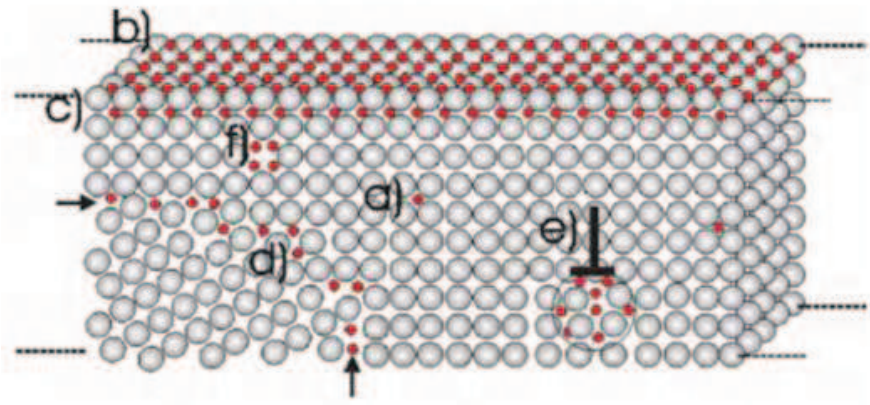

Fig. 1.3 Diagram of potential hydrogen diffusion and trapping sites in a crystalline material: (a) interstitial site, (b) surface and (c) subsurface sites, (d) grain boundaries, (e) dislocations and stress fields and (f) vacancies [1].

1.4 Manuscript objectives and organization

In the following pages, the role that hydrogen may play in SCC, more specifically in addressing the H-material interactions, primarily focusing on diffusion and trapping phenomena, will be explored in-depth and discussed. To understand these phenomena an approach coupling experimental results with a numerical simulation method will be used to determine both the diffusion coefficient and kinetic trapping and detrapping constants associated with various types of trap sites (dislocations, precipitates, etc.) present in industrial materials.

This manuscript is separated into five proceeding chapters, first a bibliographic review on the subject (Chapter 2), then the materials and experimental method used along with the presentation of the developed numerical method (Chapter 3). The notable experimental and simulation results will be presented in Chapter 4, followed by discussion and some perspectives for the study (Chapter 5). Finally, Chapter 6 will conclude the manuscript with a brief summary of the work that has been accomplished and most importantly how this work contributes to the field, and other domains where H-material interactions prove very important (i.e. steel making, H-storage applications, etc.), and opens to many new perspectives.

Chapter 2

Literature Review

As suggested in some literature, during the corrosion processes taking place along the structural pieces made of A600 and SS316L, or at a smaller scale locally at crack tips in particular case of SCC, hydrogen may be incorporated in the alloys exposed to the primary medium. This study is more specifically focused on the possible interactions and transport of hydrogen in the alloys, i.e. diffusion and trapping of H after absorption by the alloy. Hydrogen may indeed play a role in both embrittlement or [mechanical] property degradation of the material itself and more specifically it may participate in SCC crack propagation.

This chapter is aimed at presenting a bibliographical review of hydrogen material interactions like diffusion and trapping. It is divided into several sections (i) SCC in NPPs, (ii) the role of hydrogen in SCC, (iii) a review of hydrogen absorption mechanisms in metallic alloys (in both gaseous and aqueous environments) and (iv) an overview of diffusion and trapping in metals. These sections are then followed by (v) a review of experimental and numerical methods used for the analysis of these interactions.

2.1 Stress Corrosion Cracking in NPPs

In the late 1950's cracking was observed by Coriou *et al.* [2] in Ni base alloy 600 exposed to high temperature water. Ni base alloy 600 is commonly used to fabricate the **S**team **G**enerator (SG) tubes in PWRs. These tubes serve as the physical barrier between the primary nuclear power plants and secondary circuits. They are in contact with primary water (Table 2.1) on the other side and saturated steam or secondary water the other, furthermore cracks have been observed on both the primary and secondary sides [3]. Similar cracking was later observed in some internal vessel components and structural elements often made from stainless steels such as SS316L.

Table 2.1 Characteristic PWR primary water conditions.

Temperature	558 - 598	K
Pressure	155	bar
Boron (H_3BO_3)	10 - 1200	ppm
Lithium (LiOH)	0.7 - 2.2	ppm
Hydrogen (H_2)	25 - 50	$cm^3.kg^{-1}$(NPT)
pH_{573K}	≈ 7	

Under reactor operating conditions, the components made of nickel base alloys 600 and 690 and SS316L, already containing a lot of residual stresses (tube/component forming), are subjected to a **H**igh **T**emperature, **H**igh **P**ressure corrosive en-

vironment, plus in some cases external stresses and specifically concerning SS316L a significant neutron flux, leading to subsequent structural irradiation damage.

As these structural materials, Ni base alloys and stainless steels alike, normally present good corrosion resistance, a particular cracking mechanism was proposed to explain the degradation observed in these situations and is known as **S**tress **C**orrosion **C**racking (SCC) or **I**rradiation **A**ssisted SCC (IASCC). This environmental degradation mechanism is the result of a combination of both internal (material) and external (environmental) factors. For example some internal factors may include: (i) microstructure/metallurgical properties (chemical composition, grain boundary chemistry, precipitates, etc.) and (ii) internal/residual stresses present in the formed component whereas external factors include environmental conditions: (i) temperature, (ii) pressure, (iii) applied stress, (iv) solution/environmental chemistry (pH, $p(H_2)$, etc.).

Material degradation caused by this phenomenon is often separated into two steps: an (i) incubation/initiation period (for crack formation) which is followed by (ii) crack propagation which may lead to component failure. Fig. 2.1 shows an example of an experimentally observed SCC crack [2]. Incubation can be further separated into three stages: (i) precursor (no penetration, but an accumulation of the necessary conditions for SCC to occur takes place), (ii) incubation (negligible [intergranular] penetration, changes in film composition, local creep) and (iii) slow growth slow/small penetration (visible by optical microscopy and includes everything up to early coalescence) [4].

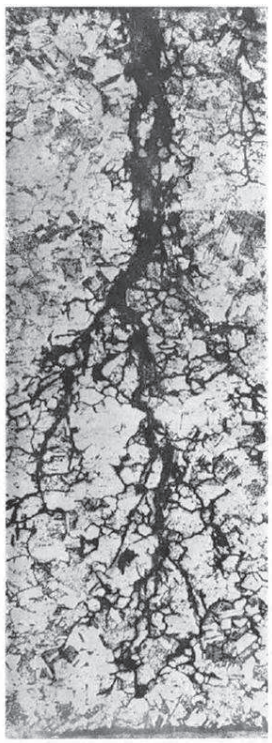

Fig. 2.1 Stress corrosion crack in Ni base alloy 600 after exposure in high temperature water [2].

Since the observation of SCC degradation, researchers have proposed a vast number of mechanisms that explain this phenomenon all in search of one universal mechanism, but it seems that [to date] no single mechanism/model is capable of adequately assessing or predicting SCC damage as there is a large amount of scatter in the

experimental observations. Some of these mechanisms include: (i) slip dissolution-film rupture [5], (ii) coupled environmental fracture [6] and (iii) internal oxidation mechanisms [7]. None of these mechanism can claim to be a completely predictive model or adequately assess all situations where SCC has been observed.

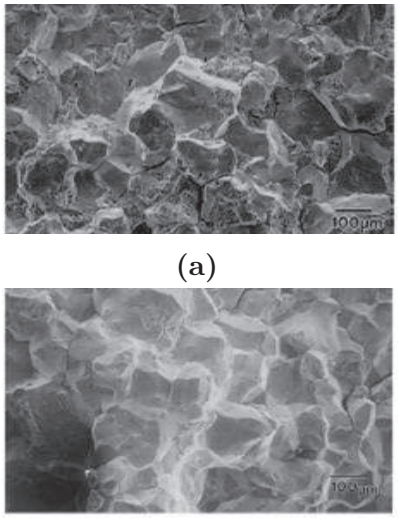

(a)

(b)

Fig. 2.2 Fracture surfaces of Ni-base alloy X-750 specimens tested in (a) hydrogenated gas at 611 K and (b) hydrogenated water at 633 K [8].

Among environmental effects, the impact of hydrogen (present in the primary circuit of PWR NPPs as H_2O, H^+ ions and dissolved $H_{2(g)}$) is continuously brought-up in proposed SCC mechanisms, but its role and importance is still highly debated [3, 7, 9]. Some remarkable similarities were observed in the fractography of specimens tested in high temperature water environments (cracking attributed to SCC) and those in hydrogen gaseous environments (**H**ydrogen **E**mbrittlement (HE) rupture) [8, 10, 11]. Fig. 2.2 shows microstructure of the fracture surfaces of Ni-base alloy X-750 tested in a HT (611 K) H_2 gas environment (Fig. 2.2a) and HT (633 K) water environment (Fig. 2.2b). These similarities led researchers to propose a link between hydrogen uptake by a material and SCC susceptibility. An attempt at developping on this point will be the subject of the next section.

2.2 Role of hydrogen in SCC

Hydrogen is present in primary water of PWRs (H_2O with 20 - 50 $cm^3.kg^{-1}$ (NPT) dissolved H_2, see Table 2.1). Researchers have suggested that the presence of dissolved hydrogen may increase SCC sensitivity and play an important role in SCC initiation and propagation in Ni base alloys and stainless steels, more specifically affecting (i) the formation and nature of the oxide scale formed on the alloy and (ii) after absorption modifying the alloy [mechanical] properties [9, 11, 12, 13, 14, 15, 16].

Concerning specifically Ni base alloys, the presence of dissolved hydrogen in PWR primary water has been shown to play a role in the reduction of the corrosion potential of alloy 600, lowering it to a value close to the value of the hydrogen

electrode (H^+/H_2) equilibrium potential [15]. This promotes the cathodic process and increases both the critical and passive current densities as dissolved hydrogen content increases [15]. This thereby reduces the passivity of the alloy [15] and has an effect on the nature of the oxide scale formed by both Ni base and stainless steel alloys [12, 17, 18, 19, 20].

Furthermore, Bandy *et al.* [9] observed an accelerating effect of H_2 (same partial pressure as that in primary water) on intergranular SCC in A600 in high temperature water (638 K) with an 84 % failure ratio of U-bend specimen subjected to high temperature hydrogenated water testing versus only 2 % in pure deaerated water and therefore concluded that hydrogen clearly caused more severe SCC in this alloy. Contrary to these findings, F. Meng *et al.* [14] have found that as H_2 partial pressure is increased from 5 to 50 cm^3 (STP) H_2/kg H_2O, the crack growth rate is decreased in uni-directionally cold work nuclear grade 316 stainless steel, leading them to conclude that an elevated partial pressure of dissolved hydrogen in PWR primary medium is not enough to increase SCC crack growth. Such an increase is thus a combination of many factors, including cold working degree, cold working direction and the resulting microstructure [14]. Among the microstructural features that may affect SCC and IGSCC is carbide precipitation (stainless steels and Ni base alloys) [21, 22, 23].

Moreover, researchers have also found that hydrogen absorption at the crack tip may in fact play a role in [SCC] crack propagation by changing the local mechanical properties, by hydrogen degradation mechanisms for example **H**ydrogen **E**nhanced **L**ocalized **P**lascticity (HELP) [24, 25], **H**ydrogen **E**nhanced **DE**cohesion (HEDE) [26], **C**orrosion **E**nhanced **P**lasticity **M**odel (CEPM) [27] or mechanisms affected by hydrogen for example creep [28], ahead of the crack tip. In order to look more closely at these hydrogen enhanced SCC mechanisms, it is important to first understand how the hydrogen atoms enter the metal and what interactions take place once absorbed.

2.3 Hydrogen absorption mechanisms

Before hydrogen can play a role in crack propagation mechanisms it has to enter the material. This mechanism may differ between materials and environments. In the following sections, the general mechanisms for hydrogen absorption in gaseous and aqueous environments is detailed along with hydrogen absorption mechanisms in PWR primary water.

2.3.1 Hydrogen absorption in gaseous environments

The absorption of hydrogen by a metal in a gaseous environment can be described by three step processes: (i) physisorption, (ii) chemisorption or adsorption dissociative, (iii) dissociation, (iv) adsorption then (v) absorption. Physisorption, a completely reversible process, occurs instantaneously as a result of interactions between Van der Waals forces of the material surface and the adsorbent and is accompanied by an energy exchange which can be taken to be approximately equal to the heat of condensation of the adsorbent ($\leq$ 20 kJ.mol^{-1}) [29].

Then, chemisorption can occur; this sorption takes place when H_2 dissociation occurs due to a chemical reaction taking place on the surface.The energy needed for H_2 dissociation/adsorption is much larger than that required for physisorption and is therefore much less reversible than physisorption [29]. The dissociation/adsorption step can be considered as the limiting step in this process. Finally, after chemisorption which leads to H_2 dissociation, H adsorption can take place on the metal surface followed by absorption of H into the bulk. These reactions can be considered as

$$2M + H_2 \rightleftharpoons 2M - H_{\text{ads}} \tag{2.1}$$

for adsorption, followed by

$$M - H_{\text{ads}} \rightleftharpoons H_{\text{abs}} + M \tag{2.2}$$

for absorption. In these reactions M represented a metal atom, M-H_{ads} adsorbed hydrogen and H_{abs} absorbed hydrogen. Furthermore, the reaction described by Eq. (2.2) (hydrogen absorption) is very difficult to identify.

2.3.2 Hydrogen absorption in aqueous environments: cathodic charging

Hydrogen ad- then absorption and diffusion in metal and metal oxides has been highly studied and discussed in literature [30, 31, 32, 33, 34, 35, 36]. Hydrogen absorption mechanisms in aqueous environments are linked to the hydrogen reduction reaction that may take place on the metal surface. In this section a very simplified mechanism for hydrogen absorption in a crystalline metal is detailed. The global cathodic reaction leads to the release of hydrogen at the cathode surface and/or the absorption of H by the metal.

This adsorption step may be coupled with a Tafel type desorption reaction [32], which can be considered as for a neutral or alkaline environment, where the main source of H^+ atoms may be considered the reduction of water [31]. This adsorption step may be coupled with a Tafel type desorption reaction [32], which can be considered as

$$2M - H_{\text{ads}} \rightleftharpoons H_2 + 2M \tag{2.3}$$

in parallel H_{ads} can also be absorbed by the material and becomes H_{abs}

$$M - H_{\text{ads}} \rightleftharpoons H_{\text{abs}} + M \tag{2.4}$$

and can diffuse in the crystallographic network [36].

In PWR representative conditions, hydrogen may be absorbed directly from its gaseous phase (dissolved H_2) or by an electrochemical process bringing into play proton reduction. However, after reduction, in reactor conditions the process is not as simple as previously mentioned, as oxide formation is taking place at the same time. The formation of an oxide scale causes several changes to the system, this can include: (i) surface modification and therefore an evolution in surface reactivity and dissociation reactions, etc., and (ii) the formation of a H diffusion barrier, i.e. the oxide itself.

2.3.3 Hydrogen absorption mechanisms in primary water

In primary circuit water, Table 2.1, hydrogen uptake by the alloy components can occur. Recently two different H absorption mechanisms in simulated PWR primary water, one for Ni base alloy [17, 18, 19] and another for 316L stainless steel [20] have been proposed. In these studies, the same approach was used in order to investigate the link between concomitant hydrogen absorption and corrosion processes. Both "one-stage" and "two-stage" corrosion experiments were performed on Alloy 600-like single crystals [17, 18, 19] or SS316L [20]. Samples were exposed to simulated primary water medium here the hydrogen or oxygen atoms of either the water or the H_2 gas has been labeled using ^2H or ^{18}O.

From "one-stage" corrosion experiments, these studies have shown that the reduction of water molecules is the main source of H uptake by both alloys [17, 18, 19, 20]. These values can be considered equivalent given the error of the measurement. However, the study of the diffusion of ^2H and ^{18}O through the oxide scale via "two-stage" corrosion experiments has highlighted that different H transport mechanisms take place in the oxide formed on each alloy. For that reason, Jambon *et al.* [18, 19] proposed an absorption mechanism linked to hydroxide ion (OH^-) transport across the oxide followed by H uptake by the Ni base alloy whereas Dumerval *et al.* [20] proposed a H-absorption mechanism for stainless steels linked to proton (H^+) transport across the oxide, followed by hydrogen absorption by the alloy. Moreover Dumerval *et al.* [20] highlighted a deuterium build-up in the alloy underlying the internal oxide scale. This same "hydrogen" (H or one of its isotopic tracers) ion build-up has also been observed after corrosion experiences by Qui *et al.* [15].

Dumerval *et al.* [20] suggested that this build-up may be attributed (i) to slower diffusion of H in the alloy (SS316L) than in the oxide scale or (ii) if diffusion is faster in the alloy than in the oxide, a trapping mechanism taking place in the alloy under the scale, for example in the vacancies created during the formation of the external oxide layer grown by a cationic diffusion process through the internal oxide layer [20, 37, 38, 39].

After hydrogen transport across the oxide scale, it may be absorbed by the metal; once absorbed its transport across the material can occur. Hydrogen transport can occur by interstitial diffusion in the alloy crystal lattice. Such diffusion can be affected by crystallographic defects present in the material. These sites may modify the electronic environment of the H as compared to "normal" interstitial sites and therefore trap the hydrogen.This trapping phenomenon may subsequently cause very localized H build-up in the material which has been thought to be at the center of environmental degradation processes linked to hydrogen uptake. The interactions between absorbed hydrogen and the alloy, specifically concerning diffusion and trapping phenomenon at potential **T**rap **S**ites (TS) is at the center of this study and is discussed in-depth in the following sections.

2.4 Hydrogen diffusion and trapping in metals

After absorption, hydrogen will diffuse across a metallic material. Diffusion of atomic species in solids has been a subject of high importance for the comprehension of material properties and the diffusion of H in metals has been extensively studied using numerous experimental techniques and simulation methods. These studies have resulted in enormous amounts of hydrogen diffusion information and diffusion coefficients spanning many orders of magnitude, especially at low temperature, for the same material [40, 41, 42, 43, 44, 45, 46, 47, 48, 49]. It is considered that the hydrogen diffusion in f.c.c. crystal structures occurs between the nearest neighbor interstitial sites [50].

During the diffusion process hydrogen may interact with the crystallographic heterogeneities intrinsically present in the material. These sites may include: (i) point defects such as vacancies and hetero-atoms, (ii) one-dimensional sites like dislocations and triple junctions, (iii) two-dimensional sites including grain boundaries and interfaces along with (iv) three dimensional sites such as voids, precipitates and inclusions. These aforementioned "imperfections" may have an important effect on the H diffusion in the metal. Darken and Smith [51], first noticed a significantly slower diffusion rate of H in pre-deformed iron samples (as compared to non-deformed samples). They proposed the concept of hydrogen "trapping" at the dislocations created during the pre-deformation and the idea of an apparent diffusion coefficient (D_{app}) which takes into consideration the interstitial diffusion

(D) and the effect of trapping simultaneously taking place in the metal without distinguishing between the two separated contributions. Diffusion and trapping interactions have since been investigated by numerous research groups, all hoping to better understand this phenomenon and its role in H-assisted degradation mechanisms.

A review of hydrogen diffusion and trapping interactions in metals will be detailed in the following sections, first beginning with a review of the (i) diffusion of hydrogen and its isotopes in Ni-base alloys and stainless steels and followed by a presentation of (ii) hydrogen trapping as described in literature.

2.4.1 Diffusion interactions

2.4.1.1 Interstitial diffusion

Interstitial diffusion of hydrogen in metals is often described by Fick's second law of diffusion, which can be seen below for one dimension in Eq. (2.5):

$$\frac{\partial \mu}{\partial t} = D\frac{\partial^2 \mu}{\partial x^2} \tag{2.5}$$

This equation describes the evolution of the local concentration of a species (in our case hydrogen) in the metal, μ (mol.cm^{-3}) in function of time (t) and position in the sample (x). The diffusion coefficient, D, of hydrogen in a given metal is often considered to follow an Arrhenius relationship. This assumption gives the coefficient its temperature dependence, see below Eq. (2.6):

$$D = D_0 \exp \frac{-sE_D}{RT} \tag{2.6}$$

where D_0 is the pre-exponential constant and E_D is the activation energy associated with interstitial diffusion, R is the ideal gas constant and T the temperature. The diffusion process is often represented using a simple "energy diagram", see Fig. 2.3. In this diagram, the valleys of the wave can be considered the individual interstitial sites in which the H is diffusing. The ability of the H atom to "hop" from one interstitial site to the next depends on the probability of this happening, i.e. magnitude of the pre-exponential constant, and the energy needed to overcome the barrier between the interstitial sites, i.e. the diffusion activation energy. Two interstitial site types can be distinguished: (i) tetrahedral and (ii) octahedral. In *fcc* materials it has been shown that this interstitial diffusion is more favorable from octahedral to octahedral sites via the metastable tetrahedral site [50]. This description is a rather simplified description view of the diffusion process in metallic alloys as interstitial sites are not the only available sites in these materials.



Fig. 2.3 Schematic energy diagram for interstitial diffusion in a *fcc* material.

2.4.1.2 Grain boundary diffusion

Researchers have often commented on the effect of **G**rain **B**oundaries (GB) on the diffusion of atomic species in metals. It has been proposed that, concerning H transport, GB may play either (i) a short-circuit or enhanced diffusivity role (i.e. D_{GB} (diffusion coefficient at grain boundaries) $\gg D$) [52, 53, 54, 55, 56, 57, 58] or (ii) a trapping role, due to the dislocations and vacancies stored at GBs [57, 59, 60]. It should be mentioned that the majority of studies involving grain boundary diffusion have been conducted in highly pure [mainly fine grained often nanocrystalline] metals [53, 54, 55, 56, 57, 59, 60] and a literature review has resulted in only some studies focusing on grain boundary effects in alloyed materials [58, 61, 62, 63, 64].

Concerning short-circuit diffusion there are a lot of discrepancies in the measured D_{GB} values. H diffusion acceleration at grain boundaries has been measured as 8 to 100 times greater than that of interstitial H diffusion in pure Ni [54]. This huge range of values may be linked to the experimental methods used to acquire this data and the difficulty in data interpretation and/or exploitation. The grain boundary diffusion coefficient cannot be determined alone from results as experimentally a mixture of interstitial diffusion and grain boundary diffusion is observed. Many researchers use electrochemical permeation techniques coupled with analysis using the relationship [65]:

$$D_{\mathrm{eff}} = [D_{\mathrm{GB}} \times s \times f] + [D \times (1 - f)] \tag{2.7}$$

where D_{eff} is the experimentally measured diffusion coefficient, s represents the segregation factor ($s = \alpha_s \exp[-E_{\mathrm{s}}/RT]$, where α_s is a pre-exponential factor and E_s represents the chemical potential difference between an octahedral site in lattice and a site in the GB [65]) and f the volume fraction of grain boundaries ($f = 3\delta/\bar{l}$, where δ is the GB width and $\bar{l}$ is a first approximation of the mean linear intercept of the grains) to approximate the grain boundary diffusion coefficient in the material [53, 54, 55, 58, 66, 67]. Eq. 2.7 was developed by L.G. Harrison [65] for diffusion in a mixed regime: a regime where diffusion along grain boundaries and in volume are important enough contributions to affect the hydrogen diffusion in the alloy. In order to determine the GB diffusion coefficient both s and f must

be known or approximated. Grain boundaries were found to play an accelerating role in nickel [52, 53, 54, 55, 66] and austenitic materials alike [58, 61, 62, 63, 64].

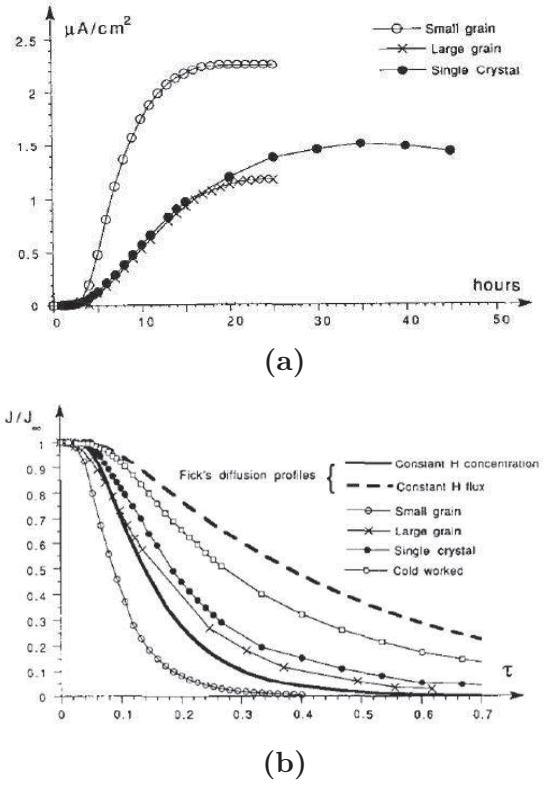

Fig. 2.4 Room temperature (a) permeation and (b) degassing data in (i) single crystal (ii) small (25 μm) grain, (iii) large (150 μm) grain and (iv) in (b) cold worked pure Ni specimen showing the influence of microstructure (specifically grain size) on diffusivity and hydrogen flux [54]. The simulated Fick's diffusion profiles for constant H concentration and constant H flux can also be seen in (b) [54].

A-M. Brass and A. Chanfreau studied the diffusion of hydrogen along grain boundaries in three types of pure nickel specimen: (i) single crystal, (ii) small grained (25 μm grain size) and (iii) large grained (150 μm grain size) using an electrochemical permeation technique at room (298 K) and elevated (333 K and 373 K) temperatures [53, 54]. They observed an accelerated diffusion in the small grained specimen from room temperature permeation and degassing data, see Fig. 2.4. A comparison of steady state permeation current densities between the different microstructures reveals the highest current density for small grained specimen whereas the larger grained and single crystal current densities are almost equivalent, Fig. 2.4a.

When the interstitial diffusivity of hydrogen in pure Ni is plotted (Fick's diffusion profiles) in Fig. 2.4b, the observed H diffusivity in the small grained material is slightly faster (about 2-7 times larger than interstitial diffusion in pure Ni), whereas that of the large grained, single crystal and cold worked is slower. Furthermore the electrochemical permeation results, showing enhanced diffusion along grain boundaries at low temperatures were confirmed by tritium (^{3}H) audioradiolographic results, Fig. 2.5. These audioradiographs show a preferential location of the tritium (lighter areas) along the

grain boundaries of the material after a short aging time of the tritiated specimen (Fig. 2.5a) [53]. This hints at a preferential desorption of ^{3}H along the grain boundaries at short aging times. Then after 10 days of aging there is no more preferential desorption of tritium along the grain boundaries, and consequently no more tritium mapping along grain boundaries (Fig. 2.5b) [53].

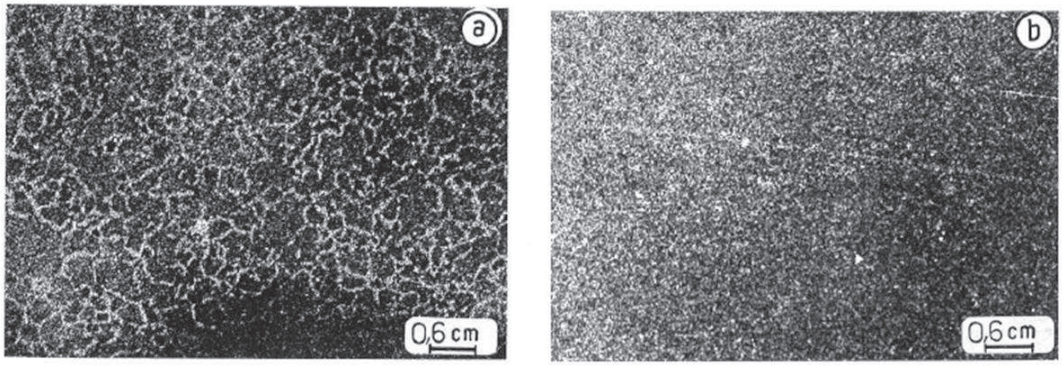

Fig. 2.5 Audioradiographs of a polycrystalline pure nickel specimen exposed 46 h at 253 K to tritium (a) after 24 h of aging and (b) after 10 days of aging [53] at 253 K. The light areas highlight the location of tritium in the specimen.

When these experiments were repeated at high temperature (373 K), see Fig. 2.6, the small grained material reproduces the Fickian diffusion profile for constant concentration simulation [53, 54]. The diffusion of H in the large grain material is still slightly delayed but it can be considered that the grain size has a negligible effect on diffusion at this temperature [53, 54]. This same accelerating effect in small grained specimen as compared to their larger grained counterparts has been observed by numerous research groups in Ni [55, 56, 66] along with different materials as well, for example austenitic alloys including Fe-Mn-C alloys at 353 K [58] and 304L stainless steels and 316L stainless steels at temperatures up to 495 K [61, 62, 63, 64]. Concerning the literature data for these austenitic materials, these authors seem to be in agreement that at low temperatures an accelerated diffusivity may be observed and can be linked to short circuit diffusion taking place in the grain boundary network. As temperature is increased, it seems that the accelerating effect disappears in Ni and Ni-base alloys in the temperature range of 273 - 293 K whereas in stainless steels it has been observed experimentally an effect of grain boundaries at temperatures up to about 500 K.

Oudriss *et al.* [57] also studied the influence of GBs on diffusion at 298 K in high purity polycrystalline Ni for a range of grain sizes (10 nm - 168 μm). They have constructed diagram relating grain size to effective diffusion coefficient which can be seen in Fig. 2.7. This figure has been separated into three domains. Do-

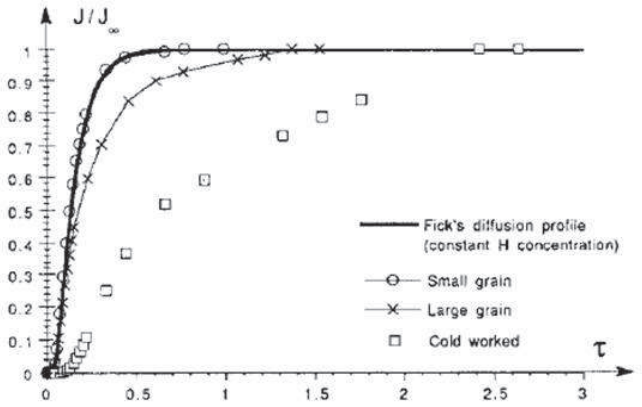

Fig. 2.6 High temperature (373 K) permeation in (i) small (25 μm) grain, (ii) large (150 μm) grain and (iii) in (b) cold worked pure Ni specimen as compared to Fick's diffusion profile showing the influence of microstructure (specifically grain size) on diffusivity.

main I, large[r] grains, shows an increase in D_{eff} with decreasing grain size until a critical grain size is reached, referred to in Fig. 2.7 as d_c, which suggests the preferential diffusion along GB as their density is increasing [57]. After reaching this critical grain size D_{eff} then begins to decrease with decreasing grain size. The authors have attributed this decrease to the increase in grain boundary mismatch and the number of "**G**eometrically **N**ecessary **D**islocations" (GNDs) created by the increased grain boundary density. Then, moving into Domain III the effective diffusion coefficient increases again, despite the higher GND. They have hypothesized that this could be attributed to short-circuit GB diffusion at the increased number of triple junctions [57]. Furthermore, their measures have shown that the grain boundary density effect on D_{eff} is not straight-forward and additional criteria need to be considered when determining the effect of grain boundaries, for instance: (i) grain size, (ii) triple point density, (iii) nature of GBs, etc. It seems they have confirmed the accelerating effect of grain boundaries for small grained pure nickel at room temperature evoked by [53, 54], but for grain sizes greater than 10 μm and smaller than 100 μm, there seems to be a trapping effect or short-circuit effect dependent on grain size [57]. It would seem from these analyses that the effect of grain boundaries at 298 K in fine grained pure metals is coherent but more research would need to be carried out for larger grained materials (> 10 μm) which are more commonly used for industrial purposes.

It can also be pointed out that a number of researchers debate that grain boundaries would not play a short-circuit diffusion role, but rather have a slight trapping effect on hydrogen transport in polycrystalline materials [57, 59] or present lower

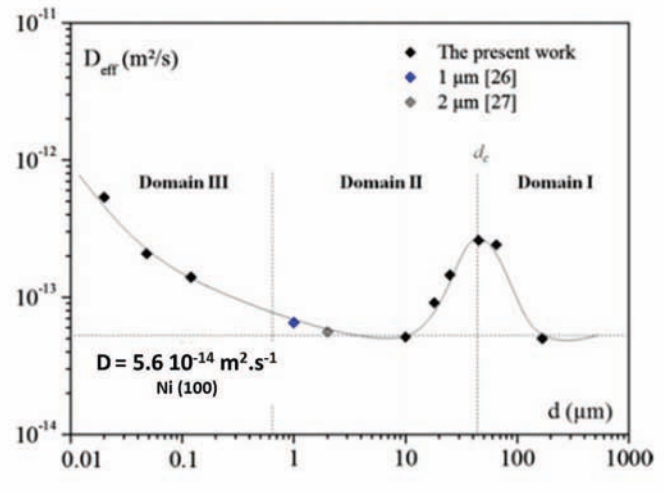

Fig. 2.7 Effective diffusion coefficient (D_{eff}) of H in high purity (99.99%) polycrystalline Ni (grain size 10 nm - 168 μm) at 298 K with regards to grain size as reported by Oudriss *et al.* [57].

solubility as compared to the bulk material [63]. Yao *et al.* [59] state that although experimental analyses have hinted that H diffusion along grain boundaries is faster than in the lattice, the mathematical analysis methods used are only applicable to systems where grain boundary diffusion is dominant, and the diffusing atom is a substitutional element diffusing via a vacancy mechanism in the lattice. Furthermore they go on to say that since hydrogen is a very small atom, diffusion in the bulk lattice is by an interstitial mechanism, and therefore it would be reasonable to consider diffusion in the lattice and along grain boundaries to be of the same order [59]. Furthermore, as also observed in [57], grain boundaries induce a number of GNDs in the material which may prove to have a trapping and therefore slight "slowing" effect on effective hydrogen diffusion in polycrystalline materials [59] at room temperature.

As the debate continues on the role of grain boundaries and the extent of their effect on hydrogen diffusion [and trapping] in metals, it may seem that the most important thing to settle this issue depends on improvements in experimental analysis methods and ways to address uniquely diffusion at grain boundaries. Until then it seems that the issue will not be resolved and will need to be handled diligently by researchers on a material to material basis (i.e. for specific chemical compositions and microstructures), making sure to look at the effect GBs may play in their specific material before drawing any conclusions on H-material interactions.

2.4.1.3 Isotopic H tracers

Hydrogen is a naturally abundant element, which may cause difficulties in analyses of hydrogen in materials. Some researchers have adopted the use of isotopic tracers, to better differentiate against residually present H (i.e. surface polution, H from elaboration processes, organic H_2O pollution, etc.) and the H due to an experimental approach, for example absorbed during cathodic charging. Commonly used hydrogen tracers are deuterium (^{2}H) and tritium (^{3}H), both presenting very low natural abundances (about 1.2 10^{-4} atom ^{2}H per atom H and 10^{-18} atom ^{3}H per atom H). In a first approach, the diffusion of isotopic H tracers can be related to the diffusion of H by Eq. 2.8 [68].

$$D_{\text{isotope}} = D_H \sqrt{\frac{m_{\text{isotope}}}{m_{\text{H}}}} \tag{2.8}$$

It is interesting to note that this isotopic correction factor has very little effect on the experimental determined diffusion coefficients for hydrogen tracers in the studied alloys (A600 and SS316L).

2.4.1.4 Review of published diffusion data

The diffusion of H, and its isotopes: deuterium (^{2}H) and tritium (^{3}H), in A600 [40, 41, 43, 42] and SS316L [44, 45, 46, 47, 48] has been thoroughly studied using a wide variety of both experimental and numerical methods and has provided a large amount of data, for a large range of temperatures. Arrhenius plots of the H, ^{2}H and/or ^{3}H diffusion coefficient in these alloys are shown in Fig. 2.8a and Fig. 2.8b. In these plots the diffusion coefficient has been corrected to for the isotopic effect of the studied species (H, ^{2}H or ^{3}H) using Eq. (2.8).

As discussed in Sec. 2.4.1.2 it has been demonstrated that grain boundaries may act as short circuit diffusion pathways at temperatures inferior to 373 K for fine grained microstructures [53, 54] but for grain sizes between 10 μm and 100 μm depending on orientation GBs may act as trap sites or short-circuit pathways. Not all grain sizes were specified by authors in the publications used to construct Fig. 2.8a; Chêne *et al.* [42] determined the diffusion of deuterium in an A600 alloy with grain sizes ranging from 10 μm - 50 μm and Ulhemann *et al.* [43] studied hydrogen diffusion in a material with grain sizes between 10 μm and 80 μm (with a majority of grain sizes between 20 μm and 30 μm). Furthermore, regardless of grain size the hydrogen diffusion data for Ni alloy 600 seems very coherent over a large range of temperatures, from 298 K to approximately 1000 K, and range of grain sizes (10 μm - 80 μm [42, 43]) and does not hint at a change in the diffusion mechanism (i.e. going from a grain boundary controlled diffusion where $D_{\text{GB}} \gg D$, to one where diffusion in volume is the major contribution).

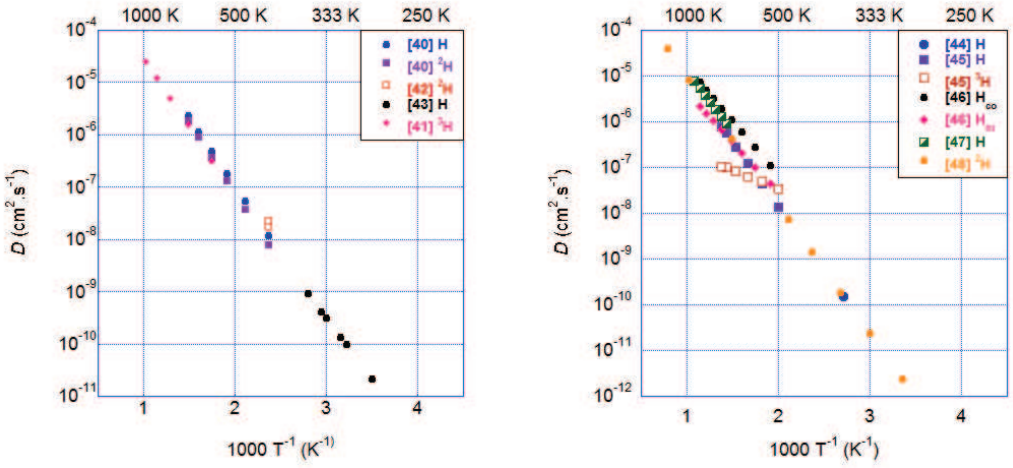

(a) (b)

Fig. 2.8 Arrhenius plot of [corrected (Eq. (2.8) [65])]diffusion data for H and its isotopes in Ni-base alloy 600 [40, 41, 42, 43] and (b) in stainless steel 316L [44, 45, 46, 47, 48].

While the overall trend of the data shown in Fig. 2.8b for H diffusion in SS316L is consistent there is larger scatter in the data, compared to A600. The grain size of the alloy used was only specified by Brass *et al.* [44] and was for large grained, either 140 μm or 300 μm, SS316L. This data happens also to be the only lower temperature data point and the only in the temperature range where the grain boundaries have been show to possibly create a short-circuit diffusion network [61, 62, 63, 64]. This could be due to the slightly different chemical compositions (although the alloys were within the nominal composition tolerances) or the thermal or thermomechanical treatments the alloys were previously subjected to.

Furthermore, especially in the case of SS316L, most of the diffusion data is for high temperature ranges and diffusion data at lower temperatures ($T \leq 500$ K) is missing, except for one data point at room temperature from Brass *et al.* [44] and the low temperature measurements by P. Tison [48].

2.4.2 Trapping interactions

2.4.2.1 Energetic description of trapping

In parallel with its diffusion process, hydrogen may interact with different sites that slow the overall diffusion of H across the material or cause local hydrogen accumulation. Fig. 2.9 is a general energy diagram representation of hydrogen

diffusion and trapping in the case of transport in the presence of one **T**rap **S**ite (TS) (Fig. 2.9a) or two TS (Fig. 2.9b).

In these energy diagrams, the TS present themselves as deeper "potential wells" having a larger activation energy for detrapping (E_p) as compared to interstitial diffusion (E_D) or trapping activation energies (E_k) which in this energy diagram appear to be of equal energies. Often researchers refer to the difference in the activation energies of interstitial diffusion and detrapping as the trap site binding energy ($E_b = E_p$ - E_k). In this energy diagram E_D is equal to the trapping activation energy (E_k), but most often researchers assume a different activation energy referred to as an energy barrier for trapping [69]. An energy diagram for diffusion with trapping assuming an energy barrier for trapping is shown in Fig. 2.10 [69].

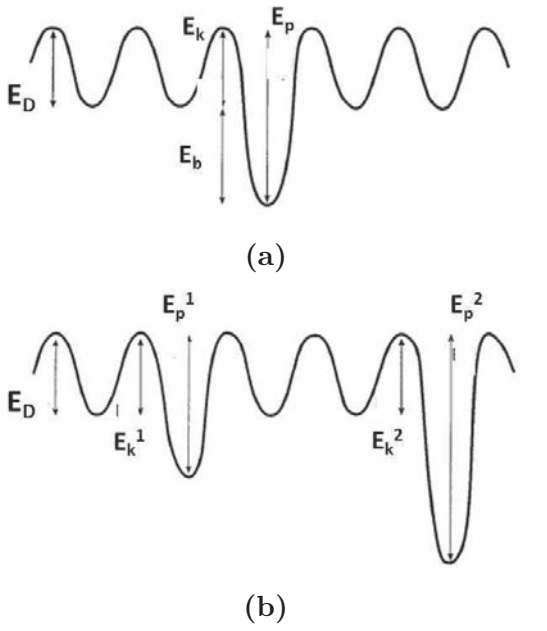

Fig. 2.9 Schematic diagram of diffusion and trapping at (a) one TS or (b) at two TS. E_k^1 and E_k^2 and E_p^1 and E_p^2 are the respective trapping and detrapping activation energies associated with the trap site types.

The presence of these TS, and their effect on hydrogen diffusivity, may have a negative effect on material properties and render the material more susceptible to hydrogen induced degradation mechanisms. The basic kinetic reaction between a TS and an atom of hydrogen is presented in Eq. (2.9) where $[\ \ ]_{\text{trap}}$ represents a possible TS and $[H]_{\text{trap}}$ a trapped H atom. This kinetic reaction is governed by both a forward and backward reaction rate, respectively referred to as a trapping (k) and detrapping (p) kinetic constants.

$$H + [\ \ ]_{\text{trap}} \underset{p}{\overset{k}{\rightleftharpoons}} [H]_{\text{trap}} \tag{2.9}$$

Like a diffusion coefficient (see Eq. (2.6)) these kinetic constants are often considered to follow an Arrhenius relationship, which gives them their temperature dependence. The trapping (k) and detrapping (p) kinetic constants are presented in their developed form in Eq. (2.10a) and Eq. (2.10b) were k_0 and p_0 are the

respective trapping and detrapping pre-exponential constants

$$k = k_0 \exp\left(\frac{E_k}{RT}\right) \tag{2.10a}$$

$$p = p_0 \exp\left(\frac{E_p}{RT}\right) \tag{2.10b}$$

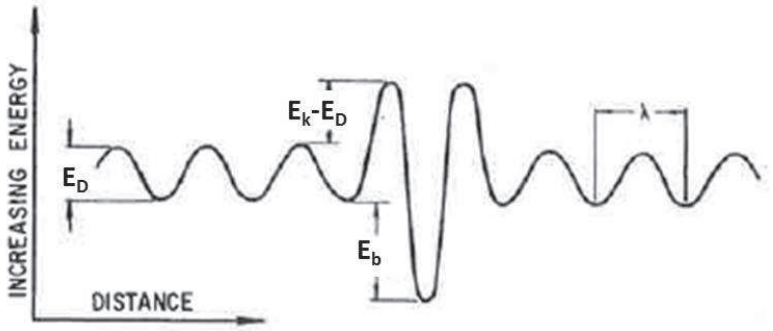

Fig. 2.10 Trap model energy schematic diagram as presented by Oriani [69]. In this diagram λ refers to the lattice spacing in the matrix.

2.4.2.2 Nature of trap sites

Trap sites are often classified in two general categories: (i) reversible and (ii) irreversible [70]. This type of classification should be avoided as "reversibility" and "irreversibility" are relative to the considered temperature and therefore this type of TS classification will not be used in this manuscript.

Trap sites will just be classified by their type, some example of TS types may be dislocations, vacancies, precipitate interfaces, grain boundaries, etc. In the following short sections some types of potential hydrogen trap sites are detailed: (i) dislocations, (ii) vacancies and (iii) chromium carbides providing some insight on the further debate and necessity to study these interactions in-depth. These trap site types are of particular interest to this study as they may play a role in the stress corrosion cracking phenomenon.

i. *Hydrogen-dislocation interactions*

Hydrogen-dislocation interactions have been the center of numerous studies [10, 71, 72, 73] and their role in hyrogen enhanced environmental degradation processes, i.e HELP, HEDE and CEMP degradation models, has been hypothesized. A number of studies have focused on understanding the interactions taking place between hydrogen and dislocations and their influence on [effective] diffusion in

metals. Brass *et al.* [73] conducted a study on the role of dislocations on hydrogen absorption and desorption from *bcc* and *fcc* metals and alloys.

Electrochemical permeation curves for recrystalized, single crystal and 98 % cold worked pure Ni specimen, shown in Fig. 2.11a show a delayed permeation in the pre-deformed pure Ni materials and in Fig. 2.11b the effect of degree of cold working on the diffusivity of hydrogen in a high strength low alloyed (HSLA) steel [73] at 293 K. The decreased permeabilities and diffusivities have been associated with trapping taking place at dislocations [and other defects] present in the materials [73]. They have also evidenced the preferential accumulation of tritium along dislocations in stainless steel 304L at 293 K, once aging linked to trapping taking place at dislocations.

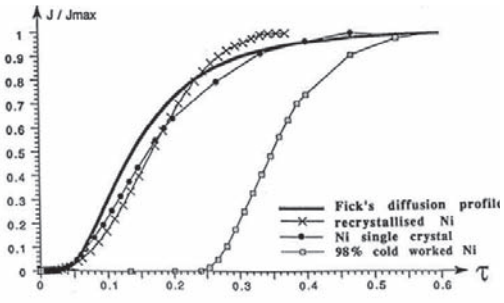

(a)

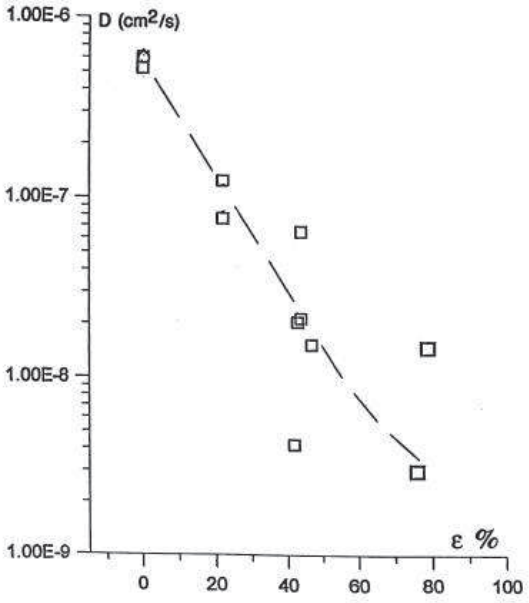

(b)

Fig. 2.11 (a) Electrochemical permeation curves for recrystalized, single crystal and 98 % cold worked pure Ni specimen and (b) decreased diffusivity of H in a HSLA steel in function of cold working percent [73] at 293 K.

They have also observed an enhanced [early stage] tritium desorption in pre-deformed pure nickel samples, see 2.12a. This enhanced desorption may be linked to a "pipe-diffusion" phenomenon taking place in the dislocation network [73].

Furthermore strain enhanced tritium transport was studied by monitoring tritium desorption from a γ-Ni base super alloy single crystal during tensile testing at room temperature. These experiments evidenced an increased tritium desorption with applied strain, see Fig. 2.12b at 293 K (which is not linked to native passive film disruption during tensile testing). This enhanced desorption may be explained by mobile dislocation transport during applied strain or to short circuit ^{3}H transport along the dislocation network [73]. Other researchers have studied the influence of hydro-

gen on mechanical properties by *in-situ* hydrogen charging during tensile testing which has also evidenced a possible hydrogen transport by dragging by mobile dislocations [10, 73]. In conclusion, it would seem that hydrogen-dislocation-matrix interactions are very complex and can result in contradicting results for different material and conditions, i.e. dislocations acting as potential trap sites or enhancing diffusion due to short-circuit network.

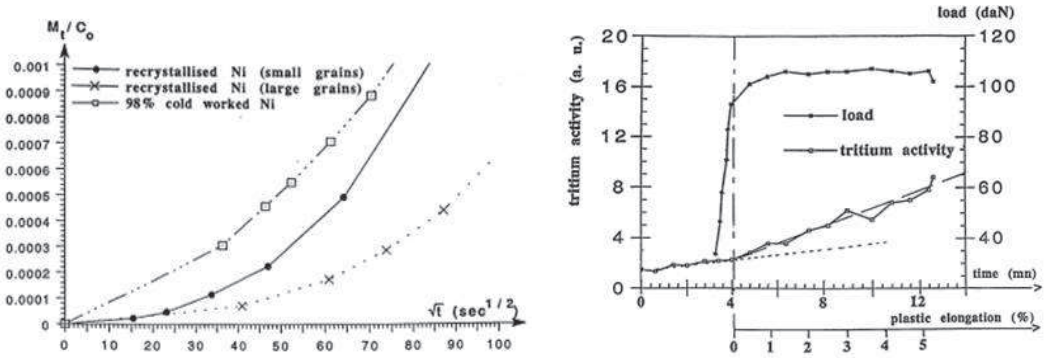

(a) **(b)**

Fig. 2.12 (a) Early-stage tritium desorption from small grained, large grained and 98 % predeformed pure Ni specimen measured by β counting at 298 K and (b) ^{3}H desorption from a pre-charged (in tritiated molten salts) γ-Ni base alloy single crystal during tensile testing measured by liquid scintillation counting [73].

ii. *Hydrogen-vacancy interactions*

It has been argued that hydrogen embrittlement and hydrogen enhanced degradation mechanisms are significantly influenced by the presence of vacancies in the crystallographic structure. Nagumo *et al.* [74, 75] proposed a **H**ydrogen **E**nhanced **S**tress **I**nduced **V**acancy (HESIV) mechanism in which hydrogen stabilizes and enhances vacancy concentrations in the matrix.

Concerning the trapping of H at vacancies great deal of interest has been taken to understanding the possible hydrogen-vacancy interactions in metallic materials. Most of these results have been obtained by *ab-initio* or first-priciple calculations based upon **D**ensity **F**unctional **T**heory (DFT). Counts *et al.* [76] studied H-point defect interactions and trapping using DFT base first-principle calculations and found that vacancies presented themselves as strongest type of trap site in a *bcc* iron matrix, when compared to various solute atoms. A "strong" trapping of hydrogen at vacancies has also been observed by other research groups using DFT based calculations.

Hydrogen-vacancy interactions and H-vacancy cluster formation has been studied by different groups using various different experimental techniques: (i) implantation annealing, (ii) ion-implantation [77] and (iii) thermal desorption mass spectroscopy [78, 79, 80, 81]. Fukai *et al.* [79] used XRD and resistivity measurements to quantify the concentration of vacancies in metals. This analysis was then coupled with thermal desorption mass spectroscopy analyses, see Fig. 2.13, where the binding energy of hydrogen at vacancy clusters was determined. They determined very high binding energies for hydrogen at vacancy clusters ($\geq$ 70 kJ.mol^{-1}, see Table 2.2) which are in very good accordance with DFT based calculations [79].

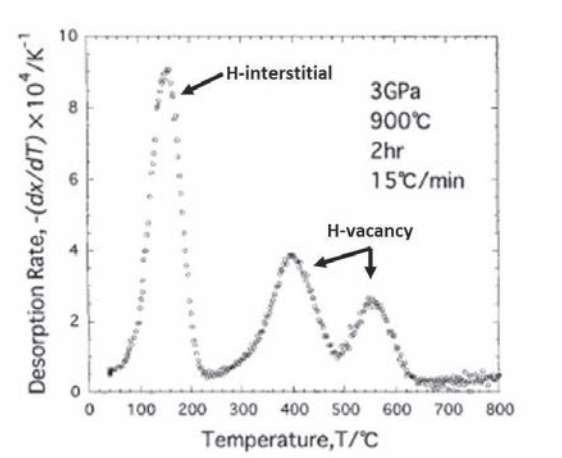

Fig. 2.13 Thermal desorption mass spectroscopy analysis results for hydrogen-vacancy clusters in Ni. The first desorption peak was associated with interstitial diffusion and the two higher temperature peaks were attributed to H binding with vacancies [79].

It seems that [super-abundant] vacancies may serve as very strong potential hydrogen trap sites, but their influence on diffusion and trapping in alloys would need to be studied more in-depth for situations when they are not "super-abundant" and the primary potential trap site.

iii. *Hydrogen-chromium carbide interactions*

Trapping at precipitates and/or phase boundaries, such as chromium carbides [8, 10, 22, 82], titanium nitrides [83, 84, 85, 86], ferrite/cementite interfaces [87], etc., has been studied in various alloys and pure metals. The role chromium carbides might play in trapping phenomenon has been discussed [8, 22, 82]. The presence of chromium carbides may prove beneficial from a corrosion point of view, having a higher passivation rate than the alloy in which they are precipitated in (i.e. A600) thereby decreasing metal dissolution and hydrogen production [8], but their presence along grain boundaries shows negative effects on the fracture resistance of alloy 600 in the presence of hydrogen [8, 10].

Young *et al.* [82] studied the trapping phenomenon at chromium carbide precipitates in Ni base alloys using thermal desorption mass spectroscopy. They observed different trapping "strengths" for the differently annealed materials; different annealing procedures can lead to a preferential precipitation of a type of

chromium carbide, i.e. Cr_7C_3 observed in mill annealed alloy ($T < 1273$ K) or $Cr_{23}C_6$ observed in a sensitized alloy ($T < 873$ K). Cr_7C_3 carbides present a higher detrapping activation energy (and therefore binding energy) of hydrogen than $Cr_{23}C_6$ (see Table 2.2). In a later study by Symons *et al.* thermal desorption mass spectroscopy was used to study trapping at chromium carbides, which they have identified as Cr_7C_3 and presented a detrapping activation energy of about the same energy as $Cr_{23}C_6$ in the earlier study, see Table 2.2.

It seems as though the general consensus in literature is that hydrogen is trapped at chromium carbides in nickel base alloys, but the trapping "strength" at these sites is debatable, as different studies have evidenced different detrapping activation energies in [very] similar alloys.

2.4.2.3 Review of some published trapping data

Table 2.2 shows a compilation of trapping and detrapping kinetic constants found in literature, for example the respective trapping and detrapping activation energies associated with a trap site type in a specific metal or alloy as presented in literature. It becomes clear by looking at this table (Table 2.2) that the data is incomplete and somewhat incoherent. A large range of detrapping and binding energies for the same trap site type in the same material (Table 2.2) has been reported.

Most of the experimentally determined data is for detrapping activation energies (E_p) or trap site binding energies (E_b). There is very little information pertaining to parameters including: (i) trapping activation energies (E_k), (ii) pre-exponential trapping constants (k_0) and (iii) pre-exponential detrapping constants (p_0). These three parameters have been shown to be extremely important to trapping and detrapping phenomena [88, 89, 90] and are often neglected using standard H-trapping/detrapping analysis methods. The lack of information pertaining to the pre-exponential constants and trapping activation energy may be behind the inconsistencies in detrapping and/or binding energies. If a general comparison of binding energies between the different crystal structures it would seem that in general the binding energies for *bcc* materials are slightly lower than those observed in *fcc* metals and alloys.

Furthermore, determining all four experimental trapping and detrapping parameters is difficult and it would be necessary to develop a procedure coupling experimental results and simulation to be able to determine a robust set of these kinetic parameters. Many researchers have worked towards establishing a numerical model to describe these interactions and have eventually made suggestions of specific experimental tests or methods that may be used to exact this kinetic information.

Table 2.2 Literature review of hydrogen trapping constants at various TS.

			k		p		
			k_0	E_k	p_0	E_p	E_b
TS	Material		(cm^3s^{-1})	($kJ.mol^{-1}$)	(s^{-1})	($kJ.mol^{-1}$)	($kJ.mol^{-1}$)
Dislocation	pure α-iron (*bcc*)	[91]	–	–	–	26.8	19.2
" "	tempered m.[a]	[92]	–	–	–	–	33.9
" "	tempered m.[a]	core [93]	–	–	–	57.9	–
" "	steel (*fcc*)	[83]	–	–	–	–	29.9
" "	steel (*fcc*)	[83]	–	–	–	–	24.1
" "	Ni (*fcc*)	[94]	–	–	–	–	18.3, 24.1 ± 2.9
" "	high purity Al (*fcc*)	[95]	–	–	–	(43.5 ± 17.5)	–
" "	high purity Al (*fcc*)	[96]	–	–	–	47.3	–
" "	Al-Li-Cu-Zr alloy (*fcc*)	[97]	–	–	–	46.8	31.7
Grain boundary	α-Fe (*bcc*)	[91]	–	–	–	17.2	9.6
" "	tempered m.[a]	[92]	–	–	–	–	25.2
" "	steel (*fcc*)	average value [83]	–	–	–	–	26.1
" "	steel (*fcc*)	high angle [83]	–	–	–	–	53.1 - 58.9

[a]martensite

Table 2.2 continued.

TS	Material		k		p		E_b
			k_0 (cm^3s^{-1})	E_k ($kJ.mol^{-1}$)	p_0 (s^{-1})	E_p ($kJ.mol^{-1}$)	E_b ($kJ.mol^{-1}$)
Interface	Fe (*bcc*)	TiC [84]	–	–	–	86.9	28.1
" "	Fe-0.5Ti alloy (*bcc*)	TiC [98]	–	–	–	> 61	–
" "	Fe-0.05C-0.22Ti-2.0Ni steel (*bcc*)	TiC [85]	–	–	–	85.7	–
	0.42C-0.30Ti steel (*bcc*)	TiC[a] [85]	–	–	–	116	–
" "	Fe-0.05C-0.2Ti-2.0Ni steel (*bcc*)	TiC[a] [86]	–	–	–	55.8	–
" "	Fe-0.05C-0.2Ti-2.0Ni (*bcc*)	TiC[a] [86]	–	–	–	68 - 137	–
" "	Fe-0.05C-0.2Ti-2.0Ni (*bcc*)	TiC[b] [86]	–	–	–	55.8 - 100	–
" "	LC[c] steel (α) (*cc*)	ferrite/cementite [87]	–	–	–	18.35	–
" "	steel (added V) (*fcc*)	VC [99]	–	–	–	33 - 35	–
" "	steel (*fcc*)	TiC [83]	–	–	–	94.06	–
" "	steel (*fcc*)	TiC[d] [83]	–	–	–	77.2 - 94.6	–
" "	sensitized Ni-17Cr-8Fe (*fcc*)	$Cr_{23}C_6$ [82]	–	–	–	67.7 - 78.6	19.9 - 27.4
" "	as-annealed A690 (*fcc*)	$Cr_{23}C_6$ [22]	–	–	–	–	37
" "	10 % CW[e] A690 (*fcc*)	$Cr_{23}C_6$ [22]	–	–	–	–	41
" "	mill-annealed Ni-17Cr-8Fe (*fcc*)	Cr_7C_3 [82]	–	–	–	106.8	55.0
" "	as-annealed A600 (*fcc*)	Cr_7C_3 [22]	–	–	–	–	26
" "	10 % CW[c] A600 (*fcc*)	Cr_7C_3 [22]	–	–	–	–	28
" "	30 % CW[c] A600 (*fcc*)	Cr_7C_3 [22]	–	–	–	–	36
" "	high purity Al (*fcc*)	[95]	–	–	–	(84.8 ± 32.2)	–
" "	Al-Li-Cu-Zr alloy (*fcc*)	δ' phase [97]	–	–	–	40.3	25.2

[a] semi-coherent
[b] side incoherent
[c] low carbon
[d] incoherent
[e] cold worked

Table 2.2 continued.

TS	Material		k k_0 (cm^3s^{-1})	k E_k ($kJ.mol^{-1}$)	p p_0 (s^{-1})	p E_p ($kJ.mol^{-1}$)	E_b ($kJ.mol^{-1}$)
Voids	α-steel (*bcc*)	[83]	–	–	–	–	>21.3
" "	α-Fe (*bcc*)	micro-void [91]	–	–	–	37.15	27.6
" "	α-Fe (*bcc*)	vacancy [76]	–	–	–	–	55
" "	Fe (*bcc*)	mono-vacancy[a] [100]	–	–	–	–	51.2 ± 6.7
" "	Fe (*cc*)	vacancy cluster[a] [100]	–	–	–	–	75.3 ± 7.7
" "	Ni (γ) (*fcc*)	vacancy [77]	–	–	–	–	23
" "	Ni (γ) (*fcc*)	multi-vacancy [77]	–	–	–	–	41
" "	Ni (*fcc*)	vacancy cluster [79]	–	–	–	–	70.4, 85.9
" "	Cu (*fcc*)	mono-vacancy [101]	–	–	–	–	42.5
" "	Cu (*fcc*)	vacancy [102]	–	–	–	–	> 38.6
" "	Al high purity (*fcc*)	[96]	–	–	–	20.0	–
" "	Mo (*bcc*)	vacancy cluster [103]	–	–	–	–	111.0
" "	Mo (*bcc*)	mono-vacancy[b] [103]	–	–	–	–	99.3
" "	Mo (*bcc*)	mono-vacancy[c] [103]	–	–	–	–	77.2

[a]He implanted
[b]low occupancy
[c]high occupancy

Table 2.2 continued.

TS	Material		k		p		E_b
			k_0 ($cm^3 s^{-1}$)	E_k ($kJ.mol^{-1}$)	p_0 (s^{-1})	E_p ($kJ.mol^{-1}$)	E_b ($kJ.mol^{-1}$)
Other	high purity Al	blister [96]	–	–	–	76.3	–
" "	Al-Li-Cu-Zr alloy	solid solution Li [97]	–	–	–	17.7	2.6
Non-specified	13% Cr m.[a] steel	"reversible" [104]	$(4.8 \pm 1.3)\ 10^{-2}$	–	$(3.4 \pm 1.6)\ 10^{-2}$	–	(38.7 ± 1.0)
" "	13% Cr m.[a] steel	"irreversible" [104]	$(4.8 \pm 1.3)\ 10^{-2}$				
" "	LAC[b] steel (α)	[105]	$2.63\ 10^6$	5.69	$2.1\ 10^7$	53.69	48.0
" "	SS316L	irradiation[c] [106]	–	–	–	86.8	12.5 - 30.0

[a] martensitic
[b] low-alloy Carbon
[c] implantation at 1-10 keV He^+

2.4.3 Models describing hydrogen - trap site interactions

To address hydrogen diffusion interactions, a number of numerical models with different degrees of complexity have been proposed in literature. These models may be split into three categories based upon their considerations: (i) diffusion and trapping models [69, 107, 108, 109, 110, 111], (ii) non-uniform solubility models [112, 113, 114], and (iii) dislocation-transport models [83, 115, 116, 117]. In the following sections, a selection of these models will be presented, detailed and discussed. These sections will focus on the works of (i) A. McNabb and P.K. Foster [107], (ii) R.A. Oriani [69], (iii) R. Kirchheim *et al.* [109, 110, 118, 119] and (iv) J.B. Leblond and D. Dubois [112, 113, 114] and (v) T. Kasuya and M. Fuji [108]. These models will be discussed in the following sections along with the pros and cons of each model and for what systems they are applicable.

2.4.3.1 Diffusion and trapping according to A. McNabb & P.K. Foster

A. McNabb and P.K. Foster proposed a physical model for the analysis of hydrogen interactions in iron and ferritic steels [107]. They first discuss the large scatter that is observed in experimentally determined diffusion coefficients in these materials and highlight the observations made by Darken and Smith (see Sec. 2.4) [51] on the slower diffusion rate of hydrogen in deformed specimen versus non-deformed specimen of the same type. These findings served as the motivation behind this work and to demonstrate the need of a more complete model for H diffusion.

In order to describe trapping interactions during diffusion, a modified version of Fick's second law was proposed by McNabb and Foster [107]. In addition McNabb and Foster couple the modified Fick's second law (Eq. (2.11a)) with the trapping rate deduced from the chemical reaction step shown in Eq. (2.9), assuming a first order reaction for trapping and detrapping. This set of coupled partial differential equations can be seen below in Eq. 2.11a and Eq. 2.11b:

$$\frac{\partial \mu}{\partial t} + N\frac{\partial \theta}{\partial t} = D\frac{\partial^2 \mu}{\partial x^2} \tag{2.11a}$$

$$\frac{\partial \theta}{\partial t} = k\mu(1-\theta) - p\theta \tag{2.11b}$$

In these equations, θ represents the fraction of traps occupied, N the trap site density. Due to the highly coupled nature of these equations, there is no simple analytical solution and therefore a numerical method is required for their resolution.

In this set of equations [a minimum of] five unknown parameters must be determined experimentally: (i) N, (ii) D, (iii) k, (iv) p and (v) μ_0 (initial surface concentration). At the time of publication, they had no experimental results;

therefore McNabb and Foster made some propositions for the experimental determination of these parameters by using well defined **E**lectrochemical **P**ermeation (EP) experiments. They hypothesize that μ_0, N, D and the ratio of k/p may be determined directly from steady state experiments, whereas to determine k and p individually the decay rate would need to be measured as well. They also state that the scatter in the apparent diffusion constants is directly due to trapping and is on the order of magnitude of $D_{\text{app}} = D/(1 + Nk/p)$ (for thick specimen); this expression is extremely dependent on N as the apparent diffusivity will dramatically decrease as N increases. This first proposition of "trapping theory" inspired numerous research groups to further elaborate, and try to simplify, this "diffusion and trapping" model.

2.4.3.2 The model of R.A. Oriani

Oriani *et al.* [69] proposed a simplified set of equations for hydrogen diffusion and trapping in metallic materials based upon the McNabb and Foster equation system (Eq. 2.11a and Eq. 2.11b [107]). This analysis imposes a set of hypotheses and restrictions that allowed him to develop a simplified analytical model that is widely used in diffusion and trapping analyses today.

These hypotheses include: (i) one atom of H per TS, (ii) only one type of TS present in the system, (iii) very low local H concentrations, (iv) restricted degree of TS occupancy and (v) "local equilibrium between the mobile and trapped [hydrogen] populations" [69]. These assumptions allows for the use of an apparent diffusivity (D_{app}) which is related to interstitial diffusivity (D) by

$$D_{\text{app}} = D\frac{dc_L}{dc_T} = D\frac{c_L}{c_L + c_x(1-\theta_x)} \tag{2.12}$$

which becomes

$$D_{\text{app}} = D\left(1 + \frac{KN_x}{N_L}\right)^{-1} \tag{2.13}$$

through a series of considerations detailed in [69]. In these equations c_L is the local interstitial hydrogen concentration, c_T is the total local hydrogen concentration, and c_x the local trapped hydrogen concentration, θ_x the fraction of occupied trap sites, K the equilibrium constant for the interstitial and trapped populations in Eq. (2.13), and N is the density of respective trap (x) and interstitial (L) sites [69]. Furthermore as interstitial and trap sites are considered to exist in finite populations the respective interstitial (c_L) and trapped (c_x) H concentration can be considered to be the product of the number of respective sites (N) and the fraction of occupied sites (θ): $c_L = N_L\theta_L$ and $c_x = N_x\theta_x$.

He has then gone ahead and compared analyses using the developed model to available literature data and has found some good correlation with experimental results where the local thermodynamic equilibrium hypothesis can be considered applicable. For a more complex system, for example one with multiple [possible interacting] TS populations, they have highlighted that analyses using the developed model may not be able to adequately treat the system. Furthermore in order to improve upon this model, more experimental data is needed, specifically concerning important input parameters such as (i) H adsorption and absorption kinetics and thermodynamic constants (i.e. fugacity measurements at the metal/solution interface), (ii) microstructural information (i.e. in-depth characterization, trap site types and distributions etc.). For the latter difficulty they suggest experimental analyses should be done on "**M**odel" **M**aterials where the number of TS types has been limited (i.e. isolated type of TS) and where the specimen surface conditions are controlled (i.e. by a well defined polishing procedure).

While this proposed numerical method seems to adequately describe diffusion and trapping in "simple" systems it seems limited in its applicability to the analysis of more complex material systems or by experimental analyses methods where temperature is evolving (non-equilibrium conditions) and the system cannot reach equilibrium at every point in the sample in a period compatible with experimental durations. Furthermore, the use of an apparent diffusion coefficient (D_{app}) is a subject of debate as it is based upon the assumption of local thermodynamic equilibrium between trapped and interstitial hydrogen. This would imply that both the trapping (k) and detrapping (p) constants tend towards infinity, see Eq. 2.9, and therefore it would be impossible to determine the kinetic parameters associated with these interactions [120]. The validity of the local thermodynamic equilibrium hypothesis has been since explored and debated by many authors [108, 121, 122, 123] and may be applicable for only specific materials under certain experimental conditions, for example for *bcc* materials where the diffusion of hydrogen is very fast and under a constant and sufficiently high temperature.

2.4.3.3 Diffusion and trapping model from R. Kirchheim *et al.*

R. Kirchheim *et al.* [109, 110, 118, 119] have studied intensely over the past several decades H diffusion and trapping in alloys and disordered amorphous systems. Their work focuses mainly on the solubility and diffusivity of hydrogen in dilute alloys and/or amorphous materials and its interactions with dislocations and defects [124]. In their work the H chemical potential (in function of the microstructure), needs to be determined, as the presence of trap sites such as dislocations have an important effect on this parameter. The equation for H chemical potential is coupled with an equation describing the apparent diffusion coefficient, Eq. (2.14) (where μ is the total hydrogen concentration, $\bar{C}$ and $\bar{G}$ represent the H chemical

potential and trap site enthalpy), which can be used to describe the interactions taking place between H atoms and impurity atoms, dislocations, crack tips etc. [109]. This approach, using a chemical diffusion coefficient (which is dependent on the local environment of the hydrogen atom), has been more recently applied and developed for experimental analysis methods by Svoboda *et al.* [122, 123].

$$D_{\text{app}} = D\frac{\partial}{\partial\mu}(1-\mu)^2 \exp\left(\frac{\bar{C}-\bar{G}}{RT}\right) \tag{2.14}$$

Although the proposed model takes into consideration more complicated hydrogen-material interaction systems intrinsically (i.e. dislocations, etc.) by using the H chemical potential, which varies according to the local environment and can change in the present of trap sites such as dislocations and stress field. This model still derives an apparent diffusion coefficient (D_{app}) which is based upon the Oriani assumptions [69], see Sec. 2.4.3.2 and therefore its validity in non-equilibrium situations can be discussed.

2.4.3.4 The "non-uniform solubility" model by J.B. Leblond & D. Dubois

Leblond and Dubois *et al.* [112, 113, 114] further worked towards a mathematical formulation of hydrogen diffusion and trapping systems in steels using Boltzmann-type transport equations and Fermi-Dirac statistics for random movements of hydrogen atoms in the system to elaborate on a modified Fourier type equation (Eq. (2.15)) which they refer to as the **N**on-**U**niform **S**olubility (NUS) model.

$$\frac{\partial n}{\partial t} = \nabla \cdot \left[DS\nabla\left(\frac{\bar{n}}{S}\right)\right] \tag{2.15}$$

In Eq. (2.15) $\bar{n}$ represents the [total] hydrogen concentration, t time, D the diffusion coefficient, and S the solubility of hydrogen in the matrix. At equilibrium the concentration can be considered equal to the solubility ($\bar{n} = S$).

After re-derivation and calculation of the transport equation, they propose a general hydrogen diffusion equation, see Eq. (2.16), accounting for temperature, stress and material dependences (i.e. composition and microstructure) which is then simplified for the case of "physical" TS [83]. k and l represent different types of sites, m represents the class of TS, $\bar{p}$ the volumic proportion of the specified type of site around a point r, τ is the relative time of H transfer from one site type to another and ψ the capture probability.

$$\frac{\partial \bar{n}_k}{\partial t} = -\bar{n}_k \sum_{l=1}^{m} \frac{\bar{p}_l}{\tau_{kl}} + \sum_{l=1}^{m} \frac{\bar{p}_l \bar{n}_l}{\tau_{lk}} + \sum_{l=1}^{m} \Delta(D_{lk} \bar{p}_l \bar{n}_l) - \sum_{l=1} m D_{kl} \bar{n}_k [\Delta \bar{p}_l + 2\nabla \ln \psi \cdot \nabla \bar{p}_l] - 2 \sum_{l=1}^{m} \nabla \cdot (D_{lk} \bar{p}_l \bar{n}_l \nabla \ln \psi_k) \quad (2.16)$$

As Eq. (2.16) has a large number of unknown parameters and is therefore difficult to work with as-is, a series of simplifications are then applied to this formula to relate it to "physical" type [83] trapping systems by using the hypothesis that the capture probability (ψ) is the same for all TS, as shown in Fig. 2.14 [112] and Eq. 2.16 can be reduced and simplified down to:

$$\frac{\partial \bar{n}_k}{\partial t} = \gamma P \left[-\frac{\bar{n}_k}{S_k} + A \right] + \nabla \cdot (\tilde{f} \nabla A) \quad (2.17)$$

where permeability γ is a term corresponding to hydrogen atom jump probability, (P) can be considered the product of D_l and S_l and the activity A is equal to $\sum_{l=1}^{m} \frac{p_l n_l}{S_l}$, thereby reducing the system down to only four unknowns, and making the system more manageable for numerical resolution and experimental parameter determination.

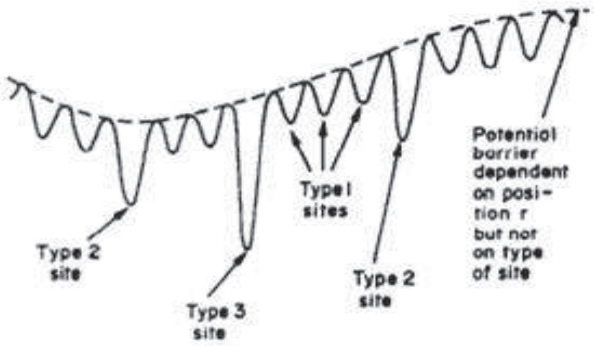

Fig. 2.14 Schematic diagram for diffusion and "physical" trapping in the lattice. Two types of "physical" TS are represented (Type 2 and Type 3) along with normal lattice sites (Type 1). All sites have the same potential energy barrier (dotted line), and therefore the H has the same capture probability (ψ) for all sites [112].

Furthermore, using their NUS model, they have shown that previously proposed models [69, 107, 115] can be recovered in specific cases such as: (i) when the

transfer time (τ) from one site to another is small allowing for local equilibrium between the different sites to be assumed, (ii) for systems where trap site occupation is low ($\theta \ll 1$), (iii) only one type of TS (i.e. two site types (interstitial sites and TS)), (iv) uniform σ and (v) uniform temperature (T). Furthermore their analysis has provided some insight on the applicability of previously presented models (i.e. [69], [107], [115] etc.). The model proposed by J.B. Leblond and D. Dubois is extremely complete and allows for the consideration of many [important] phenomena that were not addressed in previous models, such as (i) local stress fields and (ii) interacting trap sites. Due to the model's integrity it is extremely complex and poses difficulties when dealing with both numerical resolution of the system and more importantly requires many experimental input parameters that are very difficult to determine individually.

2.4.3.5 Diffusion and trapping at multiple trap sites by T. Kasuya & M. Fuji

Kasuya *et al.* [108] then adapted the aforementioned numerical models to account for multiple TS types (with different binding energies) for one-dimensional analysis when traps are homogeneously distributed through out the specimen. They proposed a **N**on-**E**quilibrium **M**odel (NEM), using the McNabb and Foster equations [107], along with a **L**ocal **E**quilibrium **M**odel (LEM), using the Oriani equations [69]. In their analyses, they have assumed a dilute system, i.e. the TS coverage ratio is very low ($\theta \approx 0$), which allowed them for NEM type analysis to simplify the kinetic trapping equation(s), Eq. 2.11b, to

$$\frac{\partial \theta_j}{\partial t} = k_j c - p_j \theta_j \tag{2.18}$$

this equation was then coupled with the McNabb and Foster equation for multiple types of TS:

$$\frac{\partial c}{\partial t} + \sum_{i=1}^{n} N_i \frac{\partial \theta_i}{\partial t} = D \frac{\partial^2 c}{\partial x^2} \tag{2.19}$$

The use of a dilute system also simplifies the respective LEM analysis equation from Eq. 2.12 to:

$$\frac{\partial c_T}{\partial t} = D_{app} \nabla'^2 c_T \tag{2.20a}$$

where

$$\nabla'^2 = \frac{\partial}{\partial x'^2} + \frac{\partial}{\partial y'^2} + \frac{\partial}{\partial z'^2} \tag{2.20b}$$

(x'^2, y'^2, z'^2) are coordinates,

$$D_{\text{app}} = \frac{D}{1 + \sum_{i=1}^{n} \frac{N_i k_i}{p_i}} \tag{2.20c}$$

and

$$c_T = c_L + N\theta \tag{2.20d}$$

Simulations for the NEM and LEM models were done for two systems for both one and two types of TS. A first system (i) for a homogeneously "pre-charged" specimen (i.e. trapped and interstitial hydrogen concentrations are fixed [homogeneously] before and at the start of simulations), and a second system (ii) recreating an electrochemical permeation type experimental situation where trapped and interstitial hydrogen concentrations are fixed to zero at the start of simulation then a H concentration is imposed at one sample face and the hydrogen flux through the sample is monitored by simulation.

Their analysis and comparison of the resolution of the two models (LEM and NEM) for the two systems (homogeneous repartition at $t = 0$ and electrochemical permeation like system) resulted in (i) the derivation of an analytical solution for a dilute system with multiple TS types using the NEM and (ii) the conclusion that over short periods of times the NEM model may demonstrate faster H transport but at longer times the difference between the NEM and LEM solutions becomes smaller. Moreover, the interstitial transport of H atoms is highly dependent on initial H concentrations (interstitial and trapped) [108]. This last point is extremely important and is not able to be addressed when assuming local thermodynamic equilibrium between trapped and interstitial hydrogen in the material [108] and questions the applicability of **L**ocal **E**quilibrium **M**odel(s) such as that of R.A. Oriani [69].

2.4.3.6 General comments on numerical models for the analysis of diffusion and trapping systems

The previous subsections have presented several of the widely used models for concomitant H diffusion and trapping in metallic materials. An important point that should be mentioned is the general applicability of these models and what systems they can adequately describe. The developers of the aforementioned models all seem to be in agreement on one thing: before choosing a model the system conditions must be known as it would seem that no one model is perfect for every system. Every set of equations presented and proposed, is heavily dependent on the initial interstitial and trapped hydrogen distributions in the system.

Many of the more simplified analytical models [69, 109] impose "Oriani type assumptions" [69], i.e. (i) the assumption that local thermodynamic equilibrium is achieved between trapped and interstitial hydrogen in the system, (ii) one atom of H per trap site and (iii) one type of trap site present in the system. The use of these assumptions imply that the trapping and detrapping kinetic constants tend towards infinity and thereby indeterminable [90, 120]. It would seem that the more complex models, such as those of J.B. Leblond and D. Dubois [112, 113, 114], A. McNabb and P.K. Foster [107] and possibly that of T. Kasuya and M. Fuji [108] are more versatile and therefore able to take into consideration more complex system interactions. The ability to handle more complex (non-equilibrium) systems is extremely important when dealing with industrial materials (i.e. complex microstructures, multiple trap sites, strain fields, stress gradients, etc.) and the H-material interactions taking place in evolving systems (i.e. variable temperature, non-uniform H concentrations, evolving system boundary conditions, etc.).

Unfortunately as diffusion and trapping models become more complex, more unknown parameters need to be determined. These unknown parameters must be determined experimentally through specific and rigorous experimental techniques. Furthermore, as model complexity increases, resolution becomes more difficult and the calculation becomes more costly. Therefore, a middle ground needs to be found between the possibility to handle complex material systems and lengthy computing possibilities. This compromise may be achieved through the use of the McNabb and Foster diffusion and trapping model [107]. This system is complex enough to take into consideration an evolving system (temperature variations), non-homogeneous and strong H concentration gradients and, if slightly modified, multiple trap site types.

2.5 Experimental analysis of H-material interactions

2.5.1 A brief review of common methods

Numerous different experimental methods are used for the study of H diffusion and trapping in metallic materials. Some of the most common approaches include (i) hot extraction, (ii) electrochemical permeation and (iii) thermal desorption mass spectroscopy techniques just to name a few. Each experimental approach presents its own set of advantages and drawbacks.

2.5.1.1 Hot extraction

Hot extraction or fusion measurements are often used for studying the interstitial diffusion in metals and involve [rapidly] heating and melting of a material while monitoring the desorption of a desired species using calorimetry techniques or even a mass spectrometer. This is a destructive technique as the sample is melted and post-analysis material characterizations would be impossible. This technique was developed and is most often used to determine the total quantity of hydrogen in the material (sum of trapped and interstitial). Some research groups also use this method to determine diffusion information and to evaluate trapping or short-circuit diffusion[1] [56, 57]. This method [normally] imposes a very fast temperature ramp ($\phi \geq 60$ K.min^{-1}) and some researchers have stated that a "fast" temperature ramp in thermal analyses may result in a loss of important information and increase difficulties in analysis and separation of diffusion and trapping information [125, 126].

2.5.1.2 Electrochemical permeation

Electrochemical **P**ermeation (EP) techniques have been historically used for the study of hydrogen transport across a [thin] metal membrane and is a powerful method for studying hydrogen diffusion and trapping interactions. This method can allow for the flux or the concentration to be controlled at the "entry side". The "entry side" is subjected to a controlled cathodic charging conditions where the current density evolution is measured. Simultaneously the flux from the "exit side" which is exposed to an anodic environment is measured. A schematic diagram of a traditional EP experimental set-up and generalized electrochemical reaction equations can be seen in Fig. 2.15. This technique may be able to provide information on the hydrogen fugacity at the surface and therefore is useful in determining the boundary and absorption conditions for example determining if the permeation system is under constant surface H concentration or constant surface H flux on the "entry side".

- ***EP analysis methods***

To analyze diffusion in materials using EP experimental technique, the derivative of Fick's first, see Eq. (2.21), and second laws, see Eq. (2.5), are commonly used. In Eq. (2.21), j is the current density, $\bar{f}$ represents the Faraday constant (≈ 9.65 10^4 C.mol^{-1}).

[1] The technique of hot extraction/fusion should not be confused with Thermal Desorption mass Spectroscopy as some limitations to this method are encountered that are not in Thermal Desorption mass Spectroscopy techniques.

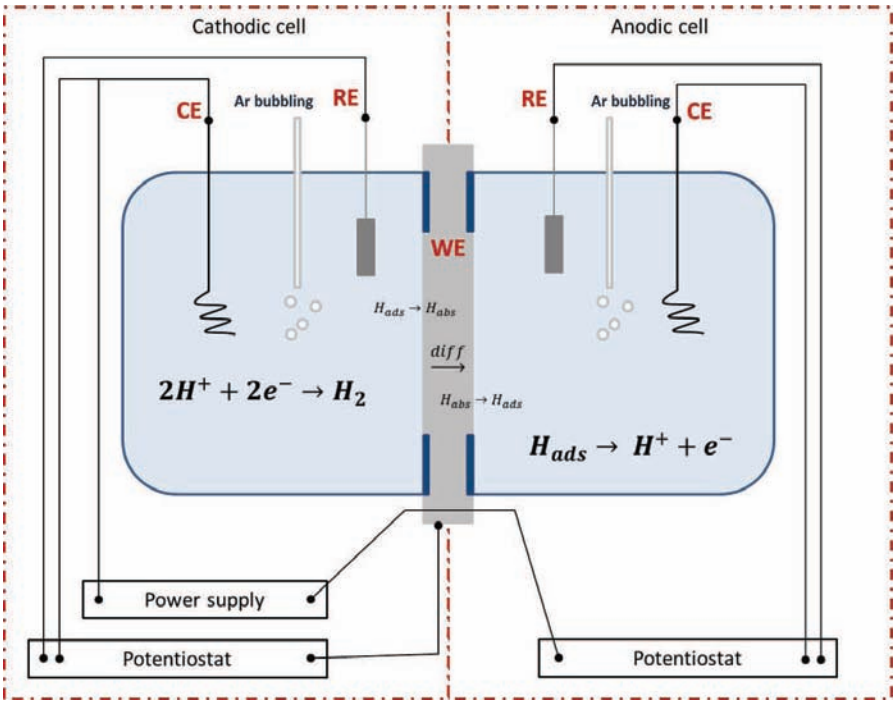

Fig. 2.15 Electrochemical permeation cell diagram. The set-up is split into two electrochemical cells exposing the specimen, the working electrode (WE) to a cathodic environment on the "entry side" and anodic environment on the "exit side" (CE = counter electrode, RE = reference electrode, H_{ads} = adsorbed H, H_{abs} = absorbed H, and $\xrightarrow{diff}$ = H_{abs} diffusion across the membrane).

$$j = -\bar{f} D \frac{\partial \mu[x,t]}{\partial x} \tag{2.21}$$

Whereas permeation techniques are extremely useful in determining surface fugacity and diffusivity, their efficiency and applicability to studying diffusion and trapping systems may be hindered due to temperature limitations (374 K for liquid phase measurements [54, 127]) and time constraints, i.e. lag time for materials with slower diffusion coefficients or thick specimens that may cause laboratory experiments to be extremely long.

- ***Electrochemical permeation analysis techniques and trapping***

When trapping interactions are taken into consideration in electrochemical permeation analysis, modifications to the traditional methods need to be made. For example Eq. (2.21) needs to be modified to consider trapping effects. Caskey *et al.* [128] presented an interesting analysis method for EP curves based upon simulation using a finite difference method for the resolution of the McNabb and Foster equations [107]. They simulate the EP curves using various parameters and compare that to experimental results, where they conclude that the reproduction using this method is much better than that of time-lag and inflection point analysis techniques (which do not consider trapping) and the use of these methods could result in very high errors in the H diffusion coefficient and solubility in the matrix. They also conclude that EP experiments should be conducted and compared to simulated curves to better evaluate trapping.

While Caskey *et al.* [128] propose a data fitting approach using modified McNabb and Foster equations [107], the majority of analyses of EP data for diffusion and trapping interactions are done using analytical method and Oriani type approximations [69]. For example one method to determine "reversibly" trapped H uses experimental "entry" and "exit" side decay desorption flux are compared to those calculated from the solution of the Fick's equation. The difference in the experimental and simulated decay desorption flux integrated over time is equal to the quantity of "reversibly" trapped hydrogen [129, 130]. Electrochemical permeation analysis methods are very much based upon the assumption of "reversible" and "irreversible" trapped populations.

Recently a series of research articles authored by Svoboda *et al.* [122, 123] and Fischer *et al.* [131, 132] discussed the applicability of several other numerical models, more specifically using the models based upon Oriani analysis methods [69] ("c_L-concept" [131]) and the chemical diffusion coefficient ($\tilde{D}$, "Kirchheim-c-concept" [131]) for studying trapping interactions by permeation techniques. While this definition of diffusion is highly based upon the Oriani [69] concepts and the local thermodynamic equilibrium assumption, they have found very good correlation between simulation and experimental results, but have observed and reported

difficulties encountered in simulations compared to experimental results where (i) the material presents a complex microstructure (i.e. many/several different TS) and (ii) when there is a strong H concentration gradient in the material [123]. These two downfalls to their method pose problem when the creation of a general diffusion and trapping model is desired. Furthermore experimental analysis is made more difficult as on the entry and exit sides of the specimen, an oxide scale can form over time; in this case experimental corrections and considerations need to be made.

2.5.2 Thermal desorption mass spectroscopy

Thermal **D**esorption Mass **S**pectroscopy (TDS), sometimes referred to as **T**emperature **P**rogrammed **D**esorption (TPD) [depending on the signal acquisition technique used], is a very powerful experimental approach that has often been used to study hydrogen - material interactions. This technique was first developed for the study of adsorbate - surface interactions and was then applied to hydrogen systems in the late 1970's and early 1980's by several research groups, notably by Wilson *et al.* [106], who studied deuterium trapping in stainless steels, and Mendelsohn *et al.* for the study of hydride stability in zirconium alloys [133]. The general experimental technique involves subjecting a specimen to a temperature ramp (traditional approach for ex. [89, 91, 105, 134, 135, 136]) or at an isotherm or series of consecutive isotherms at increasing temperature [125, 126, 137, 138] and monitoring the pressure evolution of the system [133] and/or the desorption flux of desired molecular species. The acquired data results in a desorption spectrum, examples in Fig. 2.16, which, if the latter technique is used, can be related to desorption flux (mol.s^{-1}) of the desired species as a function of time (t) and temperature (T), i.e. $\int_0^t J(t)\,dt$ (Fig. 2.16a) or $J[t,T]$ (Fig. 2.16b). An example desorption spectrum can be seen in Fig. 2.16; the desorption flux in function of time (t) and temperature (T) is plotted.

Concerning more specifically the use of this technique for the study of hydrogen diffusion and trapping interactions in metals, literature states that some important information can be derived from these spectra. This may include (i) the total amount of hydrogen present in a sample, (ii) the repartition of trapped and interstitial H between different sites, (iii) trap site densities and (iv) trap site detrapping activation energies (E_p) [87, 91].

2.5.3 TDS spectral analysis

Depending on the experimental method and analysis method used, the obtained information, concerning diffusion and trapping interactions, can be very different and results in large scatter in the data, see Table 2.2. In the following sections

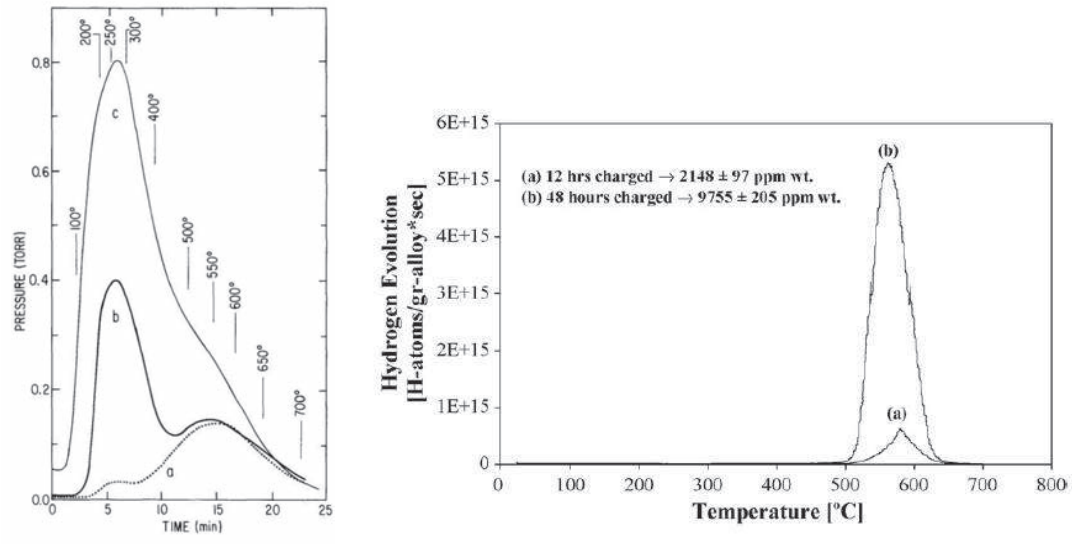

(a) **(b)**

Fig. 2.16 Example desorption spectra for a (a) TPD spectrum acquired by M. Mendelsohn *et al.* on hydrogenated zirconium alloy specimen where system pressure evolution was measured in function of time during a temperature ramp [133] and (b) TDS spectrum acquired by E. Tal-Gutelmacher *et al.* on hydrogenated titanium alloy specimen [139]

several widely employed spectral analysis methods (analytical and numerical) are presented and discussed.

2.5.3.1 "Choo-Lee plots"

One of the simplest and most commonly used methods for thermal desorption spectral analysis was developed by Choo and Lee in the 1980's [91]. This method uses the derivation of Kissinger's equation [140], see Eq. (2.22) for assigning an activation energy (E_p) associated with hydrogen detrapping from a TS in the specimen.

$$\frac{E_p}{R} = \frac{\partial \ln \frac{\phi}{T_m^2}}{\partial \frac{1}{T_m}} \tag{2.22}$$

In this equation ϕ represents the imposed experimental temperature ramp rate, T_m the temperature at which maximum desorption occurs and R the ideal gas constant. In this method, several desorption spectra are acquired by imposing various temperature ramp rates (ϕ). The ramp rate affects the maximum desorption temperature (T_m). As the ramp rate is known and the maximum desorption temperature can be observed from the experimental spectra, the TS detrapping activation energy (E_p) can be determined from the slope ($\frac{E_p}{R}$) of the $\ln \frac{\phi}{T_m^2}$ vs. $\frac{1}{T_m}$ plot. This type of plot is commonly referred to as a "Choo-Lee plot" [91]. This method is widely accepted and employed by many researchers; this may explain why a literature review of trapping kinetic constants, Table 2.2, resulted in primarily only values for detrapping activation energies (E_p) from various metals and alloys.

To determine the number and location of desorption peaks, a Gaussian decomposition method is sometimes used [82, 141]. Fig. 2.17b shows a typical Gaussian spectral decomposition. In this figure the spectrum has been decomposed into four different [overlapping] peaks. After locating the desorption peak(s), the T_m of each of these desorption peaks is recorded when the experimental temperature ramp rate (ϕ) is varied, see Fig. 2.17a [141]. The detrapping activation energy E_p is then determined using Eq. (2.22) and a "Choo-Lee" plot is constructed. Fig. 2.18 shows a "Choo-Lee" plot constructed from this analysis [141]. Furthermore, from these analyses often researchers attribute the "lowest" energy peak to interstitial diffusion [141], which goes against the fundamental assumptions of this method as diffusion is neglected in this analysis.

While this analytical method is relatively fast and the numerical cost of these calculations is negligible, along with a low experimental cost (material and experimental time), one clear downside to the approach is that all spectral contributions are attributed to a trapping mechanism and diffusion is neglected. Furthermore

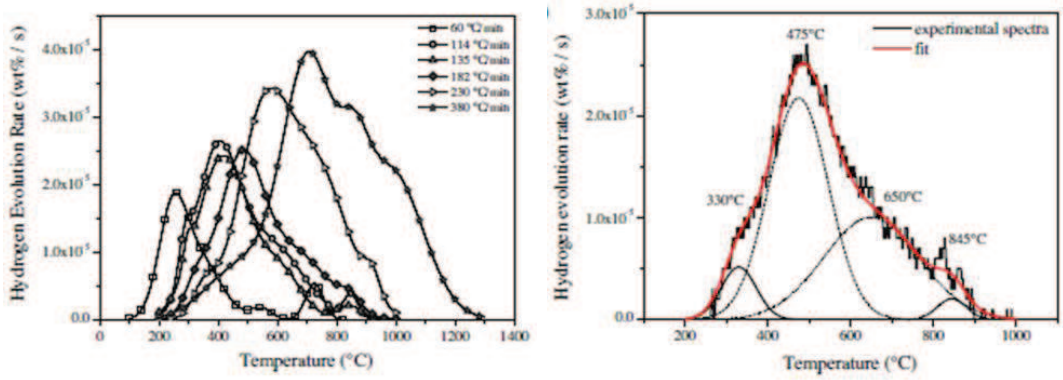

(a) **(b)**

Fig. 2.17 Example of (a) spectral acquisitions[a] for "Choo-Lee plot" construction and analysis and (b) Gaussian decomposition of an experimental spectrum [141].

[a]It should be noted that these spectra were acquired using a Jobin Yvon Horiba EMGA-621W gas analyzer system and not a traditional TDS technique. These figures were choosen just for demonstrative purposes.

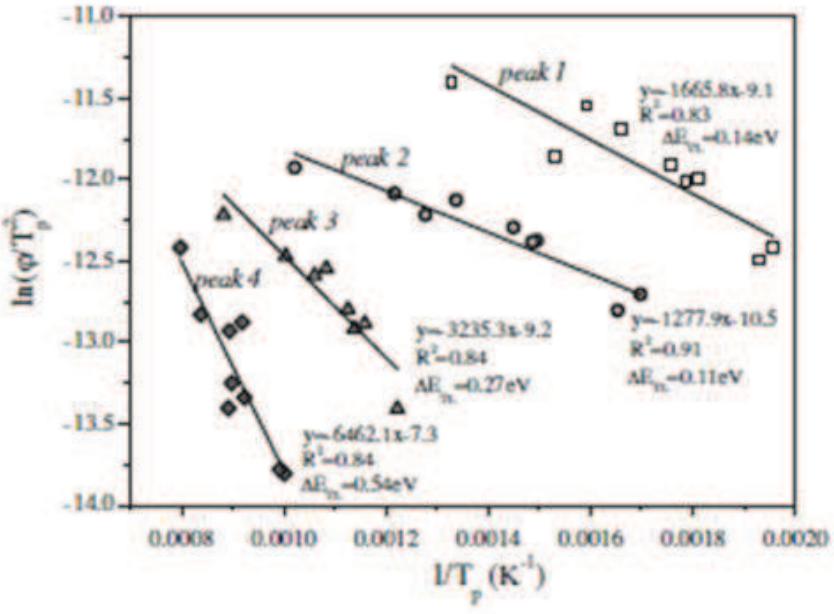

Fig. 2.18 "Choo-Lee" plot analysis for the "TDS" spectra presented in Fig. 2.17 [141].

each desorption peak is associated with a separate kinetic [detrapping] process, for example a TDS spectrum presenting two desorption peaks would be immediately considered to have two TS types [91, 87]. These assumptions have been shown to be misleading and may prove false, except in specific cases [89, 90, 142]. One specific case where Choo-Lee plot trapping analysis may be applicable is for homogeneously charged material with a very "fast" [interstitial] H diffusion coefficient (i.e. pure Fe or low-carbon steel) [90].

In light of these drawbacks and in search of more complete spectral analysis methods, researchers have begun to work with some more sophisticated numerical models, based upon the McNabb and Foster equations [107] or the simplified versions proposed by Oriani *et al.* [69] and successors.

2.5.3.2 Yagodzinskyy *et al.* fitting

Yagodzinskyy *et al.* [134] and Todoshchenko *et al.* [135, 136, 143] have used a numerical model for the derivation of trapping information from an experimental TDS spectrum. They use an approach simulating experimental steps (cathodic H charging, aging, and experimental TDS testing). In order to determine an interstitial H concentration profile in the specimen, they have simulated only diffusion interactions for the hydrogen charging step by solving the diffusion equation and assuming a fixed hydrogen surface concentration (c_0) over the entire charging time:

$$C(x) = \frac{4c_0}{\pi} \sum_{n=0}^{\infty} \frac{(-1)^n}{2n+1} \cos \frac{(2n+1)\pi x}{L} \times \left(1 - \exp -\frac{\pi^2 (2n+1)^2 D_{\text{eff}}(T_s) t_s}{L^2}\right) \times \exp -\frac{\pi^2 (2n+1)^2 D_{\text{eff}}(T_d) t_d}{L^2} \qquad (2.23)$$

where L is specimen thickness, $D_{\text{eff}}(T)$ is the effective diffusion coefficient at temperature T, T_s and t_s are the temperature and duration of charging and T_d and t_d the temperature and time for desorption (i.e. aging before testing). They determine c_0 based upon a relationship between hydrogen activity in the metal and the applied cathodic charging potential.

It has been assumed that during the charging stage the hydrogen trapping reaction is preferential and H absorbed will become trapped creating a sharp "trapping front" (ahead of the trapping front located at distance X_C in the specimen the hydrogen concentration is assumed to be zero) and the TS occupancy behind the front is approximately one ($\theta \approx 1$). Then for desorption experimental stages trapping is no longer considered the major contribution and therefore only detrapping

is considered. Therefore a linear heating rate ($T(t) = T_0 + \phi t$ where T_0 is the temperature at the start of the TDS testing) allows for the construction of the analytical desorption flux ($J(t)$) expression:

$$J(t) = \frac{8sD(t)}{L}\sum_{n=0}^{\infty}\Bigg[c_0 - N_T\left(1 - \frac{L}{\pi(2n+1)X_C}\sin\frac{\pi(2n+1)X_C}{L}\right) \times \exp\left(-\frac{\pi^2(2n+1)^2\int_0^t D(\tau)d\tau}{L^2}\right) + pN_T\left(1-\cos\frac{\pi(2n+1)X_C}{L}\right) \times \int_0^t d\tau \exp\left(-\frac{\pi^2(2n+1)^2}{L^2}\int_0^{t-\tau} D(\xi)d\xi - \rho\tau\right)\Bigg] \quad (2.24)$$

where s is the specimen surface area and $p \approx p_0 \exp(-\frac{E_p}{k_B T})$ is the detrapping kinetic constant as a function of temperature. The fitting parameters are considered to be c_0, D_0, E_D, N_T and E_p (respectively the initial H surface concentration, the pre-exponential factor and activation energy for interstitial diffusion, the TS density and the detrapping activation energy). Using these equations, experimental TDS spectra can be fit. Nonetheless, Yagodzinskyy *et al.* [134] encountered some difficulties with spectral reproduction that they attribute to the simplifications of the system which includes: (i) only one type of TS is considered, (ii) no detrapping during the H charging and (iii) no (re)trapping of hydrogen during TDS/desorption. Furthermore, this fitting method assumes a linear temperature ramp [and not the experimental $T(t)$], something that may not correspond to reality [89, 90, 144].

2.5.3.3 Kirchheim "diffusion-controlled" analysis

R. Kirchheim recently proposed a type of diffusion-controled TDS spectral analysis method using an "energy box" approach [145] for homogeneous H distributions in pure iron. This analysis is based upon the Oriani assumptions [69]. Kirchheim highlights, in the beginning of his analysis, that the Kissinger equation-Choo-Lee plot analyses neglect the interstitial diffusion taking place in the specimen during thermal analysis (as diffusion is a major spectral contribution) and the need for sample thickness considerations [145].

Through a set of simplifications and thermodynamic considerations, an equation for diffusion and trapping interactions during TDS analysis can be developed:

$$\frac{\partial c_f}{\partial T}\left(1 + \frac{c_{t0}y_t}{c_0(y_t + \frac{c_f}{c_0})^2}\right) = \frac{D_f}{\phi}\frac{\partial^2 c_f}{\partial x^2} - \frac{c_{t0}c_f y_t E_t}{RT^2 c_0(y_t + \frac{c_f}{c_0})^2} \quad (2.25)$$

where c_f represents the interstitial hydrogen concentration, c_0 the concentration of normal interstitial sites (it should be noted that homogeneous interstitial and trapped hydrogen dispersions were assumed), c_{t0} is the concentration of all trap sites, y_t can be further defined by the equation $y_t = y_{t0}\exp(\frac{E_t}{RT})$ and for simplification y_t is set equal to 1, D_f the diffusion coefficient of H in normal lattice, ϕ is the heating rate ($\frac{dT}{dt} = \phi$) and E_t the trapping activation energy [145].

This diffusion and trapping equation is then evaluated using a finite difference method by imposing surface sample boundary conditions and calculating the desorption flux during the linear temperature ramp. The calculated desorption spectra can then be compared to experimental TDS spectra and may provide information concerning trapping (i.e. determining a range of activation energies and treating different trap site occupation fractions). This spectral simulation proves very interesting but its validity should be verified when working with non-homogeneous dispersed trapped and/or interstitial hydrogen populations.

Furthermore, in his keynote lecture at Steelyhydrogen [145], R. Kirchheim discussed another interesting TDS analysis method which takes into consideration a range of activation energies associated with trapping at a TS, i.e. at different locations in a dislocation or precipitate/matrix interfaces presenting different coherencies with the matrix. He called this the "Energy Box" analysis approach. This is an extremely interesting approach, but may be too simplified as it would allow for the assignment of a large range of detrapping activation energies for a given trap site type. Associating a large range of activation energies to one specific trap site may not allow for a precise analysis of trapping and therefore further complicate identification and deconvolution of spectral contributions in a situation where a material has more than one type of trap site.

2.5.3.4 General comments on spectral analysis methods

Today, TDS spectral analysis used in the framework of H-material interaction studies is a highly debated issue and many different methods are available. In this section several spectral analysis methods have been presented, each based upon fundamentally different assumptions and hypotheses, but are all aimed at addressing the same problem and analyzing the same type of experiment. Furthermore, it might seem that no single spectral analysis method is adapted to all material systems and each spectral analysis method presents its own advantages and draw-backs; ranging being too simplified and neglecting important information to being very complex and therefore creating high computing time costs. It would seem that the most important factor when choosing a spectral analysis method would be knowing the material system

studied and being aware of what the method is capable of and for what type of system the method is most suited. It would be very beneficial to the field if a general spectral analysis method were available that was capable of taking into consideration the most important parameters and able to extract data directly comparable with different experimental approaches.

2.6 Conclusions

Under PWR operating conditions the structural materials, Ni base alloy 600 and stainless steel 316L, have been found susceptible to **S**tress **C**orrosion **C**racking (SCC). This environmental degradation mechanism is the result of a combination of both internal (material) and external (environmental) factors. For example some internal factors may include: (i) microstructure/metallurgical properties (chemical composition, grain boundary chemistry, precipitates, etc.) and (ii) residual stresses present in the formed component and external factors include environmental conditions: (i) temperature, (ii) pressure, (iii) applied stresses, (iv) solution chemistry (pH, $p(H_2)$, etc.). There have been numerous cracking models proposed to explain the occurrence of this degradation but to date no one model is capable of accurately explaining and predicting this degradation mechanism. One common point brought up by many researchers is the presence of hydrogen (as dissolved hydrogen and/or as the solvent itself) in primary circuit medium.

During the oxidation process and under reactor operating conditions, hydrogen may be absorbed by the alloy. After absorption H will be transported across the material and interact with the different crystallographic sites present in the material, these sites may include: (i) normal interstitial lattice sites, (ii) point defects such as vacancies and hetero-atoms, (iii) one-dimensional sites like dislocations and triple junctions, (iv) two-dimensional sites including grain boundaries and interfaces along with (v) three-dimensional sites such as voids, precipitates and inclusions. The goal of this work will be (i) to better understand the interactions taking place between the absorbed H and the alloy, more specifically concerning diffusion and trapping of hydrogen during transport, (ii) to develop a numerical model capable of simulating these interactions in industrial alloys and (iii) to determine the H diffusion coefficient and the trapping/detrapping kinetic constants for hydrogen at various trap sites present in the studied alloys. To study these interactions an approach coupling experimental results with numerical simulation was used.

One concept that is continuously mentioned by researchers developing numerical models for the study of these diffusion and trapping interactions is the need

for experimental results acquired using a well defined model type materials. This means that all the possible diffusion and trapping interactions taking place in the material are well known and therefore can be taken into consideration in the model. This suggestion will be used for our analysis: materials presenting isolated trap site types will be used in this study to characterize the specific trapping interactions taking place at that site. These materials will be analyzed experimentally using **T**hermal **D**esorption mass **S**pectroscopy (TDS), one of the most adequate experimental techniques to study hydrogen-material interactions as presented in this chapter. The numerical model that was developed for the analysis of experimental results is based upon the McNabb and Foster equations [107]. Their model provides us with an easily adaptable mathematical representation of concomitant diffusion and trapping taking place in metallic materials. While it may not be as complete a model as some proposed in [112, 113, 114] they provide an easily adaptable way of simulating trapping at one or more [108] trap site type for a constantly evolving non-isotherm system (i.e. during TDS) without imposing a set of constricting hypothesis (i.e. local thermodynamic equilibrium between trapped and interstitial H) as done by some other models [69, 108, 124, 134, 145].

The body of this manuscript is separated in three additional chapters. First, a presentation of the materials used and the experimental and numerical methods employed in this study is carried out. The experimental results and discussion are presented together in the next chapter, followed by a chapter focused on the conclusions and perspectives for this study.

Chapter 3

Materials and Method

An austenitic nickel base alloy type 600, referred to as "**A600**", and a commercial grade austenitic stainless steel of type 316L, referred to as "**SS316L**", were used in this study. These two materials are commonly used as PWR structural materials for the **S**team **G**enerator (SG) tubes (A600) and internal reactor vessel components (SS316L).

This chapter will be separated into three sections: (i) material fabrication and characterization, (ii) experimental method and (iii) numerical simulation method used for the analysis of H-material interactions in the alloys.

The first section, Sec. 3.1, will describe the preparation of what are referred to in this manuscript as "**M**odel **M**aterials" (MM), in which TS density can be considered negligible or where one type of **T**rap **S**ite (TS) is predominant, along with material characterizations. The microstructure has been characterized mainly by microscopic observations. These observations have allowed the identification and characterization of different TS types.

To study the H-material interactions **T**hermal **D**esorption Mass **S**ectroscopy (TDS) was used and will be detailed 3.2. This method involves monitoring the desorption flux of molecular species from a material during a temperature ramp or at an isotherm. This section will also provide insight on pre-TDS sample preparation, including mechanical polishing and deuterium charging conditions along with the TDS approach.

Finally the last section, Sec. 3.3, will describe in detail the numerical method (simulating all experimental steps) using the McNabb and Foster equations for predicting hydrogen diffusion and trapping across a material and TDS experimental spectral analysis. A set of hypotheses and important parameters will be presented in order to better describe the reasons for choosing this simulation method. The numerical method coupling experimental TDS results with numerical simulation for the derivation of diffusion and trapping parameters will be presented.

3.1 Model material fabrication & characterization

Two industrial austenitic alloys: a Ni-base alloy of type A600 (heat WL344) provided by Imphy and a commercial grade stainless steel type 316L were used in this study. An A600-like single crystal, with a $< 111 >$ growing axis direction, provided by the Ecole Nationale Supérieure des Mines de Saint-Etienne (Saint-Etienne, France) was also studied. Their chemical compositions can be seen in Table 3.1.

Table 3.1 Chemical composition (wt.%) of studied alloys: an industrial Ni-base alloy 600 (A600 heat WL344, Imphy), an A600-like single crystal (s.c.) (Ecole Nationale Supérieur des Mines de Saint-Etienne), and a commercial grade stainless steel of type 316L (SS316L)

Element	C	Mn	Si	S	P	Ni	Cr	Cu	Co	Fe	Ti	Mo	N	Al
A600-WL344	0.06	0.82	0.31	< 0.001	0.008	base	15.8	0.01	0.01	9.6	0.196	-	98	0.164
A600-like s.c.	n.s.[a]	0.01	0.08	0.01	0.01	base	16.99	0.02	0.01	5.57	<0.01	-	-	-
SS316L	0.019	1.33	0.33	<0.003	0.025	10.36	16.94	0.23	0.10	base	0.024	2.08	-	<0.01

[a] non-specified

After a brief presentation of the microscopy techniques used for material characterization the materials will be characterized, first in their **A**s-**R**eceived (AR) state and then in their model material states. These model states refer to: (i) **P**ure **D**iffusion **S**ystems (PDS) and (ii) **D**iffusion and **T**rapping **S**ystems (DTS). The term PDS refers to a material fabricated from the as-received industrial alloy heat (A600 and SS316L) in which the residual TS density is negligible leaving a microstructure in which all H-material interactions can be attributed to interstitial diffusion, whereas DTS model materials are fabricated directly from PDS by recreating a specific trap site type in a controlled manner, through thermal or thermal-mechanical treatments.

3.1.1 Material characterization techniques

Several microscopy techniques were used to characterize the alloys and will be briefly described in the following subsections. The material characterization methods include light **O**ptical **M**icroscopy (OM), **S**canning **E**lectron **M**icroscopy (SEM), **T**ransmission **E**lectron **M**icroscopy (TEM), and nanoindentation.

3.1.1.1 Light optical microscopy (OM)

Light optical microscope (OM) observations using an Olympus GX51 inverted metallurgical microscope were made to characterize the surface and microstructure of samples in their as-received and model material states. The OM was available in the **L**aboratoire d'**E**tude de la **C**orrosion **N**on-**A**queuse (LECNA, Non-Aqueous Corrosion Laboratory) at the CEA Saclay. Before observation, samples were mirror polished and then [if necessary] electrochemically etched to highlight the grain structure and precipitates or phases, the electrochemical etching solutions and conditions used can be seen in Table 3.2.

Table 3.2 Dilute electrochemical etching solutions used to reveal the microstructure of austenitic materials.

Solution	Conditions		Structure
	E (V)	t (s)	revelation(s)
Oxalic acid (10 %)	3	var.[a]	Grain boundaries
Orthophosphoric acid (10 %)	6	var.[a]	Chromium carbides

[a]etching time at room temperature was variable and depended on both the material and extent of structure revelation needed.

3.1.1.2 Scanning electron microscopy (SEM)

Two scanning electron microscopes were used for imagery in this study: (i) a Karl Zeiss 1525 equipped with a **F**ield **E**mission **G**un (FEG) and **E**nergy **D**ispersion X-Ray **S**pectroscopy (EDS) capabilities and (ii) a LEO 1450VP equipped with EDS capabilities. Both SEM were available in the **L**aboratoire d'**E**tude de la **C**orrosion **A**queuse (LECA, Aqueous Corrosion Laboratory) at the CEA Saclay. SEM observations allowed for more precise microstructure and surface characterizations of the materials in their AR and MM states to be made. EDS is a technique that allows for the elemental analysis of a sample and was used to characterize the precipitates observed in the material. Before observation all samples were polished up to a mirror finished and then [if necessary] electrochemically etched to highlight the microstructure.

3.1.1.3 Transmission electron microscopy (TEM)

Transmission electron microscopy observations and thin foil preparation were carried out by Mme Marie-Christine Lafont of CIRIMAT-ENSIACET at the I.N.P. Toulouse, France. This observation technique was used to characterize the dislocation structure and [when possible] estimate the dislocation density of deformed and non-deformed model materials and the chemical composition of the chromium carbides present in model materials.

Thin foils were prepared by first mechanically polishing samples down to a thickness of 80 μm using SiC polishing papers. Then, 3 mm diameter discs were taken from the sample and thinned using an electrolytic polishing technique with TENUPOL-5 Struers. The thickness of the observed zones ranged from 0 nm to 100 nm depending on their location. The electrolyte was 75 % methanol, 8 % perchloric acid, and 17 % 2-butoxyethanol (ethylene glycol monobutyl ether) solution cooled to between 263 - 268 K with liquid nitrogen. After preparation, the thin foils were observed using a FEG equipped JEOL JSEM 2100F.

While TEM is an extremely powerful technique and provides access to information that the previously mentioned analysis techniques do not, there are some drawbacks and limitations to these observations. For example, only very small zones are observed and therefore a statistical analysis of [all] observed zones needs to be done in order to draw conclusions. Furthermore, the observations are "bulk" observations as thin foils are sectioned from the center of the sample and not from a zone very close to the surface.

3.1.1.4 Nanoindentation

Nanoindentation measures were carried out on polished mirror finished samples (see polishing protocol as described in Sec. 3.2.1) and were used to get more in-

formation concerning the mechanical properties of the model materials in close proximity to the surface ($\leq$ 2 μm). Nanoindentation measurements were done by Mme. Sylvie Poissonnet of DEN/DANS/DMN/SRMP at the CEA Saclay using a Micro Materials NanoTest™ NTX system equipped with a Berkovitch tip nanoindenter. A diagram of the system can be seen in Fig. 3.1.

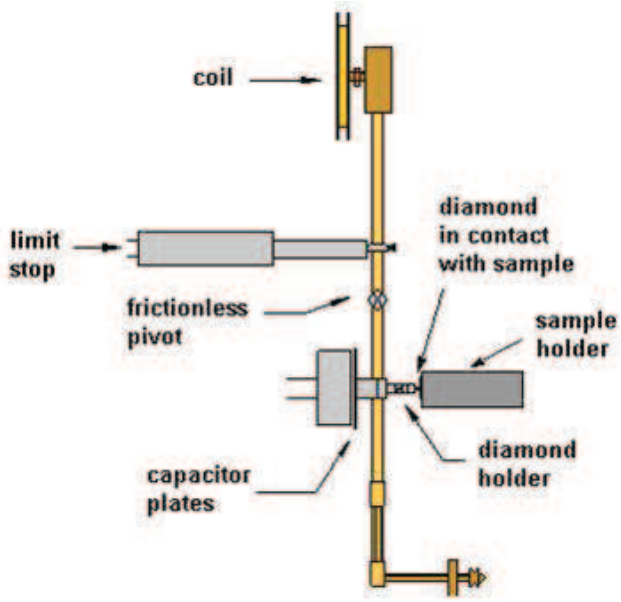

Fig. 3.1 Schematic diagram of the NanoTest pendulum. [Original design-[146]]

The sample is held at a constant temperature (300 K) for all measures in order to avoid any variation in material properties on the nanoscale due to temperature fluctuations. The NanoTest™ NTX system measures the movement of the indenter tip pressed into a surface up to a predetermined maximum load. Force, displacement and time are continuously monitored for the duration of the indentation using the data acquisition system (DAQ NI 6289) and Bespoke Micro Materials data analysis software. Twenty indentations were done for each depth ranging from 50 nm to 2000 nm. Information concerning hardness (GPa) in function of distance from the sample surface was acquired using this technique.

3.1.2 As-received material characterizations

The AR materials, A600 heat WL344 (Imphy) and commercial grade SS316L (CEA) were characterized upon reception.

3.1.2.1 A600-AR material characterizations

Before reception, the heat of A600 had been subjected to an austenitization **T**hermal **T**reatment (TT) of 1 h at 1083/1096 K in air. The slabs sectioned from the large cylinder of A600-WL344, present a banded structure (bands of large and small grains) as shown in Fig. 3.2. The grain sizes for both the small and large grains are 120 ± 5 μm and 55 ± 7 μm respectively. The small black spots present in the micrographs are chromium carbides and the larger black structures have been identified as titanium carbon nitrides (TiCN) by EDS analysis. Furthermore, in Fig. 3.2, it would seem to be the bands of small grains, present higher quantities of chromium carbides.

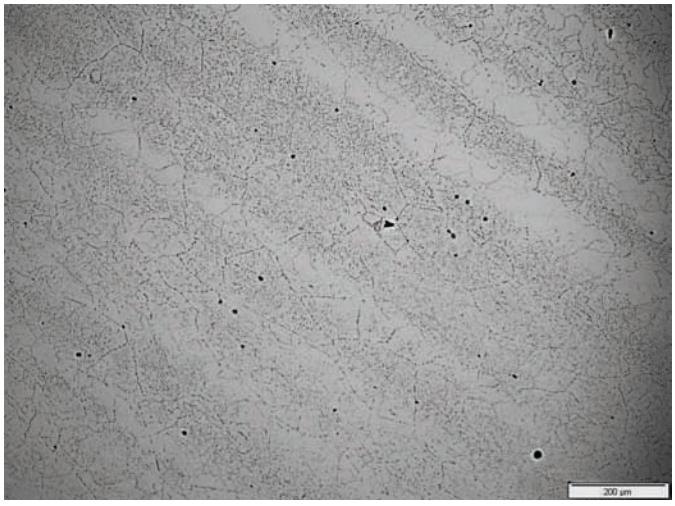

Fig. 3.2 OM image of A600 heat WL344 (Imphy) in its as received material state. The small black spots seen in the image are chromium carbide (Cr_xC_y) precipitates and the larger more angular black structures have been identified as TiCN by SEM-EDS analysis.

3.1.2.2 SS316L-AR material characterizations

The as-received commercial grade SS316L had been previously subjected to an austenitization TT (2 h at 1323 K), and will serve as the AR stainless steel material. To reveal the microstructure, the sample was electrochemically etched in a 10% oxalic acid solution. SEM observations were then carried out, and the resulting microstructure can be seen in Fig. 3.3. The material is characterized by a homogeneous grain size ($\approx$ 36 ± 9 μm) and structure. The dark black elongated shapes seen in the image have been characterized as retained ferrite. Some of the retained ferrite phases are indicated in Fig. 3.3 by white arrows. The average

ferrite content in the slab of SS316L-AR was estimated using a Fischer Feritscope FMP30 and was determined as $< 1\%$ (vol.). Image analysis, using a Python script (Pillow 2.7.0.), gave a ferrite surface fraction of 0.2 %.

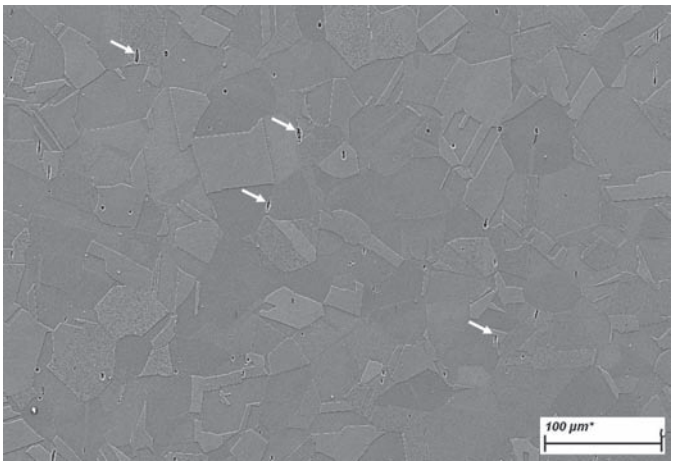

Fig. 3.3 SEM image of the as-received commercial grade SS316L (CEA). The white arrows indicate some of the isolated retained ferrite phases present in the slab.

3.1.3 Pure diffusion system (PDS)

The microstructure of the AR materials is complex and the types and quantities of TS are not controlled (i.e. presence of dislocations, [non-homogeneous repartitions of] chromium carbides, vacancies, TiCN, grain boundaries, etc). A less complex material needs to be used to study hydrogen diffusion in these alloys. In order to "simplify" this material (eliminate the majority of TS) a series of **T**hermal **T**reatments (TT) were used, see Fig. 3.5. In the following sections, the TTs will be detailed and the material characterizations for the resulting **P**ure **D**iffusion **S**ystem (PDS) materials will be presented.

3.1.3.1 PDS elaboration

To study the interstitial diffusion of hydrogen in industrial alloys, all, or at least a large majority of, possible trap sites need to be eliminated. These trap sites include [but are not limited to] dislocations (residual cold working and internal stresses), chromium carbides (Cr_xC_y), and vacancies [83]. The majority of residual cold working, stress, vacancies and Cr_xC_y precipitates (for A600) were eradicated by a series of TT, see Fig. 3.5.

First, metal slabs (150 mm x 22 mm x 1.1-1.5 mm) were heated to 1453 K for 1 h under vacuum followed by a rapid water quench. Vacuum was essential to these thermal treatments as to avoid extensive specimen oxidation and the creation of an important "dechromized" zone at the slab surface, subsequent oxygen uptake and [chromium and/or oxygen] gradient that would modify the solubility and diffusivity of H in the lattice. This high temperature TT-water quench combination was made possible by encasing the slabs in quartz tubes which were pumped down to a primary vacuum. These tubes had at one end the specimen and at the other zirconium chunks. Zr was then heated to eliminate the O_2 left in the tube before sealing the tube in the middle (along the dotted line in Fig. 3.4) therefore isolating the slabs from the Zr-chunks and keeping them under vacuum[1]. The tube side with Zr chunks was then removed from the system. Then the quartz tube holding the specimen was placed in a furnace for the thermal treatments (1 h at 1453 K) and then quickly broken during the water quench[2].

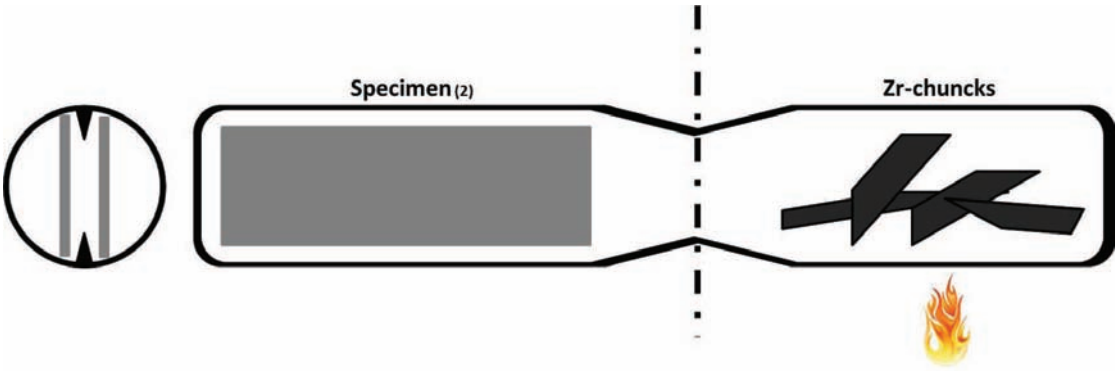

Fig. 3.4 Diagram of quartz tube encasing used for the TT under vacuum. Two material plaques where encased in each tube and separated by quartz points so as not to touch during the TT.

The temperatures of the TT was chosen to solubilize the carbides and also subsequently annihilate the dislocations. It may induce slight grain growth. Quenching was performed to block carbide formation and keep the C in solution. During the rapid water quench, it can be assumed that a significant amount of thermal vacancies were created. To annihilate the thermal vacancies the slabs were tempered for 15 h at 573 K in air then slowly cooled down to room temperature in the furnace. The tempering, does not effect the stability of the C kept in solution, as this temperature is less than the minimum temperature for carbide formation given

[1]The quartz tubes - samples under vacuum combinations were fabricated by M. Bruno Coltrinari (DSM/IRAMIS/NIMBE/LCM) at the CEA Saclay

[2]These TTs and quenchs were done by M. Daniel Nunes (DEN/DANS/DMN/SRMA/LTMEx) at the CEA Saclay

the carbon content of the A600 heat used in this study. During these TT a very thin oxide layer was formed on the slab surface. This oxide, along with dechromed zone, is very easily removed by surface preparation procedures (mechanical polishing, detailed in Sec. 3.2). Furthermore, during this series of thermal treatments, the residual amount of hydrogen present in the as-received industrial alloy was desorbed.

The resulting model material is considered to be a **P**ure **D**iffusion **S**ystem or PDS, i.e. interstitial [and grain boundary] diffusion is[/are] the predominant H-material interaction[s] expected with this model material and the only one leading to significant contribution to TDS desorption spectra. The question of trapping or short-circuit diffusion taking place at grain boundaries will be discussed in a following subsection (Sec. 3.1.3.4).

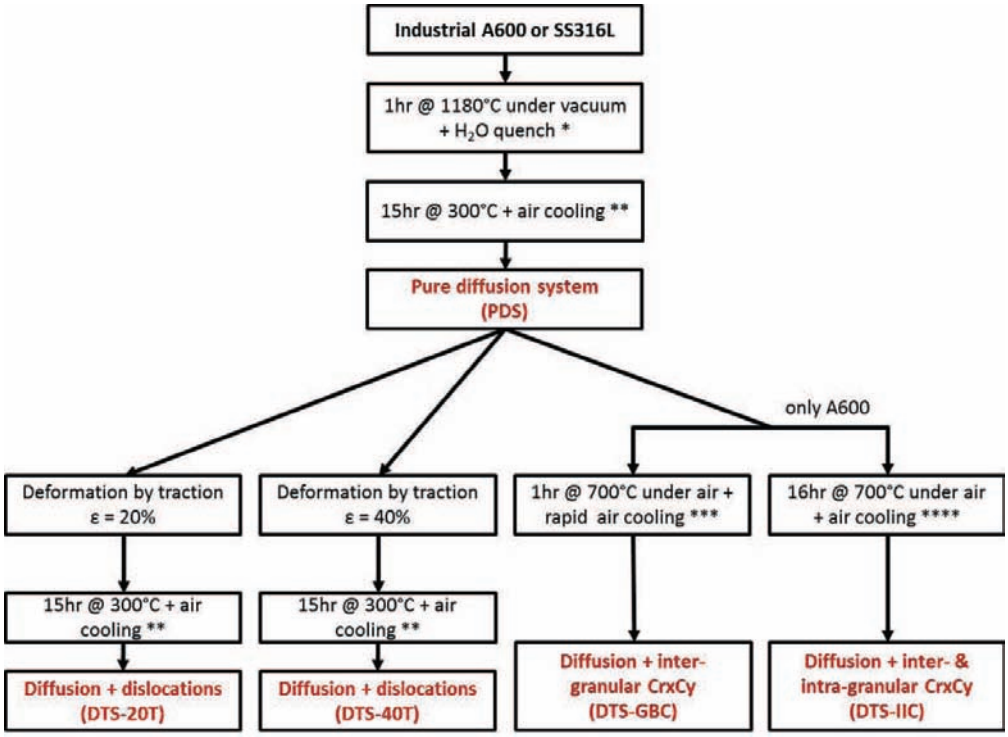

Fig. 3.5 Diagram detailing the series of thermal and if desired mechanical treatments used to create the studied model materials (MM). * elimination of residual cold working, chromium carbides (if A600) and recrystallization, ** elimination of [thermal] vacancies, *** and **** precipitation of new chromium carbides (A600 only).

3.1.3.2 A600-PDS material characterizations

The A600-PDS final microstructure can be seen in Fig. 3.6a. Before OM and SEM observations, the grain structure was revealed by an electrochemical etching process which involved first etching the sample in a 10% oxalic acid solution, in order to reveal the grain boundaries, and then etching in a 10% orthophosphoric acid solution (Table 3.2), in order to reveal any chromium carbides that may have re-precipitated. When the AR microstructure, Fig. 3.2, is compared to the PDS microstructure, Fig. 3.6a, it is clear that [the majority of] the Cr_xC_y have been solutionized, as they are not visible along the grain boundaries or inside the grains. A few TiCN can still be observed in the grains in Fig 3.6a and are indicated by white arrows. Slight grain growth was also observed after this heat treatment with the larger grains measuring 127 ± 16 μm and the smaller grains 68 ± 9 μm. While a banded grain structure is still observed, the demarcation of bands is much less exaggerated and the zones of large grains have become much thicker whereas the zones of smaller grains thinner.

TEM thin foils were also prepared and observed to verify the annihilation of dislocations. Fig. 3.6b reveals very few dislocations. When dislocations were encountered they were either found isolated, in parallel bands, or accumulated along grain boundaries. The dislocation density $\rho_{\text{dislocation}}$ was estimated by determining the total length of dislocations in an image ($L_{\text{dislocation}}$) and dividing that by the analyzed volume corresponding to the TEM image (V_{image}). The thin foil thickness was assumed to be on average 100 nm. This value was then multiplied by a factor K_d which takes into account the dislocations that lie parallel to the thin foil normal, this value was taken to be 2 [147]. Several images were analyzed using Eq. (3.1). The average dislocation density was calculated as (3.6 ± 0.1) 10^8 cm^{-2}.

$$\rho_{\text{dislocation}} = K_d \left(\frac{\sum L_{\text{dislocation}}}{V_{\text{image}}} \right) \tag{3.1}$$

3.1.3.3 SS316L-PDS material characterizations

The SS316L PDS material was observed after electrochemical etching in a 10% oxalic acid solution to reveal grain boundaries (Table 3.2), as seen in Fig. 3.7. These observations reveal, as in its AR state, a homogeneous grain size and structure along with some isolated retained ferrite phases. These isolated ferrite phases are the black elongated marks in Fig. 3.7. Very little grain growth was observed and the average grain size can be considered equivalent to that in the AR material state ($\approx 36 \pm 9$ μm).

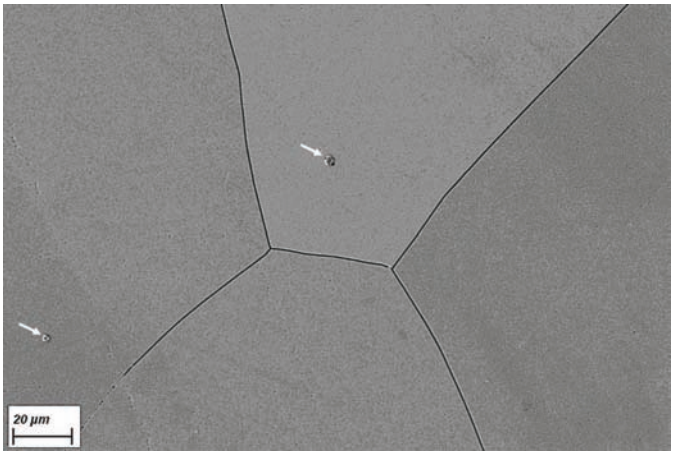

(a)

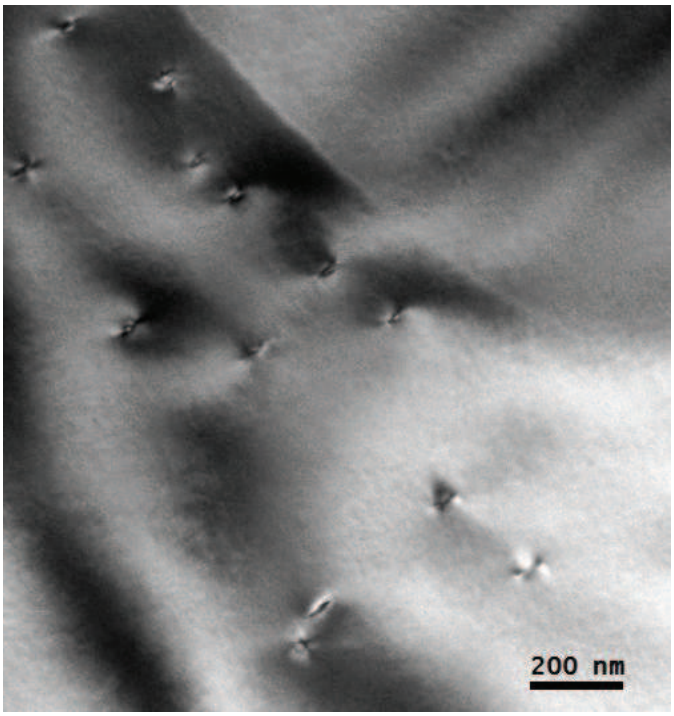

(b)

Fig. 3.6 (a) SEM and (b) TEM micrograph of A600-PDS MM. In Fig. 3.6b some isolated dislocations can be observed. The white arrows in Fig. 3.6a indicate the TiCN present in the material.

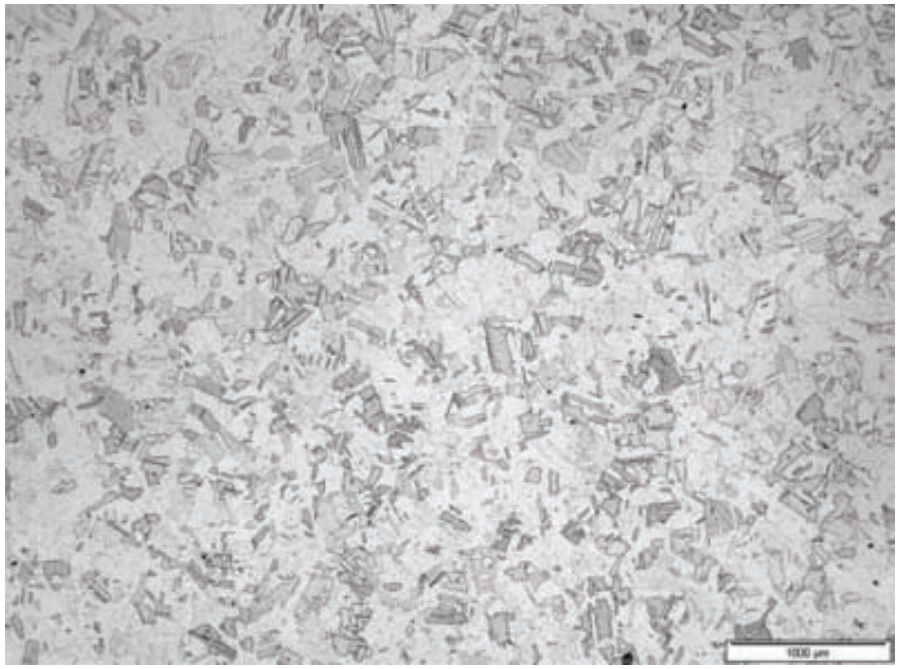

Fig. 3.7 OM image of a SS316L-PDS model material.

3.1.3.4 Influence of "residual" trap sites

As discussed in the previous subsections, the PDS model materials for A600 and SS316L are polycrystalline, i.e. have **G**rain **B**oundaries (GB). Along with the GBs, the TiCN (A600) and isolated retained ferrite phases (SS316L) were not eliminated from the material. This results in "as-model-as-possible" materials as the residual cold working (i.e. the majority of dislocations), a majority of dislocations, vacancies and chromium carbides (A600) have been eradicated.

Researchers have commented on the possible trapping and/or short-circuit diffusion interactions taking place respectively at precipitates or phase boundaries and grain boundaries in metals [53, 54, 56, 57]. The possible hydrogen trapping phenomenon that may occur at ferrite/austenite boundaries is a subject of great interest, especially for example in duplex type SS which are characterized by mixed phases of austenite and ferrite [148]. The stainless steel 316L used in this study, presents a small quantity of isolated retained ferrite phases in the austenite structure. Pertaining to these isolated phases, several things must be addressed: the possible effect (i) on H diffusion in the alloy ($D^H_{\text{ferrite}} >> D^H_{\text{austenite}}$ [149, 150]), (ii) on H solubility in the alloy ($S^H_{\text{bcc}} << S^H_{\text{fcc}}$ [149]), and (iii) of trapping at the ferrite-austenite interfaces [148]. It should be mentioned that the effect of ferrite phases on hydrogen diffusion, solubility, and trapping in an alloy has been majority studied in dual-phase alloys presenting far more important quantities of ferrite, i.e.

for example in duplex SS. Furthermore, the isolated retained ferrite present in the SS316L used in this study was estimated as < 1 % (ferritscope and image analysis techniques, see Sec. 3.1.2.2) and is significantly lower than that in duplex SS. It may be therefore argued that its effect on H diffusion and solubility is negligible and possible trapping interactions at these phase interfaces are very minor.

While ferrite is not present in the A600 studied, the $Ti_xC_yN_z$ precipitates/matrix interface can be considered a phase boundary and their influence should be addressed. It can be imagined that H trapping at these interfaces may occur. This subject seems to not have been studied in-depth in literature and focus seems to have been made on trapping phenomenon at chromium carbides [22, 82] and in TiC precipitates in *bcc* Fe base alloys [84, 151]. However, there are very few TiCN present in the AR and PDS A600 materials, and the question may arise to the detectability of hydrogen trapping at these interfaces that exist in such small quantities.

Regarding GBs, some researchers consider an apparent H diffusion coefficient (D_{app}) [54, 56, 57] in the material which takes into consideration both interstitial diffusion in volume (D) and diffusion along the grain boundaries (D_{GB}), often defined as:

$$D_{\text{app}} = (1 - f)D + fD_{\text{GB}} \tag{3.2}$$

where f represents the volume fraction of grain boundaries in the material. It is important to consider the segregation factor (s) in grain boundary diffusion [58, 67]. Often for alloys, s is already taken into consideration in the D_{GB} [67] and is not presented as a separate variable in Eq. 3.2, as D_{GB} in literature is often in fact the product of $s.D_{\text{GB}}$. The grain boundary volume fraction can be calculated, if the grains are considered to be cubic, from :

$$f = \frac{3\delta}{d} \tag{3.3}$$

where δ is equal to the average GB thickness and d the average grain size [53]. If the GB thickness is taken to be 5 Å and the average grain size that of the A600 PDS material, f would be on the order of 1.5 10^{-5} (assuming an average grain size in the A600-PDS material of 100 μm). A GB diffusion coefficient of hydrogen in A600 was unable to be found in an extensive literature review, therefore a value of D_{GB} and D in pure Ni at room temperature will be used [53, 54]. If D_{app} is calculated using Eq. (3.2), using the D_{GB} (4 10^{-6} cm^2.s^{-1}) and D (9 10^{-10} cm^2.s^{-1}) as published by Oudriss *et al.* [56], the resulting apparent diffusion coefficient at room temperature is very close to that of D ($D \pm 6\%$). Furthermore, this conclusion that GBs have little to no effect on the diffusion of H in the studied alloys is in agreement with the conclusions drawn by some researchers [59].

Even with this first rapid discussion hinting that the effects of grain boundaries, TiCN (A600) or "residual" ferrite phases can be neglected for the model materials, their possible contributions to TDS spectra will be addressed experimentally through the use of A600, by comparing A600-PDS model materials with the grain boundary and TiCN free A600-like single crystal specimen. It would also be interesting to verify these points on a SS316L austenite single crystal, something that unfortunately was not able to be done in this work as this type of single crystal was not available. If the contribution of "residual" sites (GBs and TiCN or retained ferrite) can be neglected in the model material systems, the focus can be placed on studying the other TS present in high quantities in the AR industrial materials, for example: dislocations (A600, SS316L) and chromium carbides (A600).

3.1.4 Diffusion and trapping system - Dislocations

During component elaboration, for example SG tube forming using Ni-base alloy 600, the industrial materials may be deformed to achieve the desired final shape, etc. This working and deformation process may create a high quantity of dislocations and very high residual stresses in the material. Since researchers often consider dislocations as important hydrogen TS [11, 42, 73, 83, 152, 153], a strong focus has been made on studying the interactions taking place between H and this type of site.

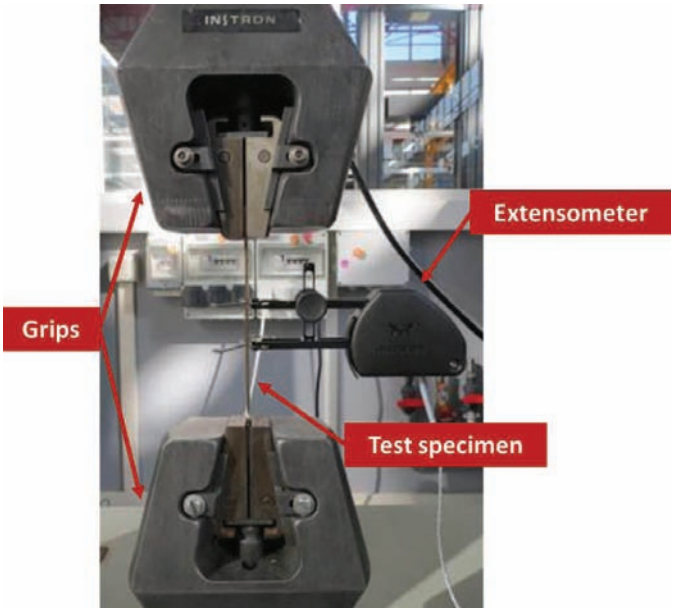

Fig. 3.8 Photo of tensile test specimen with extensometer before tensile testing. The grip, extensometer, and test specimen are indicated by the labeled red arrows in the figure.

To understand the H-dislocations interactions a model material presenting quasi-uniquely dislocations as potential TS needed to be elaborated. An elaboration process, which included first controlled material deformation (creation of dislocations) followed by tempering (elimination of vacancies created during deformation) was adopted. The DTS-dislocations (DTS-D) model material for A600 and SS316L were then characterized.

3.1.4.1 DTS-dislocation (DTS-D) elaboration

The DTS-D model materials were fabricated from the final PDS materials. A general overview of their fabrication can be seen in Fig. 3.5. The PDS model material was first machined by **E**lectrical **D**ischarge **M**achining (EDM), commonly referred to as "spark erosion", into tensile test specimen and then deformed by tensile testing (deformation rate of $\dot{\varepsilon} = 2.5\ 10^{-4}\ s^{-1}$), using an Instron 5500R apparatus. Tensile tests were interrupted at desired deformation percent: (i) ϵ=20% and (ii) ϵ=40%. The two different final deformations were chosen as to create different dislocation densities which would result in two different trap site densities (n).

Extensometers, type Instron 2630-112, were attached to the specimen to more precisely measure the local deformation in the reduced sample section. This allowed for a closer monitoring of the local strain, therefore giving insights on the homogeneity of specimen deformation as compared to the global strain. A photo of the tensile test specimen and extensometer set-up can be seen in Fig. 3.8. The resulting stress-strain curves estimated for both materials (A600 and SS316L) can be seen in Fig. 3.9. After deformation the specimen was tempered (15 h at 573 K) to annihilate the [majority of] vacancies created during tensile testing. This tempering may also [slightly] decrease the dislocation density. This series of thermo-mechanical treatments results in a material presenting almost only dislocations as possible hydrogen TS.

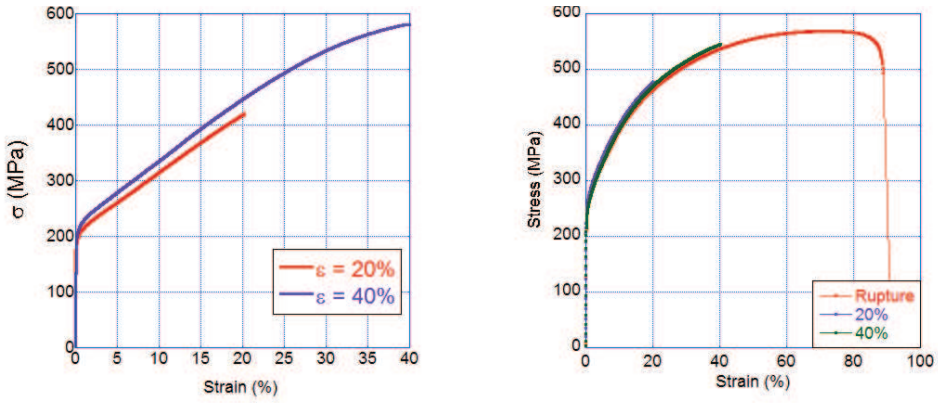

(a) **(b)**

Fig. 3.9 Experimental stress-deformation curves for tensile tests interrupted at ϵ=20% and ϵ=40% and continued until rupture (only for (b)) for (a) A600 and (b) SS316L.

3.1.4.2 A600-DTS dislocations material characterizations

After elaboration, the A600-DTS-D model materials were characterized using several microscopy techniques: OM and TEM. OM observations of pre-deformed $\epsilon = 20$ % and $\epsilon = 40$ % can be seen respectively in Fig. 3.10a and Fig. 3.10b. The grains are highly deformed in these images and show some twins and slip lines. TEM thin foils were prepared and observed for the $\epsilon = 40$ % MM, see Fig. 3.11. There are too many dislocations present in the zone to evaluate the dislocation density ($\rho_{\text{dislocation}}$) with any certainty using the line-intercept method or any image correlation method, as done previously for the PDS model material.

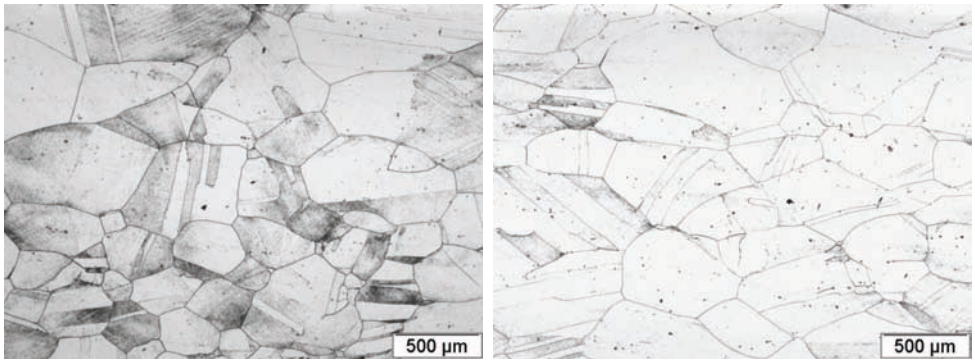

(a) **(b)**

Fig. 3.10 OM images of A600-DTS-D MM (a) $\epsilon = 20\%$ and (b) $\epsilon = 40\%$ after polishing and electrochemical etching.

Bailey *et al.* [154] proposed a method for calculating the dislocation density of fcc materials which correlates the total stress to the dislocation density, immediately after traction. This correlation can be seen in Eq. (3.4). In this equation σ is the stress, α is the neighbor stress, assumed to be 0.5, m is the Taylor factor, which is 3.067 for fcc materials, b is the Burgers vector, which for a *fcc* metal is equal to $\frac{a\sqrt{3}}{2}$ where a is equal to 0.35 nm for A600 [155], and $\bar{\mu}$ is the shear modulus of the material taken as equal to 81.6 GPa [156, 157].

$$\rho_{\text{dislocation}} = \left(\frac{\sigma}{\alpha m b \bar{\mu}}\right)^2 \tag{3.4}$$

As previously mentioned in Sec. 3.1.4.1, after interrupted tensile testing the slabs were tempered. This tempering, may induce slight lattice relaxation and therefore a slight modification of the dislocation density that is not taken into account by Bailey equation dislocation density estimation. Despite this discrepancy the Bailey equation will still be used to estimate the dislocation density in our MM states.

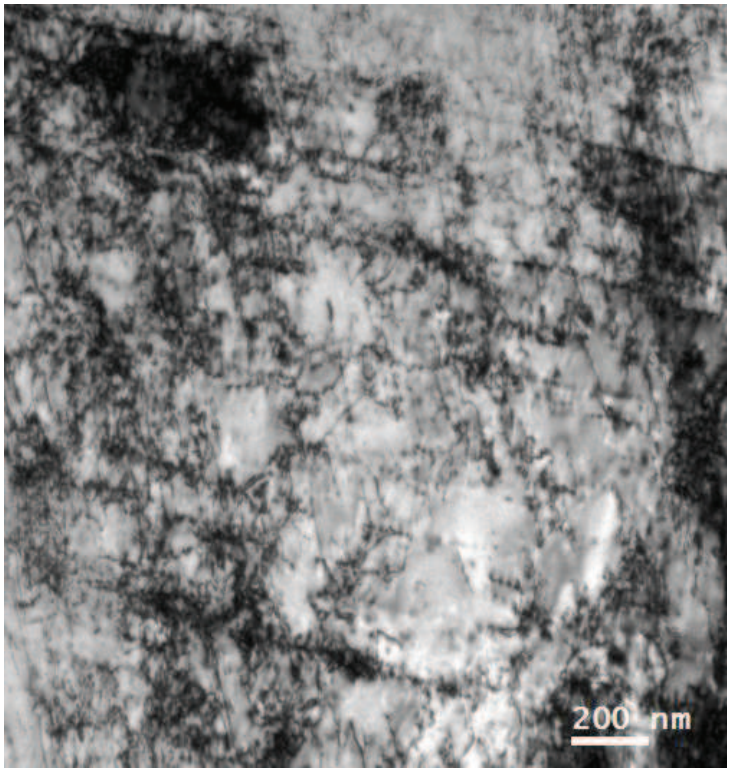

Fig. 3.11 TEM thin foil observation of A600-DTS-D ($\epsilon = 40\%$) MM.

The calculated $\rho_{\text{dislocation}}$ for deformations of 20 % and 40 %, along with a TEM estimated dislocation density for the non-deformed specimen are shown in Table 3.3.

Table 3.3 Dislocation density for A600-DTS-D (ϵ=20% and ϵ=40%) estimated using the Bailey equation [154], Eq. (3.4), and an average value for a non-deformed PDS material estimated from TEM micrographs using the numerical method presented in Eq. (3.1).

Deformation (%)	Stress (MPa)	$\rho_{\text{dislocation}}$ (cm^{-2})
0	–	$(3.6 \pm 0.1)\ 10^8$
20	420	$1.2\ 10^{10}$
40	580	$2.3\ 10^{10}$

3.1.4.3 SS316L-DTS dislocations material characterizations

Optical microscope observations revealed high grain deformation and the presence of slip lines and some twins, see Fig. 3.12. The dislocation density was calculated using these tensile test data (Fig. 3.9b) and the Bailey equation [154] where the shear stress was taken to be 80.8 GPa [158] and a was considered to be 0.36 nm. The dislocation density ($\rho_{\text{dislocation}}$) for deformed samples is shown in Table 3.4.



Fig. 3.12 Optical microscope observations of the SS316L-DTS-D MM (ϵ=40%).

Table 3.4 Dislocation density calculated for SS316L-DTS-D MM (ϵ=20% and ϵ=40%) using the Bailey equation [154], Eq. (3.4). A typical dislocation density for heat treated (1.5 h at 1373 - water quench) non-tempered SS316L [159] is given for a comparative purpose.

Deformation (%)	Stress (MPa)	$\rho_{\text{dislocation}}$ ($\text{cm}^{-}2$)
0	–	$< 10^{10}$ [159]
20	477	$1.5\ 10^{10}$
40	545	$2.0\ 10^{10}$

3.1.5 Diffusion and trapping system - Chromium carbides ($\mathbf{Cr}_x\mathbf{C}_y$)

The Ni base alloy 600 commonly used for SG tubes in PWR nuclear power plants can have an important carbon content (max 0.15 wt%). The A600 used in this study (Imphy heat WL344) has a carbon wt% of 0.06, see Table 3.1. This carbon content can lead to the precipitation of chromium carbides in the alloy during elaboration and thermal treatments. Hydrogen may accumulate at the Cr_xC_y/matrix interfaces [22] and trapped due to lattice mismatch and induced stress-strain fields. This H build-up may have a negative effect on the mechanical properties of the material. In recent years, understanding these H-chromium carbide interactions has been at the center of numerous studies [22, 82, 160] and their characterization has been a main focus of this work.

As the majority of pre-existing TS, including Cr_xC_y, were eradicated from the A600 during the PDS elaboration TT, the chromium carbides needed to be recreated in a controlled manner. In this section, a method for the reprecipitation of chromium carbides, preferentially either at grain boundaries, referred to as a DTS-GBC (**G**rain **B**oundary **C**arbides) from this point forward, or inter- and intragranularly, referred to as a DTS-IIC (**I**nter-**I**ntragranular **C**arbides), in a controlled manner will be presented [72]. Microstructural characterizations of these model materials will then be presented and discussed.

3.1.5.1 DTS-chromium carbide fabrication

Using the PDS model material as a starting point, preferential precipitation of chromium carbides along grain boundaries (DTS-GBC) can be achieved through a heat treatment at 973 K for 1 h in air followed by rapid air cooling [10], whereas homogeneous reprecipitation of Cr_xC_y (DTS-IIC) was achieved by a heat treatment at the same temperature for 16 h followed by very slow air cooling [down to room temperature] in the furnace [10]. The grain growth experienced during these thermal treatments can be considered negligible.

3.1.5.2 Material characterizations

The microstructure of both these model materials was observed using both OM and SEM techniques after revealing the chromium carbides by electrochemically etching the specimen in a 10% orthophosphoric acid solution.

Fig. 3.13a shows the A600-DTS-GBC MM with chromium carbides along the grain boundaries and Fig. 3.13b shows the A600-DTS-IIC MM with chromium carbides reprecipitated inter- and intragranularly. The DTS model material micrographs differ greatly from the PDS micrographs (Fig. 3.6). For a pure diffusion system no Cr_xC_y are observed along the GBs, but for both DTS model material (GBC and IIC) they can be observed along GBs (Fig. 3.13a and Fig. 3.13b) or as for A600-DTS-IIC also in grain volume (Fig. 3.13b).

The OM micrographs, seen in Fig. 3.13, were converted to black and white images (black pixel = Cr_xC_y, white pixel = matrix) using a Python script (Pillow 2.7.0.). The surface fraction of chromium carbides preferentially reprecipitated only at grain boundaries, i.e. A600-DTS-GBC (Fig. 3.13a) is about 0.85 % whereas for a model material having been subjected to the TT for homogeneous reprecipitation, i.e. A600-DTS-IIC (Fig. 3.13b) the surface fraction is 8.35 %. Characterization of the Cr_xC_y themselves was carried out by TEM observations of a DTS-IIC MM (chromium carbides present at both grain boundaries and in grain volume), see Fig. 3.14. Several chromium carbide precipitates are indicated in this image by white arrows. The intergranular precipitates measured on average between 400 nm and 1 μm whereas the intragranular precipitates were smaller measuring between 250 and 500 nm.

Furthermore these [intergranular] precipitates were identified as orthorhombic Cr_7C_3 carbides by electron diffraction pattern indexation, see Fig. 3.15. From these observations it is impossible to draw any conclusions concerning the interface coherency between the Cr_7C_3 and the alloy.

3.1.6 Material overview

In the previous sections the as-received (AR) and set of model materials (MM) were presented. The complexity of the AR materials: A600 and SS316L was highlighted through microstructural observations (Sec. 3.1.2). These materials included chromium carbides (A600), titanium carbon nitrides (A600), retained ferrite phases (SS316L), grain boundaries (A600 and SS316L), non-homogeneous grain sizes (A600) along with the presence of residual cold working. All the aforementioned crystallographic anomalies or metallurgical defects intrinsically present in the AR industrial materials, possibly due to forming processes or crystallization during the casting, may act as possible TS and could create complex H-material interaction systems, i.e. with more than one type of TS.

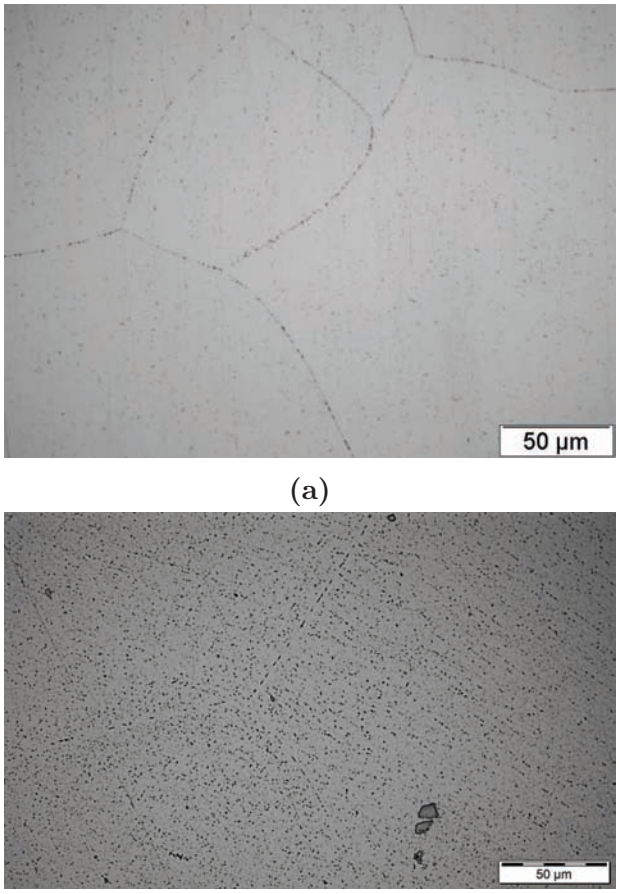

(a)

(b)

Fig. 3.13 OM image of (a) A600-DTS-GBC and (b) A600-DTS-IIC. Micrograph (a) shows the preferential localization of Cr_xC_y along the GBs, whereas (b) a relatively homogeneous reprecipitation along GBs and in volume.

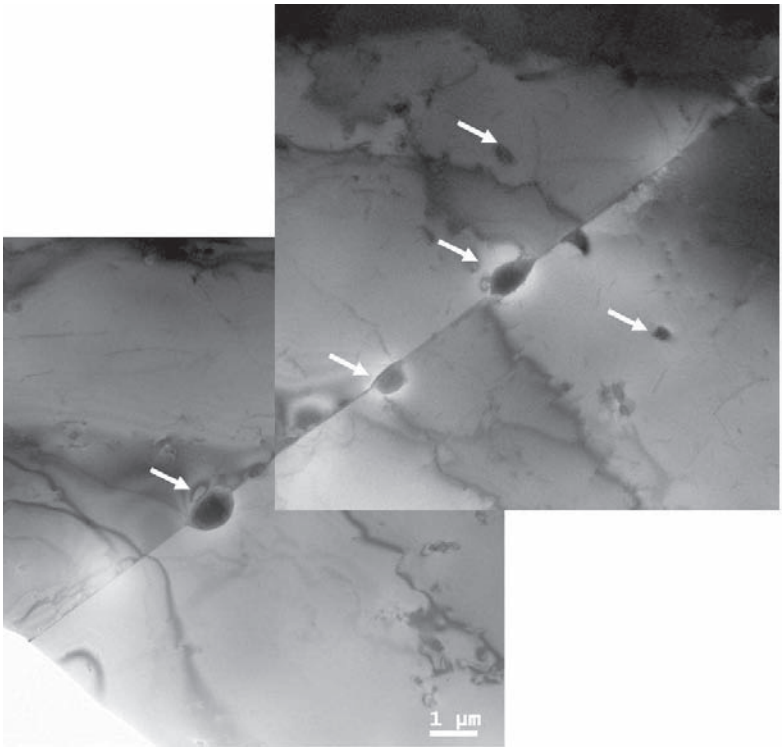

Fig. 3.14 TEM image of A600-DTS-IIC. The white arrows indicate some of the observed chromium carbide precipitates.

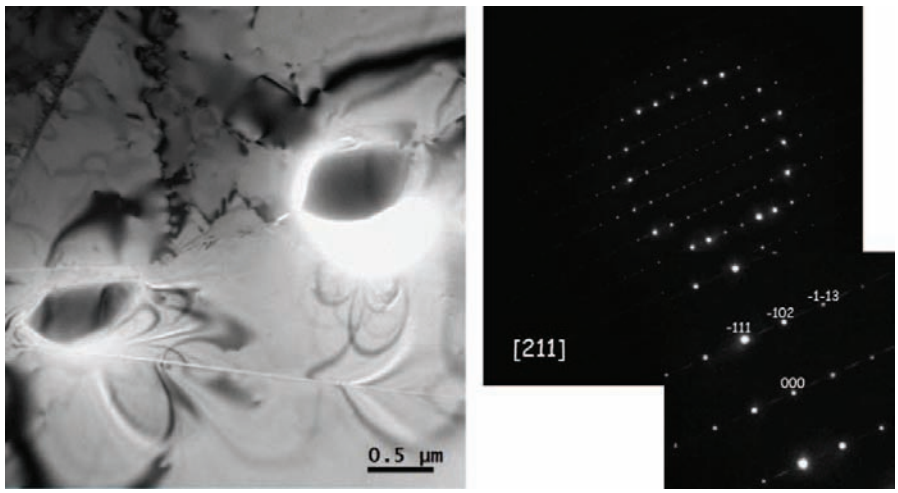

Fig. 3.15 TEM image of A600-DTS-IIC and electron diffraction pattern allowing for their identification as Cr_7C_3 type chromium cabrides.

In order to study H-material interactions in a more controlled manner model materials were created, first eradicating the possible TS present in the system (PDS) then recreating the TS in a controlled manner (DTS), see Table 3.5. The next step is to now study the hydrogen transport and interactions taking place in these model materials. To do so thermal desorption mass spectroscopy (TDS) will be used.

Table 3.5 Table of materials to be studied experimentally (s.c. = single crystal, x = to be studied, – = non-fabricated)

Model material type	A600	A600-like s.c.	SS316L
PDS	x	x	x
DTS-D (ϵ=20%)	x	–	x
DTS-D (ϵ=40%)	x	–	x
DTS-GBC	x	–	–
DTS-IIC	x	–	–

3.2 Experimental method: TDS

Thermal desorption mass spectroscopy, often referred to as TDS, was used to study the H-material interactions (diffusion and/or trapping) in the model materials presented in Sec. 3.1. Before TDS testing, the samples needed to be prepared. This preparation includes mechanical polishing, followed by cathodic charging of the specimen with deuterium (^{2}H). This process will be detailed in the following sections, followed by specific information concerning the TDS testing procedure.

3.2.1 Sample preparation: mechanical polishing

Samples were machined, from the larger heat treated slabs of each model material, using EDM, into specimen measuring about 13 mm × 13 mm with a 3 mm × 5 mm tab and a starting thickness of 0.11 cm [before mechanical polishing]. All sample edges were first ground down to SiC 1200 grit paper, this eliminated the film left on the surface by EDM. Both sample faces were mechanically polished from SiC 800 grit paper down to a mirror finish using an 0.04 μm aluminum oxide or 0.04 μm silicon dioxide colloidal suspension respectively for Ni-base and Fe-base alloys.The final step of sample polishing was 2 h on a vibrating table in the respective aluminum oxide or silicon dioxide suspension in order to minimize the surface cold working induced during the mechanical polishing process. After mechanical polishing, hardness in function of distance from the specimen surface

was measured using both nanoindentation and microindentation techniques, see Sec. 3.1.1.4. The results are displayed in Fig. 3.16.

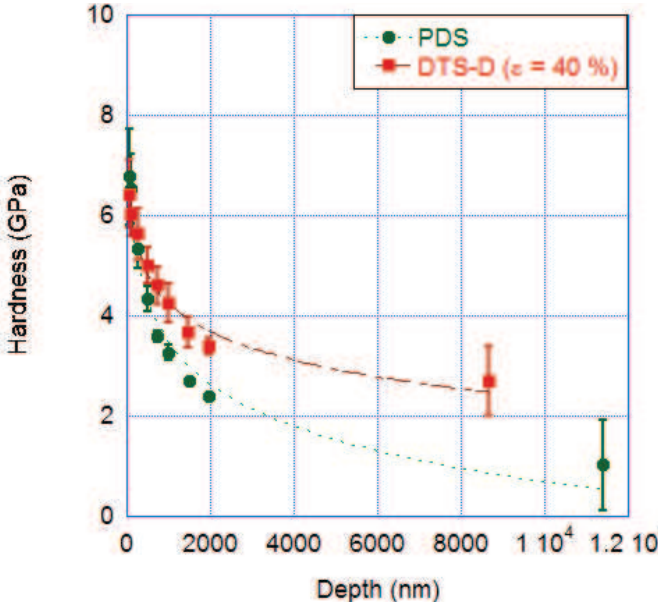

Fig. 3.16 Hardness (GPa) in function of depth (nm) measured using nanoindentation (indentation depth $\leq$ 2000 nm) or microindentation (depth $>$ 2000 nm) methods for an A600 PDS (**circles**) and A600 DTS-D $\epsilon = 40$ % (**squares**) model materials.

A maximum hardness is observed at the surface for both model materials which quickly decreases in the first 2000 nm before reaching what could be considered a stable value in volume. It is important to keep in mind that according to internal documentation, a surface hardness after mechanical polishing without a vibrating table finishing step is on the order of 20 GPa (measurement done using a nanoindentation technique). This comparison demonstrates that the surface cold working zone has been minimized but not completely eliminated. It may be argued that zone affected by surface cold working is very limited when compared to the zone affected by cathodic charging, and its impact is supposed negligible on the diffusion and trapping data derived from TDS spectra.

After mechanical polishing, sample thickness was on average between 0.7 and 0.9 mm and sample width remained nearly unchanged. Final specimen dimensions after preparation were recorded. After polishing, samples were prepared for deuterium charging. This involve first welding, by **R**esistive **S**pot **W**elding (RSW), a thin copper wire to the specimen tab. One sample face, the Cu wire, the entire tab (front and back) and all edges were protected from the charging solution using Lacomite varnish for room temperature charging. Only one sample face was left exposed [to the solution].

3.2.2 Sample preparation: deuterium (^{2}H) charging

Deuterium (^{2}H) was introduced into the material by cathodic charging in a deaerated (Ar bubbling) 0.1 M NaO^2H (99.90 % ^{2}H) solution by applying a cathodic

current, see Fig. 3.17. Specific deuterium charging conditions (time t, temperature T, and current density j) can be seen in Table 3.6. After cathodic charging, the samples were immediately transfered and stored in liquid nitrogen ($N_{2(l)}$) until TDS testing or directly transfered to the TDS setup. This cold storage ($T_{N_{2(l)}} = 77$ K) prevented deuterium desorption [or further internal diffusion] in the material before TDS testing. The transfer time, from the charging cell to $N_{2(l)}$ storage was on the order of 2 min, this time was noted and considered in analysis.

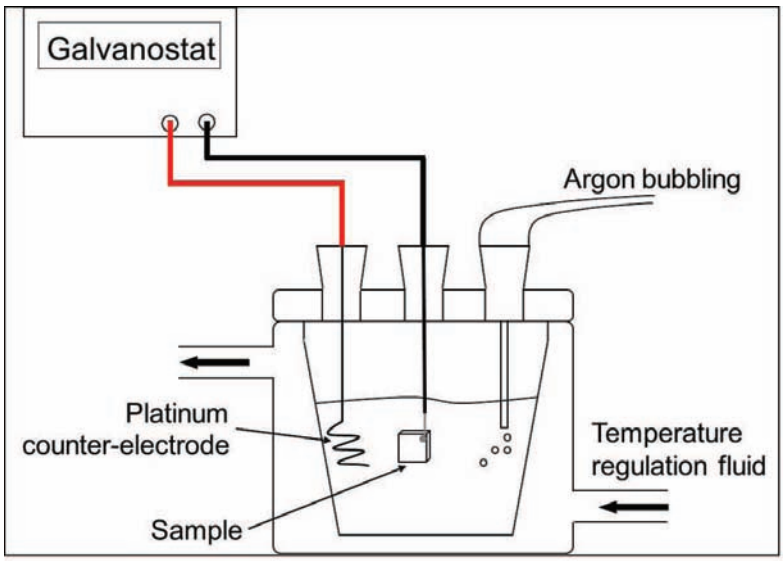

Fig. 3.17 Diagram of cathodic charging cell used for ^{2}H charging.

Table 3.6 Typical experimental cathodic [deuterium] charging conditions: solution, time (t), temperature (T), and current density (j) used in this work.

Charging type	Solution	T (K)	t (s)	j (mA.cm^{-2})
A	0.1 M NaO^{2}H	298	1800	-100

As previously mentioned, one goal of this study was to develop a numerical code capable of simulating hydrogen diffusion and trapping interactions in alloys. To develop this code, which will be presented in Sec. 3.3, it was imperative to know the boundary conditions throughout the experimental procedure starting with cathodic charging; this means that it was necessary to know if during deuterium charging the system was under a constant imposed surface ^{2}H flux or subjected to a constant imposed surface ^{2}H concentration. To have access to this information chronopotentiometry curves (potential in function of time) were obtained under galvanostatic conditions (-100 mA.cm^{-2}).

The sample potential was monitored using a three-electrode system: (i) Pt counter electrode, (ii) saturated calomel KCl reference electrode (RedRod-Radiometer Analytical), and (iii) working electrode, i.e. the sample itself. The resulting chronopotentiometry curves for SS316L and A600 specimen can be seen in Fig. 3.18.

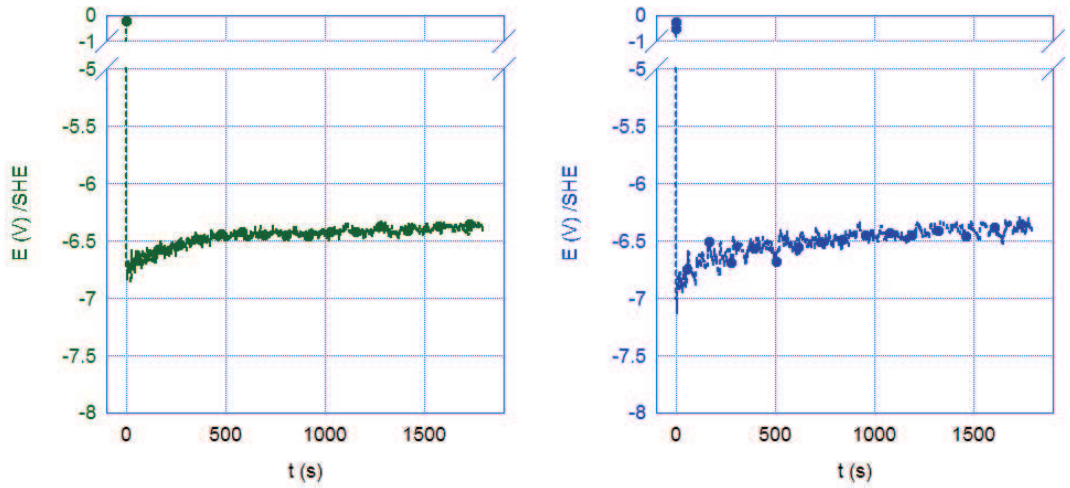

(a) **(b)**

Fig. 3.18 Chronopotentiometry results for charging conditions A, see Table 3.6, for (a) SS316L and (b) A600 materials.

The measured potentials (Fig. 3.18) can be considered quasi-constant for the duration of the cathodic charging (1800 s at 298 K) and tend to become independent of time. These experiences, evidencing a potential evolution quasi-independent of time for a constant imposed current, show that the steady-state approximation can be applied to the ^{2}H surface discharge mechanism [32]:

$$\left.\frac{\partial \mu}{\partial t}\right|_{x=0} \simeq 0 \tag{3.5}$$

where μ represents ^{2}H concentration, t represents time, and $x = 0$ the sample face exposed to the deuterium solution. This implies:

$$\mu[0, t] = \text{constant} \tag{3.6}$$

As a consequence, a constant superficial surface concentration will be imposed for numerical simulation of the system. Furthermore, this stationary potential for the duration of charging, can be related to a quasi-steady state reaction system at the surface of the sample [32].

3.2.3 TDS testing

Previously ^2H charged samples were analyzed in TDS, the whole TDS experimental set up used in this work can be seen in Fig. 3.19. TDS testing consists of monitoring the deuterium ($^2H_2$) and deuterated molecules (i.e. $^2H^1H$, ^2H_2O and $^2H^1HO$) desorption flux in function of time (t) and temperature (T). The water (H_2O) signal was monitored as an indication of vacuum chamber cleanliness, while argon (Ar), oxygen (O_2) and carbon dioxide (CO_2) were monitored as to serve as "leak detectors". The TDS setup, seen in Fig. 3.19, consists of a quartz tube under dynamic vacuum; this tube is passed through a tubular furnace and is relayed to an Inficon Transpector® H100M **M**ass **S**pectrometer (MS) under dynamic vacuum (10^{-8} mbar). The MS ionizes, separates, detects and identifies molecules (or fragments of molecules) by their mass (m) to charge (z) ratio (m/z). This is done by: (i) ionization (and fragmentation) of molecules, (ii) separation in function of their ratio m/z, (iii) the ionic charge integrated over a period of time is measured by a Faraday cup (dq/dt), and finally (iv) the signal is then amplified and transformed into an electric current in A.

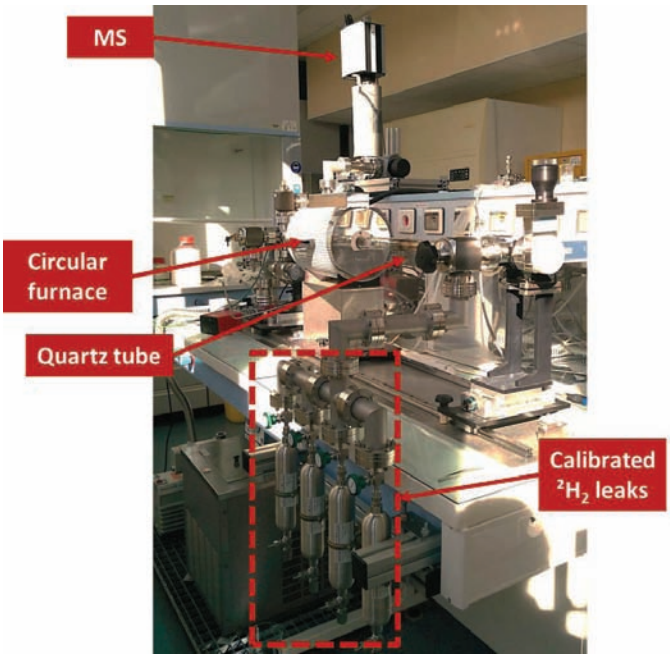

Fig. 3.19 Photo of thermal desorption mass spectrometry experimental system at the Laboratoire d'Etude de la Corrosion Aqueuse (LECA) at the CEA Saclay.

The TDS system can be separated into two chambers, see Fig. 3.20: (A) the quartz tube and furnace chamber and (B) the mass spectrometer chamber, as each has its own pumping system (respectively P1 and P2). The possibility to isolate the chambers from one another, by closing V3, allows for the mass spectrometer (chamber B) to remain under vacuum while the sample is inserted into chamber A. Once the sample has been placed in the isothermal zone of the furnace, chamber A needs to be pumped down to a sufficient vacuum for mass spectrometer operation ($2.5\ 10^{-6}$ mbar) before opening V3 thereby linking the two chambers.

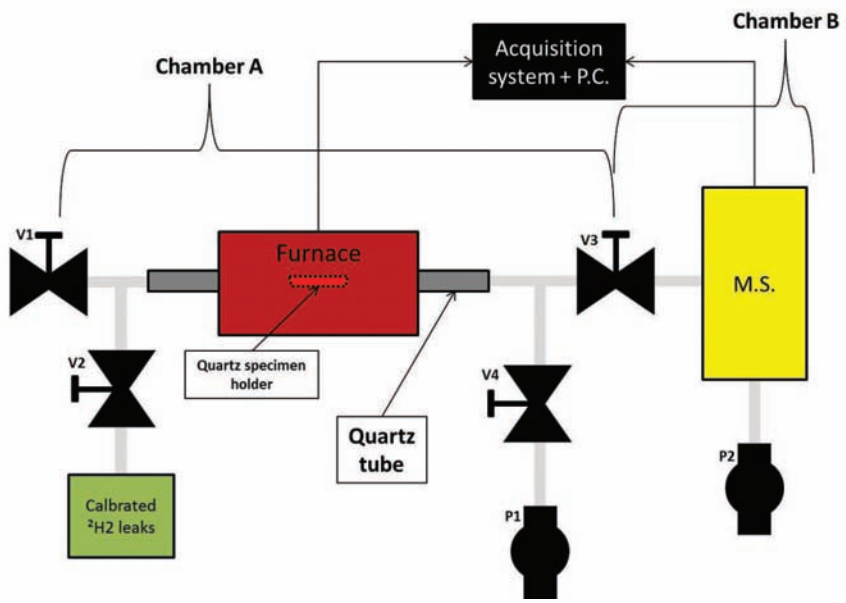

Fig. 3.20 Schematic diagram for the thermal desorption mass spectrometry experimental system at the Laboratoire d'Etude de la Corrosion Aqueuse (LECA) at the CEA Saclay. In this diagram V = valve, P = vacuum pump and M.S. = mass spectrometer.

Before starting spectrometer acquisition, the valve connecting chamber A to its pumping system (P1), V4, is closed, and the entire system is held under dynamic vacuum by chamber B's pump, P2. This forces all desorbed species to pass by the MS. Mass spectrometer acquisition, temperature and pressure measurement can then be started. An incompressible pumping time before starting the MS signal acquisition, on the order of 14 - 18 min, induces a room temperature aging of the specimen; to which the transfer time from the $^2H_2$ charging cell to cold storage and/or to the TDS setup must be added. This systematic aging period was noted at $\Delta t_{\text{transfer}}$ and taken into consideration during spectral analysis.

The specimen are then subjected to a either temperature ramp from room temperature ($\approx$ 295 K) to 1323 K, or an isotherm, during which desorption flux is monitored. The data acquired results in a "TDS spectrum". This spectrum is the deuterium desorption flux, $^2H_2$ or m/z = 4, in Ampere (A) with regards to time (t) and temperature (T). This signal can be converted to flux (mol ^{2}H.cm^{-2}.s^{-1}) through a calibration procedure, which involves recording the spectrometer signal (A) when a calibrated deuterium debit (mol $^2H_2$.s^{-1}) is leaked into the system, this is then transformed into deuterium flux by taking into consideration the desorption surface area (i.e. sample surface area).

3.2.4 TDS calibration

A set of four calibrated CALMASTER™ [3] $^2H_2$ (deuterium gas) leak standards are connected to the TDS system for desorption flux quantification purposes, see Fig. 3.21. TDS calibration is carried out on a regular basis by measuring the mass spectrometer signal (A) to a calibrated deuterium gas leak standard's flux (mol $^2H_2.s^{-1}$).

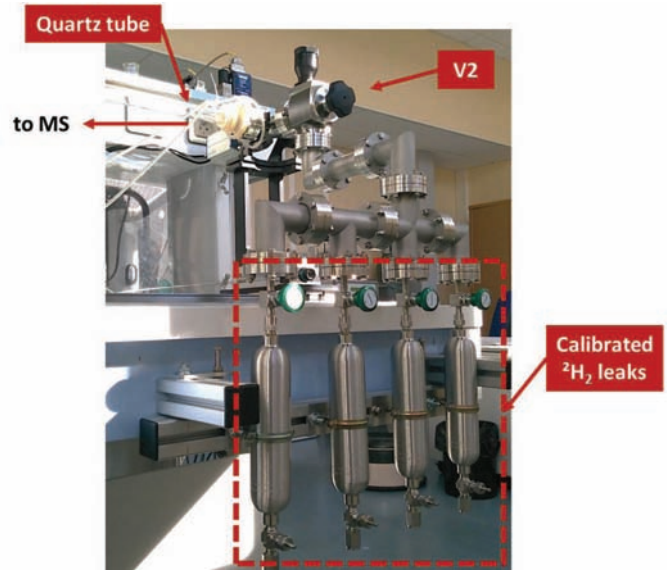

Fig. 3.21 Calibrated LACO Inc. CALMASTER™ deuterium ($^2H_2$) leak standards attached to TDS system by in V2 Fig. 3.20.

Several calibrations were performed at room temperature; the leak rates are dependent on temperature and were corrected for the daily temperature using the specified correlation[4] provided by the manufacturer. An example calibration spectrum can be seen in Fig. 3.22a. The calibration procedure involves first measuring the calibrated leaks "noise" level with all $^2H_2$ leak valves closed (t = 0-200 s in Fig. 3.22a), this "noise" level is not equal to that of the TDS system (which is measured when V2 is closed), as the calibrated leak standard's valves, see Fig. 3.21, leak at a continuous rate into vacuum even when closed. After signal stabilization, one leak (normally starting with the smallest leak rate) was slowly opened, in order to avoid dramatic pressure increases in the system (t = 200 s in Fig. 3.22a), and the new signal with $^2H_2$ flow was measured and can be recognized as the "plateau-like" signal in Fig. 3.22a (t = 200-400 s in Fig. 3.22a). After this signal stabilized the valve was closed (t = 400 s in Fig. 3.22a) and the signal was re-allowed to stabilize (t = 400-600 s in Fig. 3.22a). This procedure was repeated for each calibrated leak.

Further testing was done in order to verify the deuterium signal stability of the MS at elevated temperatures and during a temperature ramp. In order to do

[3] CALMASTER™ calibrated leak standards are fabricated by LACO Technologies Inc. (Salt Lake City, UT).

[4] The temperature dependence of the each leak standard is specified in the calibration certificates.

this, a stereotypical T ramp of $\phi = 10$ K.min^{-1} was imposed while the 5.02 10^{-11} mol $^2H_2$.s^{-1} deuterium leak was held open, the results can be seen in Fig. 3.22b, this test was repeated several times and the differences in TDS spectra can be seen on this figure. It is clear that the measured signal is stable in the range of tested temperatures and the room temperature calibration is valid for the range of temperatures ($\approx$ 295-1300 K) used in TDS testing.

The calibration results (Fig. 3.22a) were then analyzed to establish a calibration factor between the ionic current, i, in A and the actual deuterium gas flux, F, in mol $^2H_2$.s^{-1}, see Fig. 3.22c. The conversion equation was determined to be (Eq. (3.7)):

$$F = (4.4 \pm 0.3)\, i \tag{3.7}$$

where i represents the ionic current in A measured for m/z = 4 ($^2H_2^+$ ions) by the MS and F corresponds to the real molecular flux of $^2H_2$ from the calibrated leak (mol.s^{-1} into vacuum). The flux of ^{2}H atoms released from the specimen during TDS analysis will correspond to twice the value of F. This atomic ^{2}H flux (mol ^{2}H.s^{-1}) can then be converted into at. ppm.s^{-1} by taking into account the sample mass. The possibility for spectrometer calibration for the deuterium signal allows for quantitative analysis of mol $^2H_2$.s^{-1} (then converted to mol ^{2}H.s^{-1}) desorption flux to be done, providing more information on the absorption, diffusion, trapping and therefore desorption taking place in the model materials.

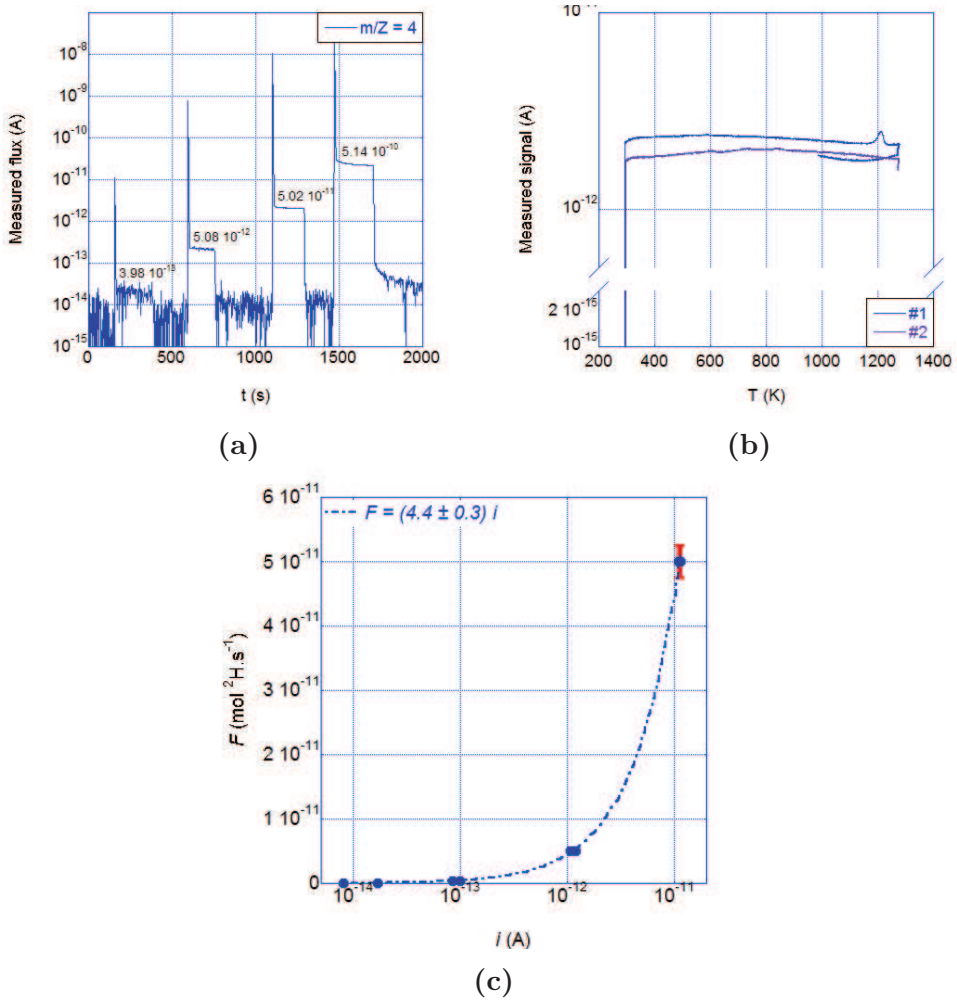

Fig. 3.22 TDS calibration spectrum: (a) raw calibration data for all four calibrated leaks, the corresponding leak rate in $mol.s^{-1}$ for each leak is shown on the graph, (b) the mesured flux for calibrated leak 5.02 10^{-11} mol.s^{-1} during a temperature ramp ($\phi = 10$ K.min^{-1}) repeated twice, and (c) the final calibration curve showing the correlation between the measured ionic current at m/z = 4 (A) and the real molecular flux (mol $^2H_2$.s^{-1}).

3.3 Numerical simulation method

As previously mentioned, the goal of this study is to construct a database of diffusion coefficients and trapping and detrapping kinetic constants related to hydrogen/industrial alloy interactions. To do so, the idea is to couple experimental TDS results with a numerical simulation routine to derive the diffusion coefficient (D) of deuterium in alloys and trapping and detrapping kinetic constants, (respectively k and p). These coefficients and constants were assumed to follow Arrhenius type temperature relationships, thereby giving the system its temperature dependence. Therefore when deriving the diffusion coefficient it is necessary to determine both the pre-exponential constant (D_0) and activation energy (E_D). Likewise, when deriving the kinetic trapping and detrapping constants, respectively k and p, it is necessary to determine the pre-exponential constants (k_0 and p_0) and activation energies (E_k and E_p) associated with them. These constants are determined using two numerical aids **W**olfram **M**athematica© and **P**ython™.

Wolfram Mathematica© is a software commonly used for engineering calculations and programing symbolic mathematics. This software has many built in functions for the resolution of [partial] differential equations and was used in the context of this study for the numerical analysis of experimental results. One problem encountered with Wolfram Mathematica© over the course of this study was linked to "memory management" in the "kernel" of Wolfram Mathematica©, which limited the size and number of consecutive co-dependent calculations that could be run. Python™ is a highly versatile open-source programing language commonly used for scientific and engineering applications that was used in this study in order to resolve highly coupled partial differential equations using the finite difference method. Two Python™ packages that made equation resolution possible were SciPy and NumPy. A computer cluster available at the CEA Saclay was used to run the calculations, increase performance and decrease total calculation time.

The numerical method used in this study is based on the original work of McNabb & Foster [107]. This method was developed for the determination of diffusion coefficient parameters and trapping and detrapping kinetic constants from experimental data and will be detailed in the following sections. Experimental spectra were gathered on "model materials" described in Sec. 3.1, in which only one type of trap site is predominant (DTS) or trap site density is negligible (PDS) to acquire a set of "model" experimental TDS spectra for each type of isolated H-material interactions. For example, the PDS material would be used to acquire a series of reference TDS spectra where the only spectral contribution is due to interstitial diffusion. These spectra would then be fit using the developed numerical routine deriving the specific diffusion parameters, D_0 and E_D, associated with interstitial diffusion in the material. This code also takes into consideration the experimental temperature ramp, sample measurements (L), and experimental conditions, i.e.

the charging and transfer time and temperature, see Fig. 3.23.

The derived diffusion parameters are re-injected into the simulation code, along with the experimental desorption flux, temperature ramp, and experimental conditions for the DTS "model" TDS spectrum. The code then determines the pre-exponential constants (k_0, p_0) and activation energies (E_k, E_p) associated with the specific trapping-detrapping system, see Fig. 3.23. To evaluate the robustness of these derived parameters, TDS spectra obtained under different experimental conditions, for example a different T ramp and/or aging period, are simulated with the aide of the numerical code using the previously determined parameters. The resulting simulated TDS spectra are then compared to the corresponding experimental spectra.

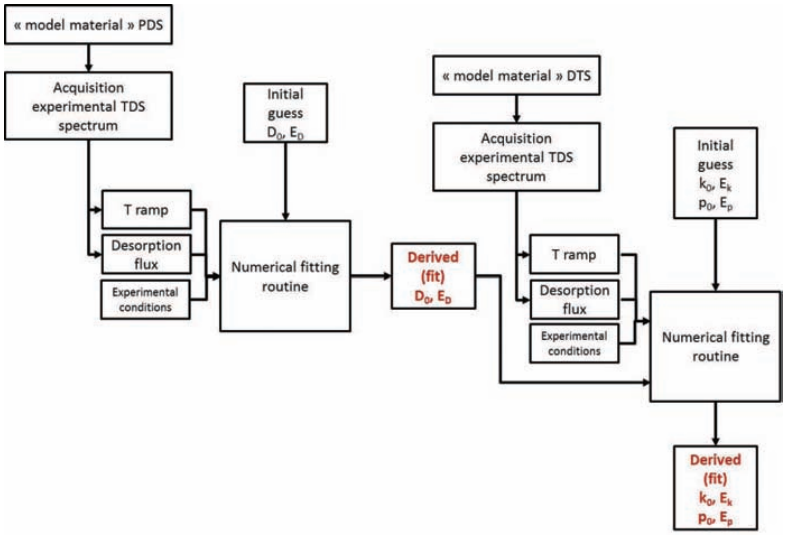

Fig. 3.23 Logic diagram for the numerical approach used to derive diffusion and trapping parameters [90].

This iterative method, coupling experimental data with numerical simulation, derives constants (D_0, k_0, p_0, E_D, E_k, E_p) associated with the diffusion coefficient and kinetic trapping interactions using a two step process. This approach would allow for the diffusion coefficient constants to be derived separately before the four kinetic trapping and detrapping parameters. Furthermore, for each diffusion and trapping system the derived kinetic reaction constants serve to construct a database of kinetic information for individual trap site types.

In this section a numerical approach for the simulation of TDS spectra using the McNabb and Foster equations [107] taking into account the entire experimental sample history and without imposing some of the traditional simplifying hypotheses (i.e. local thermodynamic equilibrium and no retrapping during TDS analysis) will be presented in-depth. The extreme sensitivity of TDS spectra on the sample

parameters and experimental conditions along with the importance of considering pre-exponential constants and activation energies associated for trapping and detrapping along with the trap site density during analysis will be discussed.

3.3.1 Mathematical model and simulation approach

In this study interstitial diffusion and trapping, at one trap site, are assumed to be the only rate limiting steps for hydrogen absorption and desorption and therefore the McNabb and Foster equations [107] can be used to model the system. Surface reaction and recombination are not considered to be rate limiting steps at this point in the model [161].

In this model, a dilute system ($\theta \approx 0$) was not assumed and thereby the $(1-\theta)$ term was not neglected, as done by Kasuya *et al.* [108]. Furthermore, the assumption of local thermodynamic equilibrium between trapped and lattice hydrogen and the use of an effective diffusion coefficient will not be used [69] as this assumption implies that trapping and detrapping kinetic constants tend towards infinity and thereby are indeterminable [120].

A uniform and homogeneous distribution of traps is assumed and the sample is considered a finite medium of thickness L. Each trap site is considered to be isolated in the material and it is assumed they do not interact directly with one another. A finite difference method was used to solve simultaneously for θ and μ, respectively the trap occupancy and lattice hydrogen concentration in Eq. (2.11). It is imperative to know the H distribution in the material in order to simulate the system. The simulation has been split into three sequential steps further "mirroring" the entire experimental protocol. This procedure includes: (i) charging the sample in hydrogen for a period of time at a fixed temperature, (ii) transfer from the charging setup to the TDS system (aging at room temperature), and (iii) TDS testing imposing a regulated temperature ramp.

Table 3.7 Boundary conditions used in simulation where L = sample thickness, t_{charging} =final charging time, and t_{transfer} =final transfer time.

	$\mu[x,t]$		$\theta[x,t]$
Charging	$\mu[0,t]=\mu_0$, $\mu[L,t]=\mu_0$ or 0	$\mu[x,0]=0$	$\theta[x,0]=0$
Transfer	$\mu[0,t]=\mu[L,t]=0$	$\mu[x,0]=\mu[x,t_{\text{charging}}]$	$\theta[x,0]=\theta[x,t_{\text{charging}}]$
TDS	$\mu[0,t]=\mu[L,t]=0$	$\mu[x,0]=\mu[x,t_{\text{transfer}}]$	$\theta[x,0]=\theta[x,t_{\text{transfer}}]$

Each simulation step uses the previous' final concentration profiles, for μ and θ as its initial concentration profiles, and it has been assumed that there is no hydrogen present in a material before charging. For the charging step (i) the

initial surface hydrogen concentration, μ_0, at the charged face(s) ($x = 0$ and/or $x = L$) is assumed to be equal to its solubility in the material and is held constant for the entire charging period. For the latter steps, (ii) transfer and (iii) TDS, the hydrogen concentration at both faces is set to zero and the desorption flux can be calculated, at $x = 0$ and $x = L$. It has also been assumed that no absorption takes place during these stages. These boundary conditions can be seen in Table 3.7. When simulating TDS spectra, the total desorption flux is considered to be the sum of the desorption from both sample faces ($x = 0$ and $x = L$) as the sample has a finite thickness.

3.3.2 Experimental parameters

3.3.2.1 Initial hydrogen concentration

As previously mentioned, simulations will be carried out using the McNabb and Foster equations, therefore injecting only a detrapping activation energy is not sufficient for simulations. An extensive literature review has resulted in finding very little information concerning the kinetic constants associated with hydrogen trapping in metals, especially concerning the trapping activation energy (E_k) and the pre-exponential constants (k_0 and p_0). The only set of complete diffusion and trapping parameters have been reported by Turnbull *et al.* [105] for 1 trap site in a low-carbon steel/pure iron of thickness 0.2 cm when imposing a TDS temperature ramp rate (ϕ) of 2 K.min^{-1}, these values have been paired with the solubility of hydrogen in pure iron as determined by A. Brass *et al.* from electochemical permeation tests [129]. All simulations in Sec. 3.3.2 will be carried out using these values, see Table 3.8 [105, 129]. The materials studied in this manuscript are limited to austenitic stainless steel and nickel based alloys, SS316L and A600 respectively, but it is important to demonstrate the validity and applicability of the developed numerical model and some experimental parameters that have an important impact on experimental TDS spectra.

Table 3.8 Diffusion and trapping simulation parameters (1 trap site) in pure iron [105, 129]

μ_0^{Fe} mol H.mol Fe^{-1}	D_0^{Fe} cm^2.s^{-1}	E_D^{Fe} kJ.mol^{-1}	k_0 s^{-1}	E_k kJ.mol^{-1}	p_0 s^{-1}	E_p kJ.mol^{-1}	N mol TS.mol Fe^{-1}
1.1 10^{-6}	7.2 10^{-4}	5.69	2.64 10^{7}	5.69	2.1 10^{7}	53.69	2.47 10^{-5}

Two different types of hydrogen charging will be looked at: (i) Type A referring to homogeneous charging of interstitial and trapped hydrogen in the material and (ii) Type B referring to a non-homogeneous charging, imposing a concentration gradient of both interstitial and trapped hydrogen in the material.

Table 3.9 Charging conditions for simulating Type A (homogeneous) and Type B (partial) charging; μ_0^{Fe} is taken to be the solubility of H in pure Fe [129]

	μ_0		T (K)	t (min)
	$x=0$	$x=L$		
Type A	μ_0^{Fe}	μ_0^{Fe}	298	90
Type B	μ_0^{Fe}	0	298	3

These charging conditions are presented in Table 3.9. The homogeneous charging of a 0.2 cm thick sample of pure iron can be achieved after 90 min of charging at both sample faces ($x = 0$ and $x = L = 0.2$ cm) at 298 K and will serve as the Type A conditions. Type B charging conditions will consist of a charging at one sample face ($x = 0$) for 3 min at 298 K. The concentration profiles immediately after charging can be seen in Fig. 3.24. If these samples are subjected immediately to TDS analysis (ϕ=2 K.min^{-1}), the resulting simulated TDS spectra can be seen in Fig. 3.25.

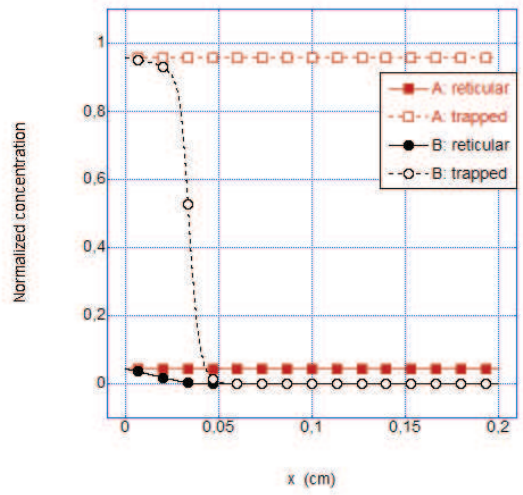

Fig. 3.24 Simulated normalized interstitial and trapped hydrogen concentration profiles after charging. Profiles are normalized to the maximum total H concentration (interstitial + trapped) for each type.

These spectra both present their strongest desorption flux at $t = 0$ s before quickly decreasing. One desorption peak can be observed for the homogeneously charged material (Type A), whereas a small desorption shoulder ($t = 1000$ s) and one desorption peak can be seen for the material charged non-homogeneously at one face (Type B). This intense desorption flux at $t = 0$ s may camouflage a significant part of low temperature spectral contributions, which may be attributed to trapping interactions, as the diffusion coefficient for H in pure iron at ambient temperature is very high therefore causing a strong and fast desorption from the sample at low temperatures.

Furthermore, it has been determined through simulations that the desorption spectra are representations of the combined simultaneous desorption of hydrogen from both sample faces, $x = 0$ and $x = L$. This can be seen in Fig. 3.25 for Type B charging (squares), where the total desorption flux, and the desorption flux from each face is shown.

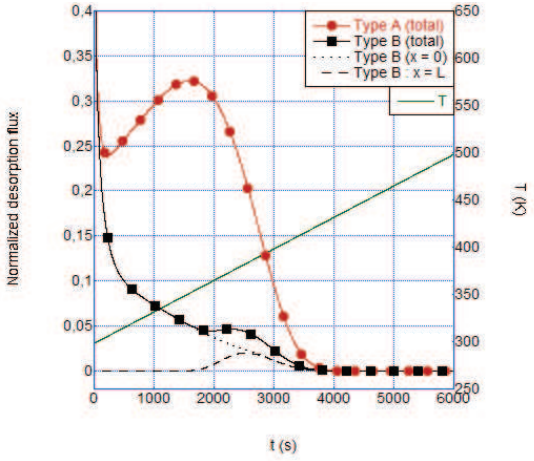

Fig. 3.25 Simulated normalized TDS spectrum immediately after hydrogen charging for Type A and Type B charging.

This demonstrates the need to know the actual hydrogen distribution and sample thickness in when simulating or analyzing TDS spectra. For a homogeneously charged material, this concurrent desorption occurs at the same intensity, as the concentration gradient in the sample is homogeneous (Type A), whereas for a "gradient" charged material (Type B), the desorption from the "non-charged" face, $x = L$, is seen much later, $t = 2800$ s. This desorption from the non-charged face, reveals the diffusion and trapping interactions taking place internally in and across the material during TDS testing.

Moreover, in experimental practices the sample is generally subjected to a transfer time between the hydrogen charging and the start of TDS testing (for example the time to pump to a sufficient vacuum for mass spectrometer usage) or maybe a room or high temperature aging period [85, 87, 134].

A transfer time of 30 min at 298 K has been selected in order to mimic this inevitable aging period. The concentration profiles for Type A and Type B charging, after this aging period, can be seen in Fig. 3.26. These profiles are significantly different from un-aged profiles, see Fig. 3.24, as the surface H concentration is significantly lower ($\mu \approx \theta \approx 0$), the concentration of trapped hydrogen has also severely diminished and in pure iron the ratio of trapped to interstitial hydrogen has drastically increased. This leaves the concentration of interstitial H negligible in comparison to the concentration of trapped H.

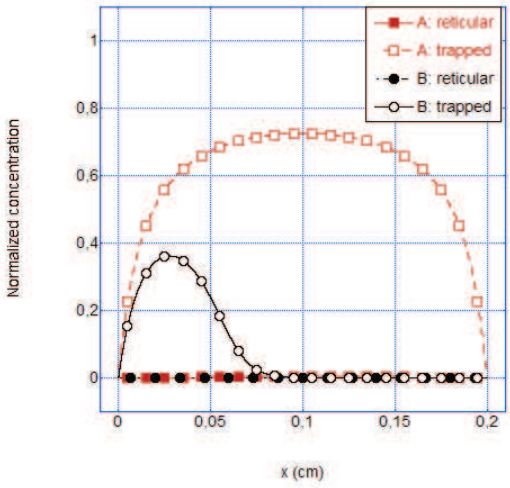

Fig. 3.26 Simulated normalized concentration profiles for charging Type A and Type B after 30 min of aging at 298 K

Furthermore for Type B (non-

homogeneous) charging, the hydrogen distribution within the sample has shifted towards the interior, demonstrating the diffusion and trapping interactions taking place at room temperature. The resulting simulated spectra can be seen in Fig. 3.27 when TDS simulation is started from these aged concentration profiles. These spectra differ greatly from the non-aged spectra (Fig. 3.25) as firstly, the desorption maximum no longer is at $t = 0$ s but later in analysis, corresponding to $T_m = 359$ K for homogeneous charging. Furthermore, two well defined desorption peaks can be observed for Type B charging, $T_m = 335$ K and $T_m = 378$ K.

In Fig. 3.27 the individual contributions of front side ($x = 0$) and back side ($x = L$) desorption are represented along with the total (sum of the two contributions) desorption flux. This figure shows clearly that, the desorption flux for a homogeneously charged material is made up of two simultaneous flux of equal intensity from both sample faces, due to the symmetry of the initial c_H profile, whereas the second peak ($T_m = 378$ K) seen for a non-homogeneously charged material is due to the H desorption flux at $x = L$.

This "double-peak" phenomenon is very troubling, as in many analytical spectral analysis methods each desorption peak is attributed to a separate trapping mechanism [85, 87, 91, 141, 162]. It should be restated that these simulations were done for a material presenting only homogeneously distributed trap sites, and therefore only one desorption peak was expected as suggested by some literature analysis methods. The fact that these simulations exhibit two peaks (due to the front and back desorption flux) shows the limits of such a classical spectral analysis technique, especially for a material presenting an internal concentration gradient.

In order to better understand this observation, a Choo-Lee plot [91] was drawn for these two different charging conditions, Type A and Type B from four simulated temperature ramps ($\phi = 2, 5, 10, 15$ K.min^{-1}); the simulated TDS spectra can be seen in Fig. 3.28 and the Choo-Lee plot can be seen in Fig. 3.29. Some general comments can be made on these simulated spectra: (i) the same general spectral shape is present for all temperature ramps respectively for each charging type (1 peak for Type A and 2 peaks for type B), (ii) with increasing ϕ the T_m (s) is shifted towards higher temperatures, and (iii) the total H absorbed (integral of spectrum) is equivalent whatever the temperature ramp.

The assigned detrapping activation energy for Type A charging was determined to be 53.4 kJ.mol^{-1}, which is very close to the imposed Ep value of 53.69 kJ.mol^{-1}. In this case Choo-Lee plot analysis seems to be a good approximation. When this analysis method was used to characterize both desorption peaks (Peak 1 and Peak 2 as assigned in Fig. 3.28b) observed with Type B charging the results are less accurate: the E_p of 50.7 kJ.mol^{-1} and 59.7 kJ.mol^{-1} were determined respectively for Peak 1 and Peak 2. These two derived E_p values cannot be considered acceptable

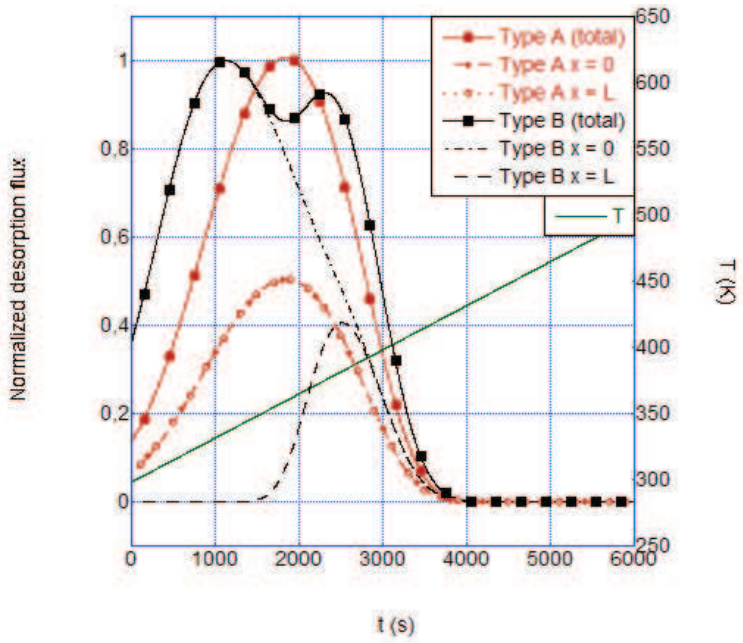

Fig. 3.27 Simulated normalized TDS spectra for Type A and Type B charging subjected to 30 min of aging at 298 K between charging and TDS ($\phi = 2$ K.min^{-1}). All desorption flux ($x = 0$ and $x = L$) are shown.

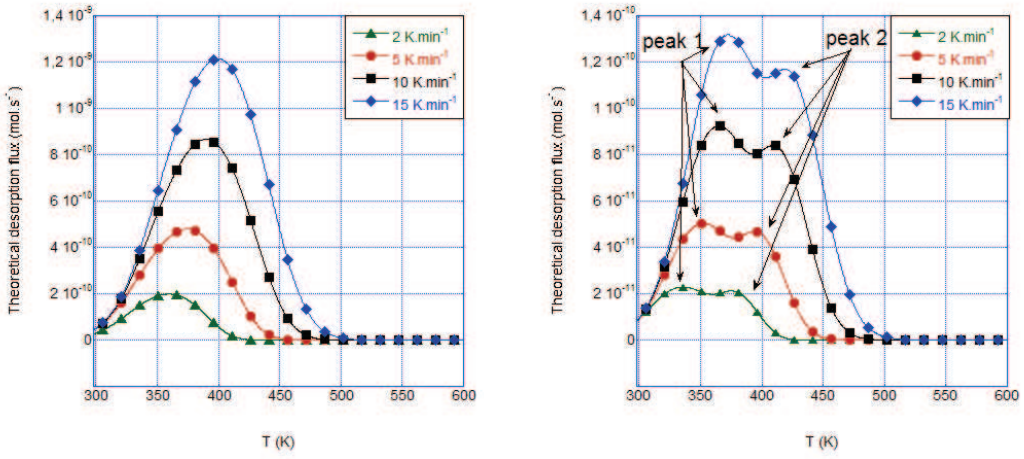

(a) **(b)**

Fig. 3.28 Simulated theoretical desorption spectra for ϕ ranging from 2 - 15 K.min $^{-1}$ for charging (a) Type A and (b) Type B. Simulations incorporated a 30 min aging period between charging and TDS analysis.

given the imposed value in simulation, see Table 3.8. This observation, thanks to this simulation method has highlighted another limit of the analytical techniques using the Kissinger equation [140], see Eq. (2.22); these results are consistent with the conclusions of Ebihara *et al.* [88, 121], who state that the models based upon the Kissinger equations are limited to desorption spectra with only one peak.

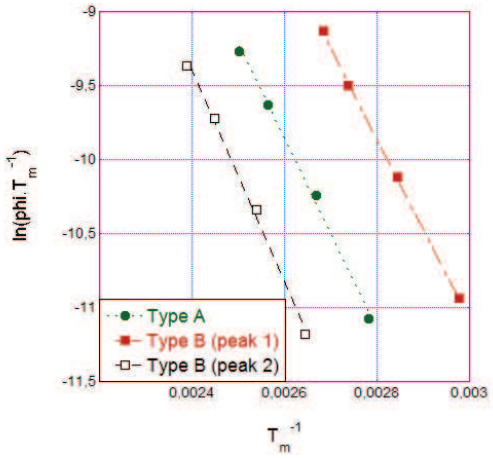

ϕ (K.min^{-1})	T_m (K) Type A	Type B Peak 1	Type B Peak 2
2	359	335	378
5	374	351	392
10	389	365	408
15	399	372	418
E_p (kJ.mol^{-1})	53.4	50.7	59.1

Fig. 3.29 Choo-Lee plots for all observed peaks in simulated TDS spectra for pure Fe charged Type A and Type B seen in Fig. 3.28 and the corresponding T_m and derived E_p values.

As previously stated, one goal of this section is to evidence the necessity for using a more complex numerical model to analyze TDS spectra. These simulations seem to disqualify the analytical Choo-Lee analysis technique [91] for non-homogeneous hydrogen charging. Moreover, these simulations were carried out on pure Fe, a material presenting a relatively high interstitial H diffusion coefficient, therefore allowing a homogeneous hydrogen distribution to be achieved at room temperature in a relatively short period of time. Now if a homogeneous charging was desired for an austenitic stainless steel or a Ni-base alloy, this charging would take upwards of days [134] or weeks depending on both the sample thickness and charging temperature. Therefore for the majority of analysis done for *fcc* materials, the conditions do not satisfy the necessary requirements for "Choo-Lee plot" analysis [91]. Furthermore, the impact of the unavoidable short aging period at ambient temperature before TDS analysis would be less significant on the H concentration profiles immediately before TDS, as in a fcc material H desorption and diffusion is much slower.

3.3.2.2 Sample thickness

Continuing the discussion concerning initial hydrogen distributions, sample thickness needs to be incorporated into analysis. Fig. 3.30 shows the effect of sample thickness (0.02 - 10 cm) for a charged (Type B) and aged (30 min at 298 K) sample on the simulated TDS spectrum (ϕ = 2 K.min^{-1}) along with a small graphic insert of the trapped hydrogen concentration profiles before TDS analysis (y-axis : theoretical trapped H concentration, x-axis : x/L). Any variation in sample thickness can have drastic effects on the resulting spectrum. This parameter not only affects T_m but also can affect the number of observed peaks which might render some analytical techniques quite difficult or false, for example the classical Choo-Lee plot method [91]. It seems that to be able to work with a single peak TDS spectrum, either a very thin or very thick sample is needed. These types of simulations, before TDS testing, appear useful when choosing the specimen geometry depending on the desired final spectrum. It would seem that in a material presenting a high diffusivity of H, pure iron for example, very small variations would have little effect, but for a material presenting a much lower H diffusivity, *fcc* materials such as stainless steel 316L or nickel alloy 600, very small variations would have drastic effects on the resulting spectrum. The effect of sample thickness has been discussed by several other authors, specifically Ebihara *et al.* [88, 121] and will not be further discussed in this section.

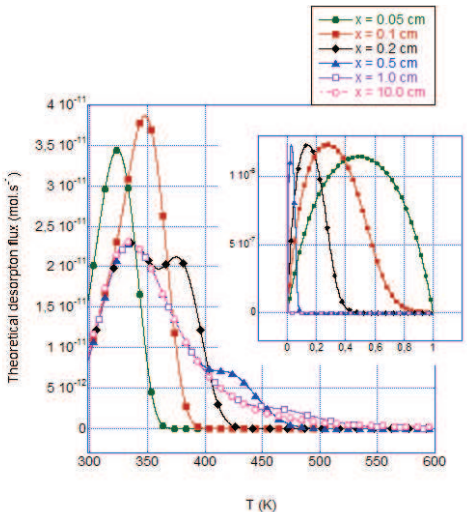

Fig. 3.30 Effect of sample thickness on final desorption spectra (ϕ = 2 K.min^{-1}) for a charging of Type B aged 30 min at room temperature between charging and TDS. The graphic insert presents the concentration profiles (after aging) before TDS with normalized L (y-axis: concentration (mol) and x-axis: normalized sample thickness (x/L))

3.3.2.3 Experimental temperature ramp

Furthermore in experimental analysis, certain experimental configurations and laboratory set-ups may not allow for a perfectly linear and reproducible TDS temperature ramp with every test. Slight differences in temperature ramp can have an important impact on the resulting TDS spectrum as D, k, and p are considered to

present Arrhenius relationships and are therefore temperature dependent. Fig. 3.31 shows the extreme sensitivity of a TDS spectrum to temperature when comparing a simulated spectrum using a linear 2 K.min^{-1} ramp rate to an experimental acquired temperature ramp of the same rate. The experimental temperature shown in Fig. 3.31, was measured *in-situ* in the TDS system at the Laboratoire d'Etude de la Corrosion Aqueuse at the CEA Saclay using a type-K thermocouple placed next to the sample, the furnace is controlled using an external system. Both the spectral form and T_m of desorption are drastically affected. In order to avoid this problem and analysis issues two solutions may be proposed: (i) taking into consideration the experimental temperature ramp ($T[t]$) in simulations [89] or (ii) the experimental temperature ramp would need to be extremely well controlled in order to assure a perfectly linear and reproducible experimental T ramp.

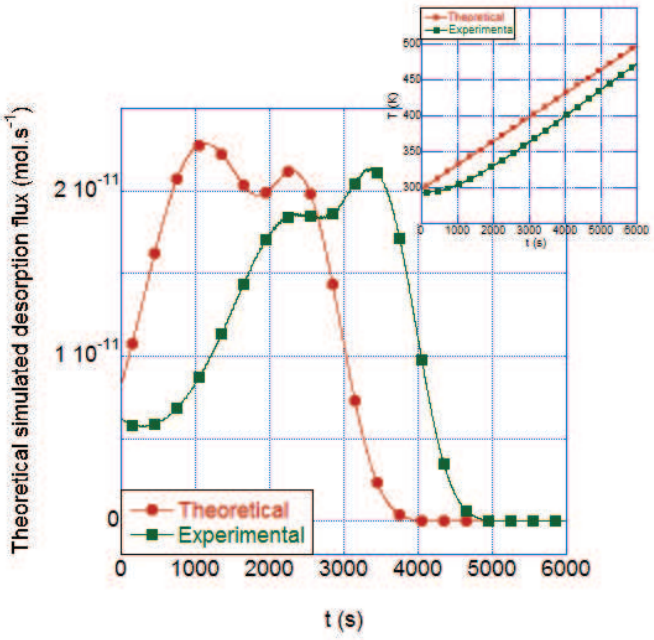

Fig. 3.31 Simulated TDS spectrum for a linear theoretical T ramp (ϕ = 2 K.min^{-1}) as compared to an experimental T ramp (ϕ = 2 K.min^{-1}). The graphic insert shows the linear T ramp as compared to an experimental acquired T ramp: y-axis: T (K), x-axis: t (s).

3.3.3 Trapping parameters

Most analysis methods are aimed at determining the detrapping energy associated with a specific trap sites, typically those using the Kissinger equation fast resolu-

tion techniques whose limits have been mentioned earlier in this paper [91], and usually neglect other important kinetic parameters such as: k_0, p_0, E_k and N respectively the trapping pre-exponential constant, the detrapping pre-exponential constant, the trapping activation energy and trap site density. However, several more recent papers have highlighted that k_0 and p_0 may be also of great importance and will therefore not be neglected in simulations [88]. In this section, the influence of these parameters on TDS spectra will be discussed.

3.3.3.1 Pre-exponential constants (k_0 and p_0)

The effect of "jump probabilities" has been mentioned in several articles [88, 142] but is neglected in analytical spectral investigation methods. When determining these parameters, analysis becomes more difficult and a more complex numerical routine is required. The pre-exponential constants, k_0 and p_0, determine the probability of hydrogen jumping from trap sites to interstitial sites and vice-versa. The following sections will demonstrate the effect of "jump-probability" variations on the resulting simulated TDS spectra. In the next section the pre-exponential constants are varied one at a time over several orders of magnitude while holding all other parameters constant (see Table 3.8). Then, the ratio of k_0/p_0 is held at 1.25 and the individual values are adjusted accordingly while all other parameters are kept constant (see Table 3.8 and Table 3.10).

i. Individual variation

Slight adjustments of the pre-exponential constants can influence the filling and emptying of trap sites. When the trapping probability (k_0) is increased, the desorption maximum is shifted towards higher temperatures, see Fig. 3.32a, whereas the inverse is observed with an increase in detrapping probability (p_0), see Fig. 3.32b. This is logical as when trapping probability is increased the likelihood for hydrogen to be trapped/retrapped is very high, and therefore hydrogen is readily trapped and/or retrapped during charging, transfer, and TDS analysis. On the other hand increasing the detrapping probability would increase the chance that the hydrogen will be released from the trap site and therefore hydrogen will be quickly detrapped from the TS. It can be concluded that individually these parameters have an important impact on the resulting TDS spectrum and should be included in analysis.

ii. Constant k_0/p_0 ratio

In studies where the pre-exponential constants are investigated, they are often analyzed by holding their ratio constant [105]. This approach will be explored in this section. These simulations were conducted by holding the k_0/p_0 ratio constant

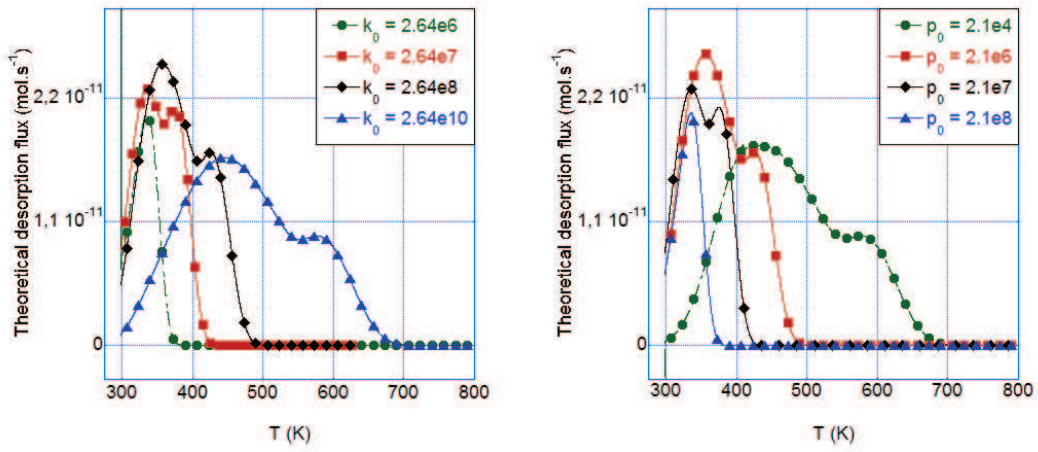

(a) **(b)**

Fig. 3.32 Effect of pre-exponential factor: (a) k_0 and (b) p_0, on simulated TDS spectra (ϕ= 2 K.min^{-1}) for aged (30 min at 298 K) samples of charging Type B

($k_0/p_0 = 1.25$), see Table 3.10 and Fig. 3.33. It is clear that even when the ratio is held constant, the individual values have an effect on the resulting TDS spectrum. For example as the jump probabilities are increased from A to F (Table 3.10), values on the order of 10^4 s^{-1} to 10^{10} s^{-1}, the T_m shifts to lower temperatures ($T_m^A > T_m^B > T_m^C$) and eventually at higher k_0 and p_0 values ($\geq 10^6$ s^{-1}) a second desorption peak appears (D−F) and at very high values of k_0 and p_0 (D−F, $\geq 10^7$ s^{-1}) the spectra are nearly identical, see Fig. 3.33.

It should be noted that the spectra (D, E, and F) are not identical but the differences in the simulated desorption values are too small to be seen in the presented figure. The forward (trapping) and backward (detrapping) reaction rates are too fast to have any further impact on the system. This might show that the "diffusion and trapping system" is approaching a pseudo-equilibrium state as the "jump-probabilities" approach infinity, but the likelihood that kinetic constants greater than 10^7 s^{-1} will need to be addressed.

Table 3.10 Simulation constants used when holding the k_0/p_0 ratio constant at 1.25. The resulting spectra can be seen in Fig. 3.33 and are labeled using an alphabetic key.

Label (Fig. 3.33)	k_0 (s^{-1})	p_0 (s^{-1})
A	2.64 10^4	2.1 10^4
B	2.64 10^5	2.1 10^5
C	2.64 10^6	2.1 10^6
D	2.64 10^7	2.1 10^7
E	2.64 10^8	2.1 10^8
F	2.64 10^{10}	2.1 10^{10}

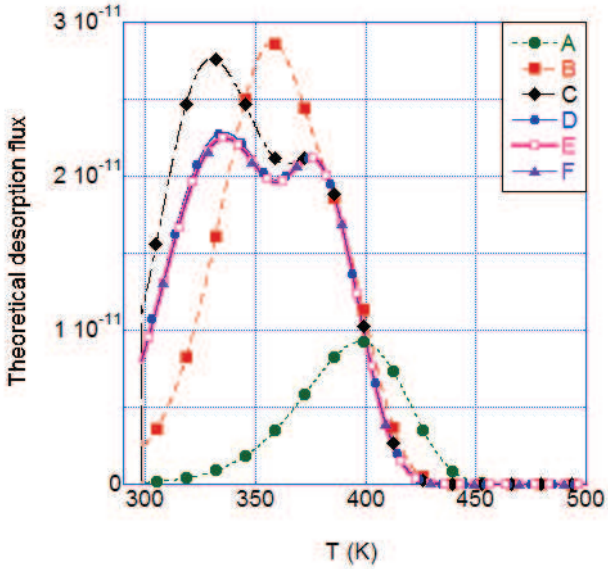

Fig. 3.33 Influence of k_0/p_0 with a constant ratio ($k_0/p_0 = 1.25$) on a simulated TDS spectrum ($\phi = 2$ K.min^{-1}), see Table 3.10 for the corresponding k_0 and p_0 simulation values (A−F). The samples were Type B charged (Table 3.9) and aged 30 min at 298 K.

Furthermore, if diffusion and trapping interactions were simulated in a material with much slower diffusion, for example a fcc metal, Ni-base alloys, or stainless steels, one can image the effect of the pre-exponential constants would be heightened. Sec. 3.3.3.1 has demonstrated the influence of the pre-exponential constants on simulated TDS spectra. It is clear that these individual parameters have a direct impact on the resulting spectra and therefore must be considered in analysis. This section has shown that when the pre-exponential constant ratios are held constant and the individual parameters (k_0 and p_0) are increased accordingly, it leads to an equivalent result as the one obtained by considering a local equilibrium hypothesis.

3.3.3.2 Activation Energies (E_k and E_p)

Most analytical methods to date focus on determining only the detrapping activation energy (E_p) [91], and consider this information sufficient for trap site characterization. The effect of both trapping and detrapping activation energies will be explored in the following sections. In the following section, simulations were conducted fixing all parameters (diffusion and trapping/detrapping pre-exponential constants) while the respective trapping and detrapping activation energies were varied individually (this changes the respective binding energy (E_b) associated

with the E_k and E_p combination), see values in Table 3.8. Then simulations were carried out when E_b has been held constant, along with all other parameters, and E_k and E_p varied accordingly, see Table 3.8 and Table 3.11.

i. Individual variation

When the activation energies are evaluated separately, some observations can be made concerning the trapping activation energy (Fig. 3.34a) and detrapping activation energy (Fig. 3.34b). When E_k is low ($E_k < E_D$, green circles Fig. 3.34a), H trapping is very easy, therefore allowing traps to become more saturated during charging and low temperature aging (i.e. 30 min at 298 K). Therefore the desorption flux is significantly more intense than when $E_k \geq E_D$. When E_k is greater ($E_k > E_D$, black diamonds and blue triangles Fig. 3.34a), the total concentration of trapped H becomes low, as during aging H diffuses very readily out of the sample and cannot be easily retrapped.

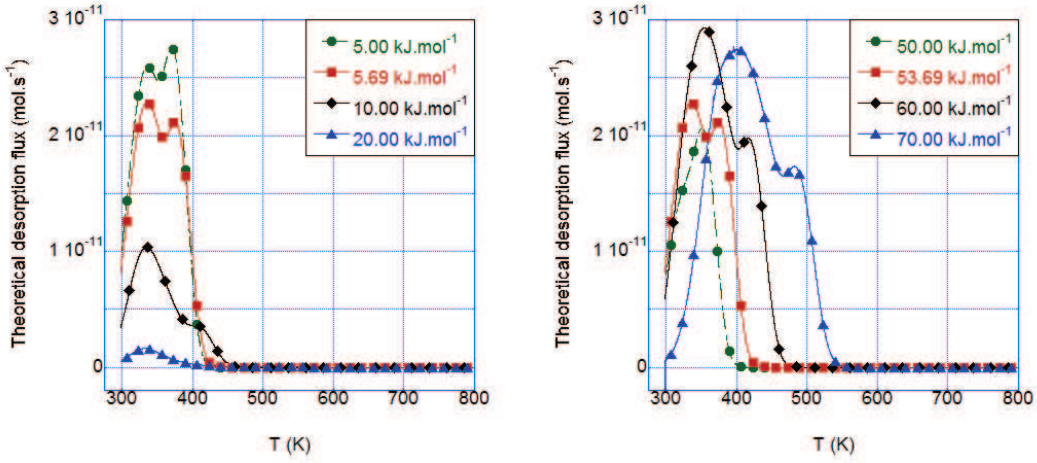

(a) **(b)**

Fig. 3.34 Effect of activation energy: (a) E_k and (b) E_p, on simulated TDS spectra (ϕ= 2 K.min^{-1}) for aged samples of charging Type B.

Concerning detrapping activation energy, when $E_p \leq E_D$ (green circles and red squares Fig. 3.34b) detrapping is as easy as or easier than diffusion. Therefore after the aging period (30 min at 298 K) very little trapped or interstitial hydrogen is left in the sample. When E_p is increased (black diamonds and blue triangles, Fig. 3.34b), detrapping becomes increasingly more difficult and H is accumulated in trap sites during both charging and aging. Moreover this "trapped" hydrogen is released at higher T during TDS, which can be attributed to the stronger E_p and "binding energy".

ii. Constant binding energy (E_b)

The trap site binding energy can be considered as the difference between the detrapping and trapping activation energy ($E_b = E_p - E_k$) and is often used by researchers in trapping analysis methods. Often simulations are carried out imposing a constant binding energy (E_b). In this section the binding energy ($E_p - E_k$) was fixed at 48.00 kJ.mol^{-1} and the E_k and E_p values were varied accordingly. The simulation values can be seen in Table 3.11. The resulting simulations can be seen in Fig. 3.35.

Table 3.11 Trapping (E_k) and detrapping (E_p) activation energies used when holding the binding energy constant (E_b) at 48.00 kJ.mol^{-1}.

Label (Fig. 3.35)	E_k (kJ.mol^{-1})	E_p (kJ.mol^{-1})
A	1.00	49.00
B	2.00	50.00
C	5.69	53.69
D	10.00	58.00
E	15.00	63.00
F	20.00	68.00

Even when E_b is kept constant, the E_k and E_p combination has an effect on the TDS spectrum. Increasing the respective E_k and E_p values from A to F results in an increase in the intensity of the first desorption peak (desorption flux from $x = 0$), an increase in the total H-desorption flux (which hits at the difference in H absorbed during charging and retention of hydrogen in the trap site during the aging period (30 min at 298 K)), and very little change in the intensity/placement of the second desorption peak (desorption flux from $x = L$). The increase in the first desorption peak's intensity can be attributed to the increasing difficulty for the hydrogen to become detrapped, and therefore a greater amount stays trapped in the trap sites close to the charged surface ($x = 0$) and less is detrapped and subsequently desorbed during the aging period. Furthermore the variation in T_m of the first desorption peak, for simulated TDS spectra A, B, C, D, and E, while being very small, is globally in good agreement with the common consensus in literature (i.e. as E_p is increased T_m will shift to higher temperatures [91]).

Furthermore, when E_k and E_p are increased (while keeping E_b constant) to much higher energies than that of interstitial diffusion (E_D, Table 3.8), for example spectrum F in Fig. 3.35, a significant decrease in the total desorption flux is observed along with a change in spectral form. Instead of having two well defined desorption peaks, the spectrum is characterized by one desorption peak (desorption flux from $x = 0$) and one small desorption shoulder (desorption flux from $x = L$). This can be explained by the difficulty hydrogen has to become trapped, $E_k > E_D$, (attributing to the overall significantly lower total desorption flux) and a great deal of H preferentially diffusing by the interstitial sites. Furthermore T_m

of the single peak is shifted to a much higher temperature hinting at a much higher E_p and demonstrating the difficulty of H to become detrapped.

In the previous sections, the simulations have shown that both the activation energy associated with trapping (E_k) and detrapping (E_p) along with their respective pre-exponential constants (k_0, p_0) are important. It is necessary to determine all these parameters in order to have accurate information concerning interstitial diffusion and trapping interactions. It can also be observed that as the activation energies (E_k and E_p) are decreased from F to A (Fig. 3.35 and Table 3.11) and as pre-exponential constants (k_0 and p_0) are increased while keeping their ratio constant from A to F (Fig. 3.33 and Table 3.10) the spectral variations become less evident hinting that the system might be approaching a pseudo-equilibrium state, and cases where a D_{eff} and the local thermodynamic equilibrium hypothesis might be applicable. Furthermore, as the influence of these four parameters on the overall system has been demonstrated and discussed in-depth, it can be concluded that in order to be able to sufficiently analyze H diffusion and trapping systems a more robust numerical method, which determines all these parameters (not only E_b or E_p and the k_0/p_0 ratio), must be used.

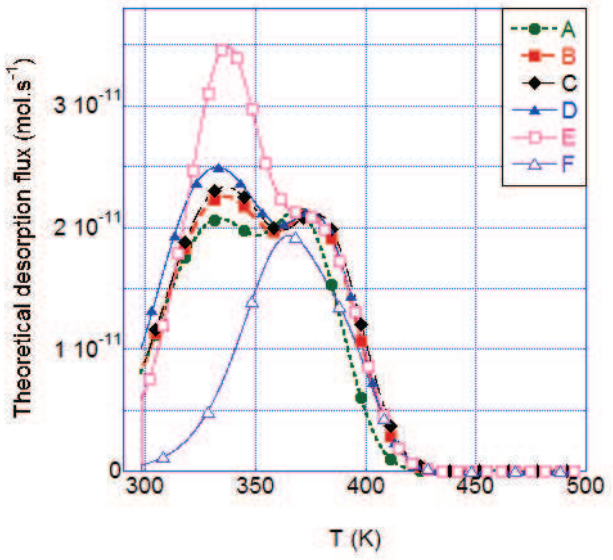

Fig. 3.35 Influence of E_k and E_p when E_b is held constant at 48 kJ.mol^{-1} on simulated TDS spectra, see Table 3.11 for the corresponding E_k and E_p simulation values (A−F). The samples were supposed charged using Type B conditions (Table 3.9) and aged 30 min at 298 K.

3.3.3.3 Trap site density (N)

One very important parameter to look at is trap site density, N. Trap site density was varied in Fig. 3.36. In this figure and in Table 3.12, "D" is the trap site density that has been imposed in all other simulations Table 3.8 [105]. All other simulation conditions (Table 3.7) and diffusion and trapping parameters (Table 3.8) have been held constant.

Variation of this parameter has a drastic effect on resulting simulated TDS spectra in both "first" desorption peak intensity and "second" peak placement. The second desorption peak of the simulated TDS spectra has been previously discussed and can be attributed to the desorption from the non-charged sample face. As trap site density is decreased from G to A in Table 3.12 and in Fig. 3.36 a decrease in the first desorption peak is observed. As this peak's intensity is drastically influenced by the trap site density, this peak is determined to be the "trapping peak".

Table 3.12 Imposed trap site densities (N) used to simulate the TDS spectra shown in Fig. 3.36.

Label (Fig. 3.36)	N (mol TS. mol Fe^{-1})
A	6.2 10^{-6}
B	8.2 10^{-6}
C	1.2 10^{-5}
D	2.5 10^{-5}
E	4.9 10^{-5}
F	7.4 10^{-5}
G	9.8 10^{-5}

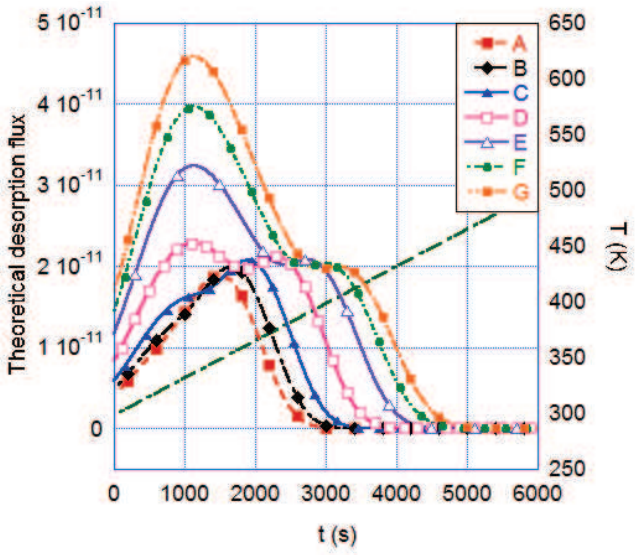

Fig. 3.36 Influence of trap site density, N, on simulated TDS spectra, see Table 3.12 for the corresponding imposed trap site densitites in simulations (A−G). The samples were supposed charged using Type B conditions (Table 3.9) and aged 30 min at 298 K.

Furthermore, when trap site density is less than 1 10^{-5} this desorption peak nearly disappears, and it would seem that trap site density is not great enough to have an observable effect on diffusion interactions in the material. While the desorption intensity is affected by this parameter, the placement of this desorption peak (in function of temperature) does not change; for all simulated desorption spectrum (C−G) this peak occurs at about 340 K. As trap site density does not seem to have an effect on peak placement [in simulations] this parameters might be very useful for experimental peak definition and association (i.e. determining which desorption peak/shoulder is due to inter-

stitial H or trapped H at one [or more] trap site) and serve as a validation of derived kinetic trapping and detrapping constant parameters.

The effect of trap site density (N) on the second desorption peak/shoulder, attributed to hydrogen desorption from the non-charged face should be discussed as well. As trap site density is increased from A to G in Table 3.12 and in Fig. 3.36 this peak shifts from low to high temperatures, from about 350 K for A to about 400 K for G). This shift is a direct consequence of the slowing effect trap sites have on the transport of hydrogen across the material, as the number of trap sites present in the material is increased. Furthermore the total amount of hydrogen desorbed increases as trap site density (N) is increased from A to G in Table 3.12 and in Fig. 3.36. This shows clearly the effect of trapping on the amount of retained hydrogen after the transfer from the charging cell to the TDS setup. The significant increase in trap sites allows for more hydrogen to be retained in the material and therefore a higher both trapping peak intensity and total desorption flux is observed on spectra with increasing trap site density.

This parameter has proven extremely important to spectral form and intensity and needs to be considered in analysis of diffusion and trapping systems. This complicated analysis as a quantification and characterization of trap site density would need to be carried out and a link between the numerical parameter trap site density, N, and quantity of trap sites present in the material would need to be achieved. Moreover trap site occupation (i.e. number of atoms of H per TS) would need to be know or determined by coupling this parameter with quantified desorption spectra.

3.3.4 Simulation advancements

This section has focused on the simulation of diffusion and trapping interactions in a one-dimensional material system with one type of trap site. The importance of using experimental conditions as input parameters and the importance of trapping and detrapping kinetic parameters (i.e. pre-exponential constants, activation energies and trap site density) has been demonstrated. Furthermore, as the McNabb and Foster equations were initially based upon a three dimensional analysis of hydrogen-material interactions, therefore these equations can are easily transposed into a numerical code for treating 3D material systems. The progression from 1D to 2D and finally 3D treatment of H diffusion and trapping systems is in progress.

To consider at system with multiple types of trap sites the McNabb and Foster equations can be developed to include multiple trapping terms (Eq. (3.8a)), each with their own respective kinetic trapping equation (Eq. (3.8b))).

$$\frac{\partial \mu}{\partial t} + \sum_{i=1}^{n} N \frac{\partial \theta_i}{\partial t} = D \left(\frac{\partial^2 \mu}{\partial x^2} + \frac{\partial^2 \mu}{\partial y^2} \right) \tag{3.8a}$$

$$\frac{\partial \theta_j}{\partial t} = k_j \mu (1 - \theta_j) - p_j \theta_j \qquad (j = 1, ..., n) \tag{3.8b}$$

This set of equations for hydrogen diffusion and trapping in the presence of multiple trap sites imposes one very large hypothesis which is that trap sites do not interact with one another and hydrogen can not pass directly from one trap site to another, it must first pass through an interstitial site. Simulations in Python™ are possible for multiple trap site types whereas using WolframMathematica© this becomes difficult due to the "kernel" size limitations.

Furthermore, the nature of the McNabb and Foster equations [107], renders them extremely versatile and highly adaptable to situations such as trap site gradients.

3.3.5 Conclusions on numerical simulation method

The previous sections have revealed the necessity of considering all kinetic trapping-detrapping parameters in diffusion-trapping systems along with the importance of injecting the experimental conditions that have an impact on the trapped and interstitial H concentration profiles. This includes the (i) experimental temperature ramp, (ii) charging duration and (iii) temperature, (iv) transfer duration and (v) temperature, as well as the (vi) sample thickness. By injecting these parameters the diffusion, trapping, and detrapping phenomena taking place during these stages are taken into consideration; as the importance of sample "history" has been demonstrated and discussed in Sec. 3.3.2.1. It appears that it will be necessary to use a numerical model which has the capability to determine simultaneously all four kinetic parameters relative to trapping and detrapping. This includes the (i) trapping pre-exponential constant, (ii) trapping activation energy, (iii) detrapping pre-expnential constant and (iv) detrapping activation energy along with trap site density (N). This would require simulation using the original McNabb and Foster equations and a numerical routine in order to determine the diffusion and trapping constants.

Thermal desorption mass spectroscopy proves to be a very powerful and useful experimental tool with the potential to provide access to kinetic information concerning hydrogen-material interactions, specifically with respect to diffusion and trapping. Simulations have revealed that today's most commonly used analytical spectral analysis techniques may give information concerning the detrapping activation energy, but only when certain conditions are met, for example a nearly homogeneous hydrogen concentration before spectral acquisition. This hydrogen homogeneity can be relatively easily met when working with a thin material presenting a high hydrogen diffusivity (i.e. pure iron and low-carbon steels), but these conditions become very difficult to achieve when this coefficient is not as high (ie. austenitic stainless steels, Ni-base alloys).

The proposed numerical model and analysis technique is easily adaptable to different types of materials and trap site types present in the material through working with “model materials” in order to construct a database of diffusion and kinetic trapping/detrapping information. Once constructed this database of kinetic constants could be used to simulate and predict H-material interactions for a material presenting numerous types of trap sites. This proposed numerical model coupled with “model materials” in order to acquire trapping/detrapping kinetic information is currently being performed for two industrial materials.

3.4 Chapter summary

This chapter was separated into three main sections: (i) a presentation of model material elaboration and material characterizations, (ii) a presentation of the experimental method (TDS) and finally (iii) a presentation of the numerical method used for spectral analysis and simulation.

In the following chapters these model materials (Sec. 3.1) will be used to acquire ”model” TDS spectra (Sec. 3.2) from which the apparent diffusion coefficient and kinetic trapping and detrapping constants will be derived (Sec. 3.3).

Chapter 4

Results

In this chapter the results for hydrogen diffusion and trapping interactions in A600 and SS316L are presented and discussed. As mentioned in the previous chapter, this study is comprised of two parts: (1) experimental, for the acquisition of model TDS spectra, and (2) simulation, used to determine diffusion coefficient parameters (D_0 and E_D) and trapping/detrapping kinetic constants (k_0, E_k, p_0 and E_p).

The first section of this chapter is separated into two parts: (i) some considerations and comments on the cathodic ^{2}H charging method followed by (ii) a presentation and analysis of purely experimental TDS results. In the second section of this chapter the numerical simulation approach presented in Chapter 3 is used to derive the hydrogen diffusion coefficient in A600 and SS316L from pure diffusion experimental results. The proposed "best-fit" approach is used to determine the kinetic constants associated with trapping at chromium carbides (A600) and dislocations (A600 and SS316L).

4.1 Deuterium charging of Model Materials

Before TDS analysis, model materials were cathodically charged with deuterium as described in Chapter 3, see Table 3.6. Some key information that is needed in the numerical model in order to interpret TDS results will be the total amount of deuterium incorporated during the charging step. This information can indirectly provide the subsurface ^{2}H concentration during charging. Due to the lack of information on the deuterium absorption mechanism and rate associated with this process, the amount of ^{2}H that was incorporated during this stage was not simply available by applying a coefficient to Faraday's law. However, the quantity of deuterium desorbed during TDS analysis may provide an estimation of the quantity of deuterium absorbed by the model material during cathodic charging. During TDS analysis, start (t_0^{TDS}) to finish (t_f^{TDS}), the desorption flux of deuterium was monitored and recorded. The mass spectrometer signal could then be quantified (mol ^{2}H.s^{-1}) using a calibration equation (Eq. 3.7). The spectrum integral (Q_{total}):

$$Q_{\mathrm{total}} = \int_{t_0^{\mathrm{TDS}}}^{t_f^{\mathrm{TDS}}} F\, dt \tag{4.1}$$

is equivalent to the total amount of deuterium desorbed from the specimen (mol). The quantified total amount of deuterium desorbed from A600 model materials, having all been charged under the same conditions (Conditions A, see Table 3.6), is presented in Fig. 4.1. In this figure a large dispersion in the amount of ^{2}H desorbed can be observed.

Variations in the total amount of desorbed ^{2}H for the different model materials, due to the different microstructures and/or trap sites present, was anticipated

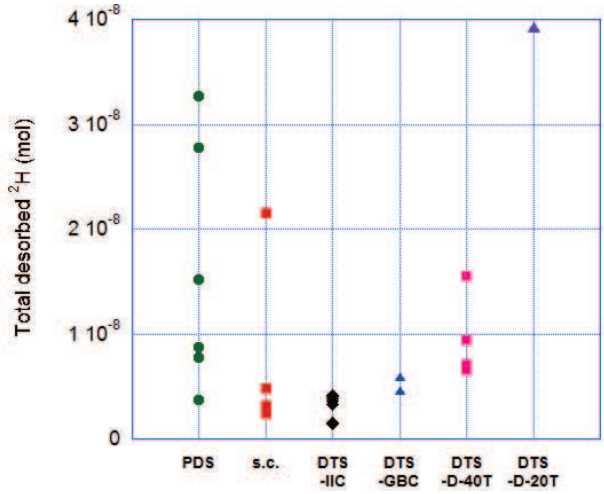

Fig. 4.1 Graphical representation of deuterium amount (mol) desorbed during TDS testing for A600 model materials: **P**ure **D**iffusion **S**ystem (PDS), A600-like single **c**rystal (s.c.), **D**iffusion and **T**rapping **S**ystem-**I**nter **I**ntra-granular **C**arbides (DTS-IIC), **D**iffusion and **T**rapping **S**ystem-**G**rain **B**oundary **C**arbides (DTS-GBC), **D**iffusion and **T**rapping **S**ystem-**D**islocations-ϵ=**40 %** (DTS-D-40T) and **D**iffusion and **T**rapping **S**ystem-**D**islocations-ϵ=**20 %** (DTS-D-20T).

whereas such a large "internal" dispersion of total amount of ^{2}H from the same model material type was not. It should be noted that every pre-charged specimen was subjected to a transfer time (t_{transfer}) on the order of 18 $\pm$ 3 min, the slight differences in these transfer times is enough to cause some small differences in the total amount of ^{2}H desorbed during TDS testing but could not entertain the amount of dispersion seen in Fig. 4.1.

It has been hypothesized that these variations may be explained by an evolution in the deuterated charging solution (0.1 NaO^{2}H) (i.e. changes in pH due to the carbonization of the solution, isotopic exchanges between the solution and the atmosphere, etc.) over the days/months the chargings were carried out. This evolution may have an influence on the surface activity of hydrogen generated during charging and therefore have an important effect on the quantity of deuterium absorbed. The highest degree of dispersion is observed with the A600 PDS and A600-like s.c. model materials, whereas for the materials with high amounts of trap sites (i.e. DTS materials) the total deuterium dispersion is much less exaggerated. One hypothesis concerning the reproducibility of the DTS desorption quantities (even with solution evolution) is that the deuterium dissociation and/or absorption mechanism may be affected by the presence of trap sites at the sample surface.

In order to overcome the differences in total amount of desorbed deuterium,

a normalization process was adopted for spectral analysis. TDS spectra were normalized with regards to their [total] spectral integral before comparison. Fig. 4.2a shows two experimental (quantified) TDS spectra and Fig. 4.2b these same spectra after normalization; after normalization these spectra can be considered identical. The only spectra that could be compared quantitatively are those for A600-DTS-IIC, A600-DTS-GBC for which the dispersion in each TS type system is relatively small.

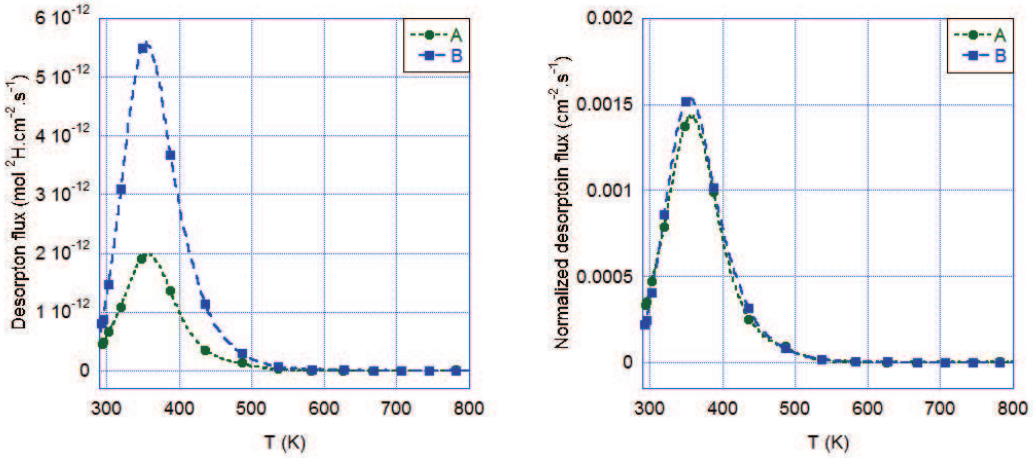

(a) **(b)**

Fig. 4.2 Two TDS desorption spectra (a) before normalization (i.e. quantified spectra) and (b) after normalization by total amount of desorbed deuterium.

4.2 Experimental TDS observations

Thermal **D**esorption mass **S**pectroscopy spectra were acquired for the different model materials. In the following sections experimental results are presented and discussed. The following sections will present and discuss (i) experimental approach, (ii) encountered problems and solutions, and (iii) the noteworthy experimental results acquired during this study.

4.2.1 TDS spectra immediately after ^{2}H charging

First, TDS spectra were acquired immediately[1] after deuterium charging (Table 4.1). The resulting quantified TDS spectra can be seen in Fig. 4.3. There

[1]Important reminder: "immediately" means after the 18 ± 3 min at room temperature for transfer time from the charging solution to TDS experimental set-up.

is a large difference in spectral intensity between the experimental spectra which was already mentioned in the previous section.

Table 4.1 Experimental TDS conditions. $T_{\text{iso-RT}}$ refers to a room temperature isothermal aging period and $T_{\text{iso-HT}}$ refers to an elevated temperature aging period.

Experimental TDS parameters		
t_{transfer}	18 ± 3	min
$T_{\text{transfer}} = T_0$	294 ± 2	K
$T_{\text{iso-RT}}$	294 ± 2	K
$T_{\text{iso-HT}}$	409 ± 1	K
T_{f}	1300	K
ϕ	10	K.min^{-1}

The spectra were then all normalized with respect to their total deuterium desorbed amount. The normalized experimental spectra can be seen in Fig. 4.4. After normalization, the desorption spectra are all quite similar. The maximum desorption flux temperatures (T_m) all occur between 350 K and 400 K. Moreover no discriminating [higher temperature] "trapping" peak is observed.

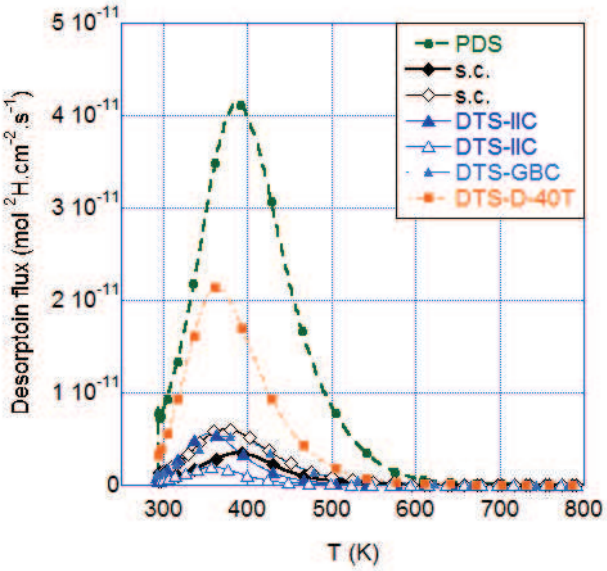

Fig. 4.3 Quantified (mol $^2\text{H.cm}^{-2}.\text{s}^{-1}$) TDS desorption spectra for A600 MM immediately after deuterium charging. All specimen were charged under Charging conditions A (Table 3.6) and analyzed in TDS using the conditions in Table 4.1

The following short sections take a closer look at the similarities and slight differences between these spectra comparing the pure diffusion system model ma-

terial (A600-PDS) to the other model materials: (i) single crystal model material (A600-like s.c.) and diffusion and trapping systems presenting (ii) chromium carbides (A600-DTS-IIC and A600-DTS-GBC) or (iii) dislocations (A600-DTS-D-40T and A600-DTS-D-20T).

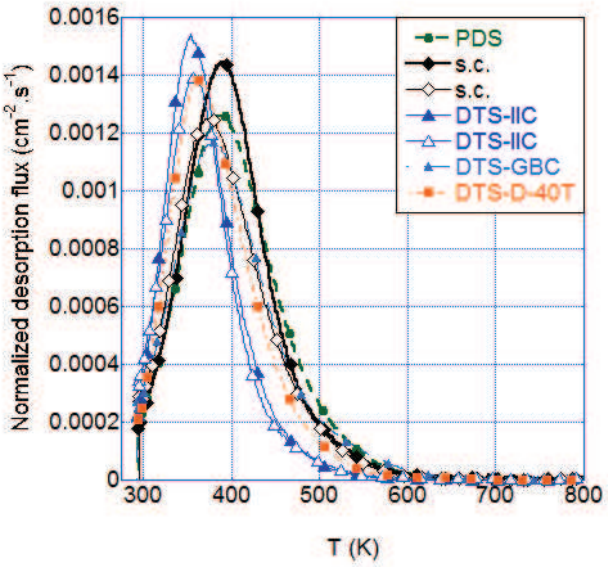

Fig. 4.4 "Normalized" (with regards to total amount of desorbed deuterium) TDS desorption spectra for A600 model materials immediately after deuterium charging. See Fig. 4.3 for quantified spectra.

4.2.1.1 Pure diffusion system compared to single crystal model material

Experimental spectra immediately after deuterium charging were acquired for polycrystalline PDS and single crystal (s.c.) type model materials. The resulting normalized experimental spectra can be seen in Fig. 4.5. This figure takes a closer look at the similarities between A600-PDS and A600-like single crystal desorption spectra. These spectra can be considered identical as (i) the maximum desorption flux occur at the same temperature, (ii) spectral intensities (after normalization with respect to total desorbed ^{2}H) are equivalent and (iii) the spectral forms are the same.

This is very interesting as the two model materials present different microstructures specifically concerning the presence of (i) grain boundaries and (ii) TiCN precipitates in the A600 pure diffusion system model material which do not exist in the A600-like single crystal.

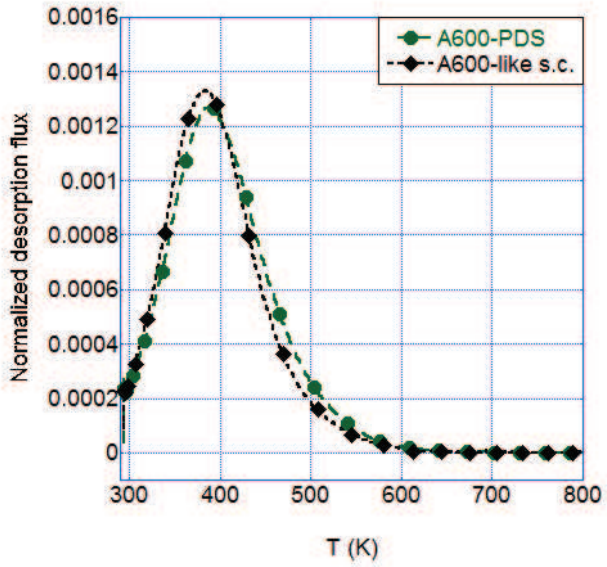

Fig. 4.5 "Normalized" desorption flux evolution for A600-PDS and A600-like s.c. MMs immediately after ^{2}H charging (Table 3.6, Table 4.1).

This experimental result serves as a first indication that these features may either (i) have a negligible effect on diffusion and trapping of hydrogen in A600 or (ii) are unable to be experimentally observed using this type of TDS analysis (i.e. TDS immediately following deuterium charging). Nevertheless, the effect of these sites, more specifically the effect of grain boundaries, will still be studied and discussed throughout this chapter.

4.2.1.2 Pure diffusion system compared to diffusion and trapping at Cr_7C_3 model material

Pure diffusion TDS spectra and spectra obtained on model materials with chromium carbides as the primary trap site type (DTS-IIC and DTS-GBC) are compared immediately after ^{2}H charging in Fig. 4.6 and Fig. 4.7. It appears that spectra obtained on the pure diffusion material and material with high densities of chromium carbides localized primarily only along grain boundaries are nearly identical, Fig. 4.6.

The spectral differences between a pure diffusion system and one presenting both inter- and intragranular chromium carbides are more striking (Fig. 4.7). There is a shift in the desorption peak maximum temperature to a lower temperature for the diffusion and trapping model material (approximately 360 K compared to approximately 395 K for a pure diffusion system) and this peak presents a higher normalized intensity. From the experimental spectral comparison of these three model materials several hypotheses can be made:

1. The quantity of trap sites in A600-DTS-GBC, chromium carbides localized along grain boundaries (i.e. lower trap site density), is very low and therefore does not have an experimentally observable effect on TDS spectra [immediately after charging]. The effect of these sites may be very small as there are not very numerous (as compared to those in A600-DTS-IIC) and therefore their effect may be "masked" in the TDS spectrum.

2. Trapping at chromium carbides, when present in very high quantities (i.e. in A600-DTS-IIC), has a significant retarding effect on deuterium apparent diffusivity in A600 during cathodic charging, transfer and TDS analysis. Therefore a slowed diffusion of ^{2}H during these stages:

   (a) would lead to a shallower deuterium penetration (^{2}H localized more in surface/trapped at chromium carbides) as compared to a A600-PDS or A600-DTS-GBC model materials and/or

   (b) the absorbed ^{2}H being localized closer to the surface ($x = 0$), it may therefore more readily desorbed consequently producing a desorption peak at a lower temperature.

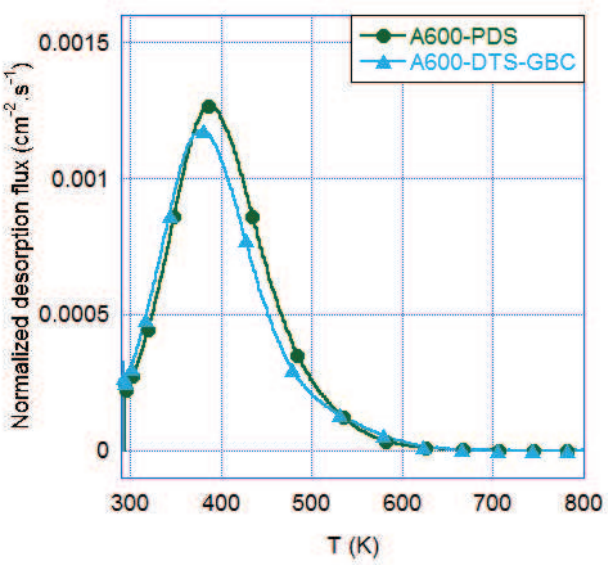

Fig. 4.6 "Normalized" desorption flux evolution for A600-PDS and 600-DTS-GBC model materials immediately after ^{2}H charging (Table 3.6, Table 4.1).

Furthermore, this desorption peak shift to a lower temperature for a material with trap sites goes against most of what has been reported in literature. Most researchers associate a high[er] temperature desorption peak(s) with trapping phenomena and the lower or lowest temperature desorption peak with the desorption of interstitial hydrogen [22, 82].

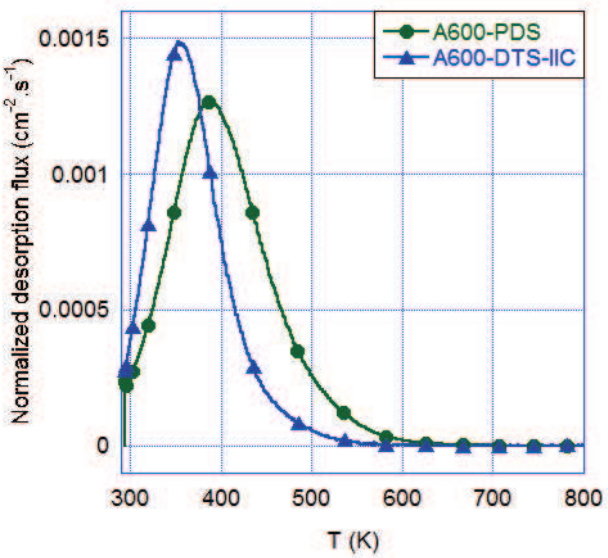

Fig. 4.7 "Normalized" desorption flux evolution for A600-PDS and A600-DTS-IIC immediately after ^{2}H charging (Table 3.6, Table 4.1).

4.2.1.3 Pure diffusion system compared to diffusion and trapping system with dislocations

When comparing an experimental A600-DTS-D-40T spectrum to A600-PDS TDS spectrum immediately after charging, Fig. 4.8: a shift of the desorption peak T_m to a lower temperature is observed and the relative "normalized" desorption peak intensity is greater for the specimen containing dislocations as the major trap site type. As for chromium carbides, the same hypothesis (hypothesis 2.) can be applied to spectral interpretation. An additional hypothesis can be proposed:

3. dislocations may form a short circuit network which might act as a preferential diffusion pathways. This phenomenon has been observed experimentally by Brass *et al.* [73] in iron and nickel base alloys. The formation of a short-circuit network could accelerate the desorption of deuterium during TDS analysis as compared to "purely" interstitial diffusion (assumed in a A600-PDS MM).

4.2.1.4 Summary: TDS analysis immediately after ^{2}H charging

Analysis of experimental TDS spectra immediately after deuterium charging has provided some interesting information. It should be noted that the charg-

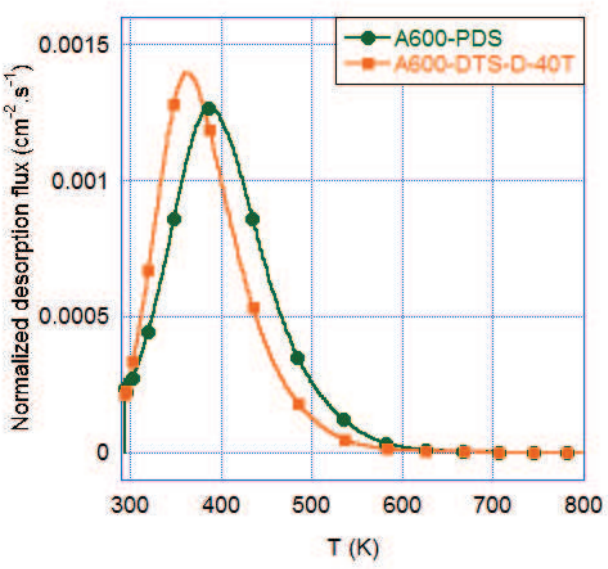

Fig. 4.8 "Normalized" desorption flux evolution for A600-PDS and A600-DTS-D-40T model materials immediately after ^{2}H charging (Table 3.6, Table 4.1)

ing conditons used in this study (i.e. 30 min of charging in a 0.1 M NaO^2H solution (99.90 % ^{2}H) at 298 K with an imposed cathodic current density of -100 mA.cm^{-2}, specimen thickness was less that 0.01 cm) created a very strong ^{2}H concentration gradient in the materials. The "classic" effects of trapping or TDS spectra, i.e. (i) the appearance of a low temperature desorption peak (associated with interstitial ^{2}H) and a higher temperature desorption peak which may be attributed to trapping interactions [22, 82] or (ii) the appearance of only one high temperature peak for materials with trap sites [CITE] (this single peak would attribute all desorbed ^{2}H to trapped ^{2}H), were not observed on the model diffusion and trapping system studied here. Consequently, it would seem that the only experimentally observable difference between normalized pure diffusion systems and systems containing high quantities of potential trap sites was a shift in the desorption peak temperature (T_m) to a temperature lower than that observed for interstitial diffusion. Some hypotheses have been made to explain this shift: (i) this low temperature desorption peak may be linked to a lower apparent diffusivity of deuterium in the material in the presence of traps or (ii) the trap sites may act as a network of short circuit diffusion pathways.

Moreover, a direct comparison of a model material with primarily only grain boundaries (A600-PDS, presence of some residual titanium carbo-nitrides

as well) as possible trap sites or diffusion short-circuits and a material without grain boundaries (A600-like s.c.) has resulted in normalized experimental spectra which are indistinguishable. This may indicate that either the effect of grain boundaries [and retained TiCN precipitates] (i) may not be detectable on experimental TDS spectra immediately after deuterium charging or (ii) have a negligible effect on hydrogen diffusion and trapping in this alloy. As these observations and preliminary conclusions provide no concrete evidence of hydrogen trapping phenomenon in Ni base alloy 600, a different experimental approach needed to be taken, in order to better highlight ^{2}H-trap site interactions.

4.2.2 TDS spectra after aging

In literature, a pre-H-charged specimen is sometimes aged isothermally before TDS analysis with the goal of isolating a trapping experimental contribution [87, 91]. For *cc* materials or materials in which H diffusion is very rapid this approach seems to work very nicely, as it allows for the majority of the interstitial H to be desorbed leaving primarily what can be considered as trapped hydrogen [90]. The austenitic alloys studied in this manuscript do not present a high H diffusivity which adds difficulty in increasing the ratio of trapped to interstitial hydrogen through aging.

In this section, several different isothermal aging approaches are presented which are aimed at increasing the $^{2}H_{trapped}$ / $^{2}H_{interstitial}$ ratio in order to isolate a trapping contribution on the experimental TDS spectrum. If a trapping contribution is isolated it may be used for the derivation of trapping and detrapping kinetic constants. In this section, first, a series of results obtained during and after **R**oom **T**emperature (RT) aging will be presented, followed by results obtained during and after **H**igh **T**emperature (HT) aging durations. Both room and high temperature aging took place inside the TDS system which allowed for *in situ* deuterium desorption monitoring for the entirety of the isotherm (room or high temperature) followed immediately by classical TDS analysis. For clarification the quasi-isothermal section of the experimental desorption spectra will be referred to as the "isothermal" contribution and the section acquired during a temperature ramp [after isothermal aging] will be referred to as the "TDS" contribution.

4.2.2.1 Room temperature isothermal aging

Before discussing the experimental results, the analysis steps and important sections of the desorption spectra will be presented using Fig. 4.9 as an aid. To have access to a maximum of information "hybrid" desorption spectra were ac-

quired. "Hybrid" refers to how each spectrum is comprised of an (i) isothermal aging for a period of time with deuterium desorption monitoring, followed by (ii) non-isothermal TDS analysis with desorption flux monitoring, respectively from t = 0 - 2.1 10^4 s and $t > 2.1\ 10^4$ s in Fig. 4.9.

From this point forward in the manuscript the total desorption spectrum is referred to as the "hybrid desorption spectrum", the isothermal part of the TDS spectrum is referred to the "isothermal desorption spectrum" and the non-isothermal classical TDS part of the spectrum is referred to as the "TDS spectrum".

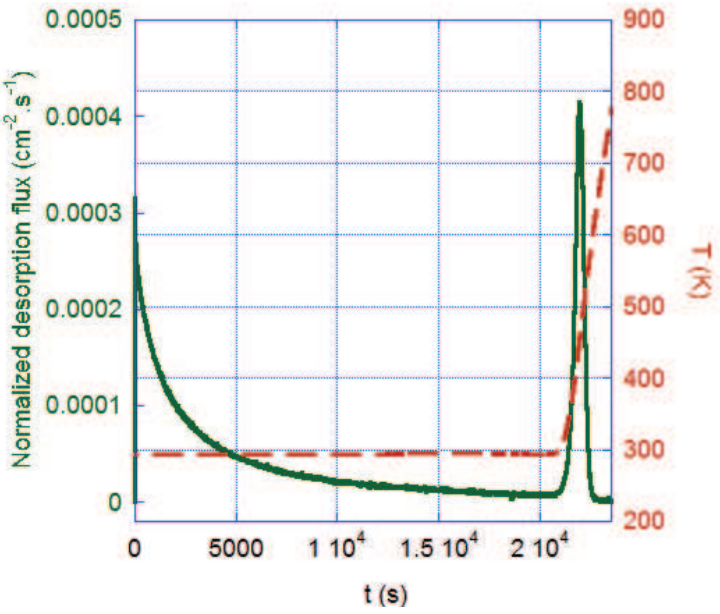

Fig. 4.9 "Normalized" desorption flux evolution of a pre-charged (Conditions A, Table 3.6) A600-PDS MM specimen subjected to 6 hr of room temperature aging followed by TDS analysis (ϕ = 10 K.min^{-1}) (normalized desorption flux evolution, experimentally measured temperature).

The isothermal aging part of the "hybrid" spectrum is characterized by a strong desorption flux at t = 0 s which declines as a function of time and the TDS part which presents a typical TDS desorption peak (as observed with specimen analyzed immediately after ^{2}H charging). Room temperature aging was carried out in TDS for durations up to 48 h. The evolution of the remaining ^{2}H (%) after various aging periods was calculated from the experimental spectra by dividing the integrated desorption flux during only TDS analysis (i.e. from $t = 2.1\ 10^4$ s in Fig. 4.9 to $t = 2.5\ 10^4$ s) by the amount of desorbed ^{2}H (i.e. from t = 0 s to $t = 2.5\ 10^4$ s in Fig. 4.9). The evolution of the total amount of deuterium desorbed during the TDS part of the test in function of aging time is presented in Fig. 4.10, with 100 % being obtained after "0 h" of aging, immediately after charging. All model materials present the same trend in decreasing TDS desorption contribution (%) with the aging durations.

In Fig. 4.11 the normalized isothermal desorption spectra have been plotted together for the different model materials. After normalization no differentiation

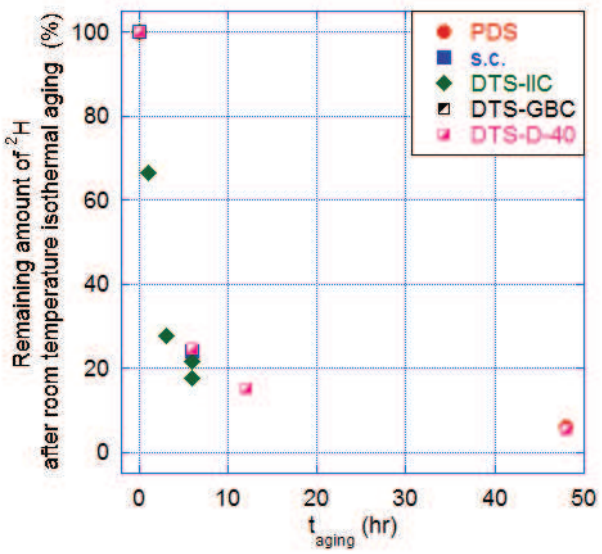

Fig. 4.10 Percentage (%) of total amount of ^{2}H desorbed during the TDS part of the "hybrid" spectra as compared to the total amount of ^{2}H desorbed from the material.

between the model materials can be made. This could hint that the desorption contribution at room temperature is comprised of primarily interstitially diffusion deuterium. A double comparison of the "hybrid" desorption spectra will be carried out comparing the recorded data for a pure diffusion system to (i) a single crystal of A600-like alloy, (ii) model materials with chromium carbides and (iii) model materials with dislocations, in order to see if any effect of trapping was nonetheless highlighted.

i. ***Comparing room temperature aged "hybrid" desorption spectra of A600-PDS to A600-like s.c.***

Literature states that H short-circuit diffusion in the grain boundary network may be enhanced at low temperatures [53, 54, 65]. Results presented in the previous section (immediately after charging for A600) seem to be consistent with a negligible effect of grain boundaries on the diffusion and trapping of hydrogen in A600. However, it proved important to check the relevance of this assumption under aging conditions.

Fig. 4.12 shows the "normalized" experimental "hybrid" desorption spectra after a 6 h aging period at approximately 294 K, followed immediately by TDS analysis for A600 pure diffusion and single crystal model materials. The "normalized" isothermal part of the desorption spectra can be considered identical (Fig. 4.12),

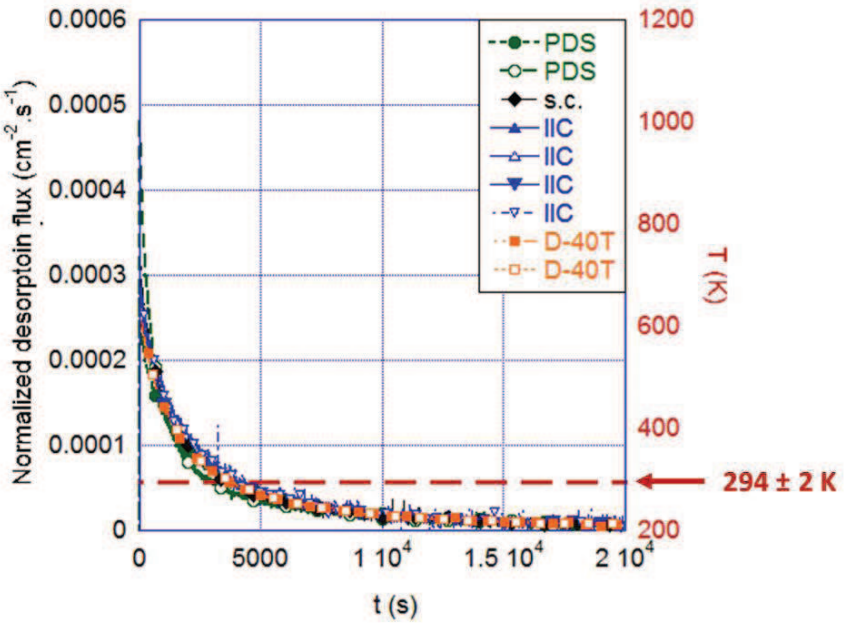

Fig. 4.11 "Normalized" isothermal room temperature (294 ± 2 K) desorption flux spectra for pre-charged (Conditions A, Table 3.6) A600 MMs. The temperature during the isotherm is indicated by the red dotted line.

but during TDS analysis some differences are observed on these spectra. First, the temperature of maximum desorption (T_m) for a A600-like s.c. occurs at a lower temperature ($\simeq$ 410 K) than that of A600-PDS ($\simeq$ 450 K) and second there seems to be a small desorption shoulder, indicated in the figure by the black arrow, at $\simeq$ 540 K. Besides these differences, the spectra present a similarity in the amount of deuterium remaining after isothermal aging which for both materials is approximately equal. Several hypotheses may be made to explain these observations:

1. The difference in maximum desorption flux temperature ($T_m^{\text{A600-PDS}} > T_m^{\text{A600-like s.c.}}$) could be attributed to:

   1a. the continuous diffusion (towards the interior of the sample) during the extended room temperature aging enhanced by a short-circuit diffusion phenomenon in the grain boundary network present in the polycrystalline (PDS) model material;

   1b. the effect of different types and amounts of residual trap sites present in the two materials.

2. The desorption shoulder observed on the A600-like single crystal spectrum may be attributed to the desorption contribution from the non-charged face

($x = L$) [89, 90] as the sample was slightly thinner (760 μm for the single crystal as compared to 820 μm for the pure diffusion model material).

If grain boundaries act as a short circuit network for hydrogen diffusion (i.e. hypothesis 1a.), one should note that the desorption during the isothermal phase would be enhanced for a PDS (polycrystalline) specimen thus decreasing the remaining amount of deuterium after aging as compared to the case of an A600-like single crystal. These experimental results, presented in Fig. 4.12, indicate that the ratio of aging to TDS contribution is approximately equal for both model materials. In conclusion, these experimental results seem to show that grain boundaries do not play the role of diffusion short-circuit networks in A600.

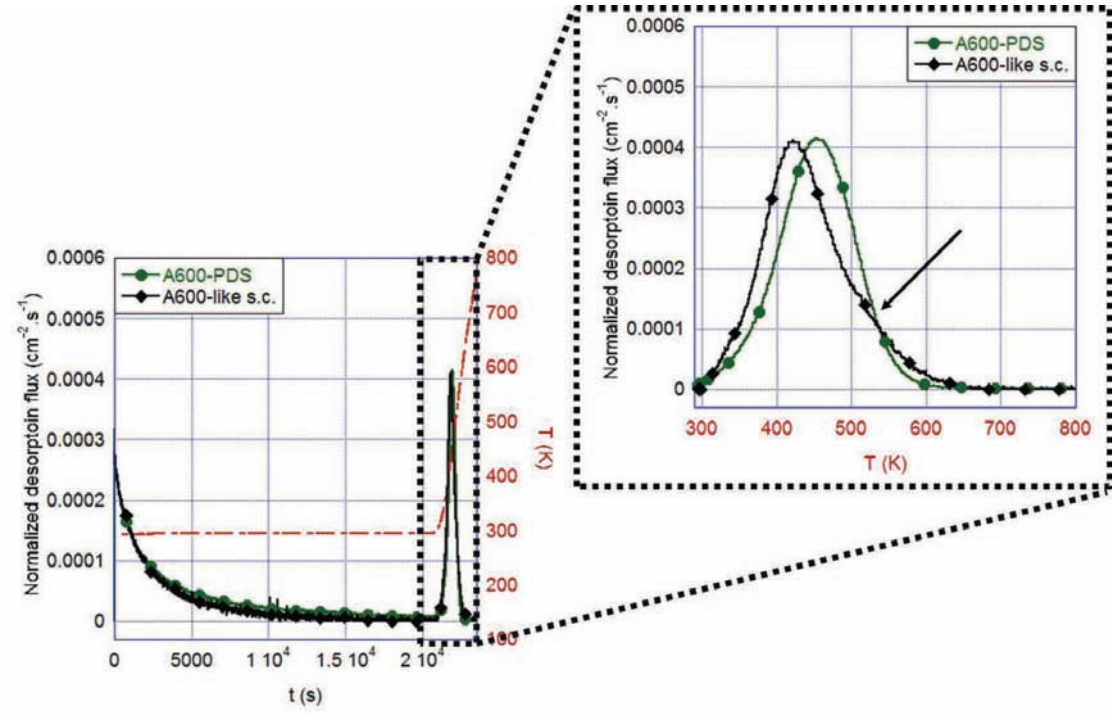

Fig. 4.12 "Normalized" experimental "hybrid" desorption spectra for 6 h of room temperature aging followed by TDS analysis ($\phi = 10$ K.min^{-1}) for pre-charged (Conditions A, Table 3.6) A600-PDS and A600-like s.c. MM. The temperature is shown in red. The axes of these two plots are not the same, on the left a "double-ordinate axis" plot can be seen with normalized desorption flux on the left-hand ordinate-axis and temperature (K) on the right-hand ordinate-axis, both presented with regards to time on the abscissa-axis, whereas in the "zoomed" plot of only TDS analysis the ordinate-axis is normalized desorption flux and the abscissa-axis is temperature.

ii. ***Comparing room temperature aged "hybrid" desorption spectra of A600-PDS to A600-DTS-IIC***

By applying this room temperature aging approach to the study of hydrogen trapping interactions at chromium carbides a spectral contribution clearly attributed to trapping at these sites was hoped to be isolated. A series of *in situ* room temperature isotherms were carried out on A600-DTS-IIC model materials. Aging periods ranged from 0 h to 24 h[2].

After 24 h of aging at room temperature the ^{2}H desorption flux was below the detection limit of the TDS system; this could be due to the significantly lower quantity of deuterium present in the A600-DTS-IIC model material immediately after charging (Fig. 4.1) compared to A600-PDS. TDS spectra after 0 h, 1 h, 3 h, 6 h and 12 h of aging are displayed in Fig. 4.13. These spectra are characterized by one well defined desorption peak and, for samples aged 3 h or more, a low[er] temperature desorption shoulder indicated by the black arrow in Fig. 4.13. From literature, one could have anticipated a high temperature desorption peak ($T \geq 675$ K) that could have been associated with trapping at chromium carbide precipitates [82]. To better analyze these room temperature aged spectra, direct comparisons to pure diffusion system results were carried out.

Fig. 4.14 compares a 6 h room temperature aged "hybrid" desorption spectrum of an A600-PDS model material to that of an A600-DTS-IIC model material. There are no observable differences between the normalized isothermal desorption spectra at room temperature ($t \leq 2\,10^4$ s in Fig. 4.14). This gives a good indication that the majority of the deuterium that leaves the sample during the isothermal room temperature aging is interstitial ^{2}H. When the TDS contributions are compared with respect to T some observations can be made:

1. The temperature of maximum desorption for the model material with trap sites ($T_m^{\text{A600-DTS-IIC}}$) is observed at a lower temperature than that of the pure diffusion model material ($T_m^{\text{A600-PDS}}$).

2. A small low temperature desorption shoulder, (Fig. 4.14) is observed on the A600-DTS-IIC spectra at ($\leq$ 350 K). A similar desorption shoulder is observed on the A600-PDS spectrum.

Based upon these observations, some hypotheses may be made concerning the influence of chromium carbides on hydrogen diffusion and trapping interactions in A600:

[2]In this study the "0 h" or "immediatley after charging" refers to the voluntary aging, meaning 0 h of voluntary aging after the transfer from the charging cell to TDS setup and start of mass spectrometer signal acquisition (i.e. 18 $\pm$ 3 min), see Table 4.1

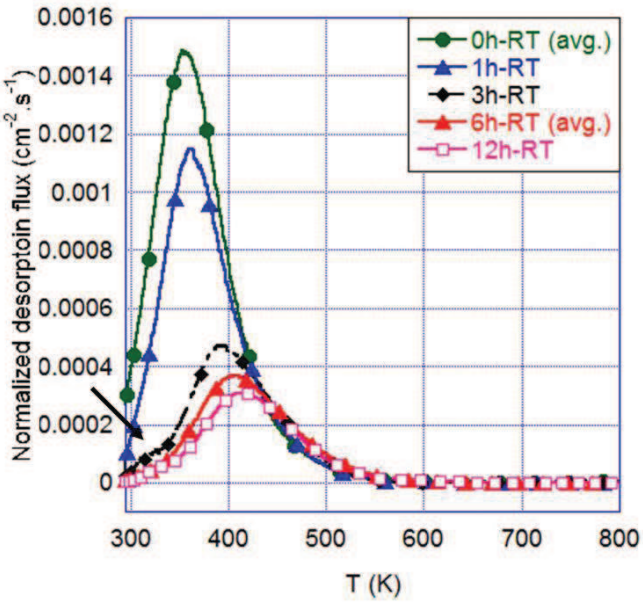

Fig. 4.13 Compilatoin of "normalized" TDS spectra performed on A600-DTS-IIC MM **immediately after charging**, **after 1 h**, **after 3 h**, **after 6 h** and **after 12 h** of room temperature aging. A small desorption shoulder is highlighted by the black arrow.

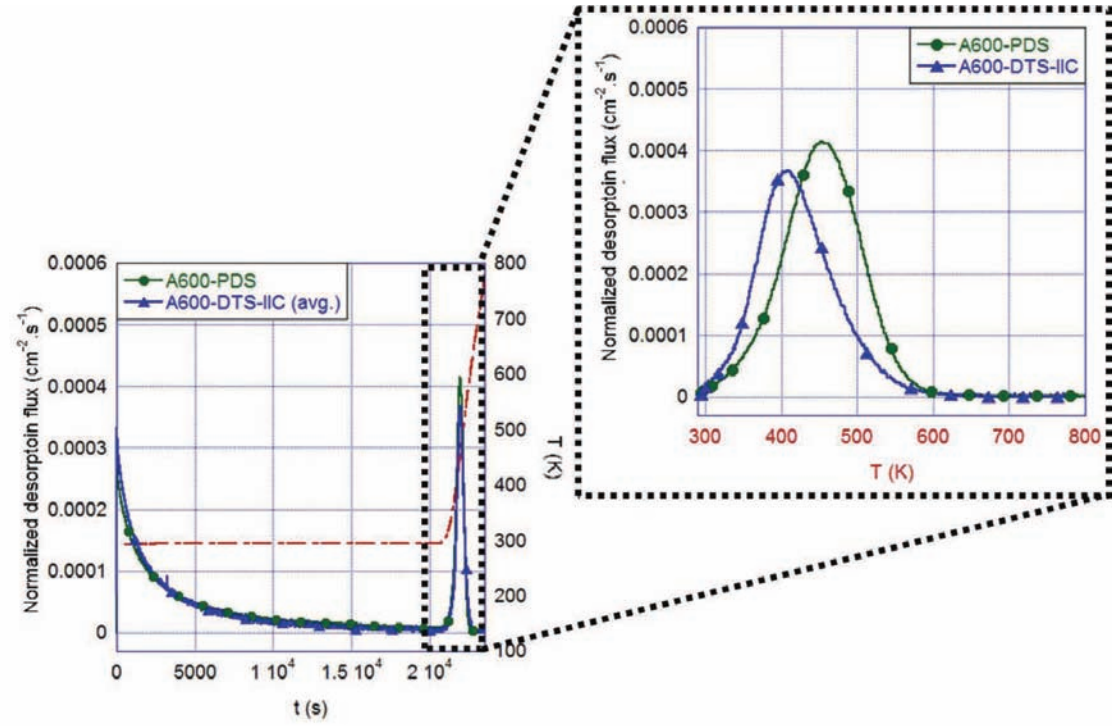

Fig. 4.14 "Normalized" experimental "hybrid" desorption spectra for 6 h of room temperature aging followed by TDS analysis (ϕ = 10 K.min^{-1}) for pre-charged (Conditions A, Table 3.6) A600-PDS and A600-DTS-IIC MM. The temperature ramp is shown in red.

1. Trapping interactions have slowed the apparent deuterium diffusion across the material and therefore the majority of deuterium has been retained closer to the sample surface ($x = 0$), thereby causing a lower temperature maximum desorption peak.

2. A second desorption peak, that could be immediately associated with chromium carbides [22, 82] is not present on the TDS spectrum. Therefore there may be an energy barrier that needs to be overcome at room temperature, as in the energy diagram for diffusion and trapping that Oriani *et al.* [69] proposed.

From these experimental analyses and comparisons it is difficult to draw any clear conclusions, let alone derive trapping and/or detrapping kinetic information, concerning the interactions taking place between hydrogen and chromium carbides. It seems as though some more fine tuned experimental analyses need to be done. These experimental analyses could include higher temperature aging or higher temperature charging.

iii. ***Comparing room temperature aged "hybrid" desorption spectra of A600-PDS to A600-DTS-D-40T***

Similar to for model materials with chromium carbides as the primary trap site type, a series of agings were carried out for durations ranging from 0 h (i.e. TDS analysis immediately after deuterium charging) to 48 h for DTS model materials with dislocations as the primary trap site type. The normalized experimental TDS spectra after room temperature aging can be seen in Fig. 4.15.

The normalized TDS peak intensity and amount of deuterium desorbed during TDS decreases significantly as aging time is increased, and the remaining percentage (%) of total desorbed deuterium remains equivalent to that for a pure diffusion model material (Fig. 4.10). There are two hypotheses that may explain these observations:

1. Only a very small amount of deuterium that is trapped at dislocations (as compared to interstitial ^{2}H, thus meaning that the ratio of $^2\mathrm{H}_{\mathrm{trapped}} \ll {}^2\mathrm{H}_{\mathrm{interstitial}}$).

2. Deuterium is readily detrapped from dislocations at room temperature.

It is interesting to note that a similar low temperature desorption "shoulder" observed for aged model materials with chromium carbides is also observed on these aged A600-DTS-D-40T spectra, black arrows in Fig. 4.15. The shoulder is first observed after 6 h of aging at room temperature spectrum at $T \leq 350$ K and then at increasingly higher temperatures as aging time is increased: $T \leq 375$ K and 400 K respectively for specimens aged 12 h and 48 h at room temperature.

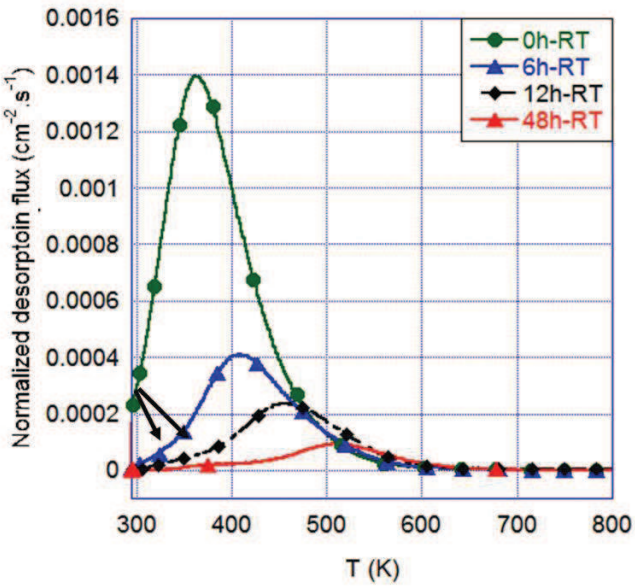

Fig. 4.15 Compilation of "normalized" TDS spectra after room temperature aging of a pre-charged for A600-DTS-D40T MM for aging durations ranging from 0 h, 6 h, 12 h and 48 h. A small desorption shoulder is highlighted by the black arrows.

"Hybrid" desorption A600-DTS-D-40T spectra for specimens aged 6 h and 48 h at room temperature are compared to pure diffusion system desorption spectra acquired under the same experimental conditions in Fig. 4.16 and Fig. 4.17 respectively. Again, no differences were observed in normalized isothermal desorption flux evolution. After a 6 h period of aging at room temperature, Fig. 4.16, a shift in T_m towards lower temperatures for A600-DTS-D-40T as compared to a "pure diffusion system", in a similar way to what was observed without aging (Fig. 4.8) or with chromium carbides (Fig. Fig. 4.7)

If we look closer at the TDS desorption spectra after a room temperature isothermal aging period of 48 h (4.17b), a low temperature desorption peak ($\approx$ 380 K) can be observed for both pure diffusion and diffusion and trapping at dislocations systems at the same temperature and normalized intensity. Furthermore, the maximum desorption temperature of the A600-DTS-D-40T MM, still occurs at a lower temperature (500 K) than that of the A600-PDS MM (540 K).

There are several, somewhat contradictory, hypotheses that may explain the peak shift associated with the most intense (highest temperature) desorption peak on these TDS desorption spectra:

1. Trapping interactions have slowed the diffusion across the material and therefore the majority of deuterium has been retained closer to the sample surface

($x = 0$) [52, 73] (similar to the hypothesis proposed for chromium carbides).

2. Dislocations act as a short-circuit diffusion network, thereby entertaining a faster apparent diffusion [and therefore desorption] from the specimen (i.e. maximum desorption peak at lower temperatures than a sample which is quasi-free of these "short-circuit" networks) [10, 73]

Regardless of the explanation of the highlighted phenomena, the experimental TDS spectrum acquired and analyzed up to this point (immediately after cathodic charging and aged to 6 h at room temperature) have not provided enough information to draw any solid conclusions concerning the nature of these interactions, let alone derive kinetic information.

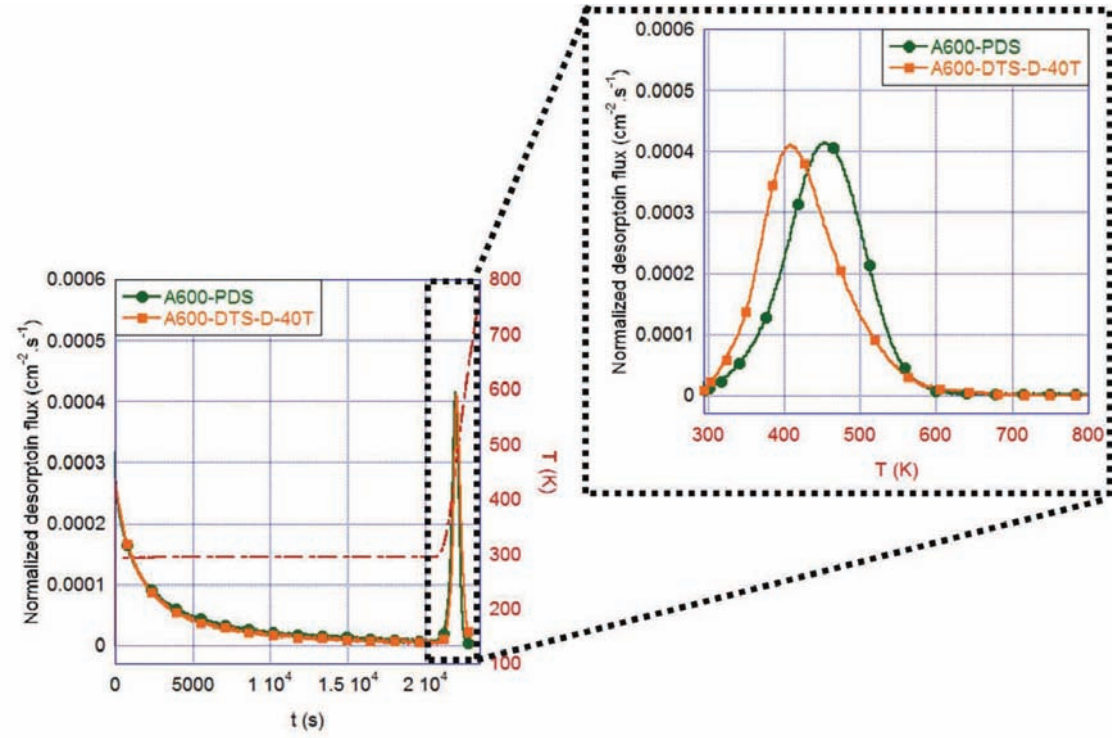

Fig. 4.16 "Normalized" experimental "hybrid" desorption spectra for 6 h of room temperature aging followed by TDS analysis ($\phi = 10$ K.min^{-1}) for pre-charged (Conditions A, Table 3.6) A600-PDS and A600-DTS-D-40T MM. The temperature ramp is shown in red.

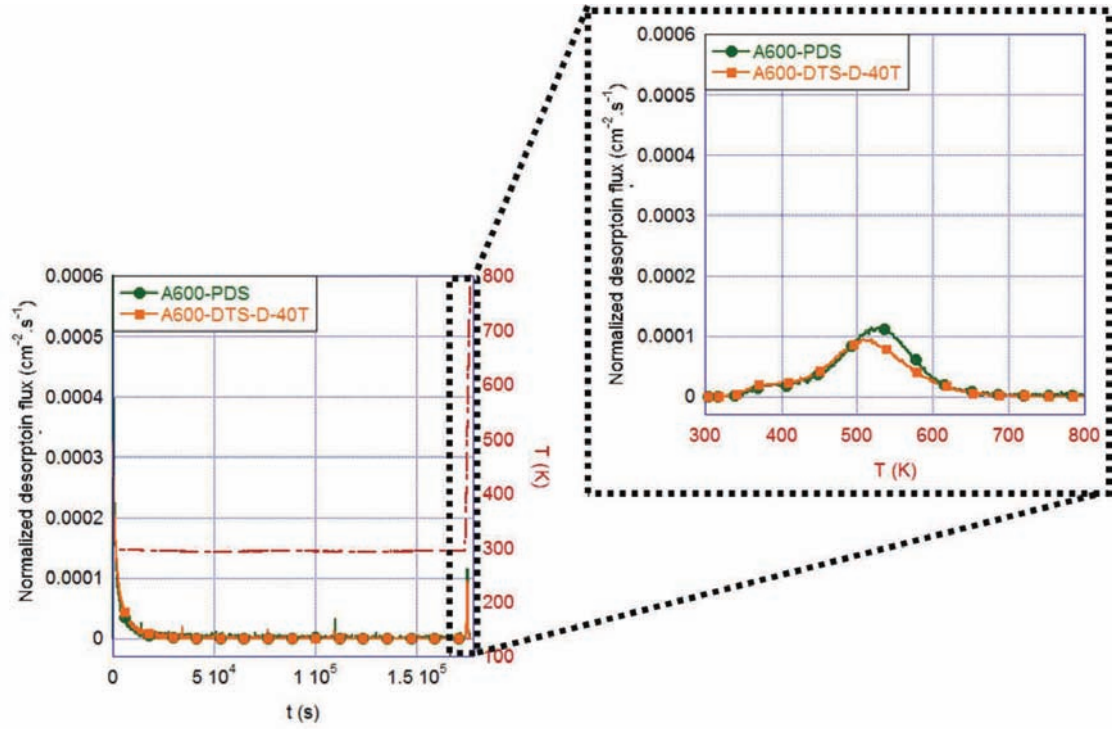

(a)

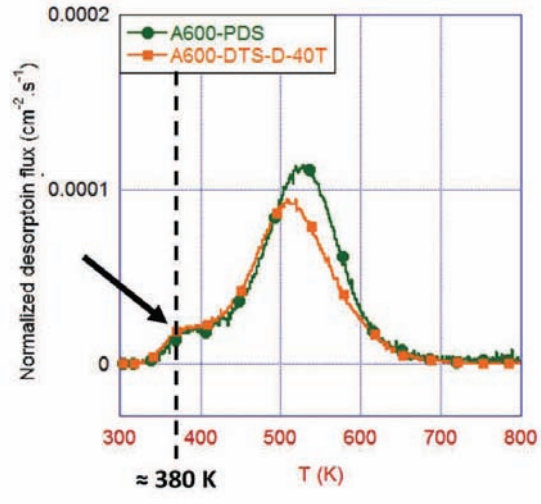

(b)

Fig. 4.17 (a) "Normalized" experimental aging (48 h at RT) and TDS desorption spectra (ϕ = 10 K.min^{-1}) for pre-charged (Conditions A, Table 3.6) A600-PDS and A600-DTS-D-40T MM and the temperature ramp is shown in red and (b) zoom on the TDS spectra after 48 h of room temperature aging.

4.2.2.2 Final remarks: Room temperature isothermal aging

The experimental results for room temperature aged sample have not provided any conclusive information concerning the nature of ^{2}H trapping interactions taking place in model materials. It would be impossible to, with any given certainty, assign kinetic trapping and detrapping constants with interactions taking place at chromium carbides and/or dislocations in these model materials. On the other hand, these results seem to hint that grain boundaries may not play the role of diffusion short-circuit pathways in nickel base alloy 600

It might be that through room temperature aging, the ratio of "trapped" to "interstitial" hydrogen was not able to be increased enough to observe a trapping contribution on TDS spectra. It is for this reason a second aging approach was adopted: high temperature aging. This approach was ultimately aimed at increasing this ratio and isolating a trapping contribution on the desorption spectra.

4.2.2.3 High temperature isothermal aging

A second type of aging was adopted which involved aging pre-charged specimen at a higher temperature (409 K) for a period ranging from 1 to 9 h. This temperature (409 K) was chosen as the temperature of maximum desorption (T_m) for an A600 pure diffusion system occurs at approximately 395 K. This temperature (slightly above this temperature) would theoretically entertain a maximum interstitial hydrogen desorption from these materials.

The current TDS experimental set-up does not allow for the insertion of specimen into the system when the furnace temperature is above 323 K. Thus, to age samples at an elevated temperature, the specimen were, first, inserted into the furnace at room temperature. Then, once mass spectrometer acquisition could begin (i.e. pumping down the system to a sufficient vacuum had finished) the furnace was quickly heated to the desired aging temperature.

The deuterium desorption flux was continuously monitored during the ramp and isothermal period and during TDS analysis creating "hybrid" desorption spectra. For high temperature aged spectra the term "isothermal desorption spectrum" will refer to the entire aging period, i.e. the ramp to high temperature and duration held at high temperature. The normalized desorption flux during aging are shown in Fig. 4.18 with a subfigure (Fig. 4.18b) focusing on the first 3500 s of desorption. These spectra are characterized by a desorption peak at approximately 1000 s which corresponds with when the sample reached between 390 K and 395 K, followed by a sharp decline in desorption flux as the temperature stabilized and the isotherm progressed ($t \geq 1800$ s).

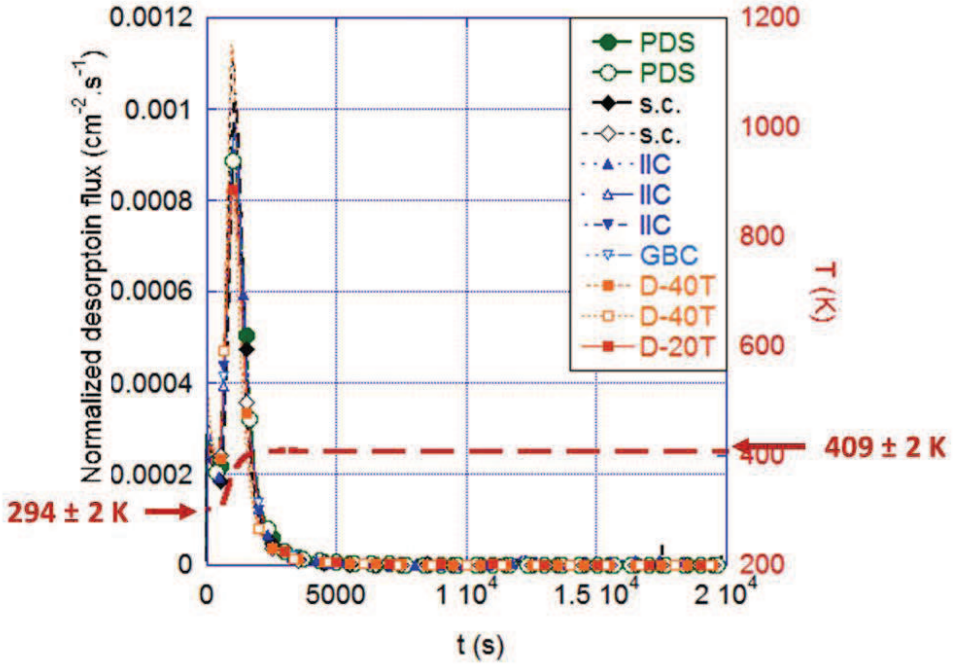

(a)

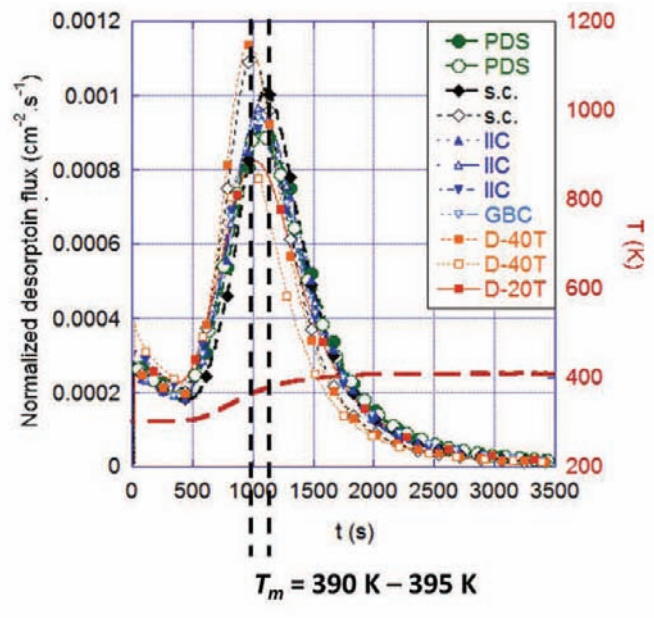

(b)

Fig. 4.18 "Normalized" high temperature "isothermal" desorption flux spectra (a) for first 2 10^4 s and (b) focused on the desorption peak during the isotherm for pre-charged (Conditions A, Table 3.6) A600 model materials. The temperature is shown in red for the aging period. In (b) the maximum desorption temperature range in t is indicated by the black vertical lines and the corresponding T_m range is written below.

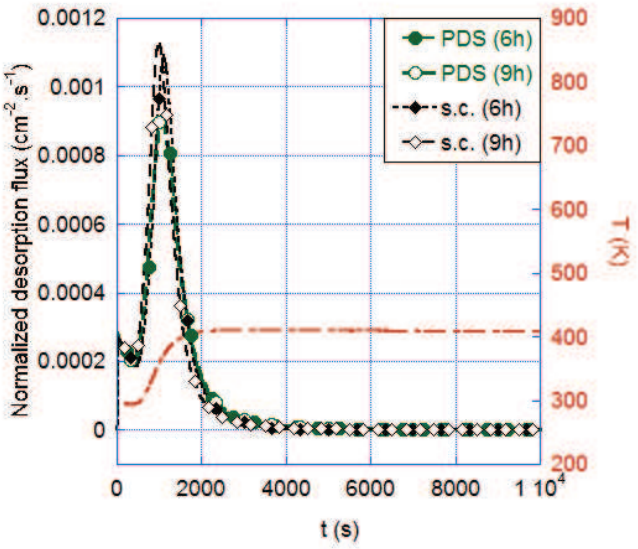

(a)

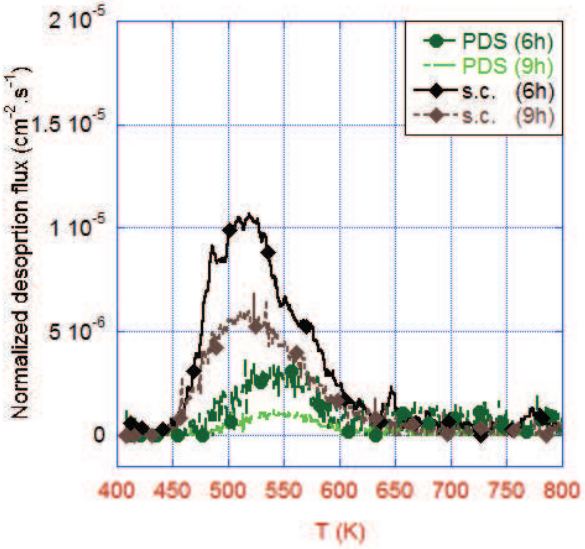

(b)

Fig. 4.19 "Normalized" experimental desorption spectra for A600-PDS and A600-like s.c. for (a) aging at 409 K (first 1 10^4 s) and (b) TDS analysis (ϕ = 10 K.min^{-1}).

i. ***Comparing high temperature aged "hybrid" desorption spectra for pure diffusion and single crystal model materials***

The normalized experimental "hybrid" spectra for a A600 pure diffusion and A600-like single crystal model material are shown in Fig. 4.19. Fig. 4.19a focuses on the first 10^4 s of high temperature (409 K) aging and Fig. 4.19b focuses on the TDS analysis ($\phi = 10$ K.min^{-1}). The normalized high temperature isothermal aging desorption spectra are quasi-identical; all four spectra (6 h aged PDS, 9 h aged PDS, 6 h aged s.c. and 9 h aged s.c.) are characterized by desorption peak at approximately the same temperature and of equivalent normalized intensity. Looking closely at the normalized aged TDS spectra, there is an observable difference in both spectra intensity and maximum desorption temperature for the two types of model materials. The maximum desorption temperature for A600-like single crystals is at approximately 515 K whereas for a pure diffusion system it is located at 550 K.
Two hypotheses may explain these observations:

1. The presence of grain boundaries in the polycrystalline PDS model material would help to explain why its maximum desorption peak is observed at a higher temperature and why this peak is less intense than that of a MM with no grain boundaries: (i) faster ^{2}H diffusion towards the interior of the specimen and (ii) more ^{2}H is lost during the aging period due to short circuit grain boundary diffusion.

2. The effect of residual trap sites present in the A600-like single crystal or in the A600-PDS (residual chromium carbides).

In conclusion, it would seem that the difference in these model materials (i.e. the presence of grain boundaries in the PDS material) may play a small role in absorption/diffusion/desorption phenomena taking place in the model material systems.

ii. ***Comparing high temperature aged "hybrid" desorption spectra for pure diffusion and diffusion and trapping-chromium carbide model materials***

High temperature agings of 3 h, 6 h and 9 h were carried out on both diffusion and trapping model materials presenting chromium carbides: (i) inter- and intragranularly precipitated and (ii) preferentially precipitated along grain boundaries. The normalized experimental TDS results as compared to a pure diffusion system can be seen in Fig. 4.20 and Fig. 4.21 for IIC and GBC model materials respectively. Some global remarks can be made:

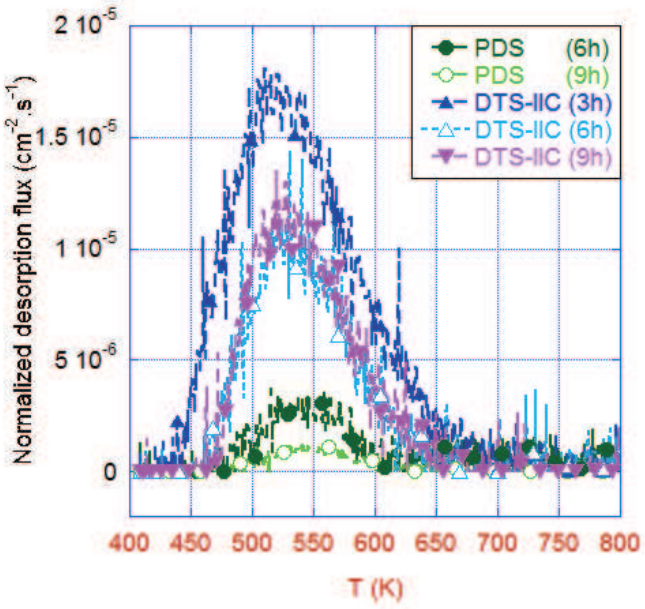

Fig. 4.20 "Normalized" TDS spectra ($\phi = 10$ K.min^{-1}) for A600-PDS and A600-DTS-IIC (inter- and intragranular chromium carbides) after aging 3 h, 6 h or 9 h at 409 K.

The "normalized" TDS desorption flux after agings for these DTS model materials is significantly more intense than that of similarly aged pure diffusion and single crystal model materials. Furthermore, after 6 h of aging at 409 K there is no further evolution in the desorption flux intensity of a DTS model material (Fig. 4.20), whereas for a PDS model material, the additional three hours at high temperature decreased its relative intensity by over 50 %.

It appears that a trapping contribution for ^{2}H at chromium carbides has been isolated after aging 6 h at 409 K, as there is no further evolution in the TDS spectral intensity. Furthermore, the maximum desorption temperatures (T_m) for both

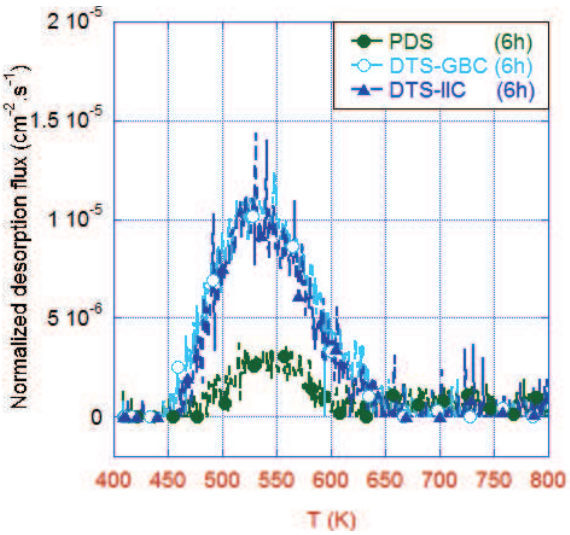

Fig. 4.21 "Normalized" TDS spectra ($\phi = 10$ K.min^{-1}) for A600-PDS, A600-DTS-GBC and A600-DTS-IIC after aging 6 h at 409 K.

model materials with chromium carbides seem to coincide (Fig. 4.20 and Fig. 4.21).

iii. ***Comparing high temperature aged "hybrid" desorption spectra for pure diffusion and diffusion and trapping-dislocation model materials***

The same high temperature aging approach was taken to isolate a trapping contribution at dislocations. Specimen were aged for 6 h and 9 h at 409 K and the resulting TDS spectra can be seen in Fig. 4.22. This figure compares diffusion and trapping at dislocation spectra to their pure diffusion system counterparts.

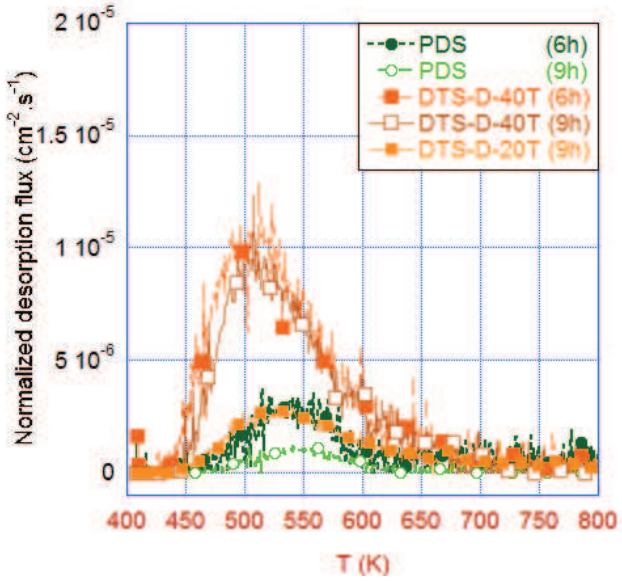

Fig. 4.22 "Normalized" TDS spectra (ϕ = 10 K.min^{-1}) for A600-PDS, A600-DTS-D-40T and A600-DTS-D-20T (diffusion and trapping systems with dislocations) after aging 6 h or 9 h at 409 K.

Some observations concerning the experimental desorption spectra can now be made:

1. The desorption peak intensity for a material with traps is more intense than its equivalent spectrum for a PDS model materials after the same aging duration.

2. The maximum desorption flux temperature occurs at a lower temperature for the A600-DTS-D-40T MM ($\approx$ 500 K for 6 h and 9 h aged) as compared to its PDS equivalent ($\approx$ 550 K for 6 h and 9 h aged).

3. There is little evolution in the TDS desorption spectra for a A600-DTS-D-40T model material aged 6 h and 9 h.

4. The desorption peak associated with A600-DTS-D-20T (9 h) actually seems to be more of a desorption "plateau" as it is characterized by a relatively stable desorption flux between 500 K and 550 K.

5. The difference in desorption peak intensity for 20T and 40T model materials my reflect the different trap site densities present in the materials.

4.2.2.4 Final remarks: High temperature isothermal aging

Experimental results for TDS spectra acquired after agings at 409 K seem to best highlight the differences between pure diffusion model materials and diffusion and trapping materials. It would seem as though trapping contributions have been magnified on TDS spectra after high temperature aging. These magnified contributions may now be used for fitting and the derivation of trapping and detrapping kinetic constants using the numerical routine and simulation approach presented in Chapter 3. The following section will present the derivation and validation of the diffusion and trapping kinetic parameters derived from these experimental spectra using the numerical code and fitting approach presented in Chapter 3.

4.3 Numerical simulation

As seen in the previous sections, experimental data has been gathered on which the analysis of H-material interactions in A600 and SS316L alloys, namely diffusion and trapping interactions at specific trap site types will be carried out. This section will present the simulation results and derived diffusion coefficient parameters, (i) D_0 and (ii) E_D, for pure diffusion model materials of Ni base alloy A600 and stainless steel SS316L. Once the diffusion coefficient has been determined and validated the trapping and detrapping kinetic constant parameters, (i) k_0, (ii) E_k, (iii) p_0 and (iv) E_p, and possibly trap site densities (N) for chromium carbides (A600) and dislocations (A600 and SS316L) can be derived from model desorption spectra on which a trapping contribution has been isolated, i.e. using high temperature aged "hybrid" desorption data.

The numerical code presented in Chapter 3 was used to fit experimental TDS spectra and derive the aforementioned parameters. This is a three step process:

(i) acquisition of experimental model TDS spectra with isolated diffusion contributions[3] and trapping contributions (see Sec. 4.2), (ii) fitting of experimental spectrum for deriving diffusion or trapping parameters and (iii) validation of these parameters. Validation of the parameters will be carried out by simulating an experimental spectra for the same model material having been subjected to different analysis conditions.

This section will be separated into two large parts. First, the (i) diffusion coefficient of ^{2}H will be derived and validated. It was necessary to determine this parameter first as it will be injected into the numerical fitting code for the second part (ii) where the trapping and detrapping kinetic constants will be determined and validated.

4.3.1 Diffusion coefficient derivation

Model TDS experimental spectra were acquired using the A600 and SS316L PDS model materials. The diffusion coefficient could be determined by fitting the spectrum immediately after charging and then tested through simulating "hybrid" room and high temperature aged desorption spectra and comparing them to the experimental "hybrid" spectra.

4.3.1.1 ^{2}H diffusion in A600

i. ***Spectral fitting***

As a first comparison, experimental TDS spectra were simulated using literature diffusion data for H (and its isotopes) in A600 [40, 41], see Table 4.2, and compared to the experimentally acquired spectrum, see Fig. 4.23. The spectra were simulated by injecting all experimental parameters which includes: (i) charging conditions (t and T), (ii) transfer conditions (t, T), (iii) aging conditions when applicable (t and $T(t)$) and (iv) TDS analysis experimental temperature ramp (t and $T(t)$) along with the actual sample thickness (L). As a whole the reproduction of the desorption spectrum is correct but there are slight discrepancies in the (i) temperature of maximum desorption and (ii) peak intensity. As mentioned in Sec. 2.4.1.3, corrections for the isotopic effect had a negligible effect on the hydrogen diffusion coefficient; therefore these corrections were not done before spectral simulations.

As spectra simulated using literature data are similar to the experimental spectrum, the pre-exponential constant (D_0) and activation energy (E_D) [specifically

[3]Pure diffusion system desorption spectra were considered to have isolated diffusion contributions.

Table 4.2 Diffusion coefficients of H (and its isotopes) in A600 reported in literature.

Isotope	T range (K)	D_0 ($cm^2.s^{-1}$)	E_D ($kJ.mol^{-1}$)	D at 298 K ($cm^2.s^{-1}$)	D at 409 K ($cm^2.s^{-1}$)
H [40]	470 - 673	0.017	49.8	$3.2\ 10^{-11}$	$7.5\ 10^{-9}$
^{2}H [40]	470 - 673	0.02	51.9	$1.6\ 10^{-11}$	$4.7\ 10^{-9}$
^{3}H [41]	573 - 973	0.013	50.6	$1.8\ 10^{-11}$	$4.5\ 10^{-9}$

the diffusion parameter values defined by Rota *et al.* [40]] will be used as initial input parameters for the numerical fitting routine.

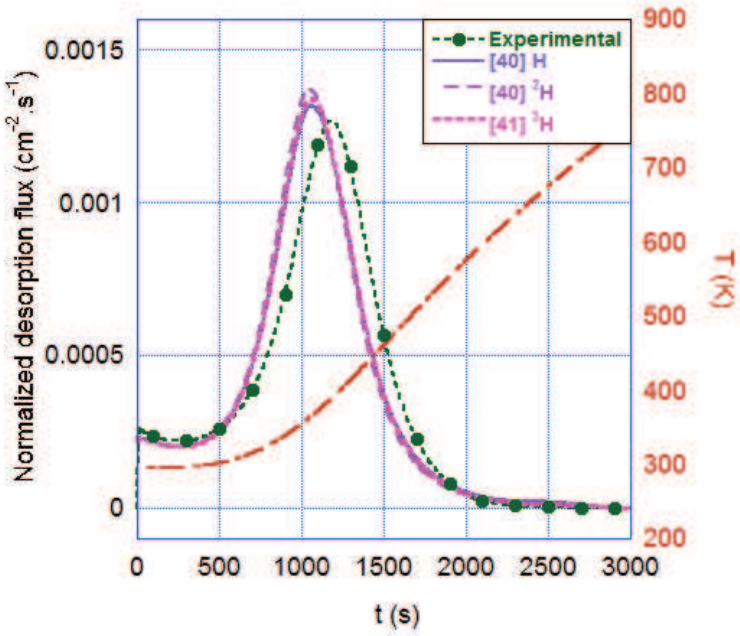

Fig. 4.23 "Normalized" experimental A600 pure diffusion system experimental desorption flux and simulated TDS spectra calculated using diffusion coefficients for H and its isotopes in A600 from literature [40, 41] in function of time (abscissa-axis) and temperature (ordinate-axis right).

After fitting the determined pre-exponential coefficient and activation energy for diffusion in A600 were evaluated as $(1 \pm 0.5)\ 10^{-2}$ $cm^2.s^{-1}$ and (45.0 ± 5.0) $kJ.mol^{-1}$ respectively, see Table 4.3. The margin of error was determined by fitting multiple pure diffusion system TDS spectra immediately after charging and comparing the derived value. The normalized "best-fit", literature simulation [40, 41] and experimental TDS spectra are shown in Fig. 4.24. The "best-fit" TDS spectrum reproduces a little better the experimental TDS spectrum, especially during the first 1000 s of thermal desorption mass spectroscopy analysis.

The tolerated error on the diffusion coefficient and resulting TDS spectrum can be seen in Table 4.4 and Fig. 4.25. The highest and slowest deuterium diffusivities

Table 4.3 Derived diffusion coefficients for a A600 pure diffusion system (PDS) model material.

Material type	T range (K)	D_0 ($cm^2.s^{-1}$)	E_D ($kJ.mol^{-1}$)	D at 298 K ($cm^2.s^{-1}$)	D at 409 K ($cm^2.s^{-1}$)
A600-PDS	294 - 800	$(1 \pm 0.5)\ 10^{-2}$	45 ± 5	$\approx 1.3\ 10^{-10}$	$\approx 1.8\ 10^{-8}$

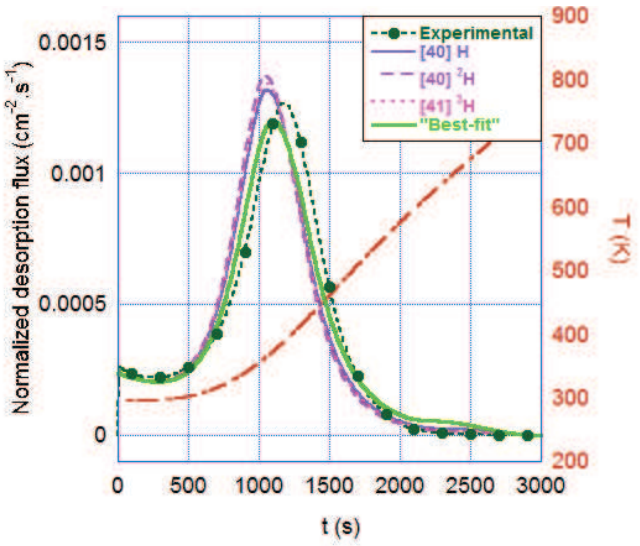

Fig. 4.24 "Normalized" experimental desorption flux acquired on an A600-PDS, simulated TDS spectra calculated using diffusion coefficients for H and its isotopes in A600 [40, 41] and the best-fit calculated using the numerical fitting routine (Table 4.3) in function of time (abscissa-axis) and temperature (ordinate-axis right)

are represented by "A" and "B". As the hydrogen diffusion in A600 is increased, a desorption shoulder (approximately 1700 s to 2300 s in Fig. 4.25) appears. This desorption shoulder is due to simultaneous ^{2}H desorption from the charged ($x = 0$) and non-charged face ($x = L$). This concept has been discussed in Chapter 3 and in previous publications and presentations [89, 90, 144].

Table 4.4 Error on diffusion coefficient values, demonstrating the "fastest" (A) and "slowest" (B) tolerated D values. Simulations using these parameter can be seen in Fig. 4.25.

Label in Fig. 4.25	D_0 ($cm^2.s^{-1}$)	E_D ($kJ.mol^{-1}$)
A	0.015	40.0
"Best-fit"	0.1	45.0
B	0.005	50.0

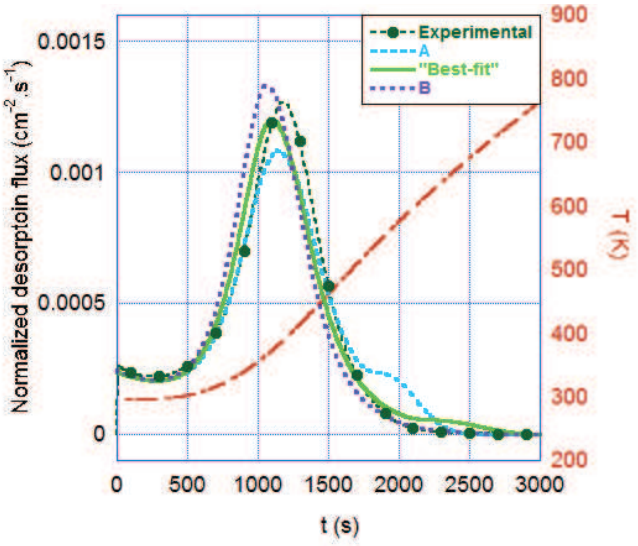

Fig. 4.25 Tolerated calculation error on derived diffusion coefficient. Simulation parameters associated with "A" and "B" can be seen in Table 4.4. Desorption spectra were "normalized" with regards to total desorbed deuterium.

ii. *Validation of the diffusion coefficient*

To test the derived pre-exponential constant (D_0) and activation energy (E_D) combination (Table 4.3) these derived values have been used to simulate a spectrum corresponding to a pure diffusion system, charged with deuterium then aged 6

h at room temperature. The resulting TDS spectrum has been compared to its experimental counterpart together with simulated spectra using diffusion coefficient values found in literature [40, 41]. The normalized simulated and experimental desorption spectra can be seen in Fig. 4.26 and Fig. 4.27. A superior reproduction of the experimental TDS spectrum is achieved using the derived diffusion parameters (Table 4.3). This better reproduction is highlighted by the similarities in (i) aging desorption to TDS desorption contribution ratios, (ii) the spectral intensity for the entire analysis (isothermal aging and TDS) and (iii) [overall] spectral form.

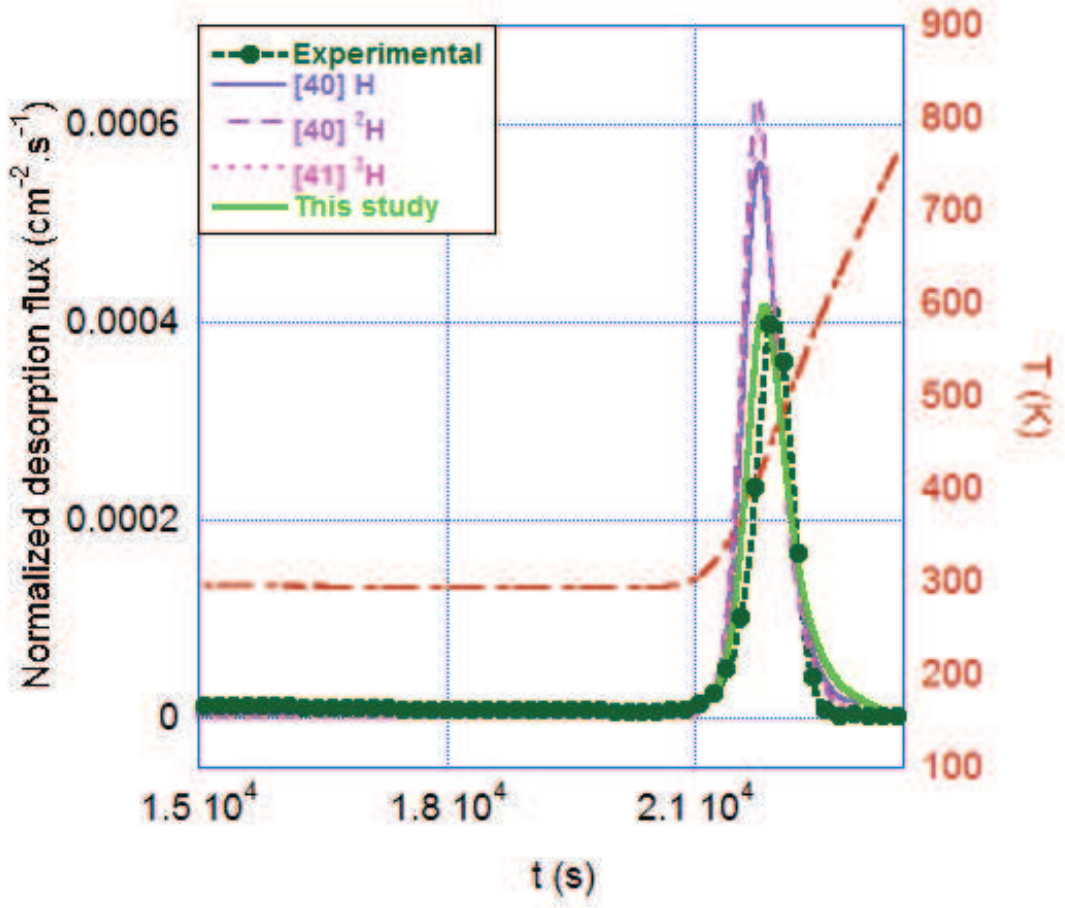

Fig. 4.26 "Normalized" experimental A600 pure diffusion system desorption flux and simulated TDS spectra (6 h isothermal aging at RT, followed by TDS testing with a $\phi = 10$ K.min^{-1} temperature ramp rate) calculated using the diffusion coefficients for H and its isotopes found in literature [40, 41] and that derived in this study from a TDS spectrum immediately after ^{2}H charging (Table 4.3).

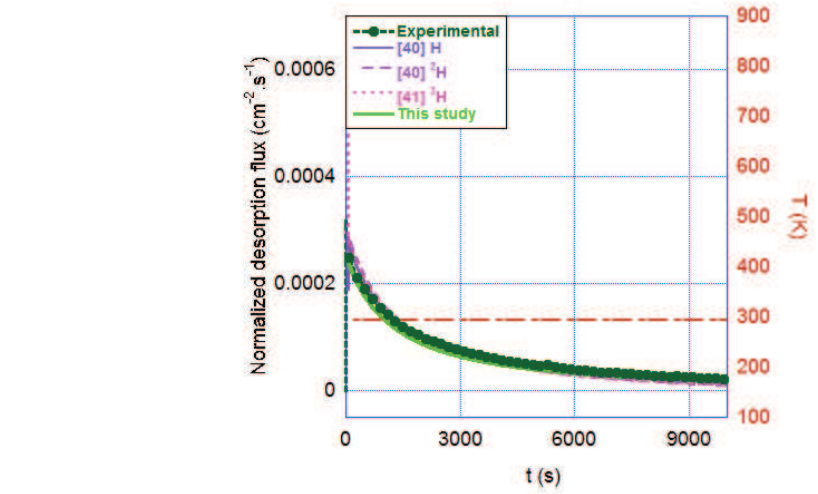

(a)

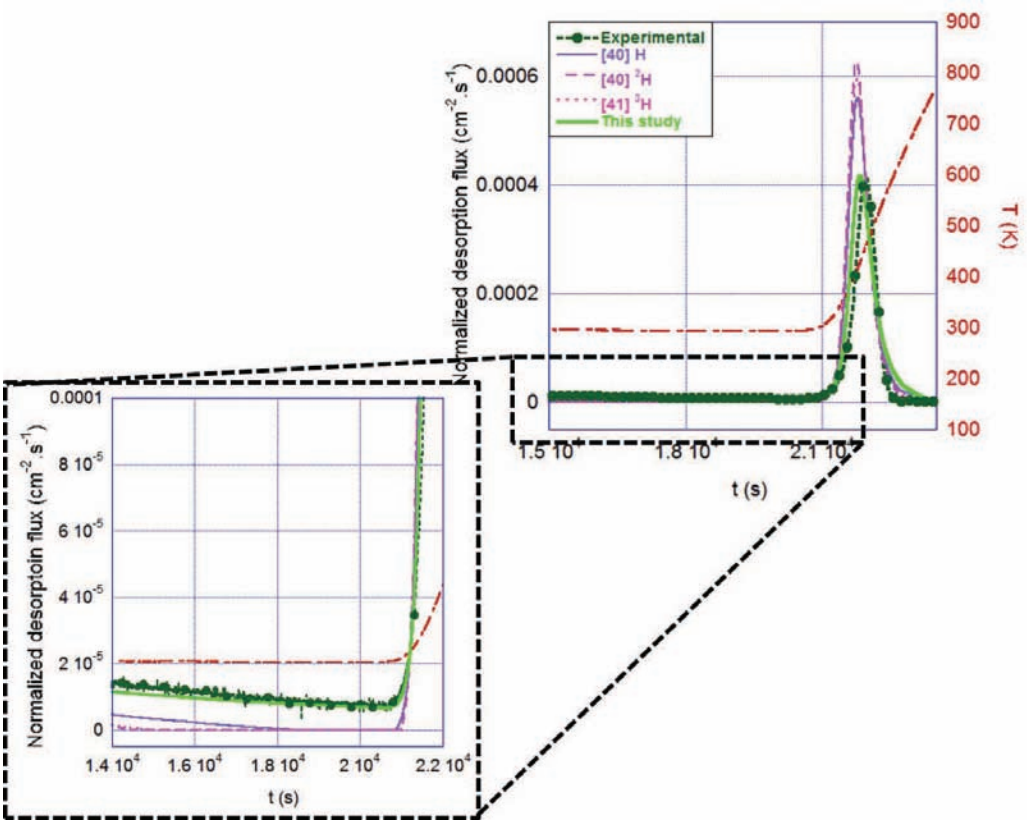

(b)

Fig. 4.27 Zooms of the pure diffusion experimental and simulated (Table 4.3,[40, 41]) spectra seen in Fig. 4.26: (a) focusing on the beginning of the isothermal (RT) desorption spectra (b) focusing on the isotherm (6 h at RT) and TDS desorption spectra ($\phi = 10$ K.min^{-1}).

Fig. 4.27 shows specific sections of the "hybrid" desorption spectrum: Fig. 4.27a highlights the first 1000 s of isothermal desorption and Fig. 4.27b the non-isothermal TDS analysis. In Fig. 4.27a the experimental desorption flux at $t = 0$ is better reproduced by using the derived parameters (Table 4.3) whereas literature values [40, 41] give slightly more intense values.

The simulated desorption spectra, using literature data [40, 41], then rapidly decrease towards zero (with a higher slope), while the simulated desorption spectrum, using previously derived diffusion parameters (Table 4.3), continues to mirror the decline in experimental flux until TDS testing (see from ($t = 1.5\ 10^4$ to $t \approx 2.1\ 10^4$) in Fig. 4.27b). Furthermore as previously mentioned the TDS spectral intensity at maximum desorption temperature for the simulated spectrum with values derived in this work (Table 4.3) is coherent with the experimental normalized intensity. This shows the robustness of both the developed numerical model and of the derived pre-exponential and activation energy combination for the diffusion of ^{2}H in A600.

As the reproduction of room temperature aged spectra was much better using the derived diffusion coefficient parameters, a reproduction of the high temperature aged spectrum was attempted. An experimentally 6 h aged at 409 K PDS spectrum was simulated (injection of all experimental conditions) using the derived diffusion coefficient and literature diffusion data [40, 41]. A comparison of the experimental and simulated desorption spectra can be seen in Fig. 4.28. The normalized high temperature isotherm experimental desorption spectrum is well reproduced using the derived diffusion coefficient (Table 4.3) concerning (i) peak placement, (ii) peak relative intensity and (iii) spectral form in Fig. 4.28a. On the other hand, when the experimental and simulated (Table 4.3 and [40, 41]) non-isothermal TDS spectra (Fig. 4.28b) are compared there are some very large discrepancies.

In Fig. 4.28b the experimental spectrum is no longer reproduced in intensity nor peak placement. Furthermore, for the simulated desorption spectra obtained using literature diffusion coefficients, two desorption peaks (^{2}H [40] and ^{3}H [41]) or a desorption "shoulder" and desorption peak combination (H [40]) are observed whereas for the derived diffusion coefficient (Table 4.3) only one peak can be seen. This "two peak" or "peak-shoulder" phenomenon is due to the asymmetric desorption from both sample faces [89, 90] linked to a non-homogeneous repartition of H (or its isotopes) in the specimen before TDS analysis, whereas the presence of a single desorption peak, in this case, is due to a relatively homogeneous repartition of deuterium in the sample after the high temperature aging and therefore simulating (approximately equal) desorption taking place at both sample faces. The difference in repartition can be explained by the difference in diffusivity at 409 K. The derived diffusion coefficient in this study (D) (Table 4.3) is slightly higher than those in literature data [40, 41] (Table 4.2) and could explain the

disappearance of the second desorption peak or shoulder.

The inconsistency between simulated and experimental TDS spectral intensity may be explained by the calculation error of the numerical method. The error on spectral integrals (i.e. mol ^{2}H desorbed) for our simulation method was on the order of 5 - 8 %. Due to this error it is impossible to simulate high temperature aged and TDS spectra normalized with regards to the total spectrum integral. A small calculation error on the aging contribution (which accounts for about 99 % of the total desorption) would induce a very high error, with regards to contribution associated with the simulated TDS spectrum.

Therefore to facilitate spectral comparisons, the experimental and simulated TDS spectra (acquired after high temperature aging) will be normalized with regards to their individual spectrum integral, i.e. the TDS spectra will be spectra by the amount of ^{2}H desorbed during the TDS (non-isothermal) part and the (isothermal) aging spectra normalized by the amount of deuterium desorbed during the aging step. Fig. 4.29 shows the experimental and simulated TDS spectra after this normalization process. Even after, the simulated TDS desorption spectra do not reproduce the experimental spectrum. This non-ideal reproduction can be explained by the error in the derived diffusion coefficient.

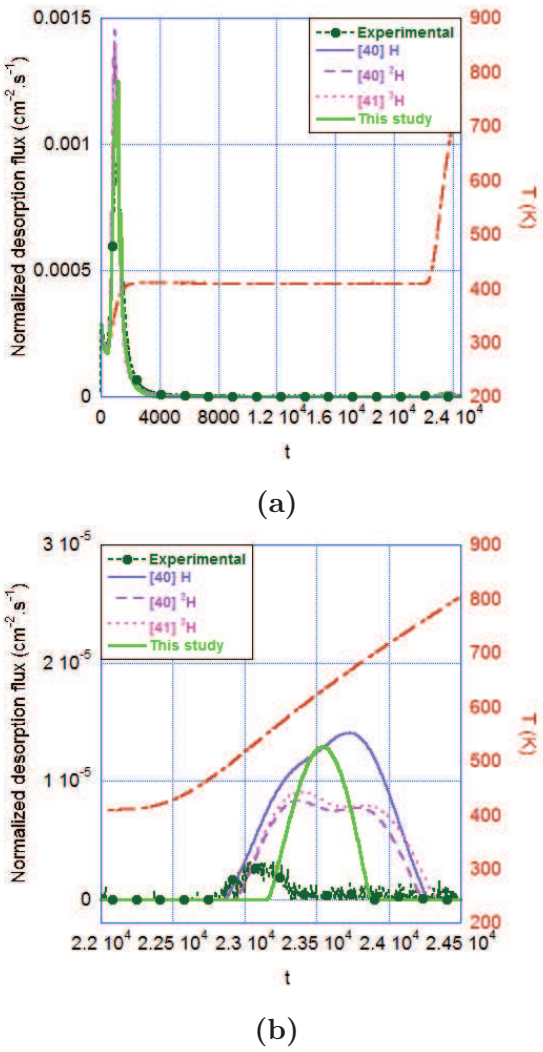

Fig. 4.28 "Normalized" PDS experimental and simulated (Table 4.3,[40, 41]) desorption spectra for 6 h aging at 409 K followed by TDS analyses (ϕ = 10 K.min^{-1}): (a) shows the total analysis (aging and TDS) and (b) is a zoom of the TDS analysis part showing experimental and simulated spectra.

If the TDS spectrum is simulated using a diffusion coefficient within the error range of the derived diffusion coefficient the spectrum can be well reproduced, see Fig. 4.30a. Fig. 4.30b shows broken down spectral contributions for the "best-fit" and for "A" (Table 4.4). In both cases the simulated desorption flux is a mixture of desorption contributions from the charged ($x = 0$) and non-charged ($x = L$) sample faces.

This spectral decomposition may help to explain the spectral form, as the well defined "A" peak is the result of a simultaneous and equivalent desorption taking place at both sample faces and indicates that a total homogeneous repartition of deuterium takes place in the model material during the six hours of high temperature (409 K) aging prior to TDS analysis. On the other hand, the wide deformed type of peak seen in "best-fit" is due to a non-homogeneous repartition of deuterium in the material thickness, with a slight localization closer to the charged face ($x = 0$), and thus a stronger desorption from this face early in analysis. This contribution was later joined at approximately 1200 s by a non-charged face desorption contribution. This analysis shows the importance of knowing the origin of desorption contributions and the use of simulation to determine the make-up of the desorption spectrum.

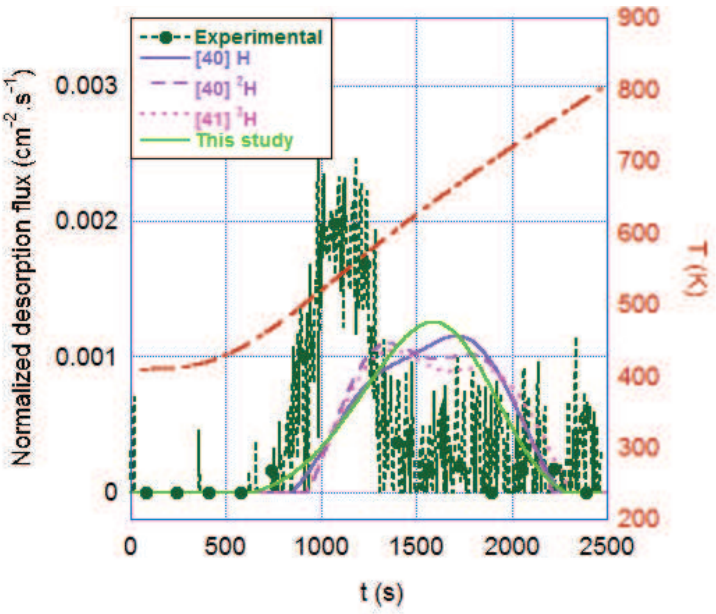

Fig. 4.29 "Normalized-TP" (i.e. with regards to "TDS part") spectral integrals A600-PDS experimental and simulated TDS desorption spectra using derived ^{2}H (Table 4.3, "This study") and literature [40, 41] diffusion data.

However it can be remarked that that both non-aged and room temperature aged [total] spectra the simulation using the derived pre-exponential constant and activation energy, Table 4.3, reproduces very well the experimental spectrum. The fact that high temperature simulations do not reproduce the experimental TDS part of the spectrum (even though they reproduce very well the ramp to high temperature aging and subsequent isothermal high tempererature aging spectrum)

hints that the experimentally observed contribution may in fact not be due to interstitial hydrogen diffusion and therefore may be attributed to a residual trapping mechanism present in the pure diffusion model materials. It will be necessary to validate this once the trapping and detrapping kinetic constants have been derived for the trap site types studied in this manuscript.

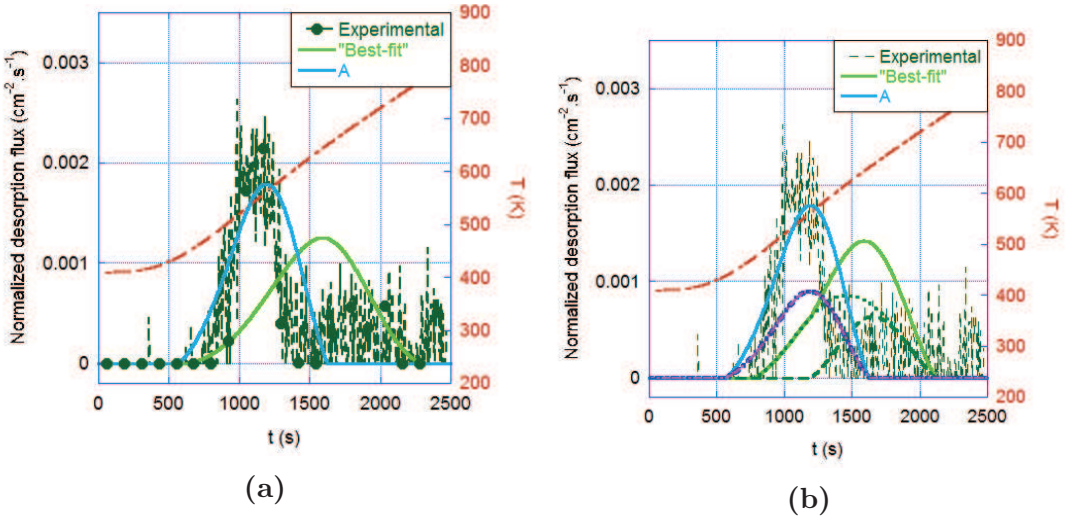

Fig. 4.30 (a) "Normalized-TP" PDS experimental and simulated TDS desorption spectra using the derived ^{2}H diffusion coefficient (Table 4.2, "This study") or "A" (Table 4.4) and (b) simulated spectral contributions with these diffusion coefficients. In (b) -0 and -L refers to the origin of the spectral contribution, respectively either the $x = 0$ face (charged face) or the $x = L$ face (non-charged) face.

iii. ***Effect of grain boundaries***

One of the primary hypotheses made in the developed model is that grain boundaries do not have a significant impact on the diffusion and trapping of hydrogen in the studied alloys. This hypothesis was verified through the comparison of experimental A600 polycrystalline PDS and single crystal model TDS spectra (i) immediately after cathodic charging (Fig. 4.5), (ii) after 6 h aging at room temperature (Fig. 4.12) and (iii) after high temperature aging (Fig. 4.19).

In the previous section the diffusion coefficient for deuterium in the model polycrystalline "pure diffusion system" material was derived and validated. If grain boundaries played a significant role in the diffusion of deuterium in A600, their role should be reflected in the derived diffusion coefficient; therefore, a single crystal experimental TDS spectrum should not be in good agreement with a spectrum simulated using these values.

It would be prudent to test this pre-exponential constant (D_0) and activation energy (E_D) combination for an A600-like single crystal in order to further validate or disprove the assumption on grain boundary diffusion in the model materials studied. A comparison of experimental single crystal spectra and simulated desorption spectra using the derived diffusion parameters seen in Table 4.3 will be carried out in the following short sections for spectra (i) immediately after deuterium charging, (ii) during and after prolonged aging (6 h) at room temperature and (iii) during prolonged aging at high temperature.

iii.a. *Simulation immediately after deuterium charging*

An experimental single crystal TDS spectrum immediately after deuterium charging was simulated using the diffusion coefficient parameters seen in Table 4.3. The normalized simulated TDS spectrum is compared to its experimental counterpart for an A600-like single crystal, see Fig. 4.31a. The simulated spectrum reproduces overall very well the experimental spectrum, with only a slight deviation in intensity and temperature of maximum desorption (T_m). These differences can be explained by the error on the derived D_0 and E_D parameters (Table 4.4 and Fig. 4.31b). Furthermore, it should be noted that the experimen-

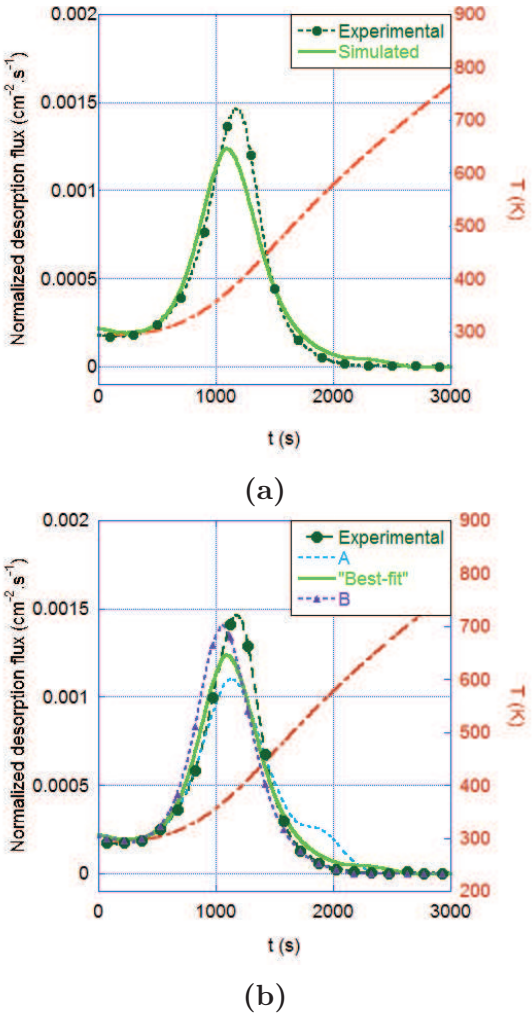

Fig. 4.31 "Normalized" A600-like single crystal experimental TDS spectrum immediately after deuterium charging as compared to simulated TDS spectra (a) using the derived diffusion coefficient parameters determined for A600-PDS (Table 4.3) and (b) using the maximum tolerated error parameters associated with "A" and "B" from Table 4.4.

tal spectrum is reproduced very well at low temperatures where grain boundary diffusion should play a more significant contribution to diffusion phenomena [65].

This comparison seems to back-up the earlier conclusion from experimental spectral comparison, that hypothetical short-circuit diffusion at grain boundaries of alloy 600 is not reflected in TDS analysis but should nonetheless be looked at again by comparing experimental and simulated TDS spectra acquired from experiments designed to highlight H-grain boundary interactions.

iii.b. *Simulation during and after room temperature aging*

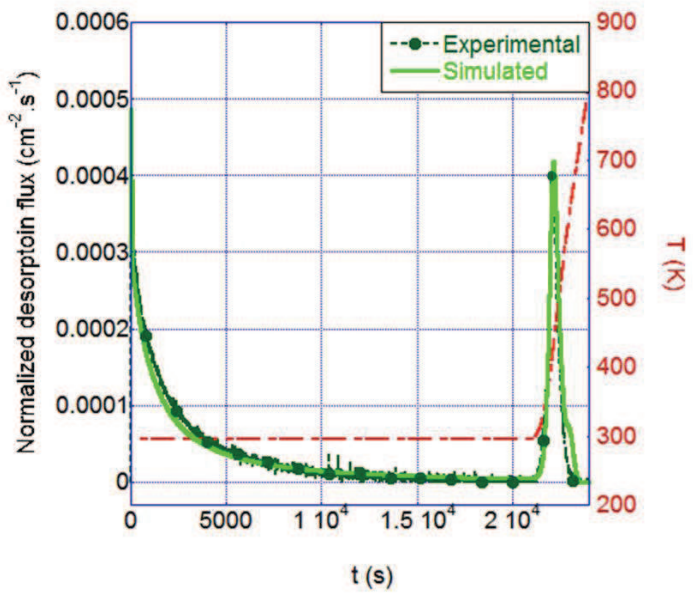

Fig. 4.32 "Normalized" experimental "hybrid" desorption spectrum acquired for an A600-like single crystal aged 6 h in TDS at room temperature ($\approx$ 295 K) followed by TDS analysis (ϕ = 10 K.min^{-1}) as compared to its simulated TDS spectrum using the derived diffusion coefficient parameters (Table 4.3) determined for A600-PDS model materials.

It seems to be a general consensus in literature that [if present] the effect of short circuit diffusion along the grain boundary network should be highlighted at low temperatures [65, 67] this has also been demonstrated experimentally [53, 54, 57]. It could be imagined that therefore H-grain boundary interactions could be highlighted by an extended "aging" at room temperature, a temperature thought to favorize grain boundary diffusion over interstitial diffusion.

Fig. 4.32 shows the experimental "hybrid" desorption spectrum (prolonged isotherm with desorption flux monitoring followed immediately by TDS analysis (ϕ = 10 K.min^{-1}) with desorption flux monitoring) for an A600-like s.c model material as compared to its simulated spectrum using the derived diffusion coefficient parameters for a [polycrystalline] A600-PDS model material (Table 4.3). The simulated "hybrid" spectrum reproduces very well the experimental spectrum for both the low temperature isothermal period

($t \leq 2.1\ 1^4$ s) and the TDS analysis ($\phi = 10$ K.min^{-1}). Based upon what is written in the literature concerning preferential grain boundary diffusion of hydrogen at low temperatures, the effect of grain boundaries was anticipated to be highlighted during this analysis, however it was not.

This result once again confirms the assumption that grain boundaries may be neglected as a short-circuit diffusion network in the analyzed model materials. To be sure a final comparison between single crystal experimental and simulated desorption spectrum, will be analyzed for the temperature transient and high temperature isotherm.

iii.c. *Simulation during high temperature aging*

The first 5000 seconds of a high temperature (409 K) aging spectrum have been simulated and compared to the corresponding experimental spectrum in Fig. 4.33. During the first 2000 s, some important changes take place in the system: (i) the temperature is relatively stable, at approximately 295 K, for the first 500 s before (ii) quickly increasing from room temperature to 409 K in less than 1300 s and finally (iii) once the temperature has stabilized it is held at 409 K for the desired duration (the entire aging period is not shown in Fig. 4.33).

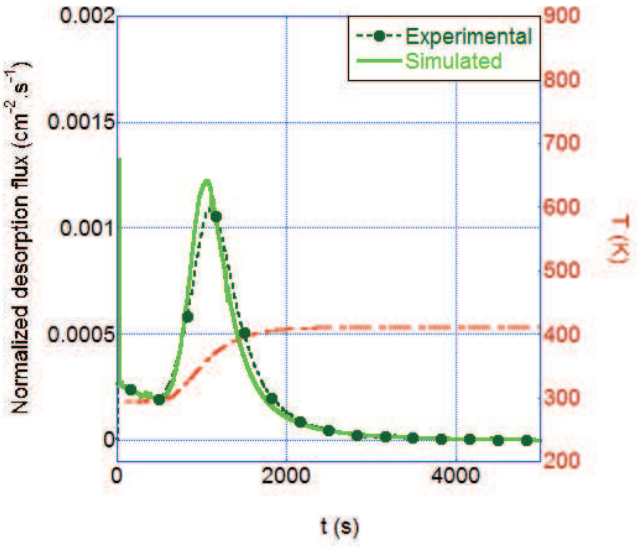

Fig. 4.33 "Normalized" isothermal spectrum acquired on desorption A600-like single crystal aged 6 h in TDS at high temperature ($\approx$ 409 K) as compared to its simulated TDS spectrum using the derived diffusion coefficient parameters (Table 4.3) determined for A600-PDS model materials. Only the first 5000 s of the experimental and simulated desorption spectra are shown in this figure to provide a better view of the reproduction of the first desorption peak.

Some remarks can be made concerning the simulated and experimental desorption spectra. Firstly, during the first 500 seconds of desorption monitoring (while the system is at room temperature), the simulated desorption flux mirrors exactly the experimental desorption flux intensity and shape. Then, at about 1200 s ($T \approx 390$ K) a desorption peak is produced on the experimental spectrum

during the temperature ramp. This peak is well reproduced in simulation using the derived diffusion coefficient constants (Table 4.3). Finally, as the temperature stabilizes at 409 K, the experimental desorption flux decreases; this decline is once again emulated in simulation.

The overall very good reproduction of the experimental desorption spectrum for three spectral sections: (i) room temperature isotherm ($T \approx 295$ K, $0 \leq t \leq 500$ s), (ii) temperature transient ($295 \leq T \leq 409$ K, $500 \leq t \leq 1900$ s) and (iii) high temperature isotherm ($T = 409$ K, $t \geq 1900$ s), seems to provide a final response confirming the validity of the major simplification that has been made in the numerical model: the disregard of grain boundaries.

4.3.1.2 ^{2}H diffusion in SS316L

The same approach for the derivation of diffusion coefficient parameters, (i) pre-exponential constant (D_0) and (ii) activation energy (E_D), was carried out for SS316L pure diffusion model materials. The diffusion coefficient data determined by Forcey *et al.* [46] for commercial 316L stainless steel was used as the initial input parameters for the numerical routine. The "best-fit" spectrum as compared with experimental TDS spectrum and simulated TDS spectra constructed using literature diffusion coefficients [45, 46] can be seen in Fig. 4.34. The derived diffusion coefficient parameters are gathered in Table 4.5.

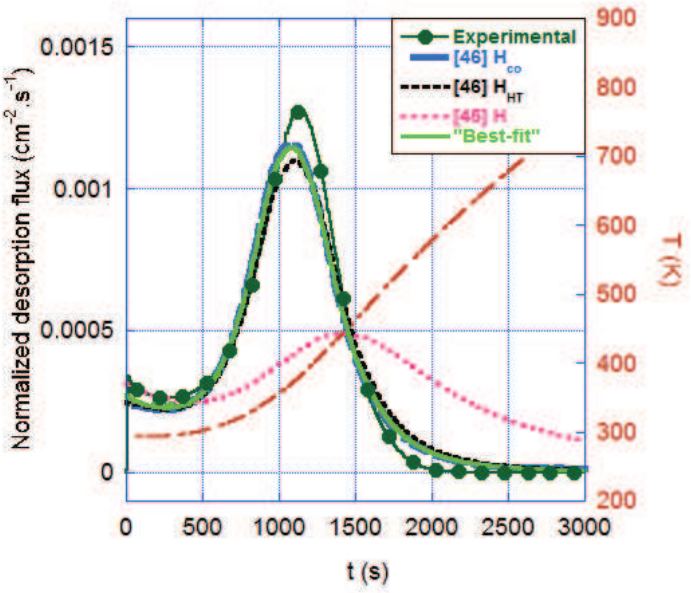

Fig. 4.34 "Normalized" experimental, literature simulated [45, 46] and "best-fit" TDS spectra ($\phi = 10$ K.min^{-1}) for SS316L pure diffusion system model material immediately after ^{2}H charging (Table 3.6).

Table 4.5 Derived diffusion coefficients for a SS316L pure diffusion system (PDS) model material.

Material type	T range (K)	D_0 ($cm^2.s^{-1}$)	E_D ($kJ.mol^{-1}$)	D at 298 K ($cm^2.s^{-1}$)	D at 409 K ($cm^2.s^{-1}$)
SS316L-PDS	294 - 800	$(1 \pm 0.8)\ 10^{-3}$	45 ± 3	$\approx 1.3\ 10^{-11}$	$\approx 1.8\ 10^{-9}$

After derivation of the diffusion coefficient, it was verified by simulating a 6 h aged room temperature spectrum. Normalized spectral comparisons between the simulated and experimental "hybrid" spectra result in no clear difference in simulations using data from Forcey *et al.* [46] and the diffusion parameters derived in this study, Fig. 4.35.

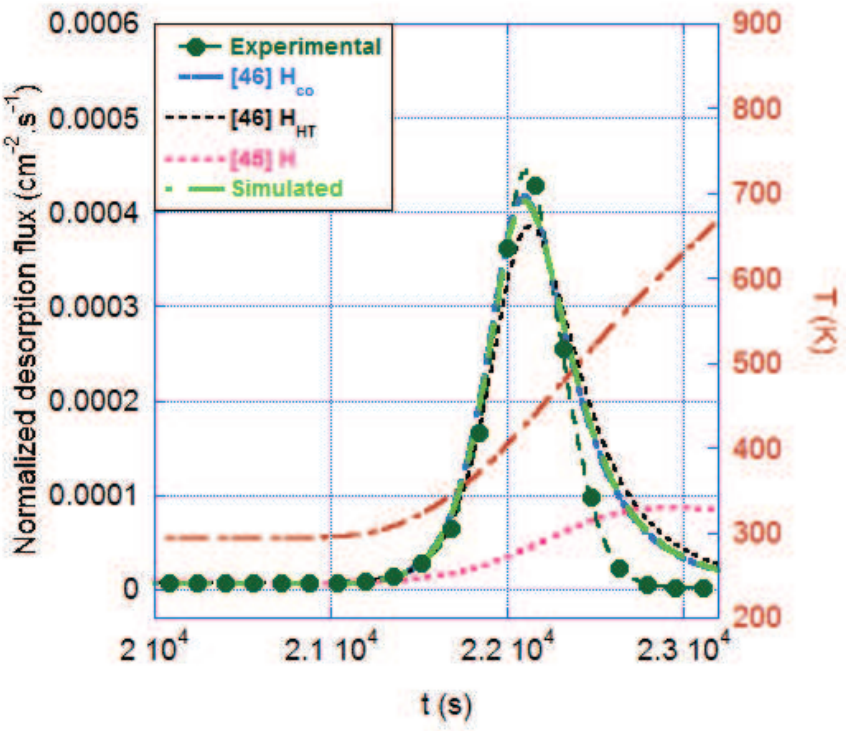

Fig. 4.35 Normalized experimental and simulated [45, 46] desorption spectra for SS316L-PDS model materials for 6 h of aging at room temperature (294 K) followed by TDS analysis ($\phi = 10$ K.min^{-1}).

4.3.1.3 Summary of simulation results for ^{2}H diffusion in A600 and SS316L

An approach coupling experimental TDS spectral data with a numerical fitting routine was used to derived diffusion coefficient parameters: (i) D_0 and (ii) E_D. The derived diffusion coefficient parameters are gathered in Table 4.6.

Table 4.6 Derived diffusion coefficients for A600 and SS316L pure diffusion system (PDS) model materials.

Material type	D_0 ($cm^2.s^{-1}$)	E_D ($kJ.mol^{-1}$)	D at 298 K ($cm^2.s^{-1}$)	D at 409 K ($cm^2.s^{-1}$)
A600-PDS	$(1 \pm 0.5)\ 10^{-2}$	45 ± 5	$\approx 1.3\ 10^{-10}$	$\approx 1.8\ 10^{-8}$
SS316L-PDS	$(1 \pm 0.8)\ 10^{-3}$	45 ± 3	$\approx 1.3\ 10^{-11}$	$\approx 1.8\ 10^{-9}$

The derived parameters were then tested by simulating "hybrid" desorption spectra, i.e. room temperature aging (294 ± 2 K) and/or high temperature (409 ± 2 K) aging desorption spectra followed by classical TDS analysis. If the diffusion parameters reproduced the aged "hybrid" spectra, the coefficient parameters were considered validated.

Furthermore, the hypothesis that short-circuit diffusion in the grain boundary network can be considered negligible or does not have a significant enough effect on experimental TDS spectra has been demonstrated as valid for the extent of this study. Room temperature isothermal agings were anticipated to possibly highlight a short-circuit diffusion mechanism [54, 65] but simulations using the derived diffusion coefficient (Table 4.6) determined over a large range of temperatures (from approximately 294 K to approximately 900 K) reproduce these isothermal periods and predict the proceeding TDS spectra. Moreover, the diffusion coefficient determined from A600 pure diffusion system (polycrystalline material) model materials simulated very well the room temperature aging, high temperature aging, and TDS desorption spectra for the A600-like single crystal. This last point demonstrates that the effect of grain boundaries on the diffusion of hydrogen in alloy 600 can be considered negligible.

Now that a set of diffusion coefficient parameters (Table 4.6) specific to the pure diffusion type model material have been determined and verified, the next phase of this study can be undertaken; that is the derivation of deuterium trapping and detrapping kinetic constants associated with interactions taking place at chromium carbides and dislocations.

4.3.2 Deriving kinetic trapping and detrapping constants

The diffusion coefficient parameters determined in a previous section (Table 4.6) will be injected as input parameters when deriving the kinetic trapping and detrapping constants for (i) chromium carbides in A600 and (ii) dislocations in A600 model materials. These model materials were fabricated in a way as to isolate the desired TS and therefore the differences in pure diffusion and these diffusion and trapping spectra can be attributed with certainty to a trapping mechanism at these isolated sites.

A "trapping contribution" was isolated after only one type of experimental analysis: "hybrid" high temperature isothermal analysis. A model high temperature aged spectrum will be fitted using the numerical code, allowing for the determination of a set of pre-exponential constants and activation energies associated with trapping (k_0 and E_k) and detrapping (p_0 and E_p). Furthermore, a [theoretical] trap site density (N) will be derived when possible; the derivation of this parameter will be discussed in detail later in this section. The other model experimental spectra will then be simulated and the validity of these kinetic constants and trap site density will be checked.

This section will be split into two parts: (i) addressing trapping interactions at chromium carbides in A600 and (ii) addressing trapping interactions at dislocations in A600 model materials.

4.3.2.1 ^{2}H trapping at chromium carbides (Cr_7C_3)

i. ***Inter- and intragranular Cr_7C_3***

A trapping contribution at chromium carbides was isolated on the TDS spectra aged 6 h and 9 h at 409 K, see Fig. 4.20 (as total TDS desorption integrated flux and maximum desorption peak temperature did not evolve with increased aging time). Using the numerical code presented in Chapter 3, injecting the experimental parameters ($T(t)$, L etc.) and injecting the previously determined diffusion coefficient parameters (Table 4.3) the TDS spectrum aged 6 h at high temperature was adjusted and the kinetic constants (pre-exponential constant and activation energies) were derived. These values are gathered in Table 4.7.

The derived constants (Table 4.7) were then submitted to a validation procedure by simulating the experimental TDS spectra obtained after 3 h (Fig. 4.37a) and 9 h (Fig. 4.37b) of aging at 409 K. The simulated TDS spectra reproduce very well the experimental spectra in: (i) spectral form, (ii) maximum desorption temperature and (iii) overall intensity. The peak intensity difference between the simulated and experimental spectra seen in Fig. 4.37a is addressed by the error in the derived parameter values (Table 4.3 and Table 4.7).

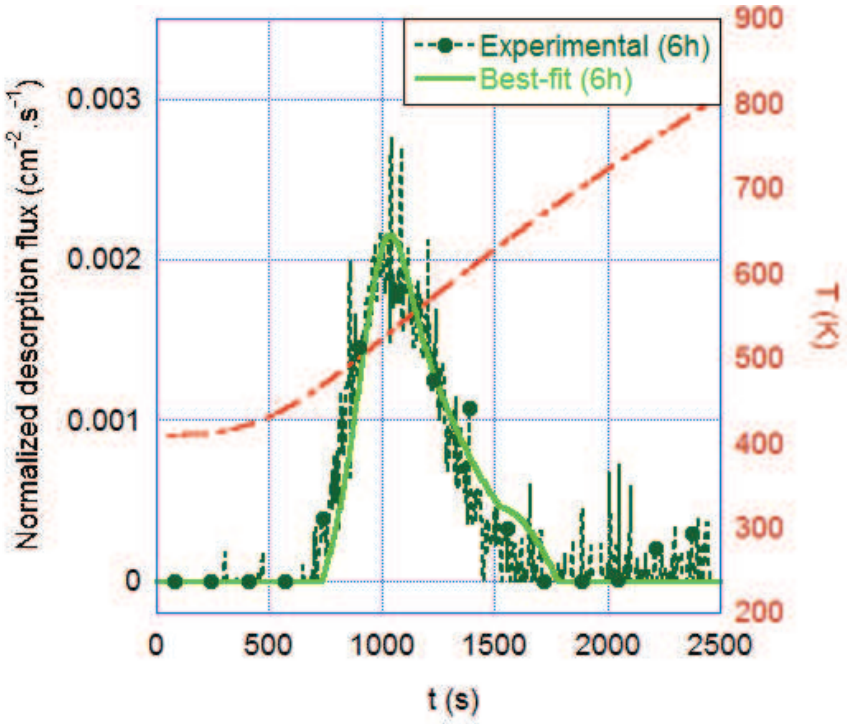

Fig. 4.36 "Normalized-TP" experimental and "best-fit" TDS spectra for trapping at chromium carbides (Cr_7C_3, according to TEM diffraction patterns, see Chapter 3) in A600 after aging 6 h at 409 K.

Table 4.7 Derived "best-fit" trapping (k) and detrapping (p) kinetic constants for trapping at chromium carbides located both inter- and intragranularly in A600. These values are coupled with the diffusion constant presented in Table 4.3.

Cr_7C_3-IIC Trapping (k)		Cr_7C_3-IIC Detrapping (p)	
k_0 (s^{-1})	E_k ($kJ.mol^{-1}$)	p_0 (s^{-1})	E_p ($kJ.mol^{-1}$)
$(1.5 \pm 0.2)\ 10^7$	50 ± 4	$(1.5 \pm 0.2)\ 10^6$	80 ± 4

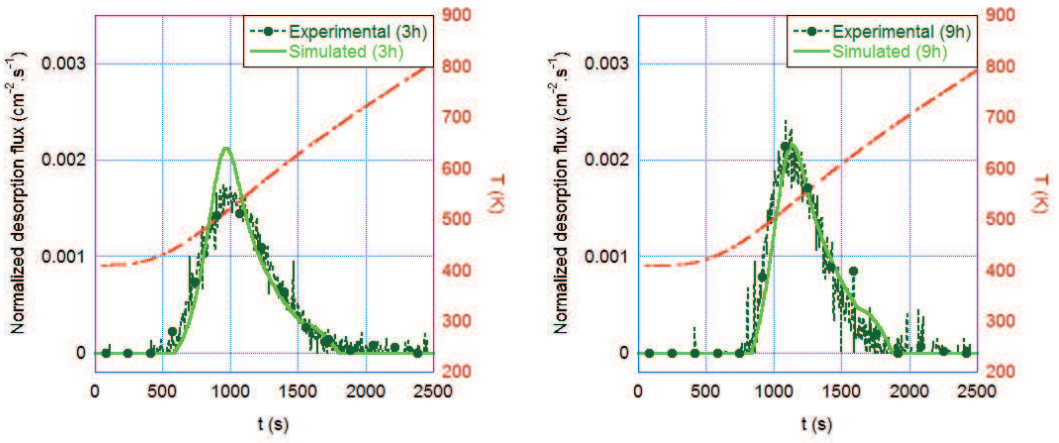

(a) **(b)**

Fig. 4.37 Experimental and simulated "normalized-TP" TDS spectra (ϕ = 10 K.min^{-1}) after (a) 3 h of aging at 409 K and (b) 9 h of aging at 409 K, used for validation of the derived trapping/detrapping parameters.

To fit and simulate TDS spectra, a trap site density (N) was required, Eq. 2.11 [107]. This value was fixed as 1.0 10^{-5} mol TS.mol A600^{-1}. This assumed value cannot be validated by normalized spectra as, except for very low values (less than 0.2 10^{-5} mol TS.mol A600^{-1}), this parameter has little to no effect on simulated TDS (i) desorption peak placement, (ii) spectral form, and (iii) normalized spectral intensity, see Fig. 4.38. This figure shows simulated TDS spectra after 6 h of HT aging with TS densities (n) ranging from 0.01 10^{-5} TS.mol A600^{-1} to 100.0 10^{-5} TS.mol A600^{-1} as compared to their experimental counterpart. As trap site density (N) is decreased to values less than [or equal to] 0.2 10^{-5} TS.mol A600^{-1} a shift in desorption peak placement and spectral form is observed, this evolution creates similarities between it and that of a simulated PDS TDS spectrum for the same experimental conditions (see Fig. 4.29). This may indicate that there is a critical TS density for chromium carbides to have an experimentally observable impact on diffusion in alloy 600. As a "precise" trap site density cannot be determined from normalized desorption spectra it would be necessary to work with quantified TDS spectra when this parameter (N) needs to be assessed.

As discussed in Sec. 4.1 there was a large variation in the total quantity of deuterium desorbed over the course of experimental analysis for most of the model materials, see Fig. 4.1, and therefore analysis of experimental results could generally be done using normalized spectra. Diffusion and trapping model materials with chromium carbides did not present this large scatter and therefore the TS density may be addressed from the quantified TDS spectra. Simulating quantified TDS spectra necessitates imposing a hydrogen surface concentration (μ_0) during

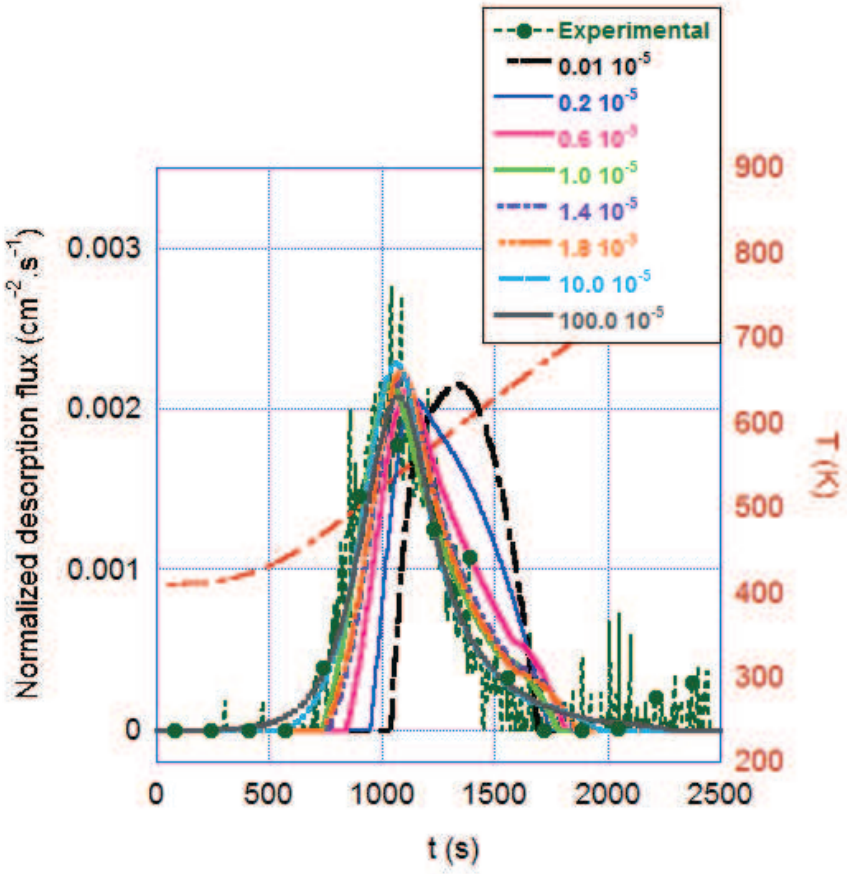

Fig. 4.38 (a) "Normalized-TP" experimental and simulated TDS spectrum (aged 6 h at 409 K, $\phi = 10$ K.min^{-1}) for a trap site densities (n) ranging from 0.01 10^{-5} mol TS.mol A600^{-1} to 100.0 10^{-5} mol TS.mol A600^{-1}.

the charging step.

This parameter was determined through using a similar numerical fitting routine, geared at determining the necessary imposed surface concentration to result in the total amount of deuterium desorbed from the specimen during desorption analysis.

Fig. 4.39a shows simulated TDS spectra for imposed TS densities ranging from 0.01 10^{-5} mol TS.mol A600^{-1} to 100.0 10^{-5} mol TS.mol A600^{-1} as compared to its experimental counterpart. Fig. 4.39b shows the spectra having a less intense desorption flux as compared to its experimental counterpart. These comparisons show the effect of trap site density (N) on TDS spectra. As TS density is increased the spectral intensity increases but for TS densities greater than or equal to 0.6 10^{-5} mol TS.mol A600^{-1} the temperature of maximum desorption flux is quasi-unchanged. For trap site densities ranging from 0.8 10^{-5} mol TS.mol A600^{-1} to 1.4 10^{-5} mol TS.mol A600^{-1} the overall spectral reproduction, (i) form, (ii) maximum desorption temperature and (iii) spectral intensity are satisfying, with a clear "best-fit" for (1.0 $\pm$ 0.1) 10^{-5} mol TS.mol A600^{-1}.

After fitting a trap site density for the model material presenting inter- and intragranular Cr_7C_3 it may be verified by simulating quantified TDS desorption spectra for the different aging times (3 h and 9 h at 409 K) and comparing them to their quanti-

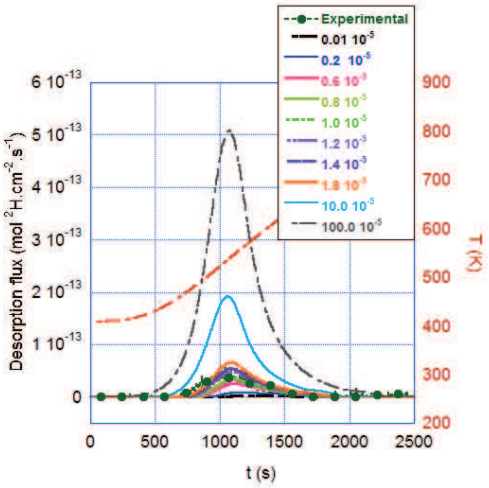

(a)

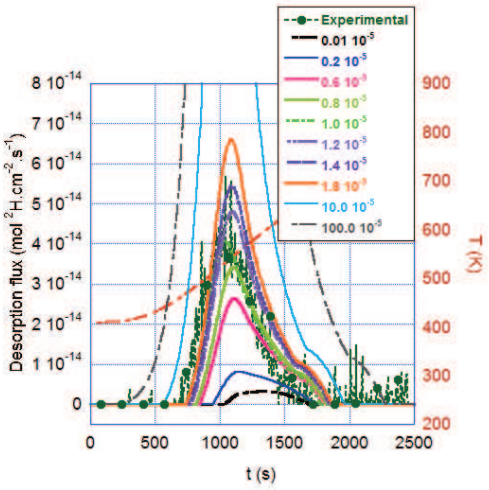

(b)

Fig. 4.39 Quantified experimental and simulated TDS spectrum (aged 6 h at 409 K, $\phi = 10$ K.min^{-1}) for a trap site densities (N) ranging from 0.01 10^{-5} to 100.0 10^{-5} mol TS.mol A600^{-1}. Figure (a) shows all simulations, and (b) shows a zoom of the experimental spectrum.

fied experimental TDS spectra. This has been done and the results may be seen in Fig. 4.40. These simulated quantified spectra reproduce extremely well the experimental TDS spectra for all aging times; this furthermore validates the derived trap site density ($N = (1.0 \pm 0.1)\ 10^{-5}$ mol TS.mol A600^{-1}) and trapping and detrapping kinetic constants (pre-exponential constants and activation energies (Table 4.7)) associated with the model materials containing mainly inter- and intragranular chromium carbides as potential trap sites.

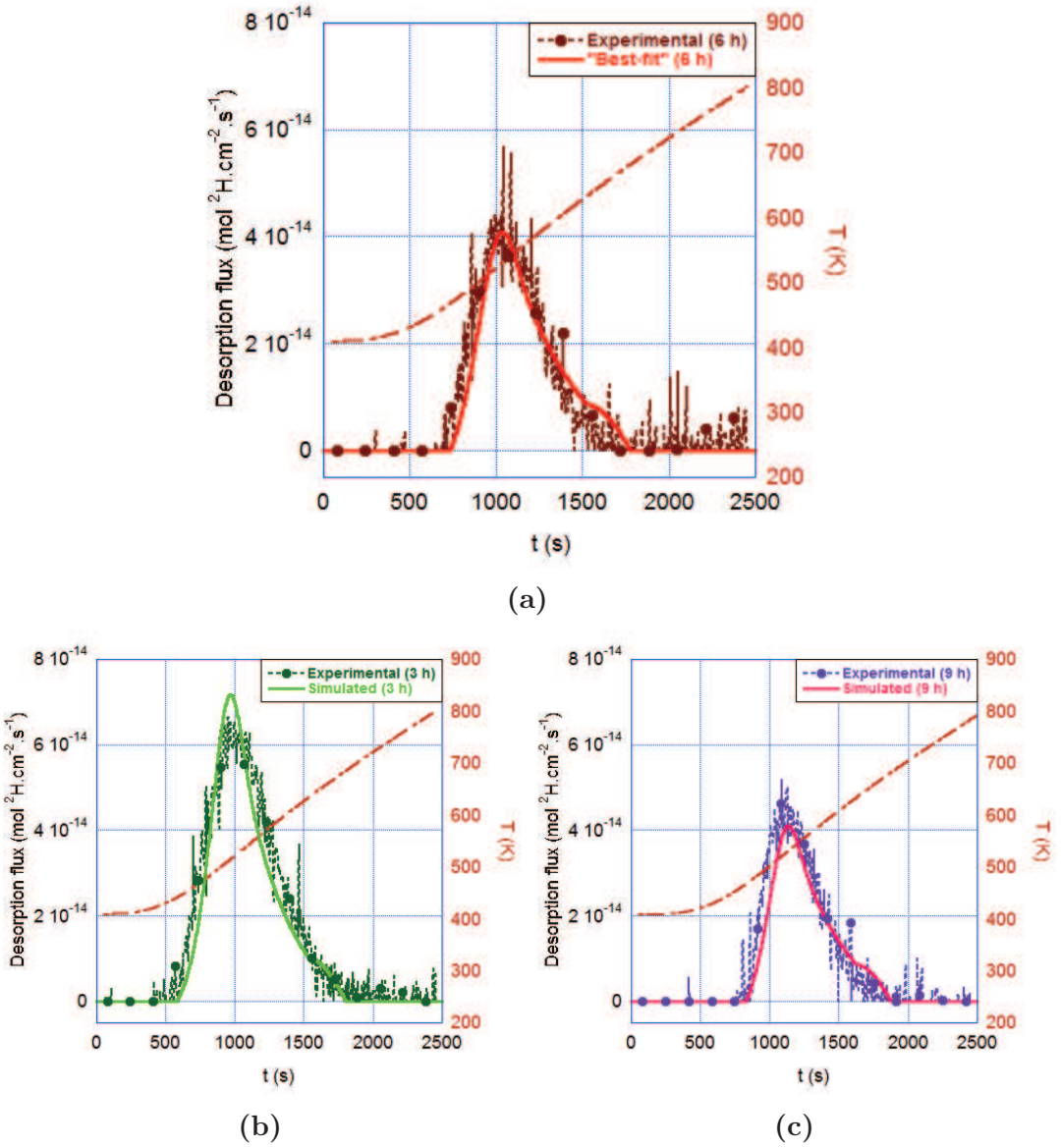

Fig. 4.40 Quantified experimental, fitted and simulated TDS spectra for high temperature agings (409 K) of (a) 6 h, (b) 3 h and (c) 9 h using the derived diffusion and trapping/detrapping at chromium carbides parameters (Table 4.3 and Table 4.7) and a trap site density (n) of 1.0 10^{-5} mol TS.mol A600^{-1}.

ii. ***Cr_7C_3 along grain boundaries***

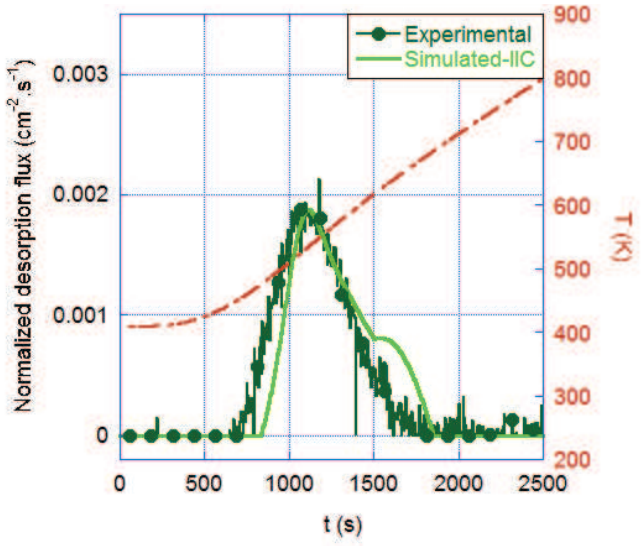

Fig. 4.41 "Normalized-TP" experimental TDS spectra for A600-DTS-GBC and a simulated (Simulated-IIC) desorption spectra for a sample aged 6 h at 409 K using the kinetic constants seen in Table 4.7.

A second type of diffusion and trapping system model material with chromium carbides was fabricated; this material had chromium carbides preferentially located along grain boundaries (A600-DTS-GBC). Before using the same "best-fit" approach to derive the diffusion and trapping kinetic constants the derived kinetic constants for inter- and intragranular chromium carbides was tested. A comparison of these spectra can be seen in Fig. 4.41. The "normalized-TP" simulated TDS spectrum using the kinetic trapping and detrapping constants derived for a material with both inter- and intragranular Cr_7C_3 reproduces roughly the experimental spectrum. This can be due to the evolution of the evolution of the chromium carbide's trapping properties depending on localization.

Therefore the same "best-fit" approach was applied for the derivation of kinetic trapping and detrapping constants for specimen with chromium carbides along grain boundaries as the major trap site type. The normalized "best-fit" simulated TDS spectra can be seen in Fig. 4.42. The derived trapping and detrapping kinetic constant parameters can be seen in Table 4.8. A trap site density of 2.5 10^{-6} mol TS.mol A600^{-1} was imposed in these simulations, and the quantified TDS desorption spectrum "best-fit" as compared to its experimental counterpart can be seen in Fig. 4.43. Compared to DTS-IIC samples, similar trapping and detrapping activation energies were determined with these sites whereas different "jump proabablities" (k_0 and p_0) were found, but due to the lack of experimental data these kinetic constants were not able to be checked experimentally. These differences may be linked to the relative interface coherence of the carbides in function of their location, in volume or along grain boundaries.

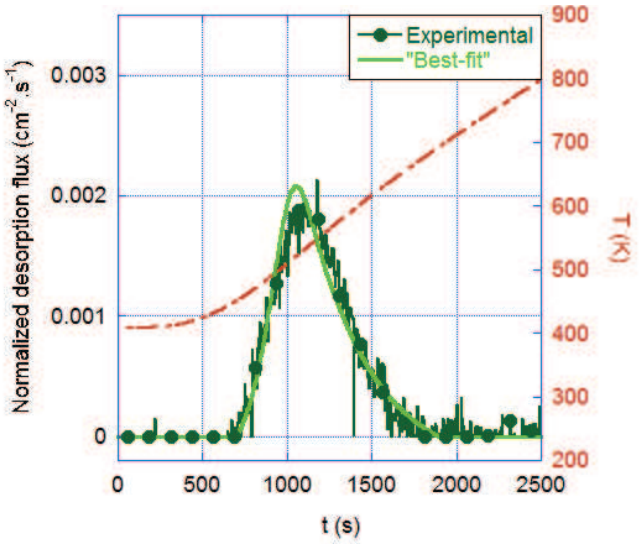

Fig. 4.42 "Normalized-TP" experimental and "best-fit" TDS spectra for diffusion and trapping in A600 with chromium carbides located along the grain boundaries after 6 h of agin at 409 K. A trap site density of 2.5 10^{-6} mol TS.mol A600^{-1} was determined from simulation.

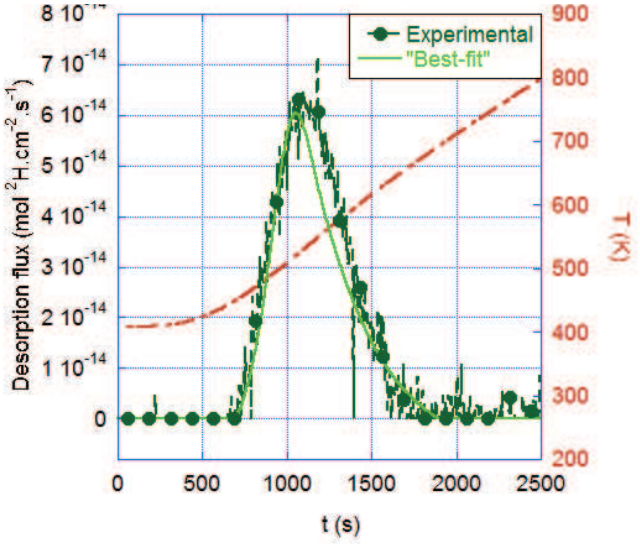

Fig. 4.43 Quantified experimental and "best-fit" TDS spectra for diffusion and trapping in A600 with chromium carbides located along the grain boundaries after aging 6 h at 409 K. A trap site density of 2.5 10^{-6} mol TS.mol A600^{-1} was imposed for this simulation.

Table 4.8 Derived "best-fit" trapping (k) and detrapping (p) kinetic constants for trapping at chromium carbides (Cr_7C_3, according to TEM diffraction patterns, see Chapter 3) along grain boundaries in A600. These values are coupled with the diffusion constant derived parameters presented in Table 4.3.

Cr_7C_3-GBC Trapping (k)		Cr_7C_3-GBC Detrapping (p)	
k_0 (s^{-1})	E_k ($kJ.mol^{-1}$)	p_0 (s^{-1})	E_p ($kJ.mol^{-1}$)
$(1.5 \pm 0.2)\ 10^8$	50 ± 4	$(1.5 \pm 0.2)\ 10^5$	78.0 ± 4.0

4.3.2.2 ^2H trapping at dislocations

A trapping contribution at dislocations was isolated on the high temperature (409 K) aged TDS spectra acquired using the model materials with dislocations as its major trap site type, see Fig. 4.22. As two high temperature aging spectra (6 h and 9 h aging) were acquired for the A600-DTS-D-40T model materials, one duration will be used for fitting and the second for simulation to test the kinetic constant combination derived from fitting. The 9 h aged spectrum was used for fitting using the numerical routine injecting the experimental conditions and derived diffusion coefficient for a PDS material (Table 4.3). The derived "best-fit" spectrum as compared to its experimental counterpart can be seen in Fig. 4.44 and the associated trapping and detrapping kinetic constants are shown in Table 4.9. These constants were coupled with an assumed trap site density (N) of 1 10^{-4} mol TS.mol $A600^{-1}$. This trap site density was chosen based upon the reproduction of the spectral shape, as earlier in this chapter (Sec. 4.3.2.1) it had been shown (with "normalized-TP" desorption spectra for A600-DTS-IIC model materials) that this value has some effect on the spectral form, and while many (elevated) trap site densities will reproduce the desorption peak placement (in temperature) only an

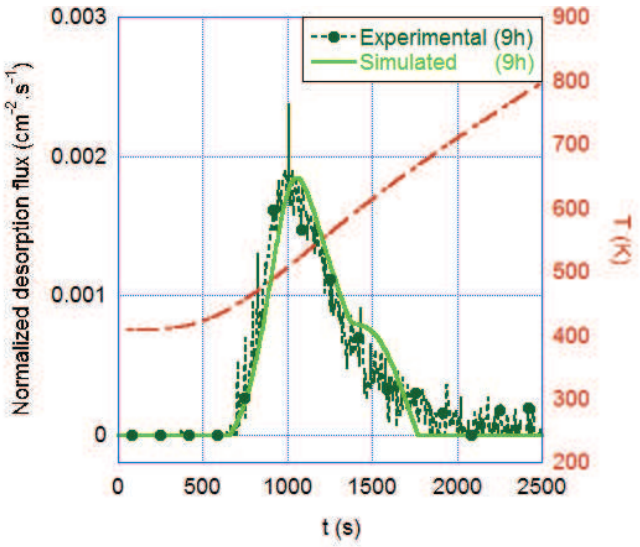

Fig. 4.44 "Normalized-TP" experimental and "best-fit" TDS spectra (Table 4.9) for trapping at dislocations in A600 after aging 9 h at 409 K.

imposed value close to the derived value will result in a good reproduction of the spectral form (i.e. width, desorption shoulder linked to ^{2}H desorption from the $x = L$ face).

Table 4.9 Derived "best-fit" trapping (k) and detrapping (p) kinetic constants for trapping at dislocations in A600. These values are coupled with the diffusion constant derived parameters presented in Table 4.3.

Dislocations Trapping (k)		Dislocations Detrapping (p)	
k_0 (s^{-1})	E_k ($kJ.mol^{-1}$)	p_0 (s^{-1})	E_p ($kJ.mol^{-1}$)
$(1.5 \pm 0.2)\ 10^6$	42 ± 4	$(1.5 \pm 0.2)\ 10^6$	76 ± 4

The derived diffusion coefficient, trapping and detrapping kinetic constants and trap sites density combination was then used to simulate the experimental 6 h high temperature aged DTS TDS spectrum (Fig. 4.45). This figure recreates rather well the experimental TDS desorption spectrum. This set of obtained values for the kinetic constants was considered validated at this point. Unfortunately the trap site density (N) cannot be validated from these experimental and simulation results as there was too much variation between the total spectral integrals between tests in order to perform qualitative simulations.

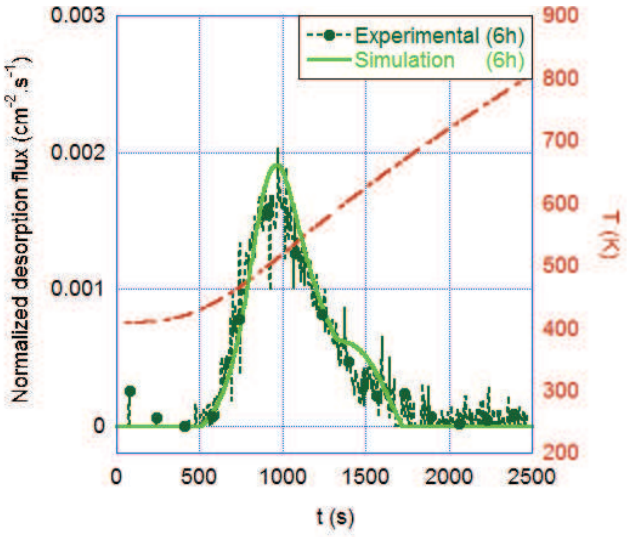

Fig. 4.45 Experimental and simulated "normalized-TP" desorption spectra for trapping at dislocations in A600 after aging 6 h at 409 K. Simulation was done using the constants seen in Table 4.9. These values are coupled with the diffusion constant presented in Table 4.3.

4.3.2.3 Summary of simulation results and derivation of kinetic trapping and detrapping constants

Looking back on Sec. 4.2.2.3, trapping contributions (at chromium carbides and dislocations) were isolated on "hybrid" desorption spectra after aging at high temperature (409 K). Then in Sec. 4.3.2 a set of kinetic constants associated with deuterium trapping and detrapping at chromium carbides (IIC and GBC) and dislocations were derived from the "hybrid" experimental desorption spectra, specifically using the isolated TDS spectral contribution, through the use of the numerical fitting routine presented in Chapter 3. After derivation, the set of trapping and detrapping kinetic constants was tested by simulating a different experimental desorption spectra to verify their applicability. The derived kinetic constant parameters are gathered in Table 4.10.

Table 4.10 Derived "best-fit" trapping (k) and detrapping (p) kinetic constants for trapping at chromium carbides (Cr_7C_3, according to TEM diffraction patterns, see Chapter 3) located both inter- and intragranularly (IIC) and at primarily grain boundaries (GBC) and dislocations in A600. These values are coupled with the diffusion constant presented in Table 4.3.

	k_0 (s^{-1})	E_k ($kJ.mol^{-1}$)	p_0 (s^{-1})	E_p ($kJ.mol^{-1}$)	N (mol TS.mol A600^{-1})
Cr_7C_3-IIC	$(1.5 \pm 0.2)\ 10^7$	50 ± 4	$(1.5 \pm 0.2)\ 10^6$	80 ± 4	$(1 \pm 0.2)\ 10^{-5}$ [a]
Cr_7C_3-GBC	$(1.5 \pm 0.2)\ 10^8$	50 ± 4	$(1.5 \pm 0.2)\ 10^6$	78 ± 4	$\approx 2.5\ 10^{-6}$ [b]
Dislocations $\epsilon = 40$ %	$(1.5 \pm 0.2)\ 10^6$	42 ± 4	$(1.5 \pm 0.2)\ 10^6$	76 ± 4	$\approx 1\ 10^{-4}$ [b]

[a] determined from quantified simulations
[b] imposed in simulations

4.4 Brief conclusions

In this chapter the major experimental results were presented in Sec. 4.2. Analysis of these experimental results was somewhat inconclusive as trapping contributions proved difficult to isolate. The only experimental desorption spectra that clearly seem to have demonstrated a trapping effect, were "hybrid" spectra having been aged at high temperature (409 K). This high temperature aging allowed for desorption of a large percentage of the "interstitial" ^{2}H contribution leaving primarily "trapped" deuterium which was released at higher temperatures during TDS analysis. Furthermore, purely based upon these experimental results it would be difficult to determine the diffusion coefficient or trapping and detrapping kinetic constants with any certainty.

It was clear that a numerical simulation aid was necessary for a thorough analysis. Using the developed numerical code and simulation method (presented in Chapter 3) coupled with experimental desorption data (Sec. 4.2) the diffusion coefficient parameters (D_0 and E_D) for interstitial hydrogen diffusion in A600 ans SS316L were able to be determined from experimental TDS results for a pure diffusion system. These coefficient parameters were then tested though the simulation of "hybrid" desorption spectra and spectra acquired under different experimental conditions. The validated hydrogen diffusion coefficient parameters are gathered in Table 4.6. Once validated, the diffusion coefficient parameters served as input parameters for the derivation of trapping and detrapping kinetic constant parameters (k_0, E_k, p_0 and E_p) from experimental desorption spectra, on which a trapping contribution had been isolated. Once again the values were tested by simulating other desorption spectra to verify an adequate spectral reproduction. The derived kinetic trapping and detrapping parameters associated with chromium carbides and dislocations in A600 are collected in Table 4.10.

One important input parameter, necessary to the numerical model, was not always able to be verified using this method; this was the trap site density (N mol TS.mol A600^{-1}). The incapability to determine this parameter is not due to a shortcomings in simulation, but can be attributed to the scatter in experimental total amount of desorbed deuterium (Fig. 4.1). Although trap site density could not always be validated, some trust may be placed in the determined value as spectral form is extremely dependent on this parameter (Fig. 4.38). A good reproduction of experimental DTS experimental desorption spectra could not be achieved without the imposition of a trap site density similar to the "real" trap site density.

Furthermore, this chapter has demonstrated the necessity for coupling experimental spectral analysis on model materials with a numerical simulation method for the derivation of diffusion and trapping and detrapping information. Without using an iterative approach some misleading conclusions may be drawn and can lead to mistaken analysis.

Chapter 5

Discussion and Perspectives

In the previous chapters an approach coupling an experimental analysis with numerical simulation was presented, discussed and used to determine diffusion coefficients and trapping and detrapping kinetic constants was described. This chapter will be broken down into several sections first discussing in-depth some important findings and comparing them to what information exists in literature: this will focus on deuterium (i) diffusion and (ii) trapping in the studied alloys. Then some (iii) technical and (iv) scientific perspectives will be discussed.

5.1 ^{2}H Diffusion in A600 and SS316L

In this study, the diffusion coefficients of deuterium in two austenitic alloys were derived over a large temperature range (294 - 800 K). Thermal desorption mass spectroscopy spectra were acquired in the range of 294 K to 1300 K but at temperatures greater than 800 K no deuterium desorption flux was detected. The derivation of diffusion coefficient parameters, D_0 and E_D (assuming an Arrhenius relationship with temperature), was done by a "best-fit" method. Fick's second law of diffusion was adjusted to an experimental TDS spectrum [immediately after electrochemical deuterium charging in a deuterated solution (0.1 M NaO^{2}H (99.999% ^{2}H)) and transfer to the TDS system], using the numerical code which had been developed (WolframMathematica©software or Python™coding). The derived parameters were then tested and subsequently validated by simulating room (294 K) and high (409 K) temperature aging TDS spectra and comparing these simulated spectra to their experimental counterparts. The derived diffusion coefficient for deuterium in A600 and SS316L are shown in Table 5.1.

Table 5.1 Derived diffusion coefficients for A600 and SS316L pure diffusion system (PDS) model materials.

Material type	T range (K)	D_0 ($cm^2.s^{-1}$)	E_D ($kJ.mol^{-1}$)	D at 298 K ($cm^2.s^{-1}$)
A600	294 - 800	$(1 \pm 0.5)\ 10^{-2}$	45 ± 5	$1.3\ 10^{-10}$
SS316L	294 - 800	$(1 \pm 0.8)\ 10^{-3}$	45 ± 3	$1.3\ 10^{-11}$

The diffusion coefficient can be corrected for the isotopic effect (deuterium to hydrogen) but this correction has a negligible effect on the diffusion coefficient as it falls in the calculation error. Arrhenius plots were reconstructed comparing literature hydrogen (and its isotopes) diffusion coefficient values to those determined in this study; these plots are shown in Fig. 5.1a for A600 and Fig. 5.1b for SS316L. The derived diffusion coefficients for Ni-base alloy A600 (Fig. 5.1a) and stainless steel 316L (Fig. 5.1b) are overall in good correlation with the majority of literature data [40, 41, 42, 43, 44, 45, 46, 47, 48] over a large range of temperatures

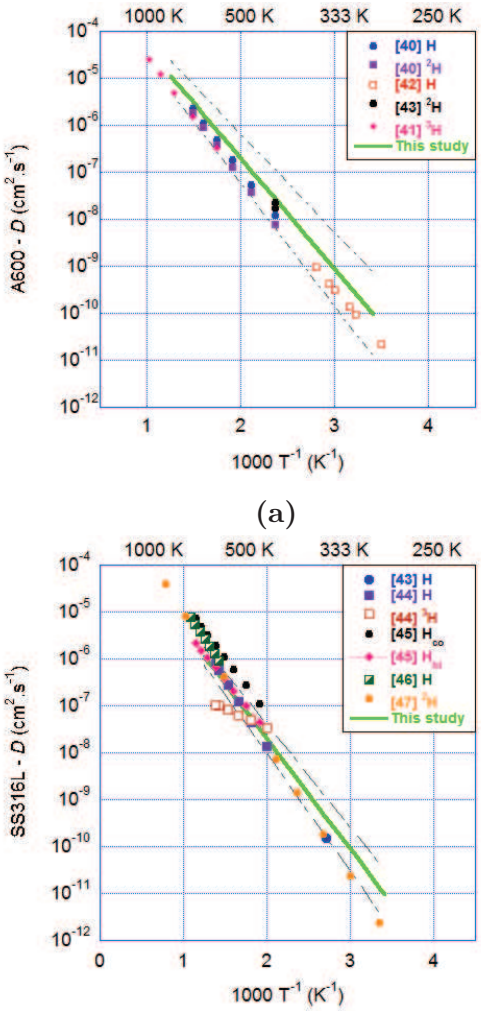

Fig. 5.1 Arrhenius plots of H diffusion data from literature in (a) A600 [40, 41, 43, 42] and (b) SS316L [44, 45, 46, 47, 48] as compared to the derived D ("This study") from A600 and SS316L pure diffusion system model materials. The error for D is indicated by the dotted gray lines. In (b) H_{co} and H_{HT} refer to the derived hydrogen diffusion coefficient in a commercial or heat treated 316L stainless steel respectively.

(with the exception of the tritium diffusion coefficient determined by Changqui *et al.* [45] in SS316L, which is not in correlation with the presented literature data [44, 45, 46, 47, 48] to begin with).

This overall good correlation with literature data validates the first hypothesis that was made in this study: the evolution of the hydrogen diffusion coefficient with temperature in A600 and SS316L alloys follows an Arrhenius law. Furthermore, the diffusion coefficient of hydrogen in these alloys, in first order, can be considered independent of local hydrogen concentration unlike what has been suggested previously by some authors, which may actually just be an artifact of confusing the interstitial hydrogen diffusion coefficient with its effective diffusion coefficient (D_{eff}).

Moreover, the experimental TDS technique proves advantageous for diffusion coefficient parameter (D_0 and E_D) derivation, as when coupled with a numerical analysis method, such as that used in this study, the diffusion coefficient can be evaluated continuously during temperature evolution (i.e. during a temperature ramp) or at an isotherm; whereas other experimental techniques such as electrochemical permeation, do not allow for a continuous measurement of the diffusion coefficient at non-isothermal conditions and requires many [sometimes rather long depending on sample thickness and material properties] experiments.

Diffusion information for hydrogen, and its isotopes, in A600 is rather readily available in a large range of temperature (room temperature to approximately 750 K), for which we demonstrate an overall good correlation (Fig. 5.1a). In the case of H, and its isotopes, diffusion in SS316L (Fig. 5.1b) there seems to be an overall lack of information in the room temperature to 525 K temperature range, with the exception of data by Brass *et al.* [44] and P. Tison [48]. We are in good agreement with their low temperature H diffusivity values.

This low to mid temperature range is considered by some authors to be the domain where H trapping phenomenon may be at its strongest. It may therefore prove difficult to asses the interstitial diffusion of hydrogen in metals as what may actually be addressed is an effective diffusion coefficient (D_{eff}) of hydrogen in the alloy. Hence the importance of using "model materials" (like those used in this study, Chapter 3 ans suggested by [69]) where H-material interactions can be linked [primarily] to interstitial H diffusion. Furthermore, this transitory temperature range is extremely important when addressing hydrogen embrittlement phenomenon. It would also prove important when working to understand the (possibly) hydrogen assisted environmental degradation process taking place in industrial alloys, such as those found in PWR reactors as reactor operating conditions fall in this transitory temperature range.

Brief summary of interstitial H diffusion

This study has served to derive the coefficient of deuterium diffusion in two austenitic alloys: (i) A600 and (ii) SS316L in model pure diffusion system materials (i.e. major elimination of trap sites), see Table 5.1. The derived diffusion coefficients were in very good correlation with experimental literature data for the entire temperature range assessed in this study; the studied temperature range was from 294 to approximately 800 K.

Furthermore, it has been shown that H diffusion in these alloys can be described by the Arrhenius equation, which indicates the temperature dependence of the coefficient, and does not indicate a diffusion regime transition at any given temperature or temperature range, i.e. a transition from grain boundary enhanced diffusion is the major contribution regime to the mainly interstitial diffusion regime. This conclusion, is in good accordance with the findings concerning the experimental and simulation analysis of ^{2}H diffusion in a pure diffusion A600 model material system and comparison to that of an A600-like single crystal.

5.2 ^{2}H Trapping in A600

Hydrogen trapping at two isolated trap site types: (i) chromium carbides [predominately] of type Cr_7C_3 and (ii) dislocations in A600, was characterized using "diffusion and trapping system" model materials. The trapping and detrapping kinetic constant parameters, (k_0, p_0, E_k and E_p) were determined by a "best-fit" approach Table 5.2. The McNabb and Foster diffusion and trapping equations [107], coupled with the derived diffusion coefficient for deuterium in A600 (Table 5.1), were used to adjust a TDS spectra on which a trapping contribution had been isolated.

The aforementioned kinetic constant parameters were then extracted using the Python™ code or WolframMathematica© software. These constants were then tested and subsequently validated by simulating DTS TDS spectra having been subjected to different experimental conditions and comparing them to their experimental counterpart. A good reproduction of experimental spectra signaled the validity of the derived parameters.

Table 5.2 Derived trapping (k) and detrapping (p) kinetic constants for trapping at chromium carbides (Cr_7C_3) and dislocations in A600.

	Trapping (k)		Detrapping (p)	
	k_0 (s^{-1})	E_k ($kJ.mol^{-1}$)	p_0 (s^{-1})	E_p ($kJ.mol^{-1}$)
Cr_7C_3-IIC	$(1.5 \pm 0.2)\ 10^7$	50 ± 4	$(1.5 \pm 0.2)\ 10^6$	80 ± 4
Cr_7C_3-GBC	$(1.5 \pm 0.2)\ 10^8$	50 ± 4	$(1.5 \pm 0.2)\ 10^5$	78 ± 4
Dislocations	$(1.5 \pm 0.2)\ 10^6$	42 ± 4	$(1.5 \pm 0.2)\ 10^6$	76 ± 4

5.2.1 Comments on derived activation energies (E_k, E_p) and their relation to the activation energy of interstitial diffusion (E_D)

5.2.1.1 Energetic description of trapping

In Chapter 2, two energy diagrams for diffusion and trapping were presented: (i) where E_D is equal to E_k (Fig. 2.9) and (ii) where E_D is not equal to E_k (Fig. 5.2). In Fig. 5.2, trapping activation energy is greater than the activation energy of interstitial diffusion presenting an energy barrier that the atom of hydrogen needs to overcome to become trapped in the respective trap site. Looking at the derived trapping activation energies (E_k) presented in Table 5.2, none of these energies are exactly equal to E_D.

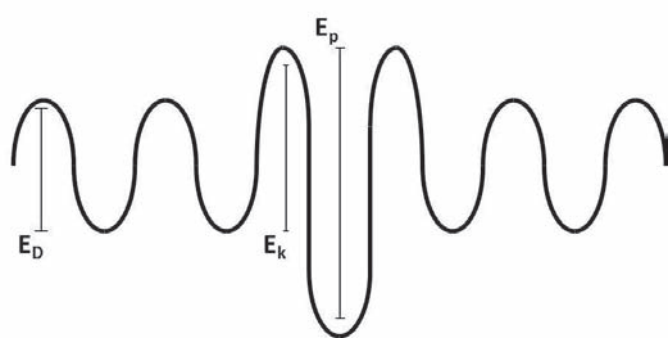

Fig. 5.2 Energy diagram for trapping when the trapping activation energy (E_k) is greater than that of interstitial diffusion (E_D), as would be suggested by the derived activation energies for H trapping at chromium carbides (Table 5.2).

The values associated with trapping at chromium carbides are both higher than that of interstitial diffusion, whereas for dislocations this parameter is lower. It would seem that the energetics of hydrogen trapping at Cr_7C_3 is adequately described by Fig. 5.2 but concerning dislocations a different diagram would need to be proposed (Fig. 5.3).

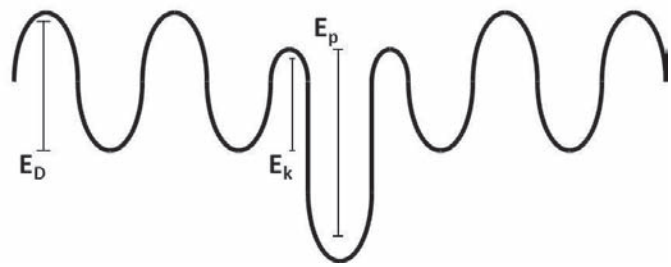

Fig. 5.3 Energy diagram for trapping when the trapping activation energy (E_k) is less than that of interstitial diffusion (E_D), as would be suggested by the derived activation energies for H trapping at dislocations (Table 5.2).

These energy diagrams (Fig. 5.2 and Fig. 5.3) recall some hypotheses made by Pressoyre *et al.* [70] on concerning the classification of trap site types. He hypothesized that traps can be attractive (like in Fig. 5.3 for dislocations) or repulsive (like in Fig. 5.2 for chromium carbides). Furthermore, an attractive type energy diagram for dislocations, is in agreement with hypothesis that attractive traps may be linked to stress fields in a matrix, i.e. the stress fields that may surround dislocations.

5.2.1.2 Assessment and comments on trap binding energy

When E_D is not equal to E_k it challenges the generally accepted, and commonly employed, way of determine the trap site binding energy (E_b). Traditionally binding energy is defined as:

$$E_b = E_p - E_D \tag{5.1}$$

Based upon the derived H trapping activation energies (E_k) derived for chromium carbides and dislocations in A600 (Table 5.2), where $E_k^{Cr_7C_3} > E_D$ and $E_k^{\text{dislocations}} < E_D$, it can be argued that the trap site binding energy would need to be calculated with regards to trapping activation energy (E_k) and not with regards to the interstitial diffusion activation energy (E_D). This binding energy can be referred to as E_b' and could be defined as:

$$E_b' = E_p - E_k \tag{5.2}$$

This may change drastically the value calculated for trap site binding energies and their respective binding energy as compared to other trap site binding energies. Both binding energies, E_b and E_b', have been calculated and can be seen in Table 5.3. If we consider the traditional E_b it would appear that binding at chromium carbides (IIC and GBC) is slightly stronger than that at dislocations, but if E_b' is used for calculation the binding at dislocations proves stronger with regards to chromium carbides.

Table 5.3 Calculated binding energies for trapping at chromium carbides (Cr_7C_3) and dislocations in A600 using the derived trapping parameters (Table 5.2). E_b refers to the traditional definition of binding energy ($E_b = E_p - E_D$) and E_b' refers to the proposed definition of binding energy ($E_b' = E_p - E_k$).

	E_b (kJ.mol^{-1})	E_b' (kJ.mol^{-1})
Cr_7C_3-IIC	35 ± 9	30 ± 8
Cr_7C_3-GBC	33 ± 9	28 ± 8
Dislocations	31 ± 9	34 ± 8

As a literature review of hydrogen trapping and detrapping in metals and alloys (Table 2.2) has resulted in little information concerning the detrapping activation energy and even less concerning the trapping activation energy, it therefore may become impossible (in most situations except, for [105]) to asses the validity of the trap site binding energies reported.

In the following sections, trapping at specific trap sites: (i) chromium carbides and (ii) dislocations will be discussed further in-depth and a qualitative and quantitative comparison to literature will be carried out.

5.2.2 Trapping at chromium carbides

Detrapping at chromium carbides of type Cr_7C_3 and $Cr_{23}C_6$ in nickel base alloy 600 has been studied by Young *et al.* [82] (Fig. 5.4) and Symons *et al.* [22] in a heat treated model A600 alloys; they analyzed TDS desorption spectra using the "Choo-Lee plot" method [91]. The derived detrapping activation energies and interstitial diffusion activation energies can be seen in Table 5.4.

Table 5.4 Collection of activation energies for diffusion and trapping in A600 as presented by Young *et al.* [82] and Symons *et al.* [22]. The activation energies (E_D and E_p) were determined by "Choo-Lee plot" analysis [91] and binding energy (E_b) was calculated by Eq. (5.1).

Material type	Trap type	E_D[a] ($kJ.mol^{-1}$)	E_p ($kJ.mol^{-1}$)	E_b ($kJ.mol^{-1}$)
A600 - sensitized[b] [82]	$Cr_{23}C_6$	52.7	78.6	25.9
A600 - sensitized[c] [22]	Cr_7C_3	48	76	26
A600 - mill annealed[d] [82]	Cr_7C_3	51.8	106.8	55.0

[a]The diffusion activation energy was determined by "Choo-Lee plot" analysis [91] using the derivative of the Kissinger equation [140] even though this equation [and analysis method] technically neglects interstitial diffusion

[b]annealing followed by 24 h at 973 K followed by air cooling

[c]annealing at 1373 K for 1 h followed by furnace cooling

[d]annealing at < 1273 K

It should be kept in mind that this analysis is debatable, as they have used an analysis method which neglects interstitial diffusion [91, 140] to determine an interstitial H diffusion or weakly trapped activation energy (E_D) from the low[er] temperature desorption peak (Fig. 5.4). Nonetheless, these values will be discussed and compared to those determined in this study (Chapter 3, Chapter 4 and [90]). The derived trapping and detrapping kinetic parameter constants for H trapping at chromium carbides in A600 can be found in Table 5.2 and the calculated binding energies can be seen in Table 5.3.

The detrapping activation energies derived in this study for chromium carbides (Table 5.2) are in relatively good correlation with chromium carbides of type $Cr_{23}C_6$ [82] and with type Cr_7C_3 precipitates [22] as presented in the literature (Table 5.4). Some literature [82] seems to suggest that Cr_7C_3 precipitations have a slightly stronger detrapping activation energy (E_p) and binding energy (E_b). This

is an interesting observation as the chromium carbide precipitations in the model A600-DTS-IIC and GBC material were determined to be of type Cr_7C_3 by electron diffraction pattern analysis. One hypothesis to explain the discrepancy between the results obtained in the compared works, would be that both types of carbides are present in the model material in a mixed nature but were just not observed as it was impossible to analyze every single chromium carbide in each specimen.

Furthermore, as previously mentioned, the authors [22, 82] used "Choo-Lee plot" analysis [91] for the assignment of an interstitial diffusion and detrapping activation energy (E_D (or weakly trapped hydrogen) and E_p), a questionable method for previously discussed reasons, Sec. 2.5.3.1. It has been demonstrated in Chapter 4 and in [90] that for a uniformly hydrogen charged [*cc*]-material specimen (i.e. pure Fe), after a 30 min of aging at 298 K the interstitial hydrogen contribution can be neglected and all [simulated] TDS desorption contributions may be attributed to trapped hydrogen. This may not be the case in *fcc* materials such as A600, as interstitial hydrogen diffusion is significantly slower. Symons *et al.* [22] have stated that specimens have been homogeneously charged with hydrogen and Young *et al.* [82] state that the sample is adequately charged for "appreciable hydrogen ingress via bulk diffusion", but no reference has been made to an aging period or transfer time (from charging apparatus to testing equipment). A set of simulations have been carried out subjecting homogeneously ^{2}H charged pure diffusion system specimen of A600 (Table 5.1) to room temperature aging periods ranging from 0 min to 1440 min, see Fig. 5.5.

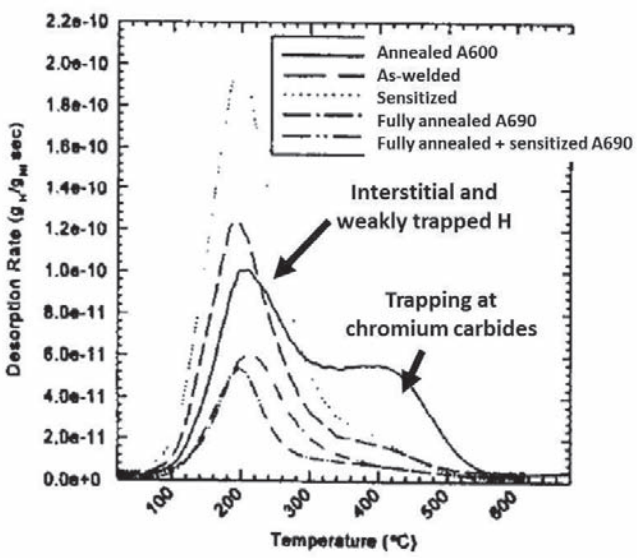

Fig. 5.4 Experimental TDS spectra as acquired by Young *et al.* [82] for trapping at chromium carbides.

A pure diffusion system was simulated for purely demonstrative purposes to see if in the absence of trap sites the majority of hydrogen could be desorbed in a short period of time. After 1 day (1440 min) of aging at room temperature (in the absence of trap sites) there is still significant amount of deuterium present in the specimen, Fig. 5.5 (for both charging types).

This demonstrated the validity of the method used as it would be necessary to address interstitial diffusion along with trapping interactions. Furthermore, if simulations are carried out using their hydrogen diffusivity [22, 82] and the kinetic trapping and detrapping kinetic constants for chromium carbides derived in this study (as they are the only complete data set, Table 5.2), spectra very similar to those of sensitized A600 (very similar heat treatment to that used for the reprecipitation of inter- and intragranular chromium carbides in this study) from Young *et al.* [82] are produced (Fig. 5.6a).

To verify the peak attribution done in [82] to the respective H population: (i) interstitial (and weakly trapped) and (ii) trapped at chromium carbides, the imposed trap site density was varied over several orders of magnitude.

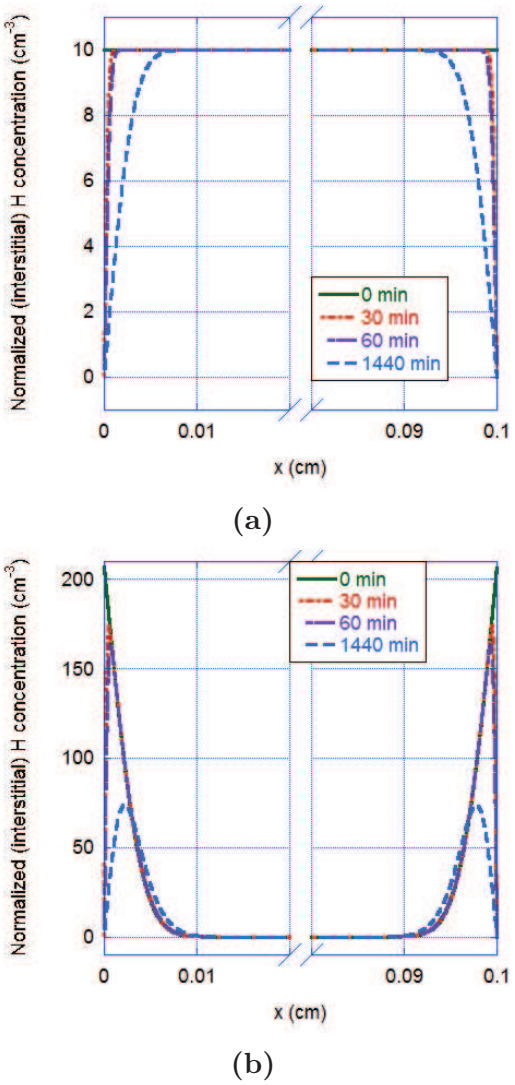

Fig. 5.5 Simulated (pure diffusion) normalized[a] H concentration profiles recreated using the charging conditions and diffusivity in the publications: (a) Symons *et al.* [22] and (b) Young *et al.* [82] after various aging periods..

[a]with regards to total amout of H in the specimen immediately after charging

Simulation can be seen in Fig. 5.6b. From the analysis in Chapter 4 it was expected that this large variation would result in differences in "trapping peak" form and relative intensity with regards to the interstitial population. No change in "trapping peak" form or relative intensity was observed. This furthermore, brings into question the validity of their analysis, as it would seem as though this second desorption peak the consequence of interstitial hy-

drogen desorption (a result of the hydrogen entering at sample face $x = 0$ cm, transporting across the specimen and desorbing from face $x = 0.1$ cm (see Fig. 5.5b)), even if the aging time and the experimental T ramp are not well known. Furthermore, the fact ours and their derived, E_p, and calculated, E_b, parameters being similar may only be a coincidence.

This brings many questions to mind concerning the validity of information from TDS spectra immediately after hydrogen charging, in particular if one can address a trapping phenomenon in *fcc* materials as the interstitial hydrogen concentration to trapped hydrogen concentration ratio is very high. In Chapter 4, one major encountered problem was locating the trapped hydrogen contribution and the only way this was achieved for trapping at chromium carbides was through a prolonged aging at high temperature (409 K).

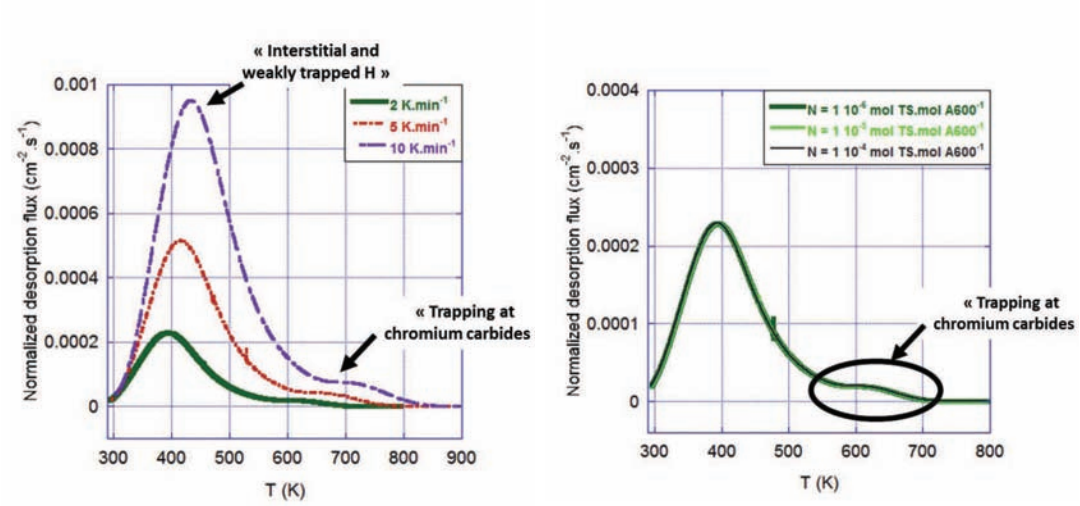

Fig. 5.6 Simulated normalized[a] TDS desorption spectra, to attempt recreation of experimental TDS spectra by Young *et al.* [82] with (a) variation in (linear) temperature ramp and (b) variation in trap site density N. The text located on the figures is to remind the reader of peak identification as stated in the publication [82].

[a] with respect to total mol H desorbed

This brief discussion and simulations shed some light on the necessity of using a more inclusive analysis method for spectral analysis, not only (i) to increase the number of assessed parameters (i.e. determining one parameter with "Choo-Lee plot" analysis (E_p) to determining at least four parameters (k_0, E_k, p_0, E_p)) but in the present case also (ii) to correctly identify spectral contributions (i.e. between

interstitial and trapped contributions).

The approach developed in this study proves to be much more in-depth as it allows for a reasonable determination of detrapping activation energy along with other important trapping and detrapping parameters which include pre-exponential constants for both trapping (k_0) and detrapping (p_0) and the activation energy for trapping (E_k).

5.2.3 Trapping at dislocations

A literature review has resulted in very little information concerning hydrogen-dislocation interactions in nickel base alloys, whereas for pure metals (i.e. *fcc* nickel and *cc* iron) and stainless steels more information is available. For most materials, with the exception of pure iron (α) [91] and a dislocation core in tempered martensite [92], dislocation binding energies (E_b) are on the order of 29 $\pm$ 5 kJ.mol^{-1}. This binding energy is similar to both E_b and E_b' determined for dislocations in A600 (Table 5.3). Furthermore, on top of the shear lack of information concerning hydrogen-dislocation interactions in nickel base alloys, no information concerning the trapping of hydrogen at these sites, activation energy (E_k) nor pre-exponential constant (k_0), or detrapping pre-exponential constant (p_0) was found in literature for all materials.

Pertaining to the derived trapping activation energy for dislocations in A600 (E_k = 42 $\pm$ 4 kJ.mol^{-1}), it is [slightly] less than the diffusion activation energy (E_D = 45 $\pm$ 5 kJ.mol^{-1}). This demonstrates that dislocations may be slightly "attractive" trap sites for hydrogen. One can hypothesize that this attraction between ^{2}H and these sites could be due to the fact that there are elastic deformation fields present around these sites. This attraction to dislocations seems to be in good correlation with some models for H-dislocation interactions available in the literature, specifically those studies carried out using DFT calculations [163]. Furthermore, at this point in time a study addressing the deuterium localization in the dislocation has not been done and it is therefore impossible to locate the trapped hydrogen.

5.2.4 General comments on k_0'/p_0 relationship

Often it is considered that the ratio of the pre-exponential constants for trapping and detrapping can be described by the relationship:

$$\frac{k_0'}{p_0} = \frac{1}{N_L} \tag{5.3}$$

where N_L is equal to the number of lattice sites per cm^3 and k_0' (cm^3.s^{-1}) is equal to $\left(\frac{k_0 \times V_m}{N_A}\right)$ in which N_A is equal to Avogadro's number and V_m is the molar volume of

the metal [105]. This is an assumption that is strongly linked to a first hypothesis that the jump probabilities are the same for diffusion, trapping and detrapping.

From the kinetic constants determined in this study the k'_0/p_0 ratios is on the order of 10^{20} or 10^{22} cm^3 and 10^{23} cm^3 respectively for chromium carbides along grain boundaries or inter- and intragranularly and dislocations in A600. This value is not a constant as would be expected by the hypothesis that k'_0/p_0 is equal to N_L^{-1}. It would seem that the assumption of a constant k'_0/p_0 ratio cannot be considered for H-trap site interactions whereas trapping is a rate controlling step.

5.2.5 Trap site density

Trap site density may be considered an important parameter and to have an impact on simulated TDS spectra, especially concerning spectral form, but the question still remains concerning this parameter's relation to the physical quantity of chromium carbides or dislocations present in the model material. The derived and validated or assigned trap site densities are compiled in Table 5.5 and Table 5.6.

These values may be converted into forms having units of number of trap sites per cubic centimeter for chromium carbides or dislocations (Eq. (5.4)). In these equations N'_{C} and N'_{d} are the trap site quantities respectively for chromium carbides and dislocations in TS.cm^{-3}.

$$N'_{\mathrm{C}} = N'_{\mathrm{d}} = \frac{N \times N_A}{V_m} \quad (\mathrm{TS.cm^{-3}}) \tag{5.4}$$

An equation relating dislocation density to the number of trap sites per Burgers vector has been proposed by Krom *et al.* [164]:

$$\alpha_{\mathrm{d}} = \frac{N'_{\mathrm{d}} \times b}{\rho_{\mathrm{dislocations}}} \tag{5.5}$$

where α_{d} is the number of TS per Burgers vector (b). Chêne *et al.* [165] reported α_{d} in literature of between one and fifty. The resulting calculations for dislocations can be seen in Table 5.5. First, N'_{d} was calculated for 40 % deformed specimen, followed by determining the number of theoretical α_{d} for dislocations. Assuming α_{d} is constant regardless of deformation percent, a theoretical N'_{d} and N could be determined for 20 % deformed specimen. Furthermore, the determined value of α_{d} falls in the range of values as presented by Chêne *et al.* [165].

Concerning chromium carbides, it was hypothesized that an α_{c} for these sites may be determined by using the following relationship:

$$\alpha_{\mathrm{c}} = \frac{N'_{\mathrm{c}}}{S_{\mathrm{if}}} \tag{5.6}$$

Table 5.5 Dislocation densities ($\rho_{\text{dislocations}}$) imposed trap site density in simulations (N) and calculated TS densities (N'_{d}) and α_{d} associated with dislocations, these parameters were determined experimentally, derived from numerical simulations, or calculated using Eq. (5.4) or Eq. (5.5).

Trap site type	$\rho_{\text{dislocations}}$ $\left(\frac{1}{\text{cm}^2}\right)$	N $\left(\frac{\text{mol TS}}{\text{mol A600}}\right)$	N'_{d} $\left(\frac{\text{TS}}{\text{cm}^3\text{A600}}\right)$	α_{d} $\left(\frac{\text{TS}}{\text{Burgers vector}}\right)$
Dislocations (40 %)	$2.3\ 10^{10}$	$1\ 10^{-4}$ [a]	$8.9\ 10^{18}$	11.8
Dislocations (20 %)	$1.2\ 10^{10}$	$5.7\ 10^{-5}$	$5.8\ 10^{18}$	11.8

[a] approximate (non-validated) value

where S_{if} refers to the theoretical surface area of interfaces in volume of chromium carbides. For intergranular chromium carbides measured on average between 400 nm and 1000 nm and intragranular chromium carbides between 250 nm and 500 nm. Assuming spherical chromium carbides the average diameter ($\bar{d}$) of intergranular Cr_7C_3 may be considered approximately 700 nm and of intragranular Cr_7C_3 approximately 350 nm. It was considered that in the A600-DTS-IIC model material all chromium carbides were intragranular and for a A600-DTS-GBC all chromium carbides were intergranular. The calculated values can be seen in Table 5.6. Between the model materials, there is a difference in the calculated α_c, this may be liked to a difference in interface coherence depending on where the chromium carbide is located (in grain volume or along a grain boundary).

Moreover, to get a better understanding of this parameter, and more importantly to validate it, it is imperative to work with quantified experimental TDS spectra. Working with quantified TDS spectra was made impossible due to the non-reproducibility of charging conditions, in terms of the total amount of ^{2}H absorbed.

Table 5.6 Average surface area of a chromium carbide in the A600 matrix (S_a), imposed trap site density in simulations (N) and calculated TS densities (N'_{c}) and α_{c} associated with chromium carbides. These parameters were determined by microscope observations and image analysis, derived from numerical simulations, or calculated using Eq. (5.4) or Eq. (5.6).

Trap site type	S_{if} $\left(\frac{\text{cm}^2\text{interface}}{\text{cm}^3\text{A600}}\right)$	N $\left(\frac{\text{mol TS}}{\text{mol A600}}\right)$	N'_{c} $\left(\frac{\text{TS}}{\text{cm}^3\text{A600}}\right)$	α_{c} $\left(\frac{\text{TS}}{\text{cm}^2\text{interface}}\right)$
Cr_7C_3-IIC	$1.3\ 10^4$	$1.0\ 10^{-5}$	$8.9\ 10^{17}$	$6.7\ 10^{13}$
Cr_7C_3-GBC	$7.3\ 10^2$	$2.5\ 10^{-6}$ [a]	$2.2\ 10^{17}$	$3.0\ 10^{14}$

[a] approximate (non-validated) value

5.3 Technical perspectives

This study has shed some light on some specific experimental improvements that can be made or further studied to provide some more information and improve and/or optimize the experimental approach. These include specifically (i) cathodic charging of specimen with deuterium [or hydrogen] and (ii) the thermal desorption spectroscopy experimental approach and apparatus.

5.3.1 Effect of charging solution

One of the largest problems encountered in this study was the inconsistencies in total deuterium desorption in TDS analysis for model materials charged in deuterium by cathodic polarization under the same conditions, see Fig. 4.1. To overcome these inconsistencies and to do a comparative analysis of results a normalization procedure was adopted. The next step in this study, to allow for quantitative analysis of all model material types would be to study the absorption mechanism of deuterium in alkaline deuterated solutions and the evolution of alkaline deuterated solutions in an air environment over time.

This study would help to better understand the boundary conditions (i.e. ^{2}H surface concentration) on the alloy faces and to confirm our hypothesis of solution evolution over time (i.e. carbonization of the solution leading to pH evolution) which would in turn have an influence on absorption conditions and possibly affect the absorption mechanism and or surface [concentration] conditions. It would be important to optimize these charging conditions by for example working with uniquely "fresh" solutions and explore the possibility of charging in an acidic environment. Furthermore, the charging temperature (T_{charging}) and time (t_{charging}) could be optimized. Manipulating these conditions could change the form (and allow us to work with homogeneously charged or saturated specimen) of the hydrogen concentration profile along with the trapping kinetics, as it was shown that at elevated temperatures trapping may be favored (i.e. isothermal aging at 409 K).

Furthermore, as it was stated in Chapter 2, the experimental cathodic charging conditions used imposed a cathodic current of -100 mA.cm^{-2}; this current may not be ideal for deuterium absorption by the material. Visual observations of the specimen during cathodic charging revealed heavy bubbling on the specimen surface. This bubbling may be a sign that a sheering on the surface by $^2H_2$ bubbles may not be negligible and lead to a lower absorption efficiency. A set of experiments can be proposed to address the cathodic charging current question: a series of cathodic deuterium chargings will be done, each imposing a different cathodic current density.

Electrochemical permeation experiments could be envisaged to determine these

optimal charging conditions and provide some supplementary information concerning the surface dissociation and absorption mechanism along with information on the hydrogen surface activity. Moreover, these analysis may be coupled with **S**econdary **I**on **M**ass **S**pectrometry (SIMS) analysis determine the ^{2}H concentration profile in the charged material. Exploring these conditions, should shed some light on the optimal charging conditions in order to favor hydrogen absorption and possibly trapping in the model materials.

5.3.2 TDS system improvements

Concerning thermal desorption mass spectroscopy experimental approach and apparatus advancements, one important part that may be improved upon would be a reduction in transfer time. This transfer time from the electrochemical charging cell to the start of desorption monitoring is on the order of (15 $\pm$ 3) min; during this period desorption flux monitoring is impossible. The majority of this time is comprised of the necessary pumping time to pump down to a sufficient vacuum for mass spectrometer operation (between 12 and 15 min).

During this transfer time, a small but not negligible amount of deuterium is desorbed; we consider this desorption to have a [slight] effect on the total amount of deuterium in the specimen. Therefore these, not always reproducible (in the range of 3 min) transfer periods may play a role in the inconsistencies seen in total amount of deuterium desorbed from the sample during desorption monitoring. Furthermore, the temperature is not perfectly controlled during the trip from the cathodic charging apparatus to the TDS system, therefore in simulations the average temperature of the day is used for simulating this period. It would be important to minimize this time in order to have the maximum accuracy on the analysis of deuterium-material interactions.

The TDS system is in the process of being adapted for a liquid nitrogen cooled cryogenic chamber where the pre-charged specimen may be held at very low temperatures (thereby minimizing H or ^{2}H desorption) before the start of TDS testing. Furthermore this chamber is of a much smaller volume and will be equipped with its own turbo pump as to further decrease pumping time and aging time before the start of TDS testing. Moreover, one TDS approach that has been used in this study was the imposition of isotherms (Chapter 4). Due to system limitations "instantaneous" heating and "fast" cooling have not been possible. It would be interesting to adopt a system that allows for this type of heat treatment for the imposition of multiple varying temperature isotherms, Fig. 5.7. For example a high temperature isotherm followed by a quench-type cooling which would "freeze" the deuterium in the trap sites followed by normal TDS testing to monitor the desorption of the trapped contribution (Fig. 5.7a) or something with multiple isothermal steps (Fig. 5.7b), etc. This "exotic" temperature ramp and/or cooling approach

may prove very beneficial for the isolation of spectral contributions (i.e. separation of convoluted desorption peaks.)

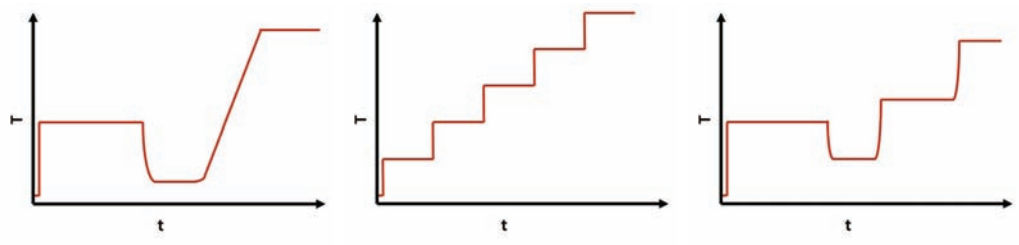

(a) **(b)** **(c)**

Fig. 5.7 Some examples of exotic isothermal and ramp desorption testing which may be interesting for trap site isolation: (a) demonstrates an instantaneous temperature jump, isotherm, freeze, TDS combination (b) consecutive instantaneous temperature jumps and isotherms and (c) a mixture of the two previous.

5.4 Scientific perspectives

5.4.1 Model materials

Two austenitic alloys were studied, (i) polycrystalline Ni-base alloy 600 and an A600-like single crystal alloy and (ii) stainless steel 316L. The model materials were fabricated through a series of thermal and or thermo-mechanical treatments creating four different types of model materials: (i) a pure diffusion material [elimination of the majority of trap sites leaving a model material with only grain boundaries], (ii) a diffusion and trapping system with chromium carbides precipitated inter- and intragranularly (only A600), (iii) a diffusion and trapping system with chromium carbides precipitated only along the grain boundaries (only A600) and (iv) a diffusion and trapping system with dislocations created by interrupted tensile testing.

It would be very interesting to create more different type of model materials presenting different trap site types and trap sites in higher and lower densities (i.e. deformation percents greater than $\epsilon = 40\%$ [with stainless steels] or by another deformation technique (i.e. cold rolling)). Some different trap sites types that may be envisaged include vacancies, other types of precipitates (i.e. phase boundaries), multiple phases (i.e. dual phases materials) and looking at model materials with multiple types of trap sites.

5.4.1.1 Multiple trap site types

At this point in time two isolated trap site types have been studied: (i) chromium carbides (IIC or GBC) and (ii) dislocations.

A set of kinetic trapping and detrapping constants were derived for these diffusion and trapping systems. The fabrication of a model material presenting both these trap site types can be easily imagined followed by TDS testing.

Once experimental spectra were acquired it would be important to test the numerical model and the derived trapping and detrapping parameters in a situation where they are not isolated. This would address one of the large hypotheses that was made during model development and a key hypotheses of the McNabb and Foster equations [107], which is that trap sites do not interact.

Some first simulations were carried out for this type of situation (i.e. the presence of two trap sites in A600). Non-aged (Fig. 5.8a) and high temperature (409 K) (Fig. 5.8b) TDS spectra were simulated using the experimental charging and transfer conditions of this study paired with a linear theoretical temperature ramp of 10 K.min^{-1}. The derived diffusion (Table 5.1) and kinetic trapping and detrapping parameters (Table 5.2) along with the derived trap site density of 1 10^{-}5 mol TS.mol A600^{-1} for inter- and intragranular chromium carbides and 1 10^{-4} mol TS.mol A600^{-1} for dislocations (40 % deformed) in A600 have been used.

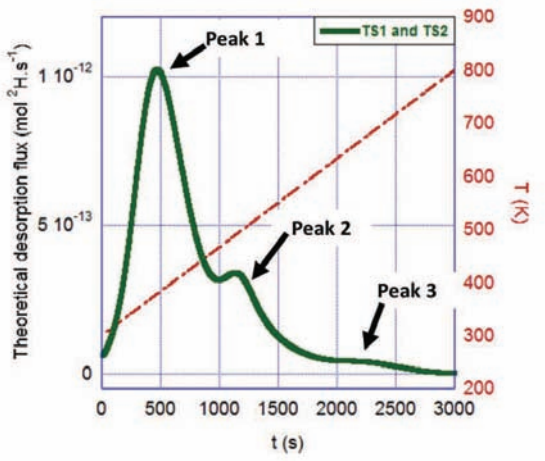

(a)

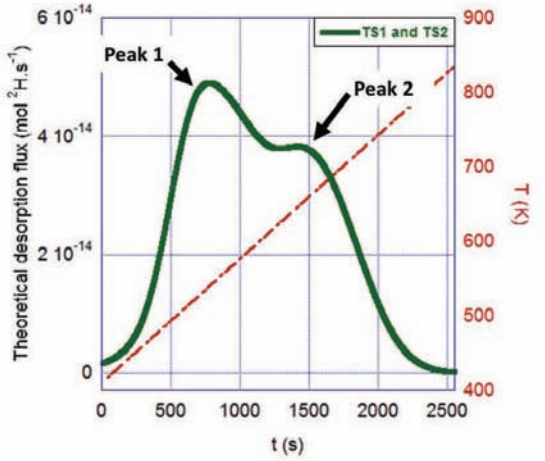

(b)

Fig. 5.8 Simulated (a) non-aged and (b) aged 6 h at 409 K TDS spectra (ϕ = 10 K.min^{-1}) for a model A600 material with two trap sites: (i) dislocations (TS1) and (ii) chromium carbides (TS2).

In the non-aged spectrum three clear peaks can be observed (indicated by the black arrows in Fig. 5.8a): one at about 500 s (390 K) one at about 1200 s (600

K) and a third at 2200 s (700 K). If we proceed with traditional spectral analysis, it could easily be assumed that the first lowest temperature peak could be attributed to interstitial hydrogen, and the second and third to either dislocations and chromium carbides.

Furthermore, when looking at the high temperature aged TDS spectrum only two desorption peaks are observed (indicated by the black arrows in Fig. 5.8b). One could proceed with assuming that the majority of interstitial hydrogen has been desorbed during the aging period leaving only the trapped hydrogen contributions; one associated with the peak at about 750 s (550 K) and the other at 1500 s (670 K). To verify the peak associations, individual simulations were carried out for a material with uniquely TS1 or TS2 present. Simulated non-aged spectra can be seen in Fig. 5.9 and for materials aged 6 h at 409 K in Fig. 5.10. From these two figures, it becomes clear that peak identification and deconvolution in systems is not as simple as it would seem.

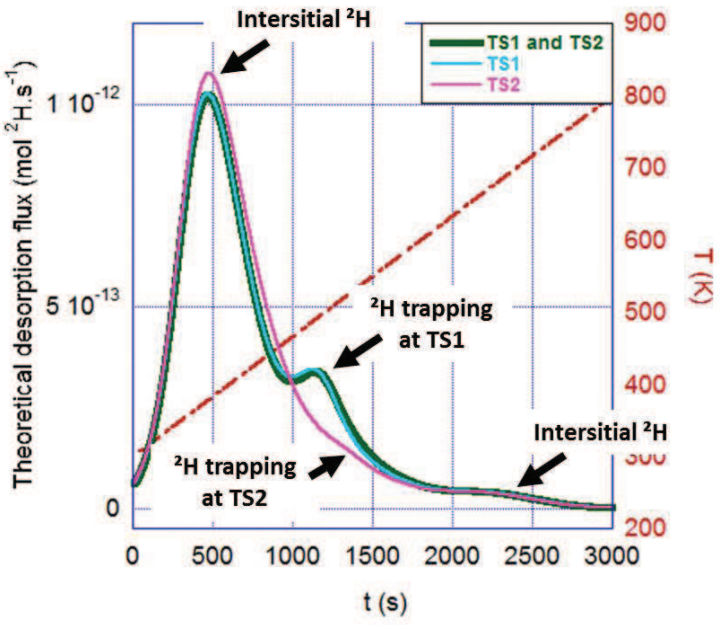

Fig. 5.9 Simulated non-aged TDS spectra (ϕ = 10 K.min^{-1}) for a material with two trap sites (TS1 and TS2) and simulated TDS spectra for each type of isolated trap site TS1 (dislocations) or TS2 (Cr_7C_3).

In the non-aged TDS spectra it would seem that the second peak, indicated in the figure by the arrow and "^{2}H trapping at TS1", would be primarily contributed to trapping at TS1, i.e. dislocations in A600. The desorption peak for trapping at chromium carbides (indicated in the figure by the black arrow and "^{2}H trapping at TS2") is completely masked by the total desorption flux in the spectrum simulated for two coexisting trap site types. This trapping contribution was completely invisible and would have been neglected or missassociated if traditional spectral analysis methods had been used.

High temperature simulation spectral contributions were evaluated in this same

way, by simulating a material with only TS1 or TS2 and comparing it to a simulated spectrum with both trap site types present together (Fig. 5.10). Once again, the trapping contributions are overlapping (black arrow in Fig. 5.10 indicating "^{2}H trapping at TS1" and "^{2}H trapping at TS2"). As with non-aged simulated TDS spectra, peak assignment would have been misleading if traditional peak association methods (i.e. Gaussian fitting and "Choo-Lee" plot analysis) were used; each peak would have been associated with a separate trapping contribution (TS1 or TS2) and interstitial hydrogen contributions would have been neglected, when in fact the first peak contains all trapping contribution (overlapping desorption peaks) and the second peak can be attributed to the desorption of interstitial hydrogen from the material in Fig. 5.10.

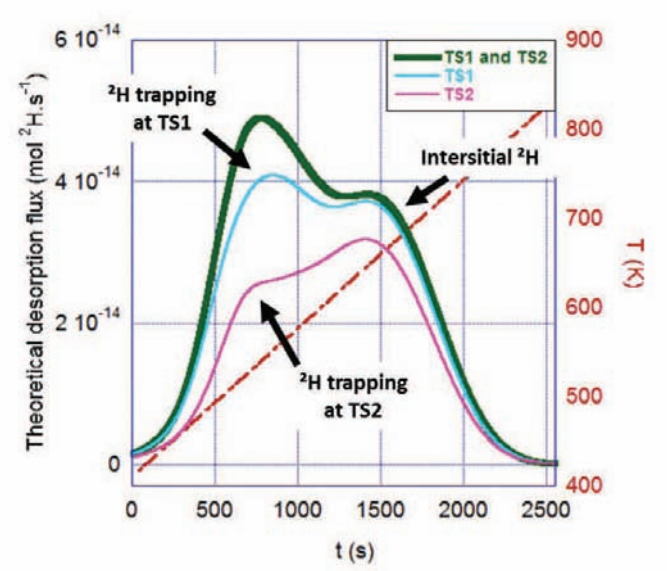

Fig. 5.10 Simulated high temperature aged (409 K for 6 h) TDS spectra (ϕ = 10 K.min^{-1}) for a material with two trap sites (TS1 and TS2) and simulated TDS spectra each type of isolated trap site TS1 (dislocations) or TS2 (Cr_7C_3).

Assuming trap sites do not interact with one another, these simulations have shed some light on the possible difficulties encountered when analyzing model materials with multiple trap site types. It seems as though it will be important to determine individual trapping and detrapping kinetic constants in order to asses and analyze desorption spectra. Furthermore, as the individual kinetic constant parameters will be known before experimental spectral acquisitions for a material with two trap site types, simulation may be used to our advantage to determine specific experimental conditions, including charging, temperature ramp rate (ϕ) and isothermal room and elevated temperature aging conditions, in order to determine the optimal experimental conditions for peak deconvolution. As

the database of diffusion and kinetic trapping/detrapping information is at this point in time limited to A600, SS316L, ^{2}H-chromium carbides (in A600) and ^{2}H-dislocation interactions (in A600) it will be evermore important to asses trapping at other potential sites in these materials along with other industrial materials.

5.4.1.2 Hydrogen vacancy interactions

A number of research groups have looked at hydrogen vacancy interactions in metals and have stated that vacancies are very strong trapping sites for hydrogen [76, 77, 80, 81], but the experimental analysis and creation of stable characterized vacancies seems rather difficult experimentally as vacancies are not stable [especially at elevated temperatures] and they may appear as monovacancies, divacancies and/or vacancy clusters.; each mono/di/cluster vacancy-H combination presents very different trapping energies, see Table 2.2 [76, 77, 80, 81] and furthermore diffusivity, making analysis even more complex.

A proposed method to create a material with a high density of vacancies would be by heating a pure diffusion material (very few trap sites present) to a temperature just below its fusion temperature and holding it at that temperature for a [short] period of time before very rapidly water quenching the material [18]. This process would allow the formation of high quantities of [thermal] vacancies then "freeze" them in the material by the rapid quench. This vacancy formation approach was attempted with the help of OCAS (Ghent, Belgium) and was unsuccessful due to unforeseen equipment difficulties but a collaboration with this group and another test using this method is planned in the future.

Differential **S**canning **C**alorimetry (DSCs) and **X**-**R**ay **D**iffraction (XRD) [166, 167] and/or four-point resistivity measurements [168] may then be used to measure the relative vacancy density or characterize the presence of vacancies in the material. Dimitrov *et al.* [168] showed that the resistivity of metals is highly influenced by the presence of vacancies and these changes in resistivity may be used to characterize the presence of these sites in metals.

As vacancies begin to diffuses more rapidly as temperature increases, it would be necessary to address the evolution of the system during the temperature ramp experienced during TDS analysis (i) experimentally and (ii) numerically. Experimentally an evolution of trap site density and distribution is anticipated. As trap site density evolution cannot be addressed *in-situ* during TDS analysis, TDS analysis would need to be coupled with another experimental technique to address these evolutions over time and with increasing temperature. Non-equilibrium DSC measurements maybe carried out by monitoring vacancy annihilation in deuterium charged and non-charged materials during over the same temperature range as an imposed temperature ramp in TDS testing. Some other commonly used methods for the assessment of vacancy density and evolution are **P**ositron **A**nnihilation

Spectroscopy (PAS) and **E**lastic **N**eutron **D**iffraction (ENS). A PAS method could be used to study the evolution of vacancies (annihilation, diffusion, apparition) in non-isothermal conditions using a heated sample holder (CEHMTI, Orleans, France) [169] or ENS method at the Laboratoire Léon Brillouin (LBB) at the CEA-Saclay.

Information concerning the diffusion of vacancies not coupled with hydrogen would be obtained from the analysis of non-charged materials and comparisons with H-vacancy couple diffusion may be done by analyzing pre-charged model materials. Once the evolution of vacancies during non-isothermal conditions have been characterized, a second problem arises concerning the numerical analysis and simulation of these interactions.

The McNabb and Foster equations [107] were not designed to address and treat systems were trap site densities are evolving with time and position, as can be assumed with vacancies (i.e. annihilation, diffusion out of the material and/or creation). The system of equations would have to be rederived (as briefly mentioned in Chapter 3) for a system which can consider trap site diffusion and trap site density evolution, as vacancies or vacancy clusters are eradicated and/or created during a temperature ramp. Furthermore the diffusion of vacancies (mono-, di- or clusters) would need to be considered along with the diffusion of hydrogen-vacancy couples as in literature different vacancy type and H-vacancy pairs present different diffusion coefficients. Hopefully non-isotherm DSC and/or resistivity measurements would be able to provide more information on this diffusion in order to inject these parameters into the numerical code.

5.4.1.3 Hydrogen stress field interactions

Industrial materials, i.e. pre-formed components, materials having formed an oxide or exposed to elevated temperatures, present complex stress fields and gradients. The presence of these stress fields has been shown to have an effect on hydrogen material interactions and plays an important role in hydrogen induced or enhanced degradation mechanisms [73, 116, 117, 170]. A next step in this study would be to look at interactions taking place under these conditions, and the effect they have on both absorption, trapping and desorption mechanisms.

Several studies have looked at the hydrogen uptake under applied stress and its influence on dislocation mobility, i.e. during tensile testing [44, 73, 130, 165]. As these experimental analyses have shown an effect of applied stress on hydrogen uptake it would seem important to study the desorption of hydrogen and/or deuterium under applied stress through *in-situ* tensile testing during TDS analysis.

During TDS analysis the temperature is ramped from room temperature to up to 1050 K. This increasing temperature may cause dislocations reorganization and evolution of their structure along with changes in microstructure. This “moving

TS" phenomenon was not taken into consideration in this study as it is too difficult to simulate at this point in time. Adding this complexity to the numerical model will be approached more directly in future studies.

5.4.2 Desorption mechanism

Using a mass spectrometer for detection of desorbed molecular species in TDS provides some significant advantages as compared to methods targeted at monitoring uniquely one species or just the total system pressure. During TDS analysis on top of monitoring the deuterium ($^2H_2$, m/z = 4) flux, other "deuterated" species were monitored. These species may include ^{2}HH (m/z = 3), ^2H_2O (m/z = 20) and ^{2}HHO (m/z = 19). The characterization of deuterated species flux, especially ^{2}HH may prove important as it's flux is significantly more intense than the flux of $^2H_2$ in TDS. The ^{2}HH signal may allow for a more precise characterization of less intense or weak spectral contributions.

Monitoring these species may also provide some information on deuterium recombination and isotopic recombination on the surface of the sample. If these isotopic recombination mechanisms can be characterized and understood, they may provide some more information on specific desorption mechanisms and insight to trapping and detrapping taking place in the material. The recombination of hydrogen and deuterium has been studied on catalyst surfaces such as platinum [171, 172], copper and nickel [173].

Leardini *et al.* [171] propose an interesting approach for studying the desorption-recombination mechanism of hydrogen and deuterium on the surface of platinum thin foils. Pre-hydrogenated and deuterated thin foils were then subjected to TDS analysis while a calibrated hydrogen or deuterium flux was passed across the sample. During the temperature ramp the charged H or ^{2}H would desorbed and undergo exchanges with the hydrogen or deuterium gas being passed over the foil. The recombination of these molecules can provide some insight on the H or ^{2}H desorption and recombination on the material surface *in situ* under non-isothermal conditions. This type of experimental approach may be adapted to our TDS system and allow for the quantification and possibly characterization of the ^{2}HH signal.

Chapter 6

Conclusions

This work was aimed at better understanding the interactions taking place between absorbed hydrogen and materials susceptible to **S**tress **C**orrosion **C**racking (SCC) when they are exposed to the **P**ressurized **W**ater **R**eactor (PWR) primary circuit medium. Two alloys were studied in-depth: (i) nickel base alloy 600 (A600) and (ii) stainless steel 316L (SS316L). These alloys which make up some important structural elements of PWRs, for example the steam generator tubes (A600) and some reactor internal component (SS316L). Hydrogen is present in the primary circuit medium in the form of dissolved hydrogen gas ($H_{2(g)}$) and water (H_2O). Thus, the interaction between primary medium and exposed alloys can lead to H uptake by the alloy.

After absorption, hydrogen can be transported across the alloy. During this transport it will interact with both the interstitial lattice sites and any heterogeneities present in the crystalline structure. These heterogeneities may include: grain boundaries, dislocations, vacancies, precipitates, etc. Hydrogen atoms may have a stronger affinity or interact differently with these sites and in turn may become trapped at these heterogeneities. This "trapping" effect may slow the apparent hydrogen diffusivity and cause a local accumulation of hydrogen at these **T**rap **S**ites (TS) in the alloy. The local accumulation of hydrogen may in turn cause a local degradation of mechanical properties and thereby increase the susceptibility of the alloy to environmental degradation mechanisms and crack formation.

6.1 General overview of the study

This study coupled an experimental approach with numerical simulation for the characterization of both the interstitial diffusion and trapping (at potential trap sites) of hydrogen in two austenitic alloys, A600 and SS316L, and two trap site types, chromium carbides (Cr_7C_3), in A600, and dislocations, in A600. In order to work with a well characterized and not too complex material system **M**odel **M**aterials (MM) were used. These materials were fabricated from the industrial base materials (A600 and SS316L) through a series of thermal or thermomechanical treatments. The first step was eliminating (the majority) of traps sites, thereby leaving a material where all interactions may be attributed to diffusion; this material has been referred to as a **P**ure **D**iffusion **S**ystem (PDS). Then from this PDS, an isolated type of trap site was recreated in a controlled manner creating a **D**iffusion and **T**rapping **S**ystem (DTS) where all H-material interactions could be associated with diffusion and trapping (at isolated traps, i.e. chromium carbides or dislocations) phenomena.

After fabrication, these model materials were charged with deuterium (^2H), a isotopic hydrogen tracer and then analyzed by **T**hermal **D**esorption mass **S**pectroscopy (TDS). The first step in hydrogen-material interaction characterization was to

characterize the interstitial diffusion taking place in the material. To do so, model TDS spectra were acquired on pure diffusion system materials. To characterized these spectra, the developed numerical code was used. This code was based upon the McNabb and Foster equations [107] for diffusion and trapping in a crystalline material. From fitting the experimental TDS spectra using a numerical routine the **hydrogen diffusion coefficient parameters (D_0 and E_D) in A600 and SS316L were derived** (Table 6.1). One large advantage of TDS analysis is that it allows for continuous monitoring in a large range of temperatures; thereby allowing for the **derivation and validation from 294 K to 800 K, in non-isothermal and isothermal situations**. After the interstitial diffusion in these alloys was characterized, the trapping and detrapping interactions taking place at one type of trap site were explored.

Table 6.1 Derived diffusion coefficients for a A600 and SS316L pure diffusion system model materials

Material type	D_0 ($cm^2.s^{-1}$)	E_D ($kJ.mol^{-1}$)	D at 298 K ($cm^2.s^{-1}$)	D at 409 K ($cm^2.s^{-1}$)
A600-PDS	$(1 \pm 0.5)\ 10^{-2}$	45 ± 5	$\approx 1.3\ 10^{-10}$	$\approx 1.8\ 10^{-8}$
SS316L-PDS	$(1 \pm 0.8)\ 10^{-3}$	45 ± 3	$\approx 1.3\ 10^{-11}$	$\approx 1.8\ 10^{-9}$

Once again, experimental TDS analyses on DTS model materials, on which a trapping contribution had been isolated, through a specific aging procedure, were coupled with the numerical simulation method and fitting routine in order to **determine the kinetic trapping and detrapping constant parameters for potential trap sites in A600** (Table 6.2). Furthermore, the derived kinetic constant parameters for chromium carbides (inter- and intragranular (IIC) and along grain boundaries (GBC)) and dislocations are the **first complete sets of kinetic trapping and detrapping constants in A600 in literature** and among the only complete sets for all alloys [105].

6.2 Final conclusions

This study has explored in-depth the hydrogen-material interactions, concerning diffusion and trapping, taking place in two austenitic alloys. It has shed some light on the difficulties that may be encountered when analyzing these interactions using traditional methods and moreover the need for coupling experimental analyses with numerical simulation in order to address these interactions and not draw misleading conclusions.

Some noteworthy contributions that have been made to the nuclear field, and other domains where hydrogen material interactions are important, are the:

Table 6.2 Derived "best-fit" trapping (k) and detrapping (p) kinetic constant parameters for trapping at chromium carbides (Cr_7C_3, according to TEM diffraction patterns, see Chapter 3) located both inter- and intragranular (IIC) or uniquely along grain boundaries (GBC) and dislocations in A600.

	Trapping (k)		Detrapping (p)	
	k_0 (s^{-1})	E_k ($kJ.mol^{-1}$)	p_0 (s^{-1})	E_p ($kJ.mol^{-1}$)
Cr_7C_3-IIC	$(1.5 \pm 0.2)\ 10^7$	50 ± 4	$(1.5 \pm 0.2)\ 10^6$	80 ± 4
Cr_7C_3-GBC	$(1.5 \pm 0.2)\ 10^8$	50 ± 4	$(1.5 \pm 0.2)\ 10^6$	78 ± 4
Dislocations	$(1.5 \pm 0.2)\ 10^6$	42 ± 4	$(1.5 \pm 0.2)\ 10^6$	76 ± 4

- **derivation of hydrogen diffusion coefficients** which have been validated over a large range of temperatures,
- **derivation of trapping and detrapping kinetic constants** pertaining to two trap sites types in A600 (chromium carbides and dislocations) and
- **demonstration that grain boundaries can be considered to have a negligible effect on H diffusion in A600 in the range of 294 K - 800 K**.

Furthermore some important **advancements in the development of a numerical code simulating and predicting these interactions based upon the McNabb and Foster** equations have been made. This includes the:

- simulation hydrogen diffusion and trapping simultaneously,
- prediction interstitial and trapped hydrogen populations and
- simulation of (experimental) desorption spectra,

for all stages in experimental analysis, thereby considering the sample "history". These conditions include the time (t), temperature (T), and temperature variations ($T(t)$ and ϕ) of H charging, transfer and/or aging and TDS analysis. Furthermore the **code is relatively easily adaptable to more complex systems**, for example:

- multiple trap site types,
- non-homogeneous distributions of trap sites,
- trap site density evolution and

- two or three-dimensional systems.

Furthermore it should be rementioned that the treatment of a system where trap site density evolves with regards to t and/or T (for example for the case of vacancies) or in order to take into consideration the effect of imposed stressed (during absorption and/or desorption) will be important when considering more complex industrial systems. The numerical code will have to be adapted to address these situations and how experimental consideration of these types of site will be done may need to be reevaluated. These improvements are part of the perspectives of the study.

The novel approach that has been developed during this study (i.e. TDS on model materials coupled with numerical fitting and simulation) has the possibility to be applied to different types of metals and alloys and is not limited to only addressing hydrogen-material interactions for nuclear energy applications, for example steel making and hydrogen storage applications.

Furthermore, the results obtained from this study have helped to lay the foundation for a much larger database of diffusion information and kinetic trapping and detrapping constants. This kinetic information may be incorporated into a much larger calculation code taking into consideration other phenomena that may play a role in the SCC of PWR component materials. Before this end goal can be achieved, this data would need to be paired with a kinetic model for the absorption of hydrogen in PWR primary medium under reactor operation conditions, with concomitant oxide scale formation in order to have a more complete vision of the role hydrogen plays in the SCC phenomenon in PWRs primary medium.

Chapter 7

Résumé en français

7.1 Contexte et objectifs

Parmi les 440 réacteurs nucléaires en service dans le monde à l'heure actuelle, près de 350 sont des **R**éacteurs à **E**au **L**égère (REL). Ces réacteurs sont souvent classés en deux catégories : (i) les **R**éacteurs à **E**au **P**ressurisée (REP) and (ii) les **R**éacteurs à **E**au **B**ouillante (REB). En France les 58 réacteurs nucléaires en service sont de type REP et assurent près de 75 % de la production nationale d'électricité. Ces réacteurs ont été initialement conçus pour fonctionner durant 30 à 40 ans. Toutefois, moyennant des investissements destinés à les actualiser, il semble aujourd'hui possible de prolonger leur durée de vie jusqu'à 80 ans. Comme la majorité des réacteurs français arrivent au terme de la durée de vie prévue initialement, la question de l'extension de cette durée de vie se pose actuellement. Une éventuelle extension de la durée de vie implique de garantir la sécurité et la sureté des installations. Durant les quarante dernières années, en plus des opérations de maintenance et des nouvelles mesures de sécurité mises en place (i. e. remplacement ou réparation des composants, amélioration des systèmes de contrôle, etc.), des recherches ont été conduites avec pour objectif de mieux comprendre les phénomènes de dégradation intervenant durant le fonctionnement des réacteurs.

Parmi les mécanismes de dégradation mis en jeu, la fissuration par **C**orrosion **S**ous **C**ontrainte (CSC) est l'un des plus délétères. Ce mécanisme de corrosion intervient lorsqu'un matériau métallique, soumis à des contraintes internes ou appliquées, est exposé à un environnement agressif. Plusieurs études ont établi un lien entre ce phénomène de corrosion et la présence d'hydrogène, introduit notamment dans le milieu primaire des REP sous la forme d'une surpression de H_2 de l'ordre de 0,3 bar à 598 K. L'objectif de cette étude est de mieux appréhender le rôle de l'hydrogène dans la corrosion sous contrainte, en se focalisant sur une meilleure compréhension des interactions hydrogène/matériau en termes (i) de diffusion et (ii) de piégeage par des défauts microstructuraux ou des impuretés, qui sont intrinsèquement présents au sein des matériaux industriels.

7.1.1 Principe de fonctionnement d'un REP

Les réacteurs à eau pressurisée peuvent être décomposés en trois circuits, Fig. 7.1 :

- le circuit primaire,
- le circuit secondaire,
- et le circuit de refroidissement qui peut être un océan, une rivière, ou un circuit fermé (non représenté sur la figure).

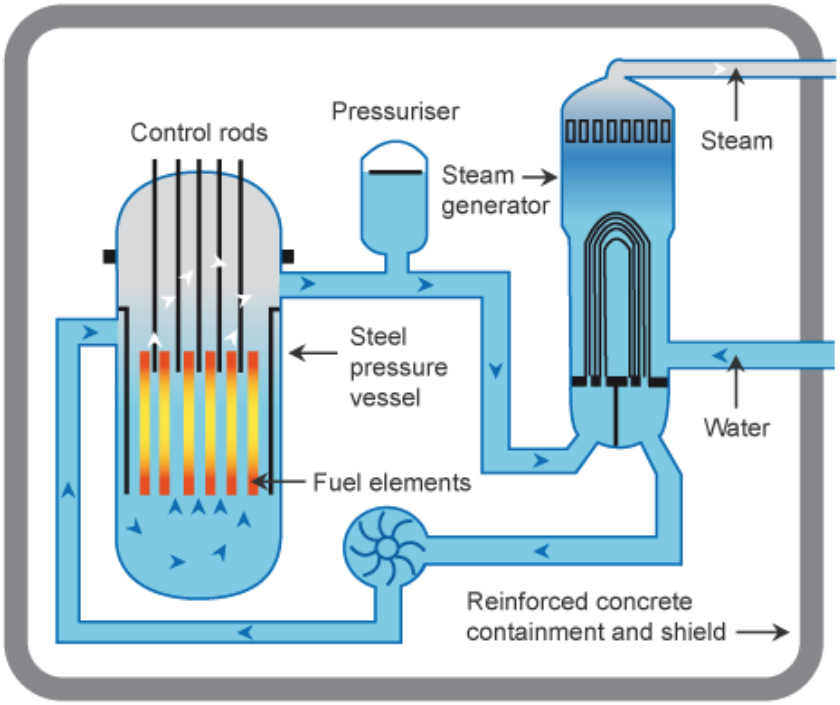

Fig. 7.1 Schéma de principe d'un réacteur à eau pressurisée (www.world-nuclear.org).

Le combustible, source de chaleur et d'énergie dans le réacteur, est l'élément central du cœur d'un réacteur nucléaire. Le combustible des réacteurs de type REP se présente sous la forme de pastilles en céramique, fabriquées par pressage et frittage de dioxyde d'uranium (UO_2). Ces pastilles sont ensuite placées dans une gaine métallique, généralement fabriquée en alliage de zirconium. Après assemblage, les gaines de combustible sont placées dans le cœur du réacteur où elles seront au contact du fluide circulant dans le circuit primaire.

Table 7.1 Conditions du milieu primaire des REP.

Température	558 - 598	K
Pression	155	bar
Bore (H_3BO_3)	10 - 1200	ppm
Lithium (LiOH)	0.7 - 2.2	ppm
Hydrogène (H_2)	25 - 50	$cm^3.kg^{-1}$(NPT)
pH_{573K}	≈ 7	

La chaleur produite par la réaction de fission est ainsi transférée au fluide primaire. La composition et les conditions de température et de pression régnant dans ce milieu sont présentées dans la Table 7.1. La chaleur transportée par le milieu primaire est ensuite transférée vers le circuit secondaire via le réseau tubulaire du générateur de vapeur (i.e. l'échangeur thermique) qui constitue une barrière physique entre les deux circuits et a donc également pour fonction de prévenir la contamination de l'environnement par les radionucléides contenus dans le circuit primaire.

Le transfert thermique entre les circuits primaire et secondaire conduit à la vaporisation du milieu secondaire. La vapeur d'eau ainsi produite circule dans le circuit secondaire jusqu'à la turbine qui permet de convertir l'énergie thermique en énergie électrique. La vapeur est ensuite condensée grâce à l'échange thermique avec le circuit de refroidissement puis l'eau issue de cette condensation circule vers le générateur de vapeur ce qui assure la continuité du cycle.

7.1.2 Hydrogène et corrosion sous contrainte

La corrosion sous contrainte est un mécanisme de dégradation des matériaux en environnement qui résulte de l'interaction entre des facteurs internes associés au matériau lui-même et des facteurs environnementaux (facteurs externes). Ce mode de dégradation affecte principalement des matériaux réputés pour leurs bonnes propriétés de résistance à la corrosion. Ce type de fissuration a été observé sur les composants des réacteurs de type REP, en particulier sur les tubes de générateur de vapeur fabriqués en alliages à base nickel et sur les composants internes de la cuve qui sont fabriqués en aciers inoxydables austénitiques.

Plusieurs études, durant les soixante dernières années, suggèrent que la présence d'hydrogène peut jouer un rôle dans le phénomène de CSC. L'hydrogène est présent

à la fois dans les milieux primaire et secondaire du réacteur (i) sous la forme d'eau (H_2O) mais aussi, dans le cas du milieu primaire spécifiquement, (ii) sous la forme d'hydrogène gazeux dissous (25 - 50 $cm^3.kg^{-1}$ (NPT)) dans le milieu (Table 1.1). Or, l'hydrogène peut impacter les processus de corrosion de différentes manières telles que : (i) avoir un effet sur la cinétique de formation de la couche d'oxyde protectrice s'établissant à la surface des parois des circuits primaire et secondaire, (ii) avoir un effet thermodynamique sur la structure et la stabilité de la couche d'oxyde se développant à la surface de l'alliage et l'hydrogène peut modifier la structure et donc la stabilité de la couche d'oxyde, (iii) avoir une influence sur les cinétiques d'amorçage et/ou de propagation des fissures, et (iv) avoir une influence, une fois absorbé, sur les propriétés mécaniques de l'alliage.

Une fois absorbé par l'alliage, l'hydrogène se propage au travers du matériau. Il peut alors interagir avec les sites interstitiels du réseau cristallin mais aussi avec différents défauts cristallographiques ou hétérogénéités présents au sein du matériau (Fig. 7.2). Les atomes d'hydrogène peuvent interagir différemment avec ces sites. Ces derniers peuvent avoir un effet de "piégeage" et ainsi ralentir la diffusion de l'hydrogène. Ce phénomène peut causer une accumulation locale d'hydrogène sur les sites de piégeage (TS) qui peut en retour induire une dégradation locale des propriétés mécaniques et par la suite sensibiliser l'alliage vis-à-vis des phénomènes de dégradation sous environnement et notamment favoriser la formation de fissures.

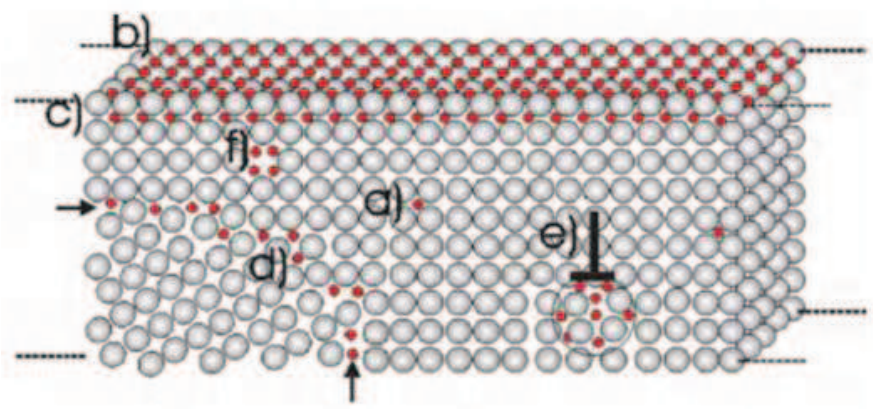

Fig. 7.2 Schéma des différents types de sites avec lesquels l'hydrogène est susceptible d'interagir dans un matériau cristallin : site interstitiel (a), sites de surface (b) et de subsurface (c), joint de grains (d), dislocation et champ de contrainte associé (e), et lacune (f) [1].

7.1.3 Plan et objectifs du manuscrit

Dans les pages qui vont suivre, le rôle que l'hydrogène peut jouer dans la CSC, spécifiquement au travers des interactions hydrogène-matériau qui résultent des phénomènes de diffusion et de piégeage, fait l'objet d'une étude approfondie. Pour comprendre ces phénomènes, une approche couplant études expérimentales et développement d'une méthode de simulation numérique a été mise en œuvre dans l'objectif de déterminer le coefficient de diffusion réticulaire de l'hydrogène ainsi que les constantes cinétiques de piégeage et de dépiégeage associées à différents types de site (dislocations, précipités, etc.) présents dans les matériaux industriels.

Ce manuscrit est scindé en cinq chapitres. La première partie dresse une synthèse bibliographique des données publiées sur le sujet (chapitre 2). Puis, les matériaux et les méthodes expérimentales utilisées, ainsi que la méthode numérique développée dans ces travaux sont présentés dans une deuxième partie (chapitre 3). Les résultats expérimentaux et de simulation obtenus sont ensuite présentés dans le chapitre 4, suivi d'une discussion des résultats et des perspectives qu'ils permettent de dégager (chapitre 5). Ce manuscrit se conclut par le chapitre 6 qui présente un bref résumé des travaux réalisés et replace cette contribution dans le contexte des études de corrosion sous contrainte spécifiquement, mais également de manière plus générale dans les domaines d'étude où les interactions H-matériaux se révèlent prépondérantes (i.e. fabrication d'acier, stockage d'hydrogène, etc.) afin d'ouvrir de nouvelles perspectives.

7.2 Etat de l'art : résumé

Dans les conditions physico-chimiques régnant dans le circuit primaire des REP, les matériaux de structure tels que l'alliage 600 et l'acier inoxydable 316L se révèlent sensibles à la CSC. Ce mécanisme de dégradation sous environnement agressif est le résultat d'une synergie entre des facteurs internes (liés au matériau) et externes (relatif à l'environnement). Parmi les facteurs internes, on peut citer à titre d'exemple : (i) les propriétés métallurgiques et microstructurales (composition chimique, chimie locale aux joints de grains, présence de précipités, etc.) ainsi que (ii) les contraintes résiduelles résultant par exemple de la mise en forme des composants. Les facteurs externes incluent quant à eux les paramètres décrivant les conditions d'exposition : (i) la température, (ii) la pression, (iii) la contrainte appliquée et (iv) la chimie du milieu (pH, $p(H_2)$, etc.). Plusieurs modèles ont été proposés pour expliquer ou prédire l'occurrence des fissures de corrosion sous contrainte mais à l'heure actuelle, aucun d'entre eux n'est capable d'expliquer ou de prédire ce phénomène de dégradation dans son ensemble. Parmi ces modèles,

nombreux sont ceux qui proposent un rôle de l'hydrogène présent dans le milieu primaire (que ce soit sous la forme d'hydrogène dissous et/ou du solvant lui-même). Au cours du processus d'oxydation en milieu primaire, de l'hydrogène peut être absorbé par l'alliage. Après absorption, l'hydrogène va progresser depuis la surface vers le cœur du matériau et interagir avec les différents sites cristallographiques existant au sein du matériau. Ces sites peuvent notamment être : (i) des sites interstitiels du réseau cristallin, (ii) des défauts ponctuels tels que des lacunes ou des hétéroatomes, (iii) des défauts à une dimension tels que les dislocations et les jonctions triples, (iv) des défauts à deux dimensions comme les joints de grains et les interfaces ainsi que des défauts à trois dimensions comme par exemple les cavités, les précipités et les inclusions (Fig. 7.2).

Un point régulièrement souligné par les chercheurs développant des modèles numériques destinés à l'étude de la diffusion et du piégeage de l'hydrogène est la nécessité d'acquérir des résultats expérimentaux à partir de matériaux dits modèles, dont l'état métallurgique est bien connu. Cette notion de matériau modèle implique que toutes les interactions relatives à la diffusion et au piégeage au sein de ce matériau sont connues et peuvent ainsi être prises en considération lors de la modélisation. La démarche présentée dans ces travaux s'appuie sur ce concept : des matériaux présentant uniquement un type de site de piégeage ont été élaborés et utilisés dans cette étude dans l'objectif de caractériser aussi finement que possible les interactions prenant place entre l'hydrogène et un type de site donné. Ces matériaux ont été analysés expérimentalement via la spectroscopie de désorption thermique (TDS) qui est une technique de caractérisation particulièrement adaptée pour l'étude des interactions hydrogène-matériau telles qu'introduites dans ce chapitre. Le modèle numérique qui a été développé pour analyser les résultats expérimentaux est basé sur les équations de McNabb et Foster [107]. Ce modèle fournit une formalisation mathématique facilement adaptable aux phénomènes de diffusion et de piégeage qui prennent place de manière concomitante dans les matériaux métalliques. Bien que ce modèle ne soit pas aussi complet que ceux proposés dans les travaux de Leblond [112, 113, 114], il permet de simuler l'évolution du piégeage sur un ou plusieurs types de site [108] pour un système dont la température évolue dans le temps (i. e. typiquement pendant une expérience de TDS) sans qu'il soit nécessaire de s'appuyer sur des hypothèses très restrictives (comme l'hypothèse de l'équilibre thermodynamique local entre l'hydrogène piégé et l'hydrogène réticulaire) comme c'est souvent le cas dans plusieurs autres modèles [69, 108, 124, 134, 145].

Le corps de ce manuscrit est constitué de trois chapitres supplémentaires. En premier lieu, une présentation des matériaux, des techniques expérimentales et de la démarche de simulation mis en œuvre est proposée dans le chapitre suivant. Les résultats expérimentaux sont ensuite présentés et discutés, avant un dernier

chapitre centré sur les conclusions et les perspectives de cette étude.

7.3 Matériaux et Méthodes: résumé

7.3.1 Matériaux

Deux alliages austénitiques industriels, un alliage à base nickel de type A600 (coulée WL344) fourni par Imphy et une nuance commerciale d'acier inoxydable de type 316L, ont été utilisés dans cette étude. Un monocristal de composition proche de l'alliage 600 et dont la direction de croissance est $< 111 >$, fourni par l'Ecole Nationale Supérieure des Mines de Saint-Etienne (Saint-Etienne, France), a également été étudié.

Afin de pouvoir étudier de manière isolée la diffusion réticulaire de l'hydrogène dans les alliages industriels, il est nécessaire d'éliminer l'ensemble, ou du moins une grande majorité des sites de piégeage éventuels existant au sein de l'alliage. Les sites de piégeage en question incluent notamment les dislocations (issues des contraintes internes et de l'écrouissage résiduel), les carbures de chrome (Cr_xC_y) et les lacunes présentes au sein du réseau cristallin [83]. La majorité de l'écrouissage résiduel, des contraintes, des lacunes et des précipités de Cr_xC_y (dans le cas de l'A600) a été éliminé via une série de traitements thermiques comme le montre la figure Fig. 7.6. Ce type de matériau est désigné par la suite via la notation PDS. Le matériau PDS de l'A600 peut être observé sur la Fig. 7.3

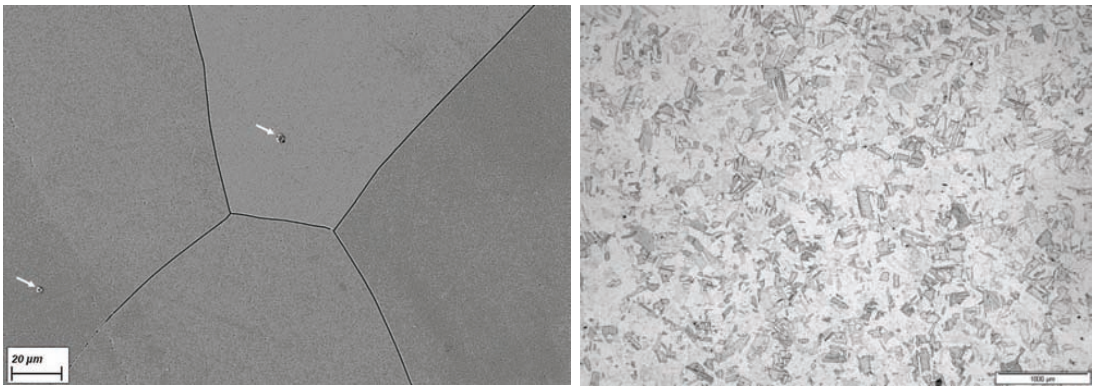

(a) **(b)**

Fig. 7.3 Observations microscopique(par microscope électronique à balayage (a) ou microscope optique (b)) du matériau modèle PDS (a) A600 et (b) SS316L. Les flèches blanches indiquent les TiCN qui restent présents dans le matériau même après le traitement thermique.

La majorité des sites de piégeage préexistants, incluant les Cr_xC_y et les disloca-

tions, ont été éliminés durant le traitement thermique permettant l'élaboration des matériaux de type PDS. L'étude des interactions entre l'hydrogène et les carbures de chrome ou les dislocations nécessite donc de recréer ce type de piège de manière contrôlée. Afin de mieux comprendre les interactions H-dislocations, un matériau modèle dans lequel les sites de piégeage potentiels sont limités de manière quasi-exclusive à des dislocations a été élaboré. A cette fin, un protocole d'élaboration a été défini. Ce protocole consiste tout d'abord en une déformation contrôlée du matériau (afin de créer des dislocations) suivie d'un revenu visant à éliminer les lacunes créées durant la déformation. Des matériaux modèles appelés DTS-D sont ainsi créés pour l'alliage 600 et l'acier 316L avant d'être caractérisés, voir Fig. 7.4. Une méthode a également été utilisée pour permettre la reprécipitation des carbures de chrome dans un matériau modèle de type A600-PDS de manière contrôlée [10], soit préférentiellement aux joints de grains (ce matériau est désigné par la notation DTS-GBC par la suite), soit dans l'ensemble du volume, ce matériau étant désigné par la notation DTS-IIC par la suite.

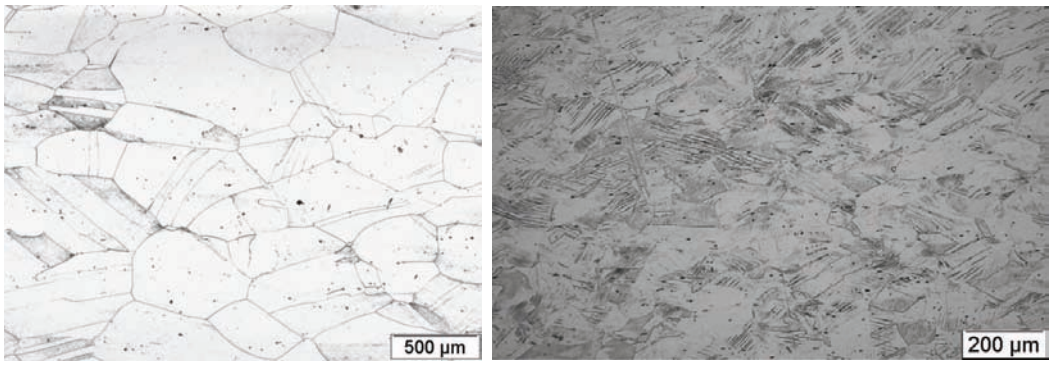

(a) **(b)**

Fig. 7.4 Observations en microscopie optiques des échantillons DTS-D en (a) A600 et (b) SS316L.

Le diagramme présenté dans la Fig. 7.6 résume l'ensemble des traitements thermomécaniques mis en œuvre dans le cadre de cette étude pour l'élaboration des différents matériaux modèles étudiés.

7.3.2 Technique expérimentale et méthode numérique

Afin d'étudier les interactions H-matériau, la technique expérimentale utilisée dans ces travaux est la TDS. Cette méthode permet l'acquisition des flux de désorption de différentes espèces chimiques issues du matériau pendant que celui-ci est soumis à une rampe de température ou à un maintien isotherme.

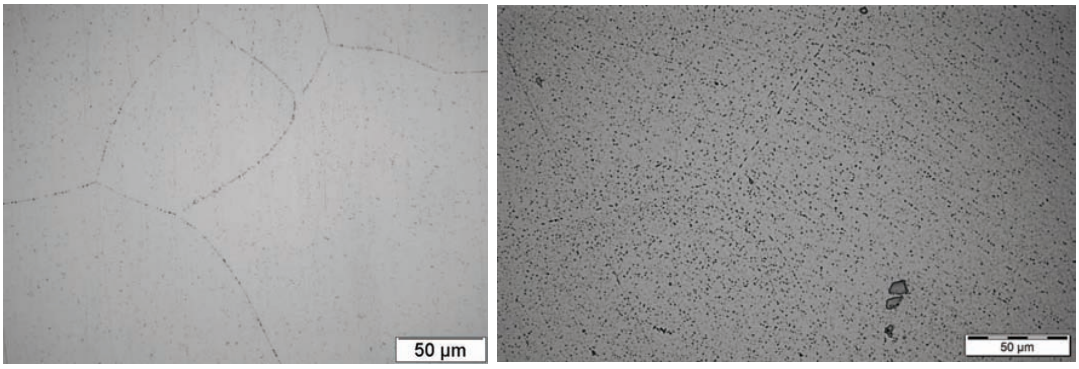

(a) **(b)**

Fig. 7.5 Observations en microscopie optique des échantillons (a) DTS-GBC et (b) DTS-IIC.

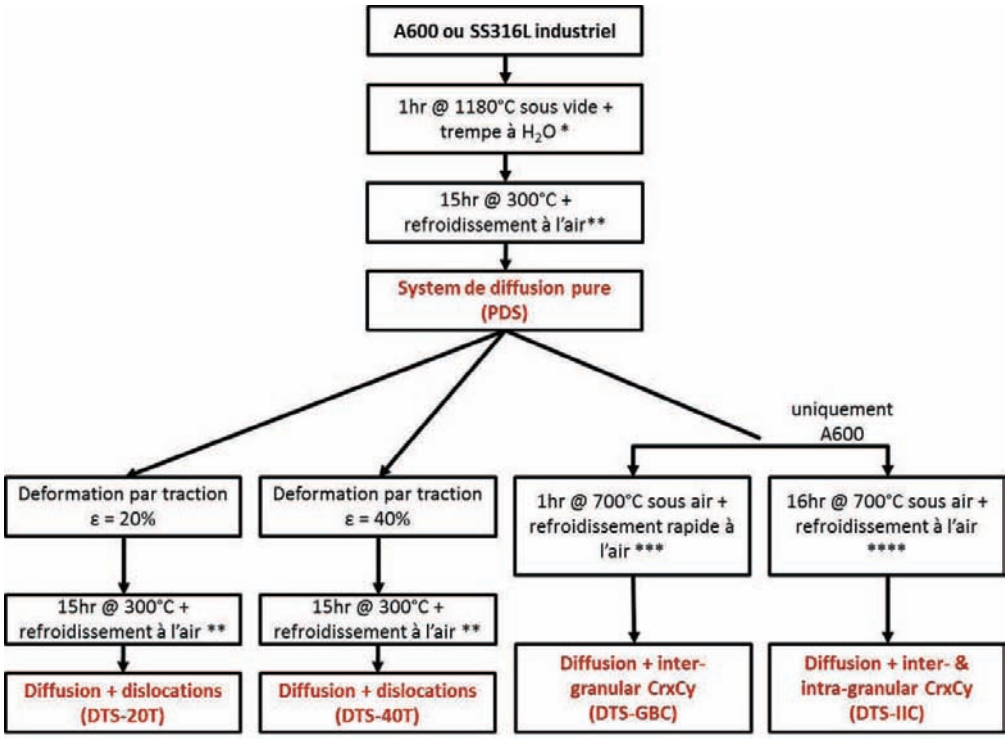

Fig. 7.6 Diagramme détaillant la série de traitements thermomécaniques mis en oeuvre afin d'élaborer les matériaux modèles (MM) étudiés. * recristallisation et élimination de l'écrouissage résiduel et des carbures de chrome éventuellement (cas de l'A600), ** élimination des lacunes, *** et **** reprécipitation de carbures de chrome (seulement dans le cas de l'A600).

Comme mentionné précédemment, l'objectif de cette étude est de construire une base de données de coefficients de diffusion et de constantes cinétiques de piégeage et de dépiégeage relative aux interactions entre l'hydrogène et certains alliages industriels. Pour se faire, l'idée est de coupler des résultats expérimentaux obtenus par TDS avec un code numérique qui permette d'extraire le coefficient de diffusion (D) du deuterium dans les alliages étudiés ainsi que les constantes cinétiques de piégeage et de dépiégeage (respectivement k et p) associées à certains types de pièges via la simulation des spectres expérimentaux obtenus. Il est supposé que l'évolution de ces coefficients et constantes avec la température suit une loi d'Arrhenius ce qui permet d'obtenir l'évolution des constantes du système étudié en fonction de la température. Dès lors, extraire le coefficient de diffusion des spectres obtenus nécessite de déterminer à la fois le facteur pré-exponentiel (D_0) et l'énergie d'activation associée (E_D). De même, l'extraction des constantes cinétiques de piégeage et de dépiégeage, respectivement k et p, nécessite de déterminer leurs facteurs pré-exponentiels (k_0 et p_0) et les énergies d'activation associées (E_k et E_p), voir Eq. (7.1). Ces constantes sont déterminées à l'aide de deux outils numériques, **W**olfram **M**athematica© et **P**ython™.

$$\frac{\partial \mu}{\partial t} + N\frac{\partial \theta}{\partial t} = D\frac{\partial^2 \mu}{\partial x^2} \tag{7.1a}$$

$$\frac{\partial \theta}{\partial t} = k\mu(1-\theta) - p\theta \tag{7.1b}$$

$$D = D_0 \exp \frac{E_D}{RT} \tag{7.1c}$$

$$k = k_0 \exp\left(\frac{E_k}{RT}\right) \tag{7.1d}$$

$$p = p_0 \exp\left(\frac{E_p}{RT}\right) \tag{7.1e}$$

La nécessité de considérer tous les paramètres cinétiques dans les systèmes mettant en jeu la diffusion et le piégeage, ainsi que l'importance de la prise en compte des conditions expérimentales ayant un impact sur les profils de concentration en hydrogène piégé et réticulaire a été démontrée précédemment [89, 90]. Cela implique la prise en compte de (i) la rampe de température expérimentale, (ii) la durée et (iii) la température de chargement, (iv) le temps de transfert de l'échantillon et (v) la température associée, ainsi que (vi) son épaisseur. En tenant compte de ces différents paramètres, les phénomènes de piégeage et de dépiegeage prenant place pendant ces différentes étapes sont pris en compte dans la simulation finale du spectre expérimental, l'importance de l'histoire de l'échantillon ayant été démontrée et discutée dans la section 3.3.2.1 du manuscrit. De plus, il

est nécessaire d'utiliser un modèle numérique qui permette de déterminer simultanément les quatre paramètres cinétiques relatifs au piégeage et au dépiégeage (i. e. k_0, E_k, p_0 et E_p) ainsi que la densité de site associée (N). Pour atteindre cet objectif, le code de simulation développé est basé sur les équations initialement proposées McNabb et Foster [107].

Il n'est plus à démontrer que la spectroscopie de désorption thermique est un outil expérimental puissant qui permet potentiellement d'accéder à des données cinétiques relatives aux interactions hydrogène-matériau, notamment lorsque ces interactions impliquent des phénomènes de diffusion et de piégeage. Les simulations présentées dans ce manuscrit ont également révélé qu'à l'heure actuelle, les méthodes d'analyse spectrale communément utilisées peuvent permettre d'acquérir des données relatives à l'énergie d'activation de dépiégeage, mais seulement lorsque certaines conditions sont réunies, telles que par exemple une concentration en hydrogène homogène au travers de l'échantillon avant le début de l'expérience de TDS. Cette condition sur l'homogénéité initiale de la concentration peut être assez facilement obtenue expérimentalement dans le cas d'échantillons fins de matériaux dans lesquels la diffusivité de l'hydrogène est grande (tels que le fer pur ou les aciers ferritiques). Cela devient en revanche beaucoup plus difficile lorsque que l'on s'intéresse à des matériaux dans lesquels la diffusivité de l'hydrogène reste relativement faible, comme c'est le cas pour les alliages austénitiques. Le modèle numérique proposé ainsi que l'analyse spectrale associée sont facilement transposables à différents types de matériaux et de sites de piégeage dès lors que la démarche expérimentale mise en œuvre s'appuie sur l'étude de "matériaux modèles" dans l'objectif de construire une base de données relative au coefficient de diffusion et aux constantes cinétiques de piégeage et de dépiégeage. Une fois établie, cette base de données peut être utilisée pour simuler et prédire les interactions H-matériau dans le cas de métaux ou alliages présentant plusieurs types de site de piégeage. Dans la suite de ce manuscrit, ce modèle cinétique et l'utilisation de "matériaux modèles" sont couplés dans l'objectif d'acquérir des données cinétiques de piégeage et de dépiégeage dans le cas de deux alliages d'intérêt industriel.

La démarche proposée pour l'extraction et la validation de données cinétiques à partir du couplage entre simulation numérique et expériences de TDS sur matériaux modèles est résumée sur la Fig. 7.7.

7.4 Résultats : résumé

Les résultats obtenus quant à la diffusion et au piégeage de l'hydrogène dans l'alliage 600 et l'acier inoxydable 316L sont présentés et discutés dans cette partie. Comme évoqué dans la partie précédente, cette étude peut être scindée en deux axes : (i) l'un expérimental, relatif à l'acquisition de spectres TDS sur matériaux

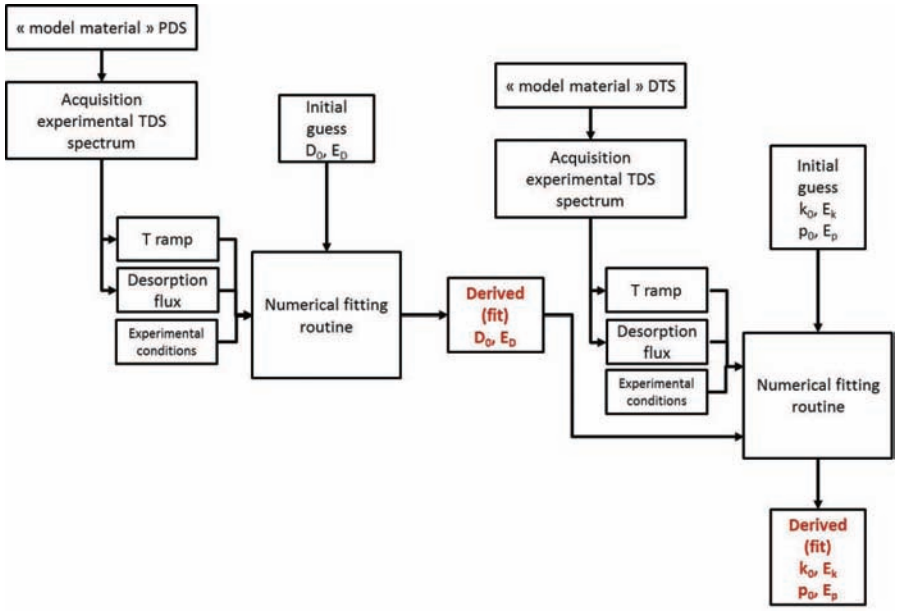

Fig. 7.7 Diagramme logique de la méthode numérique utilisée pour dériver les paramètres de diffusion et de piégeage/dépiégeage [90].

modèles et (ii) l'autre centré sur la simulation, utilisée ici pour déterminer les paramètres cinétiques liés à la diffusion (D_0 and E_D) et aux piégeage/dépiégeage de l'hydrogène (k_0, E_k, p_0 and E_p).

7.4.1 Observations expérimentales issues des spectres TDS

7.4.1.1 Spectres TDS obtenus directement après chargement en deutérium

L'analyse des spectres TDS obtenus directement après chargement en deutérium permet de mettre en évidence plusieurs éléments. Il peut tout d'abord être remarqué que les conditions de chargement mises en œuvre dans cette étude (i.e. 30 min de chargement dans une solution de NaO^2H 0,1 M (99,90 % ^2H) à 298 K sous une densité de courant cathodique imposée de -100 mA.cm^{-2}, l'épaisseur de l'échantillon étant inférieure à 0,01 cm) génèrent un fort gradient de concentration en ^2H au sein des matériaux. Les effets "classiques" du piégeage sur les spectres TDS, à savoir :

soit (i) l'apparition d'un pic de désorption à basse température (attribué à la diffusion interstitielle de ^2H) et celle d'un second pic à plus haute température généralement associé aux phénomènes de piégeage [22, 82],

soit (ii) l'apparition d'un pic unique à haute température attribué généralement

au piégeage uniquement (ce qui implique que tout le ^{2}H désorbant dans ce cas ait été préalablement piégé),

n'ont pas été observés sur les systèmes modèles de diffusion et de piégeage étudiés ici. Il semble en effet que la seule différence observée expérimentalement, entre les spectres normalisés obtenus sur des échantillons dans lesquels la diffusion est prépondérante et ceux obtenus sur des échantillons dans lesquels les phénomènes de diffusion et de piégeage coexistent, soit une diminution de la température correspondant au maximum de désorption (T_m) dans le cas des échantillons contenant des pièges par rapport à ceux qui en sont exempts. Plusieurs hypothèses ont été proposées pour expliquer ce décalage :

(i.) la plus faible température associée au maximum de désorption peut être reliée à un coefficient de diffusion apparent du deutérium plus faible dans le cas des matériaux contenant une forte densité de pièges,

ou à l'inverse (ii.) les sites de piégeage peuvent former un réseau de chemins de diffusion préférentiels.

De plus, une comparaison directe entre les spectres obtenus sur des échantillons d'A600 polycristallin (mais quasi-exempt d'autres types de défauts), dans lesquels les joints de grains peuvent jouer soit le rôle de site de piégeage soit celui de courts-circuits de diffusion, et sur un monocristal du même alliage révèle que ces deux types de spectre ne peuvent être différenciés. Ce résultat indique a priori que soit l'effet des joints de grains n'est pas détectable sur les spectres TDS obtenus directement après chargement, soit les joints de grains ont un effet négligeable sur la diffusion et le piégeage de l'hydrogène dans cet alliage.

Comme les premiers résultats obtenus directement après chargement sur des échantillons d'A600 contenant différents types de piège n'ont pas permis de mettre clairement en évidence une contribution des phénomènes de piégeage sur les spectres TDS, une approche expérimentale différente a été adoptée, dans l'objectif de mieux mettre en exergue les interactions ^{2}H-site de piégeage.

7.4.1.2 Vieillissement des échantillons à température ambiante

Les résultants expérimentaux obtenus sur des échantillons chargés puis vieillis à température ambiante n'ont pas non plus permis d'obtenir des résultats probants vis-à-vis du piégeage de ^{2}H prenant place au sein des matériaux modèles. Il n'est pas possible, à partir de ces résultats, d'extraire des constantes cinétiques relatives au piégeage et au dépiégeage du ^{2}H sur les carbures de chrome ou les dislocations présentes dans les matériaux modèles étudiés. Ces résultats semblent toutefois

confirmer que les joints de grains ne jouent pas le rôle de courts-circuits de diffusion pour l'hydrogène dans l'alliage 600.

Il semble donc qu'un vieillissement à temperature ambiante ne permette pas d'exalter suffisamment le rapport entre hydrogène "piégé" et "interstitiel" pour observer une contribution claire associée au piégeage sur les spectres obtenus par TDS. C'est pour cette raison que des vieillissements à haute température ont été testés. Cette approche a pour objectif de conduire à une augmentation du rapport mentionné précédemment et ainsi permettre d'exalter une contribution résultant du piégeage de l'hydrogène sur les spectres de désorption obtenus suite à ce type de vieillissement.

7.4.1.3 Vieillissement des échantillons à haute température

Les spectres de désorption obtenus après vieillissement à 409 K semblent mieux mettre en évidence les différences entre les échantillons dans lesquels la diffusion est prépondérante et ceux dans lesquels les phénomènes de diffusion et de piégeage coexistent. La contribution associée au piégeage est en effet exaltée sur les spectres obtenus après vieillissement à haute température. Ces spectres peuvent ainsi être utilisés pour extraire des constantes cinétiques de piégeage et de dépiégeage à partir de la méthode de simulation numérique présentée dans le chapitre 3, cf. Fig. 7.7. La partie suivante présente la démarche mise en œuvre pour extraire et valider les paramètres cinétiques relatifs à la diffusion et au piégeage de l'hydrogène à partir de la comparaison entre spectres expérimentaux et spectres simulés.

7.4.2 Simulation de la diffusion de ^{2}H dans l'A600 et le SS316L

Une approche couplant les données expérimentales obtenues par TDS (sur les échantillons dits PDS) avec un code d'ajustement numérique a été utilisée pour extraire les données cinétiques relatives au coefficient de diffusion du deutérium (i. e. D_0 et E_D) dans l'alliage 600 (Fig. 7.8) et dans l'acier SS316L (Fig. 7.9). Les paramètres de diffusion ainsi extraits sont résumés dans le tableau Table 7.2.

Table 7.2 Synthèse des coefficients de diffusion de H obtenus à partir des données expérimentales collectées sur des matériaux modèles dans lesquels la diffusion est prépondérante (PDS), pour l'A600 et le SS316L.

Material type	D_0 ($cm^2.s^{-1}$)	E_D ($kJ.mol^{-1}$)	D at 298 K ($cm^2.s^{-1}$)	D at 409 K ($cm^2.s^{-1}$)
A600-PDS	$(1 \pm 0.5)\ 10^{-2}$	45 ± 5	$\approx 1.3\ 10^{-10}$	$\approx 1.8\ 10^{-8}$
SS316L-PDS	$(1 \pm 0.8)\ 10^{-3}$	45 ± 3	$\approx 1.3\ 10^{-11}$	$\approx 1.8\ 10^{-9}$

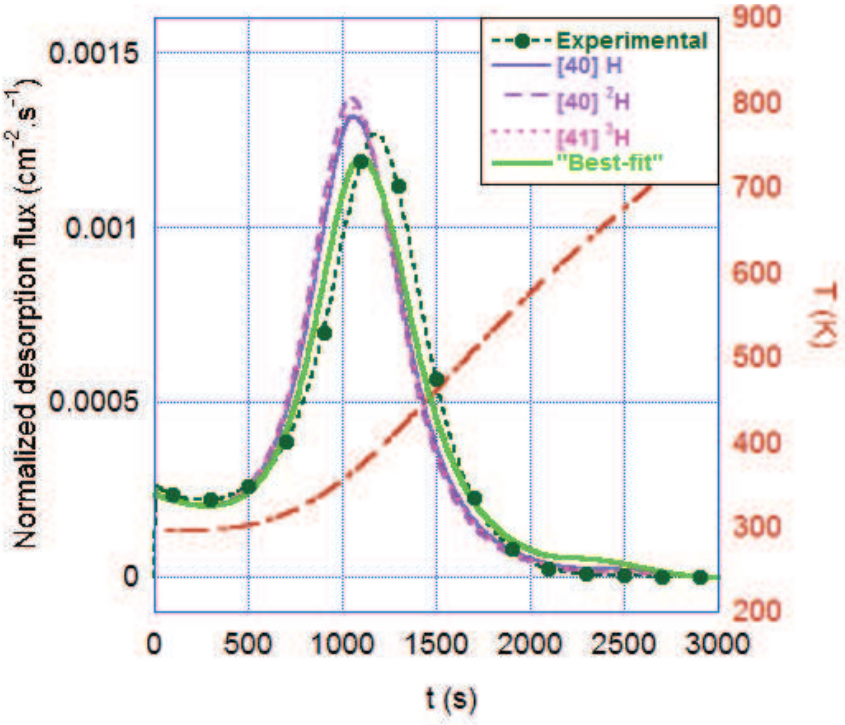

Fig. 7.8 Evolution du flux de désorption "normalisé" obtenu sur échantillon de type A600-PDS directement après chargement (Table 3.6) en fonction du temps et de la température ($\phi = 10$ K.min^{-1}) ; comparaison (i) aux spectres TDS simulés à l'aide des coefficients de diffusion de H et de ses isotopes dans l'A600 publiés dans la littérature [40, 41] et (ii) ajustement du spectre expérimental à l'aide du code numérique (Table 4.3) développé dans ces travaux.

Les paramètres ainsi extraits ont été testés via leur utilisation pour la simulation de spectres de désorption dits "hybrides", c'est à dire obtenus tout au long d'une expérience commençant par un vieillissement à température ambiante (294 $\pm$ 2 K) ou à haute température (409 $\pm$ 2 K) et se terminant par une expérience de TDS classique ($\phi = 10$ K.min^{-1}). Dès lors que les paramètres de diffusion déterminés précédemment permettent de simuler les spectres dits "hybrides", ils sont considérés comme validés (cf. Fig. 7.10 et Fig. 7.11).

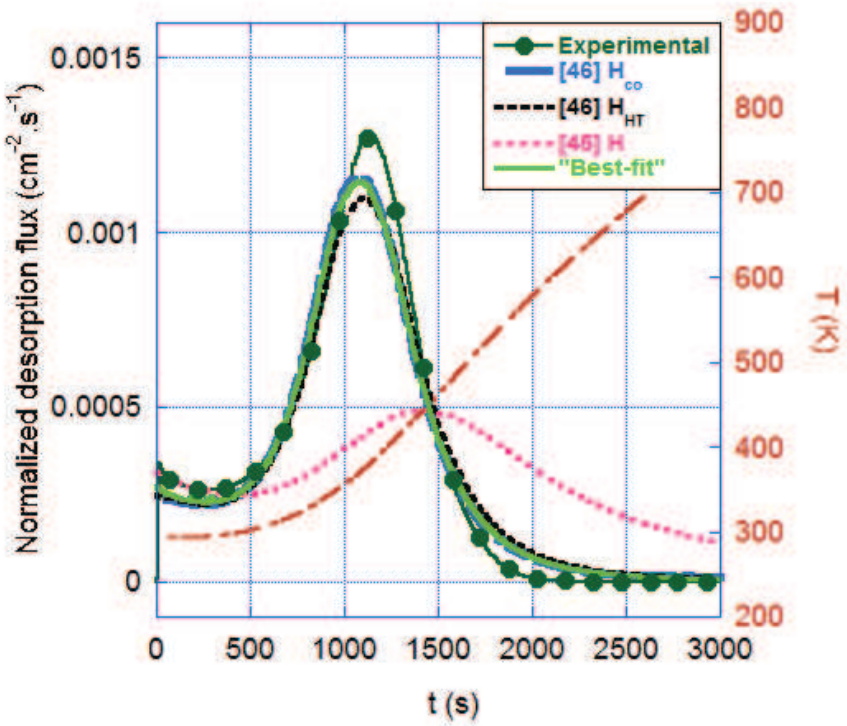

Fig. 7.9 Evolution du flux de désorption "normalisé" obtenu sur échantillon de type SS316l-PDS directement après chargement (Table 3.6) en fonction du temps et de la température ($\phi = 10$ K.min^{-1}) ; comparaison (i) aux spectres TDS simulés à l'aide des coefficients de diffusion de H dans le SS316L publiés dans la littérature [45, 46] et (ii) ajustement du spectre expérimental à l'aide du code numérique (Table 4.3) développé dans ces travaux.

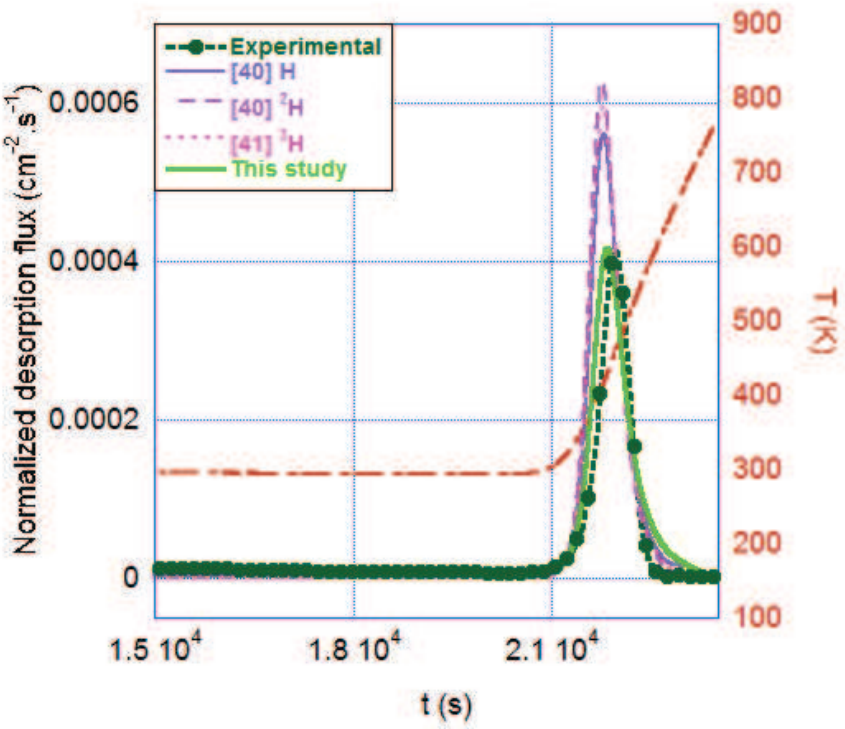

Fig. 7.10 Spectres TDS normalisés, obtenus expérimentalement ou simulés à partir des données publiées [40, 41] et collectées dans le cadre de ces travaux, dans le cas d'un échantillon de type A600-PDS vieilli 6h à température ambiante puis soumis à une expérience de TDS ($\phi = 10$ K.min^{-1}).

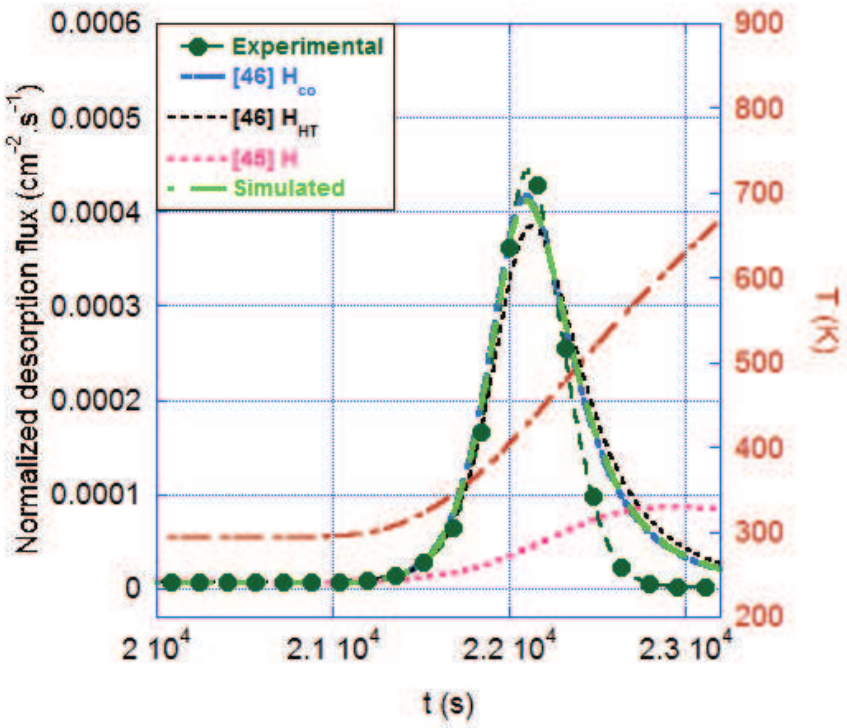

Fig. 7.11 Spectres TDS normalisés, obtenus expérimentalement ou simulés à partir des données publiées [45, 46] et collectées dans le cadre de ces travaux, dans le cas d'un échantillon de type SS316L-PDS vieilli 6h à température ambiante puis soumis à une expérience de TDS ($\phi = 10$ K.min^{-1}).

Maintenant qu'un jeu de paramètres de diffusion (Table 4.6) a pu être établi et validé à partir des expériences conduites sur des matériaux modèles dans lesquels la diffusion est prépondérante (PDS), l'étape suivante de cette étude va se focaliser sur l'extraction des constantes cinétiques de piégeage et de dépiégeage associées aux interactions prenant place entre l'hydrogène et les carbures de chrome ou les dislocations.

7.4.3 Simulation du piégeage de ^{2}H dans l'alliage 600

L'analyse de la majorité des résultats expérimentaux s'est révélée peu concluante car les contributions associées au piégeage se sont révélées difficiles à isoler par TDS dans la plupart des cas étudiés. Les seuls résultats expérimentaux permettant de mettre clairement en évidence un effet du piégeage ont été acquis à partir des spectres de désorption dits "hybrides", obtenus après un vieillissement à haute température (409 K). Ce type de vieillissement a conduit à la désorption de la majorité du deutérium "interstitiel" avant l'expérience de TDS, ce qui a permis

d'obtenir un spectre principalement représentatif de la contribution du ^{2}H "piégé" apparaissant à plus haute température que la contribution associée au deutérium diffusible. Cependant, en se basant simplement sur ces spectres, il apparaît difficile d'extraire de manière fiable un coefficient de diffusion ou des constantes cinétiques de piégeage et de dépiégeage.

Il est clair que l'extraction de données quantifiées à partir de ces spectres nécessite l'utilisation d'une méthode numérique. Les paramètres de diffusion ainsi déterminés ont ensuite été utilisés comme données d'entrée afin d'extraire les paramètres cinétiques relatifs au piégeage et au dépiégeage du deutérium (k_0, E_k, p_0 and E_p) à partir des spectres de désorption collectés sur des matériaux modèles dans lesquels un type de piège unique a été isolé (DTS). Puis, les valeurs caractéristiques du piégeage obtenues par ce biais ont été testées par la simulation de spectres obtenus sur ces mêmes matériaux mais dans des conditions expérimentales différentes. Les paramètres cinétiques de piégeage et de dépiégeage ainsi déterminés pour les carbures de chrome et les dislocations dans l'alliage 600 sont présentés dans le Table 7.3.

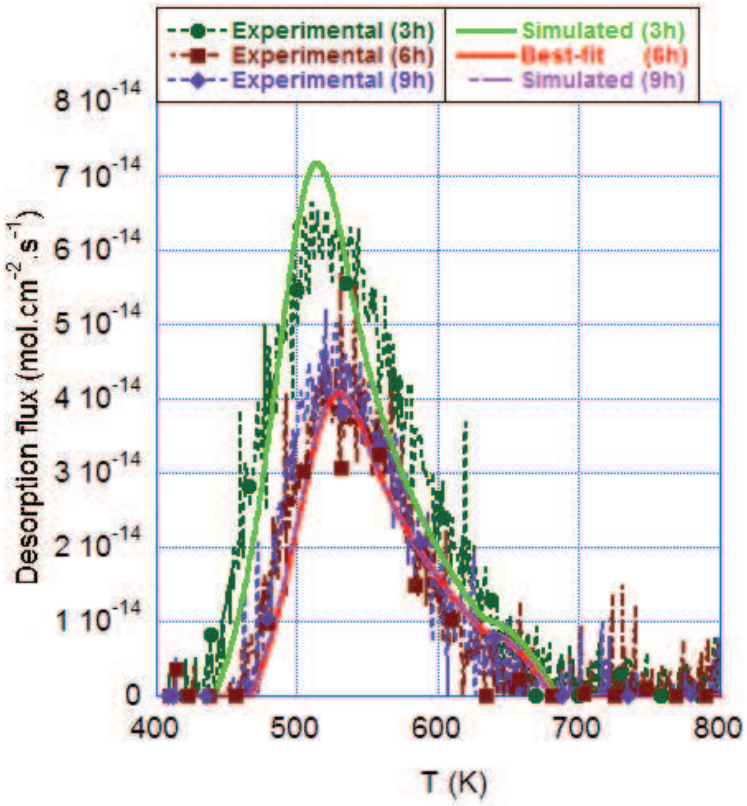

Fig. 7.12 Spectres TDS expérimentaux quantifiés obtenus sur des échantillons d'alliage 600 de type DTS-IIC après des vieillissements à haute température (409 K) de 6 h, 3 h and 9 h ; comparaison avec l'ajustement (pour un vieillissement de 6 h) et les simulations (pour des vieillissements de 3 h et de 9 h) réalisés. Ces simulations s'appuient sur les données de diffusion et les constantes cinétiques de piégeage/dépiégeage déterminées précédemment (Table 4.3 and Table 4.7) ainsi que sur une densité de site de piégeage (n) de 1,0 10^{-5} mol TS.mol A600^{-1}.

Table 7.3 Constantes cinétiques de piégeage (k) et de dépiégeage (p) du deutérium pour différents types de sites présents dans l'alliage 600 : des carbures de chrome (de type Cr_7C_3 d'après les analyses de diffraction électronique présentées au chapitre 3) inter- et intragranulaire (IIC) ou localisés principalement aux joints de grains (GBC) et des dislocations (D). Ces valeurs sont associées aux constantes de diffusion présentées dans le tableau Table 4.3.

	k_0 (s^{-1})	E_k ($kJ.mol^{-1}$)	p_0 (s^{-1})	E_p ($kJ.mol^{-1}$)	N (mol TS.mol $A600^{-1}$)
Cr_7C_3-IIC	$(1.5 \pm 0.2)\ 10^7$	50 ± 4	$(1.5 \pm 0.2)\ 10^6$	80 ± 4	$(1 \pm 0.2)\ 10^{-5}$ [a]
Cr_7C_3-GBC	$(1.5 \pm 0.2)\ 10^8$	50 ± 4	$(1.5 \pm 0.2)\ 10^6$	78 ± 4	$\approx 2.5\ 10^{-6}$ [b]
Dislocations $\epsilon = 40$ %	$(1.5 \pm 0.2)\ 10^6$	42 ± 4	$(1.5 \pm 0.2)\ 10^6$	76 ± 4	$\approx 1\ 10^{-4}$ [b]

[a] déterminé à partire des simulations quantifiés
[b] imposé en simulations

Un paramètres important, se révélant nécessaire pour les simulations numériques mais qui n'a pas toujours pu être vérifié via la démarche mise en œuvre, est la densité de site de piégeage (N mol TS.mol A600^{-1}). L'incapacité à déterminer ce paramètre de manière fiable n'est pas la conséquence d'un défaut de la méthode de simulation utilisée, mais résulte plutôt de la forte dispersion constatée sur les valeurs expérimentales associées à la quantité totale de deutérium désorbé (Fig. 4.1). Bien que la densité de site de piégeage déterminée dans ces travaux n'ait pas toujours pu être validée à partir de la simulation de spectres quantifiés, il semble qu'une certaine confiance puisse être attribuée à l'ordre de grandeur des valeurs obtenues du fait de la forte dépendance de la forme des spectres à ce paramètre (Fig. 4.38). Une bonne reproduction des spectres TDS expérimentaux obtenus sur les matériaux de type DTS n'aurait pas été possible si la valeur imposée pour ce paramètre n'était pas proche de la densité de site de piégeage "réelle".

De plus, ce chapitre a démontré la nécessité de coupler l'analyse des données expérimentales obtenues sur matériaux modèles avec une méthode de simulation numérique pour pouvoir extraire des spectres des données quantifiées quant à la diffusion et au piégeage de l'hydrogène. Une telle démarche itérative, couplant expérience et simulation, permet de limiter les risques de conclusions erronées lors de l'analyse des données expérimentales obtenues par TDS.

7.5 Conclusions

Ces travaux avaient pour objectif de mieux comprendre les interactions entre l'hydrogène absorbé et des matériaux sensibles à la **C**orrosion **S**ous **C**ontrainte (CSC) lorsqu'ils sont exposés au milieu primaire des **R**éacteurs à **E**au **P**ressurisée (REP). Deux alliages ont étudiés : (i) un alliage à base nickel (A600) et (ii) un acier inoxydable (SS316L). Ces alliages sont utilisés pour la fabrication de composants fondamentaux des REP, tels que le faisceau tubulaire des générateurs de vapeur (A600) et des composants internes à la cuve du réacteur (SS316L). L'hydrogène est présent dans le circuit primaire des REP, à la fois sous la forme d'un gaz dissous ($H_{2(g)}$) et comme élément chimique constituant du solvant (H_2O). C'est pourquoi l'interaction entre le milieu primaire et les alliages qui y sont exposés peuvent conduire à l'absorption d'hydrogène par ces derniers.

Une fois absorbé, l'hydrogène va progresser vers le cœur de l'alliage. Durant cette phase de transport, il est susceptible d'interagir avec les sites interstitiels du réseau cristallin mais également avec différentes hétérogénéités présentes au sein du matériau, parmi lesquelles on peut notamment citer : les joints de grains, les dislocations, les lacunes, les précipités, etc. Les atomes d'hydrogène peuvent avoir une forte affinité ou interagir différemment avec ces différents types de site ce qui peut éventuellement conduire au piégeage de l'hydrogène selon la nature

de ces hétérogénéités. Ce “piégeage” peut avoir pour effet de ralentir la diffusion apparente de l'hydrogène et conduire à une accumulation locale de cet élément au voisinage des sites de piégeage présents au sein de l'alliage. Or, cette accumulation peut en retour causer une dégradation des propriétés mécaniques locales et ainsi augmenter la sensibilité de l'alliage aux phénomènes de dégradation sous environnement telle que la formation de fissures de CSC.

7.5.1 Vue d'ensemble des résultats obtenus dans le cadre de cette étude

Ces travaux ont permis de coupler une approche expérimentale à la simulation numérique dans l'objectif de caractériser la diffusion interstitielle et le piégeage (sur différents types de site) de l'hydrogène dans deux alliages austénitiques, l'alliage 600 et l'acier SS316L, et pour deux types de sites de piégeage : les carbures de chrome et les dislocations. Dans l'objectif de travailler sur des matériaux bien caractérisés et non pas sur des systèmes complexes, des **M**atériaux **M**odèles (MM) ont été utilisés. Ces matériaux ont été élaborés à partir d'alliages industriels (A600 and SS316L) via une série de traitements thermiques ou thermomécaniques. La première étape de ces traitements avait pour objectif d'éliminer la majorité des sites de piégeage et d'obtenir ainsi un matériau modèle dans lequel la diffusion serait prépondérante, dit PDS. Puis à partir de ce matériau de référence, des sites de piégeages ont été générés de manière contrôlée pour produire une série de matériaux modèles dits DTS, dans lesquels les interactions H-matériau peuvent être associées à la diffusion et à un phénomène de piégeage unique, soit sur des carbures de chrome, soit sur des dislocations.

Après élaboration, ces matériaux modèles ont été chargés en deutérium (^{2}H), un traceur isotopique de l'hydrogène, puis analysés par **S**pectroscopie de **D**ésorption **T**hermique (TDS). La TDS est une technique d'analyse qui permet l'acquisition des flux de désorption de différentes espèces chimiques (en fonction du temps et de la température) désorbant d'un matériau soumis à une rampe de température ou à un maintien isotherme.

La première étape de la caractérisation des interactions H-matériau a consisté à étudier la diffusion interstitielle de l'hydrogène au sein du matériau. Pour ce faire, des spectres TDS ont été acquis sur matériaux modèles de type PDS. Afin d'extraire les paramètres cinétiques associés à la diffusion de ces spectres, une méthode numérique a été développée et mise en œuvre. Cette méthode est basée sur les équations de McNabb et Foster [107] décrivant la diffusion et le piégeage de l'hydrogène dans un matériau cristallin. A partir de l'ajustement des spectres expérimentaux via le code numérique développé, **les paramètres cinétiques associés à la diffusion de l'hydrogène (D_0 and E_D) dans l'alliage 600**

et l'acier SS316L ont pu être extraits (Table 7.2). Un des avantages de la TDS pour ce type de détermination est qu'elle permet une acquisition en continue sur une large gamme de température, et a permis ainsi **la détermination et la validation de ces paramètres sur une gamme de température allant de 294 K à 800 K, au travers d'expériences isothermes et non-isothermes**. Une fois la diffusion interstitielle dans ces alliages caractérisée, les interactions de piégeage et de dépiégeage prenant place entre l'hydrogène et un type de site particulier ont été explorées.

Les spectres TDS obtenus après vieillissement à haute température sur des matériaux modèles de type DTS, dans lesquels un type de site de piégeage particulier a été isolé, ont été ajustés via la simulation numérique dans l'objectif de **déterminer les paramètres cinétiques associés à différents types de site de piégeage existant au sein de l'alliage 600** (Table 7.3). Les constantes cinétiques ainsi obtenues pour les carbures de chrome (inter- and intragranulaires (IIC) ou localisés préférentiellement le long des joints de grains (GBC)) et les dislocations constituent les premiers jeux complets de paramètres cinétiques associés au piégeage dans l'alliage 600 disponibles dans la littérature et sont parmi les seuls disponibles quel que soit l'alliage considéré [105].

7.5.2 Conclusions finales

Cette étude a permis d'explorer en profondeur les interactions hydrogène-matériau relatives à la diffusion et au piégeage prenant place au sein de deux alliages austénitiques. Les difficultés qui peuvent être rencontrées lors de l'utilisation des méthodes traditionnellement mises en œuvre pour l'étude de ces interactions, et plus généralement l'apport d'un couplage entre expériences sur matériaux modèles et simulation numérique ont été discutées. Il a également été montré que cette dernière démarche permet de limiter les risques de conclusions erronées lors de l'analyse des données expérimentales obtenues par TDS.

Parmi les résultats obtenus dans cette étude, les plus notables, vis à vis des problématiques dans lesquelles les interactions hydrogène-matériau ont un rôle prépondérant, peuvent être résumés comme suit.

- **Le coefficient de diffusion de l'hydrogène a pu être déterminé et validé sur une large gamme de température.**
- **Un jeu complet de paramètres cinétiques relatifs au piégeage et au dépiégeage a pu être déterminé pour deux types de sites** existant au sein de l'alliage 600 (carbures de chrome et dislocations).
- **Il a pu être démontré que les joints de grains ont un effet négligeable sur la diffusion de l'hydrogène dans l'alliage 600, dans une gamme**

de température allant de 294 K à 800 K.

De plus, **des avancées importantes dans le développement de méthode numérique simulant ce type d'interactions sur la base des équations de McNabb et Foster** ont été réalisées, telles que :

- la simulation de la diffusion et du piégeage de l'hydrogène simultanément,
- la prédiction des populations respectives d'hydrogène piégé et réticulaire,
- la simulation des spectres de désorption en tenant compte des paramètres

expérimentaux ayant une influence majeure et des différentes étapes mis en jeu dans le processus expérimental, ce qui permet de tenir compte de "l'histoire" de l'échantillon.

Ces paramètres incluent notamment le temps (t), la température (T) et ses variations ($T(t)$ et ϕ) pendant les étapes de chargement en deutérium, de transfert et/ou de vieillissement et durant l'analyse par TDS. De plus **la méthode numérique développée est facilement adaptable à des systèmes plus complexes que ceux étudiés**, tels que ceux dans lesquels :

- il existe plusieurs types de site de piégeage,
- une distribution non-homogène de la densité de site doit être prise en compte,
- une évolution temporelle de la densité de site doit être prise en compte,
- il est nécessaire de généraliser la modélisation à 2 ou 3 dimensions.

Ces possibilités d'évolution du code peuvent se révéler particulièrement intéressantes dans l'objectif de traiter dans le futur des systèmes dans lesquels la densité de site évolue en fonction de t et/ou T (comme c'est typiquement le cas pour les lacunes) ou prendre en considération l'effet d'une contrainte imposée au matériau comme c'est souvent le cas dans les applications industrielles.

La nouvelle approche qui a été développée dans le cadre de cette étude (i. e. le couplage entre expérience de TDS sur matériaux modèles et simulation) peut être appliquée à différents types de métaux et alliages et n'est pas limitée aux applications d'intérêt nucléaire. Elle peut en effet s'appliquer aussi à des problématiques telles que l'élaboration d'acier ou le stockage de l'hydrogène. Enfin, les résultats obtenus dans ces travaux constituent une première

contribution à l'établissement d'une base de données relative à la diffusion et à la cinétique de piégeage et de dépiégeage dans les métaux et alliages. Les données cinétiques qui ont été obtenues et le code qui a été développé quant à la diffusion et au piégeage de l'hydrogène peuvent être incorporés dans un code de simulation plus large, prenant en compte d'autres phénomènes prépondérants dans la CSC des matériaux exposés en milieu primaire des REP. Toutefois, avant d'atteindre un tel objectif, les données acquises ici doivent être couplées avec un modèle cinétique permettant de décrire l'absorption d'hydrogène parallèlement à la formation de la couche d'oxyde protectrice qui se développe à la surface des alliages austénitiques exposés en milieu primaire . Ce couplage est nécessaire pour obtenir une vision plus complète du rôle que l'hydrogène peut jouer dans les phénomènes de CSC en milieu primaire des REP.

Bibliography

[1] A. Pundt and R. Kirchheim, "Hydrogen in metals: Microstructural aspects," *Annu. Rev. Mater. Res.*, vol. 36, pp. 555–608, 2006.

[2] M. Coriou, Grall, L. GalL, and Vettier, "Corrosion fissurante sous contrainte de l'inconel dans l'eau à haute température," tech. rep., Commissariat à l'énergie atomique, 1960.

[3] R. Rebak and Z. Szklarska-Sluakiwska, "The mechanism of stress corrosion cracking of alloy 600 in high temperature water," *Corr. Sci.*, vol. 38, no. 6, pp. 971–988, 1996.

[4] K. Arioka, T. Miyamoto, T. Yamada, and M. Aoki, "Crack initiation of TT690 and carbon steel," September 19, 2014 2014.

[5] P. Andresen and F. Ford, "Life prediction by mechanistic modeling and system monitoring of environmental cracking of iron and nickel alloys in aqueous systems," *Mater. Sci. Eng., A*, vol. 103, pp. 167–184, 1988.

[6] D. Macdonlad and M. Urquidi-Macdonald, "A coupled envoronment model for stress corrosion cracking in sensitized type 304 stainless steel in LWR environments," *Corr. Sci.*, vol. 32, no. 1, pp. 51–81, 1991.

[7] P. Scott, "An overview of internal oxidation as a possible explanation of intergranular stress corrosion cracking of alloy 600 in PWRs," in *Ninth International Symposium on Environmental Degradation of Materials in Nuclear Power Systems - Water Reactors* (F. Ford, S. Bruemmer, and G. Was, eds.), The Minerals, Metals & Materials Society (TMS).

[8] D. Symons, "The effect of hydrogen on the fracture toughness of alloy X-750 at elevated temperatures," *J. Nucl. Mater.*, vol. 265, pp. 225–231, 1999.

[9] R. Bandy and D. Van Rooyen, "Stress corrosion cracking of inconel alloy 600 in high temperature water - an update," *Corr. - NACE*, vol. 40, no. 8, pp. 425–430, 1984.

[10] F. Lecoester, J. Chêne, and D. Noel, "Hydrogen embrittlement of the Ni-base alloy 600 correlated with hydrogen transport by dislocations," *Mater. Sci. Eng., A*, vol. 262, pp. 173–183, 1999.

[11] J. Chêne and A.-M. Brass, "Role of temperature and strain rate on the hydrogen-induced intergranular rupture in alloy 600," *Metall. Mater. Trans. A*, vol. 35A, pp. 457–464, 2004.

[12] D. Caron, *Influence de l'hydrogène sur la vitesse de propagation des fissures de corrosion sous contrainte dans l'alliage 600 en milieu primaire des reacteurs nucleaires à eau sous pression.* PhD thesis, 2000, Institut national des sciences appliquées de Lyon.

[13] G. Furutani, N. Nakajima, T. Konishi, and M. Kodama, "Stress corrosion cracking on irradiated 316 stainless steel," *J. Nucl. Mater.*, vol. 288, pp. 179–186, 2001.

[14] F. Meng, Z. Lu, T. Shoji, J. Wang, E.-h. Han, and W. Ke, "Stress corrosion cracking of uni-directionally cold worked 316NG stainless steel in simulated pwr primary water with various dissolved hydrogen concentrations," *Corrosion Science*, vol. 53, no. 8, pp. 2558–2565, 2011.

[15] Y. Qiu, T. Shoji, and Z. Lu, "Effect of dissolved hydrogen on the electrochemical behaviour of alloy 600 in simulated PWR primary water at 290 C," *Corrosion Science*, vol. 53, no. 5, pp. 1983–1989, 2011.

[16] T. Terachi, T. Yamada, T. Miyamoto, and K. Arioka, "SCC growth behaviors of austenitic stainless steels in simulated PWR primary water," *Journal of Nuclear Materials*, vol. 426, no. 1-3, pp. 59–70, 2012.

[17] F. Jambon, L. Marchetti, F. Jomard, and J. Chêne, "Mechanism of hydrogen absorption during the exposure of alloy 600-like single-crystals to PWR primary simulated media," *J. Nucl. Mater.*, vol. 414, no. 3, pp. 386–392, 2011.

[18] F. Jambon, *Mécanismes d'absorption d'hydrogène et interactions hydrogène - défauts : Implications en corrosion sous contrainte des alliages à base nickel en millieu primaire des réaceurs à eau pressurisée.* PhD thesis, 2012, Université d'Evry Val d'Essonne.

[19] F. Jambon, L. Marchetti, F. Jomard, and J. Chêne, "Characterization of oxygen and hydrogen migration through oxide scales formed on nickel-base alloys in pwr primary medium conditions," *Solid State Ionics*, vol. 231, pp. 69–73, 2013.

[20] M. Dumerval, S. Perrin, L. Marchetti, M. Tabarant, F. Jomard, and Y. Wouters, "Hydrogen absorption associated with the corrosion mechanism of 316L stainless steels in primary medium of pressurized water reactor (PWR)," *Corrosion Science*, vol. 85, pp. 251–257, 2014.

[21] K. Arioka, T. Yamada, T. Terachi, and G. Chiba, "Influence of carbide precipitation and rollling direction on intergranular stress corrosion cracking of austenitic stainless steels in hydrogenated high-temperature water," *Corr.*, vol. 62, no. 7, pp. 568–575, 2006.

[22] D. Symons, G. A. Young, and J. Scully, "The effect of strain on the trapping of hydrogen at grain-boundary carbides in Ni-Cr-Fe alloys," *Metall. Mater. Trans. A*, vol. 32, pp. 369–378, 2001.

[23] R. Scarberry, S. Pearman, and J. Crum, "Precipitation reactions of inconel alloy 600 and their effect on corrosion behavior," *National Asso. Corr. Engineers*, vol. 32, no. 10, pp. 401–406, 1976.

[24] T. Matsumoto, J. Eastman, and H. Birnbaum, "Direct observations of enhanced dislocation mobility due to hydrogen," *Scripta Metall.*, vol. 15, pp. 1033–1037, 1981.

[25] H. Birnbaum, "Mechanisms of hydrogen related fracture of metals," technical report, 1989.

[26] A. Troiano, "The role of hydrogen and other interstitials in the mechanical behavior of metals," *Trans. ASM*, vol. 52, pp. 54–80, 1690.

[27] T. Magnin, F. Foct, and O. De Bouvier, "Hydrogen effects on PWR SCC mechanisms in monocrystalline and polycrystalline alloy 600," in *Ninth Int. Symp. On Environmental Degradation of Materials in Nuclear Power Systems-Water Reactors*, pp. 27–39.

[28] G. Was, D. Paraventi, and J. Hertzberg, "Mechanisms of environmentally enhanced deformation and intergranular cracking of Ni–16Cr–9Fe alloys," in *EUROCORR '96*, pp. 410–420, EFC by the Institiut of Materials.

[29] A. Barnoush, *Hydrogen embrittlement, revisited by in situ electrochemical nanoindentation*. PhD thesis, 2009, Universität des Saarlandes.

[30] J. M. Bockris, J. McBreen, and L. Nanis, "The hydrogen evolution kinetics and hydrogen entry into α-iron," *J. Electrochem. Soc.*, vol. 112, no. 10, pp. 1025–1031, 1965.

[31] A. Turnbull, "Modelling of environmental assisted cracking," *Corr. Sci.*, vol. 34, no. 6, pp. 921–960, 1993.

[32] J. P. Diard, B. Le Gorrec, and C. Montella, *Cinétique Electrochimique*, vol. 1. 1996.

[33] C. Montella, "Discussion on permeation transients in terms of insertion reaction mechanism and kinetics," *J. Electroanal. Chem.*, vol. 465, pp. 37–50, 1999.

[34] C. Montella, "Review and theoretical analysis of ac–av methods for the investigation of hydrogen insertion I. diffusion formalism," *J. Electroanal. Chem.*, vol. 462, pp. 73–87, 1999.

[35] C. Montella, "EIS study of hydrogen insertion under restricted diffusion conditions i. two-step insertion reaction," *J. Electroanal. Chem.*, vol. 497, pp. 3–17, 2001.

[36] N. Amokrane, C. Gabrielli, E. Ostermann, and H. Perrot, "Investigation of hydrogen adsorption–absorption on iron by EIS," *Electrochim. Acta*, vol. 53, no. 2, pp. 700–709, 2007.

[37] D. Lister, R. Davidson, and E. McAlpine, "The mechanism and kinetics of corrosion product release from stainless steel in lithiated high-temperature water," *Corr. Sci.*, vol. 27, pp. 113–140, 1987.

[38] T. Terachi, K. Fujii, and K. Arioka, "Microstructural characterisation of SCC crack tip and oxide film for SUS316 stainless steel in simulated PWR primary water at 320c," *J. Nucl. Sci. Tech.*, vol. 42, no. 2, pp. 225–232, 2005.

[39] S. Perrin, L. Marchetti, C. Duhamel, M. Sennour, and F. Jomard, "Influence of irradiation on the oxide film formed on 316L stainless steel in PWR primary water," *Oxid. Metal*, vol. 80, pp. 623–633, 2013.

[40] E. Rota, P. Waelbroeck, P. Wienhold, and J. Winter, "Measurements of surface and bulk properties for the interaction of hydrogen with inconel 600," *J. Nucl. Mater.*, vol. 111-112, pp. 233–239, 1982.

[41] K. Sakamoto and M. Sugisaki, "Diffusion coefficient of tritium in Ni-based alloy," *Fusion Sci. Technol.*, vol. 41, pp. 912–914, 2002.

[42] J. Chêne, F. Lecoester, A. Brass, and D. Noel, "SIMS analysis of deuterium diffusion in alloy 600: The correlation between fracture mode and deuterium concentration profile," *Corr. Sci.*, vol. 40, no. 1, pp. 49–60, 1998.

[43] M. Uhlemann and B. Pound, "Diffusivity, solubility and trapping behavior of hydrogen in alloys 600, 690tt and 800," *Corr. Sci.*, vol. 40, no. 4/5, pp. 645–662, 1998.

[44] A.-M. Brass and J. Chêne, "Hydrogen uptake in 316l stainless steel: Consequences on the tensile properties," *Corrosion Science*, vol. 48, no. 10, pp. 3222–3242, 2006.

[45] S. Changqi, W. Aiju, and C. Quingwang, "The behavior of diffusion and permeation of tritium through 316L stainless steel," *J. Nucl. Mater.*, vol. 197, pp. 322–324, 1991.

[46] K. Forcey, D. Ross, and J. Simpson, "Hydrogen transport and solubility in 316L and 1.4914 steels for fusion reactor applications," *J. Nucl. Mater.*, vol. 160, pp. 117–124, 1988.

[47] D. Grant, D. Cummings, and D. Blackburn, "Hydrogen in 316L steel - diffusion, permeation and surface reaction," *J. Nucl. Mater.*, vol. 152, pp. 139–145, 1988.

[48] P. Tison, *Influence de l'hydrogène sur le comportement des métaux, Tome I Influence des oxydes superficiels et du piégeage sur la permeabilité à l'hydrogène et ses isotopes d'alliages à base de fer, notamment des aciers de construction et des aciers inoxydables.* PhD thesis, 1983, University Pierre et Marie Curie (Paris 6).

[49] W. Robertson, "Hydrogen permeation and diffusion in inconel 718 and incoloy 903," *Metall. Trans. A*, vol. 8A, no. November, pp. 1709–1712, 1977.

[50] E. Wimmer, W. Wolf, J. Sticht, P. Saxe, C. Geller, R. Najafabadi, and G. Young, "Temperature-dependent diffusion coefficients from ab initio computations: Hydrogen, deuterium, and tritium in nickel," *Physical Review B*, vol. 77, no. 13, pp. 1–11, 2008.

[51] L. Darken and R. Smith, "Behavior of hydrogen in steel during and after immersion in acid," *Corr.*, vol. 5, no. 1, pp. 1–16, 1948.

[52] M. R. Louthan, J. Donovan, and G. J. Caskey, "Hydrogen diffusion and trapping in nickel," *Acta Metall.*, vol. 23, pp. 745–749, 1975.

[53] A. Chanfreau, *Etude de la precipitation de l'helium 3 dans un acier inoxydable 316L; Influence sur la diffusion de l'hydrogène.* PhD thesis, 1992, University de Paris-Sud Centre d'Orsay.

[54] A.-M. Brass and A. Chanfreau, "Accelerated diffusion of hydrogen along grain boundaries in nickel," *Acta Mater.*, vol. 44, no. 9, pp. 3823–3831, 1996.

[55] T. Harris and R. Latanision, "Grain boundary diffusion of hydrogen in nickel," *Metall. Trans. A*, vol. 22, pp. 351–355, 1991.

[56] A. Oudriss, J. Creus, J. Bouhattate, E. Conforto, C. Berziou, C. Savall, and X. Feaugas, "Grain size and grain-boundary effects on diffusion and trapping of hydrogen in pure nickel," *Acta Mater.*, vol. 60, no. 19, pp. 6814–6828, 2012.

[57] A. Oudriss, J. Creus, J. Bouhattate, C. Savall, B. Peraudeau, and X. Feaugas, "The diffusion and trapping of hydrogen along the grain boundaries in polycrystalline nickel," *Scripta Mater.*, vol. 66, no. 1, pp. 37–40, 2012.

[58] T. Dieudonné, L. Marchetti, F. Jomard, M. Wery, J. Chêne, C. Allely, P. Cugy, and C. P. Scott, "SIMS analysis of deuterium absorption and diffusion in austenitic Fe-Mn-C steels," *Defect and Diffusion Forum*, vol. 323-325, pp. 477–483, 2012.

[59] J. Yao and J. Cahoon, "Experimental studies of grain boundary diffusion of hydrogen in metals," *Acta Metall.*, vol. 39, no. 1, pp. 119–126, 1991.

[60] K. Ono and M. Meshii, "Hydrogen detrapping from grain boundaries and dislocations in high purity iron," *Acta Metall.*, vol. 40, no. 6, pp. 1357–1364, 1992.

[61] J. Austin and T. Elleman, "Tritium diffusion in 304- and 316-stainless steel in the temperature range 25 to 222 C," *J. Nucl. Mater.*, vol. 43, pp. 119–125, 1972.

[62] M. R. Louthan, J. Donovan, and G. J. Caskey, "Tritium absorption in type 304L stainless steel," *Nuc. Tech.*, vol. 26, pp. 192–200, 1975.

[63] P. Abraham, T. Elleman, and K. Verghese, "Diffusion and trapping of tritium in grain boundaries of 304L stainless steel," *J. Nucl. Mater.*, vol. 73, pp. 77–88, 1978.

[64] R. Calder, T. Elleman, and K. Verghese, "Grain boundary diffusion of tritium in 304- and 316-stainless steels," *J. Nucl. Mater.*, vol. 46, pp. 46–52, 1973.

[65] L. Harrison, "Influence of dislocations on diffusion kinetics in solids with particular difference to the alkali halides," *Trans. Faraday Soc.*, vol. 57, no. 1961, pp. 1191–1198, 1961.

[66] T. Harris, *Hydrogen diffusion and trapping in electrodeposited nickel.* PhD thesis, 1979, Massachusetts Institute of Technology.

[67] Y. Mishin, C. Herzig, J. Bernardini, and W. Gust, "Grain boundary diffusion: fundamentals to recent developments," *Int. Mat. Rev.*, vol. 42, no. 4, pp. 155–177, 1997.

[68] R. C. Frank, R. W. Lee, and R. L. Williams, "Ratio of the diffusion coefficients for the diffusion of hydrogen and deuterium in steel," *Journal of Applied Physics*, vol. 29, no. 6, pp. 898–900, 1958.

[69] R. Oriani, "The diffusion and trapping of hydrogen in steel," *Acta Mater.*, vol. 18, pp. 147–157, 1970.

[70] G. Pressouyre, "Hydrogen traps, repellers, and obstacles in steel; consequences on hydrogen diffusion, solubility, and embrittlement," *Metall. Trans. A*, vol. 14A, pp. 2189–2193, 1983.

[71] M. R. Louthan, G. J. Caskey, J. Donovan, and D. J. Rawl, "Hydrogen embrittlement of metals," *Mater. Sci. Eng.*, vol. 10, pp. 357–368, 1972.

[72] F. Lecoester, *Interactions hydrogène-alliage 600 (NC15Fe): application au cas des tubes de générateur de vapeur des réacteurs à eau pressurisée, soumis au milieu primaire.* PhD thesis, 1997, Université Paris-Sud, Université XI Orsay.

[73] A.-M. Brass and J. Chêne, "Influence of deformation on the hydrogen behavior in iron and nickel base alloys: a review of experimental data," *Mater. Sci. Eng., A*, vol. 242, pp. 210–221, 1998.

[74] M. Nagumo, K. Ohta, and H. Saitoh, "Deformation induced defects in iron revealed by thermal desorption spectroscopy of tritium," *Scripta Mater.*, vol. 40, no. 3, pp. 313–319, 1999.

[75] M. Nagumo, M. Nakamura, and K. Takai, "Hydrogen thermal desorption relevant to delayed-fracture susceptibility of high-strength steels," *Metall. Mater. Trans. A*, vol. 32A, pp. 339–337, 2001.

[76] W. A. Counts, C. Wolverton, and R. Gibala, "First-principles energetics of hydrogen traps in α-Fe: Point defects," *Acta Materialia*, vol. 58, no. 14, pp. 4730–4741, 2010.

[77] F. Besenbacher, "Defect trapping of ion-implanted deuterium in nickel," *J. Appl. Phys.*, vol. 53, no. 5, pp. 3536–3546, 1982.

[78] Y. Fukai, T. Haraguchi, E. Hayashi, Y. Ishii, Y. Kurokawa, and J. Yanagawa, "Hydrogen-induced superabundant vacancies and diffusion enhancement in some *fcc* metals," *Defect Diffus. Forum*, vol. 194-199, pp. 1063–1068, 2001.

[79] Y. Fukai, "Superabundant vacancies formed in metal-hydrogen alloys," *Phys. Scr.*, vol. T103, pp. 11–14, 2003.

[80] Y. Fukai, S. Yokota, and J. Yanagawa, "The phase diagram and superabundant vacancy formation in Co–H alloys," *J. Alloys Compd.*, vol. 407, no. 1, pp. 16–24, 2006.

[81] Y. Fukai and H. Sugimoto, "Formation mechanism of defect metal hydrides containing superabundant vacancies," *J. Phys.: Condens. Matter*, vol. 19, no. 43, pp. 1–24, 2007.

[82] G. Young and J. Scully, "Evidence that carbide precipitation produces hydrogen traps in Ni-17Cr-8Fe alloys," *Scripta Mater.*, vol. 36, no. 6, pp. 713–719, 1997.

[83] G. Pressouyre, "A classification of hydrogen traps in steel," *Metall. Trans. A*, vol. 10, pp. 1571–1573, 1979.

[84] H. Lee and J. Lee, "Hydrogen trapping by TiC particles in iron," *Acta Metall.*, vol. 32, no. 1, pp. 131–136, 1948.

[85] F.-G. Wei, T. Hara, and K. Tsuzaki, "Precise determination of the activation energy for desorption of hydrogen in two Ti-added steels by a single thermal-desorption spectrum," *Metall. Mater. Trans. B*, vol. 35 B, pp. 587–597, 2004.

[86] F.-G. Wei and K. Tsuzaki, "Quantitative analysis on hydrogen trapping of TiC particles in steel," *Metall. Mater. Trans. A*, vol. 37, pp. 331–352, 2006.

[87] W. Choo and J. Y. Lee, "Hydrogen trapping phenomena in carbon steel," *J. Mater. Sci.*, vol. 17, pp. 1930–1938, 1982.

[88] K. Ebihara and H. Kaburaki, "Numerical modeling of thermal desorption spectra of hydrogen : A review of thermal desorption models," *ISIJ Int.*, vol. 52, no. 2, pp. 181–186, 2012.

[89] C. Hurley, F. Jambon, F. Martin, L. Marchetti, J. Chêne, C. Blanc, and E. Andrieu, "An in-depth study of the interactions between hydrogen and microstructural defects in Fe and Ni-based alloys through thermal desorption spectroscopy (TDS) and numerical simulation," in *SteelyHydrogen 2nd International Conference on Steel and Hydrogen* (OCAS, ed.), vol. 1, pp. 315–325, OCAS, 2014.

[90] C. Hurley, F. Martin, L. Marchetti, J. Chêne, C. Blanc, and E. Andrieu, "Numerical modeling of thermal desorption mass spectroscopy (TDS) for the study of hydrogen diffusion and trapping interactions in metals," *Int. J. Hydrogen Energy*, vol. 40, no. 8, pp. 3402–3414, 2015.

[91] W. Choo and J. Lee, "Thermal analysis of trapped hydrogen in pure iron," *Metall. Mater. Trans. A*, vol. 13A, pp. 135–140, 1982.

[92] F.-G. Wei and K. Tsuzaki, "Response of hydrogen trapping capability to microstructural change in tempered Fe–0.2C martensite," *Scripta Mater.*, vol. 52, no. 6, pp. 467–472, 2005.

[93] S. Frappart, X. Feaugas, J. Creus, F. Thebault, L. Delattre, and H. Marchebois, "Hydrogen solubility, diffusivity and trapping in a tempered Fe–C–Cr martensitic steel under various mechanical stress states," *Mater. Sci. Eng., A*, vol. 534, pp. 384–393, 2012.

[94] P. Combette and J. Renard, M. Grilhe, "Internal friction in nickel containing hydrogen effect of relaxation and trapping of dislocations by hydrogen," *Phys. Stat. Sol.*, no. 11, pp. 677–686, 1972.

[95] G. Young and J. Scully, "The diffusion and trapping of hydrogen in high purity aluminum," *Acta Mater.*, vol. 46, no. 18, pp. 6337–6349, 1998.

[96] T. Izumi and G. Itoh, "Thermal desorption spectroscopy study on the hydrogen trapping states in a pure aluminum," *Materials Transactions*, vol. 52, no. 2, pp. 130–134, 2011.

[97] S. Smith and J. Scully, "The identification of hydrogen trapping states in an Al-Li-Cu-Zr alloy using thermal desorption spectroscopy," *Metall. Mater. Trans. A*, vol. 31A, pp. 179–193, 2000.

[98] T. Asaoka, G. Lapasset, M. Aucouturier, and P. Lacombe, "Observation on hydrogen trapping in Fe-0.15wt% Ti alloy by high resolution autoradiography," *Corr.*, vol. 34, no. 2, pp. 39–47, 1978.

[99] H. Asahi, D. Hirakami, and S. Yamasaki, "Hydrogen trapping behavior in vanadium-added steel," *ISIJ Int.*, vol. 43, no. 4, pp. 527–533, 2003.

[100] S. M. Myers, D. Follstaedt, F. Besenbacher, and J. Bottiger, "Trapping and surface permeation of deuterium in He-implanted Fe," *Journal of Applied Physics*, vol. 53, no. 12, pp. 8734–8744, 1982.

[101] F. Besenbacher, B. B. Nielsen, and S. M. Myers, "Defect trapping of ion-implanted deuterium in copper," *Journal of Applied Physics*, vol. 56, no. 12, pp. 3384–3383, 1984.

[102] B. Lengeler, S. Mantl, and W. Triftshäuser, "Interaction of hydrogen and vacancies in copper investigated by positron annihilation," *J. Phys. F: Metal Phys.*, vol. 8, no. 8, pp. 1691–1698, 1978.

[103] S. M. Myers and F. Besenbacher, "Trapping of ion-implanted deuterium in molybdenum," *Journal of Applied Physics*, vol. 60, no. 10, pp. 3499–3507, 1986.

[104] A. Turnbull, M. Carroll, and D. Ferriss, "Analysis of hydrogen diffusion and trapping in a 13% chromium martensitic stainless steel," *Acta Metall.*, vol. 37, no. 7, pp. 2039–2046, 1988.

[105] A. Turnbull, R. Hutchings, and D. Ferriss, "Modelling of thermal desorption of hydrogen from metals," *Mater. Sci. Eng., A*, vol. 238, pp. 317–328, 1997.

[106] K. Wilson and M. Baskes, "Deuterium trapping in irradiated 316 stainless steel," *J. Nucl. Mater.*, vol. 76 77, pp. 291–297, 1978.

[107] A. McNabb and P. Foster, "A new analysis of the diffusion of hydrogen in iron and ferritic steels," *Trans. Metall. Soc. AIME*, vol. 227, pp. 618–627, 1963.

[108] T. Kasuya and M. Fuji, "Diffusion with multiple kinds of trapping sites," *J. Appl. Phys.*, vol. 83, pp. 3039–3048, 1998.

[109] R. Kirchheim, "Solubility, diffusivity and trapping of hydrogen in dilute alloys. Deformed and amorphous metals - II," *Acta Metall.*, vol. 30, pp. 1069–1078, 1982.

[110] R. Kirchheim, F. Sommer, and G. Schluckebier, "Hydrogen in amorphous metals - I," *Acta Metall.*, vol. 30, pp. 1059–1068, 1982.

[111] R. B. McLellan, "Thermodynamics and diffusion behavior of interstitial solute atoms in non-perfect solvent crystals," *Acta Metall.*, vol. 27, pp. 1655–1663, 1979.

[112] J. Leblond and D. Dubois, "A general mathematical description of hydrogen diffusion in steels - I. derivation of diffusion equations from Boltzmann-type transport equations," *Acta Metall.*, vol. 31, no. 10, pp. 1459–1469, 1983.

[113] J. Leblond and D. Dubois, "A general mathematical description of hydrogen diffusion in steels - II. numerical study of permeation and determination of trapping parameters," *Acta Metall.*, vol. 31, no. 10, pp. 1471–1478, 1983.

[114] J. Leblond, D. Nejem, D. Dubois, and S. Talbot-Besnard, "Experimental and numerical study of diffusion and trapping of hydrogen in plastically deformed A508.C1.3 steel at room temperature," *Acta Metall.*, vol. 35, no. 7, pp. 1703–1714, 1987.

[115] G. Pressouyre, "Trap theory of hydrogen embrittlement," *Acta Metall.*, vol. 28, pp. 895–911, 1980.

[116] J. Chateau, D. Delafosse, and T. Magnin, "Numerical simulations of hydrogen-dislocation interactions in *fcc* stainless steels. Part I: hydrogen-dislocation interactions in bulk crystals," *Acta Mater.*, vol. 50, pp. 1507–1522, 2002.

[117] J. Chateau, D. Delafosse, and T. Magnin, "Numerical simulations of hydrogen-dislocation interactions in *fcc* stainless steels. Part II: hydrogen effects on crack tip plasticity at a stress corrosion crack," *Acta Mater.*, vol. 50, pp. 1523–1538, 2002.

[118] R. Kirchheim and U. Stolz, "Monte-Carlo simulations of interstitial diffusion and trapping -II. Amorphous metals," *Acta Metall.*, vol. 35, no. 2, pp. 281–291, 1987.

[119] R. Kirchheim, "Monte-Carlo simulations of interstitial diffusion and trapping -I. One type of traps and dislocations," *Acta Metall.*, vol. 35, no. 2, pp. 271–280, 1987.

[120] P. Sarrazin, A. Galerie, and J. Fouleier, *Mechanisms Of High Temperature Corrosion: A Kinetic Approach*. Zurich, Switzerland: Trans Tech Publications, Ltd., 2008.

[121] K. Ebihara, H. Kaburaki, T. Suzudo, and K. Takai, "A numerical study on the validity of the local equilibrium hypothesis in modeling hydrogen thermal desorption spectra," *ISIJ Int.*, vol. 49, no. 12, pp. 1907–1913, 2009.

[122] J. Svoboda and F. D. Fischer, "Modelling for hydrogen diffusion in metals with traps revisited," *Acta Mater.*, vol. 60, no. 3, pp. 1211–1220, 2012.

[123] J. Svoboda, G. Mori, A. Prethaler, and F. D. Fischer, "Determination of trapping parameters and the chemical diffusion coefficient from hydrogen permeation experiments," *Corr. Sci.*, vol. 82, pp. 93–100, 2014.

[124] R. Kirchheim, "Hydrogen solubility and diffusivity in defective and amporphous metals," *Prog. Mat. Sci.*, vol. 32, pp. 261–325, 1988.

[125] G. Hultquist, "Why copper may be able to corrode in pure water," *Corrosion Science*, vol. 93, pp. 327–329, 2015.

[126] G. Hultquist, M. J. Graham, J. L. Smialek, and B. Jönsson, "Hydrogen in metals studied by thermal desorption spectroscopy (TDS)," *Corr. Sci.*, vol. 93, pp. 324–326, 2015.

[127] J. M. Bockris, M. Genshaw, and M. Fullenwider, "The electro-permeation of hydrogen into metals," *Electrochemica Acta*, vol. 15, pp. 47–60, 1970.

[128] G. J. Caskey and W. L. Pillinger, "Effect of trapping on hydrogen permeation," *Metall. Trans. A*, vol. 6, pp. 467–476, 1975.

[129] A.-M. Brass, F. Guillon, and S. Vivet, "Quantification of hydrogen diffusion and trapping in 2.25Cr-1Mo-V steels with the electrochemical permeation technique and melt extractions," *Metall. Mater. Trans. A*, vol. 35A, pp. 1449–1464, 2004.

[130] L. Moli-Sanchez, *Role of tempering on the hydrogen diffusion in a 34CrMo4 martensitic steel and the related embrittlement.* PhD thesis, 2012, Université d'Evry Val d'Essone.

[131] F. D. Fischer, J. Svoboda, and E. Kozeschnik, "Interstitial diffusion in systems with multiple sorts of traps," *Modell. Simul. Mater. Sci. Eng.*, vol. 21, no. 2, pp. 1–13, 2013.

[132] F. D. Fischer, G. Mori, and J. Svoboda, "Modelling the influence of trapping on hydrogen permeation in metals," *Corr. Sci.*, vol. 76, pp. 382–389, 2013.

[133] M. Mendelsohn and D. Gruen, "Temperature-programmed desorption (TPD) studies of ZrV1.6Fe0.4Hy and ZrV1.2Cr0.8Hy," *Mater. Res. Bull.*, vol. 16, no. 8, pp. 1027–1034, 1981.

[134] Y. Yagodzinskyy, O. Todoshchenco, S. Papula, and H. Hãnninen, "Hydrogen solubility and diffusion in austenitic stainless steels studied with thermal desorption spectroscopy," *Steel Res. J.*, vol. 82, no. 1, pp. 20–25, 2011.

[135] O. Todoshchenco, Y. Yagodzinskyy, S. Papula, and H. Hänninen, "Hydrogen solubility and diffusion in metastable austenitic stainless steels studies with thermal desorption spectroscopy," in *International Hydrogen Conference : Hydrogen-Materials Interactions 2012* (B. P. Somerday and P. Sofronis, eds.), pp. 615–623, ASME.

[136] O. Todoshchenko, Y. Yagodzinskyy, and H. Hänninen, "Thermal desorption of hydrogen from AISI 316L stainless steel and pure nickel," *Defect and Diffusion Forum*, vol. 344, pp. 71–77, 2013.

[137] G. Hultquist, P. Szakalos, M. J. Graham, A. B. Belonoshko, and A. Rosengren, "Reply to Lars O. Werme et al.: "Comments on 'water corrodes copper'"," *Catalysis Letters*, vol. 135, no. 3-4, pp. 167–168, 2010.

[138] A. M. Polyanskiy, V. A. Polyanskiy, and Y. A. Yakovlev, "Experimental determination of parameters of multichannel hydrogen diffusion in solid probe," *International Journal of Hydrogen Energy*, vol. 39, no. 30, pp. 17381–17390, 2014.

[139] E. Tal-Gutelmacher, D. Eliezer, and E. Abramov, "Thermal desorption spectroscopy (TDS)—application in quantitative study of hydrogen evolution and trapping in crystalline and non-crystalline materials," *Mater. Sci. Eng., A*, vol. 445-446, pp. 625–631, 2007.

[140] H. Kissinger, "Reaction kinetics in differential thermal analysis," *Anal. Chem.*, vol. 29, no. 11, pp. 1702–1706, 1957.

[141] S. Frappart, A. Oudriss, X. Feaugas, J. Creus, J. Bouhattate, F. Thébault, L. Delattre, and H. Marchebois, "Hydrogen trapping in martensitic steel investigated using electrochemical permeation and thermal desorption spectroscopy," *Scripta Mater.*, vol. 65, no. 10, pp. 859–862, 2011.

[142] K. Ebihara, H. Kaburaki, and K. Takai, "Numerical evaluation of the Choo and Lee's method for calculating hydrogen detrapping activation energies," in *2012 International Hydrogen Conference : Hydrogen-Materials Interactions* (B. P. Somerday and P. Sofronis, eds.), pp. 553–561, ASME.

[143] O. Todoshchenco, *Hydrogen effects on austenitic stainless steels and high-strength carbon steels*. Article dissertation, 2015.

[144] C. Hurley, F. Martin, L. Marchetti, C. Blanc, and E. Andrieu, "Etude par spectroscopie de désorption thermique des interactions hydrogène-défauts microstructuraux des aciers inoxydables : approche par des défauts "purs"," 2013.

[145] R. Kirchheim, "Keynote lecture: Diffusion controlled thermal desorption spectroscopy," in *Steelyhydrogen 2nd International Conference on Steel and Hydrogen* (OCAS, ed.), vol. 1, pp. 237–253, OCAS, 2014.

[146] D. Newey, M. Wilkins, and H. Pollock, "An ultra-low-load penetration hardness tester," *J. Phys. E: Sci. Instrum.*, vol. 15, pp. 119–122, 1982.

[147] C. Panait, A. Zielinska-Lipiec, T. Koziel, A. Czyrska-Filemonowicz, A.-F. Gourges-Lorenzon, and W. Bendick, "Evolution of dislocation density, size of subgrains and MX-type precipitates in a P91 steel durring creep and during thermal ageing at 600C,"

[148] V. Olden, A. Saai, L. Jemblie, and R. Johnsen, "A finite element study of hydrogen diffusion in duplex stainless steel," in *Steelyhydrogen 2nd International Conference on Steel and Hydrogen* (OCAS, ed.), vol. 1, pp. 189–200, OCAS, 2014.

[149] A. Turnbull and R. Hutchings, "Analysis of hydrogen atom transport in two-phase alloy," *Mater. Sci. Eng., A*, vol. 177, pp. 161–141, 1994.

[150] E. Owczarek and T. Zakroczymski, "Hydrogen transport in a duplex stainless steel," *Acta Mater.*, vol. 48, pp. 3059–3070, 2000.

[151] S. Lee and J. Lee, "The effect of the interface character of TiC particles on hydogen trapping in steel," *Acta Metall.*, vol. 35, no. 11, pp. 3695–2700, 1987.

[152] W. Choo, J. Y. Lee, and C. Cho, "Hydrogen solubility in pure iron and effects of alloying elements on the solubility in the temperature range 20 to 500°C," *J. Mater. Sci.*, vol. 16, pp. 1285–1292, 1981.

[153] D. Noel, F. Lecoester, A.-M. Brass, and J. Chêne, "Hydrogen diffusion and distribution in alloy 600 and related effects on plasticity." 1998.

[154] J. Bailey, "The dislocation density, flow stres and stored energy in deformed polycrystalline copper," *Phil. Mag.*, vol. 8, pp. 223–236, 1963.

[155] F. Delabrouille, *Caractérisation par MET des fissures de corrosion sous contrainte d'alliages à base de nickel*. PhD thesis, 2004.

[156] S. Chavez, G. Korth, and D. Harper, "High-temperature tensile and creep data for inconel 600, 305 stainless steels and SA106B carbon steel," *Nucl. Eng. Des.*, vol. 148, pp. 351–363, 1994.

[157] K. Kozaczek, B. Petrovic, C. Ruud, S. Kurtz, and A. McIlree, "Microstructural modelling of grain-boundary stresses in alloy 600," *J. Mater. Sci.*, vol. 30, pp. 2390–2400, 1995.

[158] D. Umbrello, R. M'Saoubi, and J. C. Outeiro, "The influence of Johnson–Cook material constants on finite element simulation of machining of AISI 316L steel," *International Journal of Machine Tools and Manufacture*, vol. 47, no. 3, pp. 462–470, 2007.

[159] X. Feaugas, "On the origin of the tensile flow stress in the stainless steel AISI 316L at 300 K: back stress and effective stress," *Acta Mater.*, vol. 47, no. 13, pp. 3617–3632, 1999.

[160] K. Kozaczek, A. Sinharoy, C. Ruud, and A. McIlree, "Micromechanical modelling of microstress fields around carbide precipitates in alloy 600," *Modell. Simul. Mater. Sci. Eng.*, vol. 3, pp. 829–843, 1995.

[161] M. Baskes, "A calculation of the surface recombination rate constant for hydrogen isotopes on metals," *J. Nucl. Mater.*, vol. 92, pp. 318–324, 1980.

[162] J. Lee, J. Lee, and W. Choo, "Thermal analysis of trapped hydrogen in AISI 4340 steel," *Metal Sci.*, pp. 423–427, 1982.

[163] C. Domain, R. Besson, and A. Legris, "Atomic scale ab initio study of Zr-H system: II. Interaction of H with plane defects and mechanical properties," *Acta Mater.*, vol. 52, pp. 1495–1502, 2004.

[164] A. Krom and A. Bakker, "Hydrogen trapping models in steel," *Metall. Mater. Trans. B*, vol. 31B, pp. 1475–1482, 2000.

[165] J. Chêne and A.-M. Brass, "Hydrogen transport by mobile dislocatoins in nickel base superalloy single crystals," *Scripta. Mater.*, vol. 42, no. 5, pp. 537–542, 1999.

[166] D. Guedes, A. Oudriss, S. Cohendoz, J. Creus, J. Bouhattate, X. Feaugas, F. Thebault, L. Delattre, and D. Koschel, "The influence of hydrogen flux on crack initiation in martensitic steels," *Proc. Mater. Sci.*, vol. 3, pp. 2024–2029, 2014.

[167] D. Guedes, A. Oudriss, G. Courlit, S. Cohendoz, P. Girault, J. Creus, J. Bouhattate, A. Metsue, F. Thebault, L. Delattre, D. Koschel, and X. Feaugas, "The influence of hydrostatic stress states on hydrogen flux in martensitic steels," in *SteelyHydrogen 2nd International Conference on Steel and Hydrogen* (OCAS, ed.), vol. 1, pp. 267–276, OCAS, 2014.

[168] C. Dimitrov, B. Sitaud, X. Zhang, O. Dimitrov, U. Dedek, and F. Dworschak, "Radiation-induced defects in solid solutions and intermetallic compounds based on the Ni-Al system: II recovery of radiation damage," *J. Phys.: Condens. Matter*, vol. 4, p. 16, 1992.

[169] M. Alemany, P. Desgardin, A. Chabli, F. Bertin, M. Gros-Jean, and M.-F. Barthe, "Positon annihilation spectroscopy: an emerging technique for characterizaton on oxygen vacancies in Hf-based-high-K materials," in *2015 International conference on frontiers of characterization and metrology for nanoelectronics*, 2015.

[170] R. Kirchheim, "Revisiting hydrogen embrittlement models and hydrogen-induced homogeneous nucleation of dislocations," *Scripta Mater.*, vol. 62, no. 2, pp. 67–70, 2010.

[171] F. Leardini, J. F. Fernández, J. Bodega, and C. Sánchez, "Isotope effects in the kinetics of simultaneous H and D thermal desorption from Pd," *J. Phys. Chem. Solids*, vol. 69, no. 1, pp. 116–127, 2008.

[172] A. Savara, W. Ludwig, and S. Schauermann, "Kinetic evidence for a non-langmuir-hinshelwood surface reaction: H/D exchange over Pd nanoparticles and Pd(111)," *Chemphyschem*, vol. 14, no. 8, pp. 1686–1695, 2013. Savara, Aditya Ludwig, Wiebke Schauermann, Swetlana Germany Chemphyschem. 2013 Jun 3;14(8):1686-95. doi: 10.1002/cphc.201300179. Epub 2013 Apr 12.

[173] Z. B. Güvenç and D. Güvenç, "Hydrogen recombination on a mixed adsorption layer at saturation on a metal surface: H→(D+H)sat+Ni()," *Surf. Sci.*, vol. 529, no. 1-2, pp. 11–22, 2003.